Doctoral Dissertation
博士論文

Spectroscopic Study and TMT/IRIS Instrumentation for Uncovering Galaxy Formation in Gaseous Large-Scale Structures (ガスの宇宙大規模構造における銀河形成を探るための分光学的研究と TMT/IRIS の装置開発)

A Dissertation Submitted for the Degree of Doctor of Philosophy
December 2019
令和元年 12 月博士 (理学) 申請

Department of Astronomy, Graduate School of Science,
The University of Tokyo
東京大学大学院理学系研究科天文学専攻

Shiro Mukae
向江 志朗

Ph.D. Thesis Committee:

Dr. Mamoru Doi (Institute of Astronomy, School of Science, University of Tokyo); Chair

—alphabetical order—

Dr. Takeo Minezaki (Institute of Astronomy, School of Science, University of Tokyo)

Dr. Kazuhiro Shimasaku (Department of Astronomy, Graduate School of Science, The University of Tokyo)

Dr. Hideki Takami (National Astronomical Observatory of Japan)

Dr. Hidenobu Yajima (Center for Computational Science, University of Tsukuba)

Thesis Advisor:

Dr. Masami Ouchi (Institute for Cosmic Ray Research, University of Tokyo; National Astronomical Observatory of Japan)

This thesis is based on the following papers:

PAPER-I: Shiro Mukae, Masami Ouchi, Koki Kakiichi, Nao Suzuki, Yoshiaki Ono, Zheng Cai, Akio K. Inoue, Yi-Kuan Chiang, Takatoshi Shibuya, and Yuichi Matsuda
The Astrophysical Journal, 835, 281, 12pp. (2017).
"Cosmic Galaxy-IGM HI Relation at $z \sim 2-3$ Probed in the COSMOS/UltraVISTA 1.6 Deg^2 Field"

PAPER-II: Shiro Mukae, Masami Ouchi, Zheng Cai, Khee-Gan Lee, J. Xavier Prochaska, Sebastiano Cantalupo, Zheng Zheng, Kentaro Nagamine, Nao Suzuki, John D. Silverman, Toru Misawa, Akio K. Inoue, Joseph F. Hennawi, Yuichi Matsuda, Ken Mawatari, Yuma Sugahara, Takashi Kojima, Yoshiaki Ono, Takatoshi Shibuya, Yuichi Harikane, Seiji Fujimoto, Yi-Kuan Chiang, Haibin Zhang, and Ryota Kakuma
Submitted to The Astrophysical Journal.
"3D Distribution Map of HI Gas and Galaxies Around an Enormous Lyα Nebula and Three QSOs at $z = 2.3$ Revealed by the HI Tomographic Mapping Technique"

PAPER-III: Shiro Mukae, Masami Ouchi, Ichi Tanaka, and Michael Rauch
To be submitted to The Astrophysical Journal.
"Extended Hα Emission around the Slug Nebula"

PAPER-IV: Shiro Mukae and the HETDEX Collaboration
To be submitted to The Astrophysical Journal.
"HI Gaseous Large-Scale Structures around LAEs Identified in the Early HETDEX Data"

PAPER-V: Shiro Mukae, Ryuji Suzuki, Yutaka Hayano, Brent Ellerbroek, and Glen Herriot
To be submitted to The Publications of the Astronomical Society of the Pacific.
"Correcting optical distortion of NFIRAOS and IRIS by self-calibration method"

ACKNOWLEDGEMENTS

First, I would like to express my thanks to my supervisor, Masami Ouchi, for kindly providing me with exciting opportunities to work with HETDEX and IRIS right when I entered the graduate school with ambitions to work on Large-Scale Structures and Instrumentation. Importantly, he has taught me how astronomers change the world and what professionals are. I express special thanks to Yoshiaki Ono for having discussions on business and personal things in almost every weekday for five years. I also express special thanks to Takatoshi Shibuya for having discussions on business and personal things in almost every weekend for three years. I would like to thank Zheng Cai for his taking care of my research since we firstly met December 2014. It was a great honor for me to work with him for five years. I also would like to thank Nao Suzuki for his assistance to my research with strictness as well as kindness. He has told me both the hardness and fun of studying inter-galactic medium. I show my gratitude to Koki Kakiichi, Rieko Momose, and Satoshi Kikuta for having meaningful discussions on inter-galactic medium whenever we need.

I would like to express my appreciation to Andreas Schulze for giving me the wonderful opportunities to join the HETDEX collaboration and to work on the HETDEX-HSC program. I'll never forget our first and excellent HSC observations at the summit of Maunakea in May 2015. HETDEX is the best international collaboration I love. From a close distance, I got to see their enthusiasm and processes to work hard for the success of the HETDEX with the limited budget and the small members at the intersection of Astronomy, Cosmology, and Observatory. I truly appreciate our friendly folks, especially, Karl Gebhardt, Gary Hill, Eiichiro Komatsu, Donghui Jeong, Shun Saito, Maximilian Fabricius, Dustin Davis, Erin Cooper, and Ulrich Hopp.

I am deeply grateful to Yutaka Hayano for giving me the wonderful opportunities to join the IRIS-Japan team and to work at Advanced Technology Center (ATC). He enthusiastically taught me the project management. I owe Ryuji Suzuki a debt of gratitude for kindly teaching me the system engineering. As I work together with him, I seriously realized that engineers build important bases of advances in astronomy.
I would like to thank the other IRIS-Japan team members at ATC, Masayuki Hattori,

Mizuho Uchiyama, Satoshi Hamano, Fumihiro Uraguchi, Yoshiyuki Obuchi, Bungo Ikenoue, Saito Sakae, and Risa Shimizu.

Fortunately, I've been blessed with resourceful people. I wish to express my appreciation to Yoshino Aoyama. Her professionalism and vitality are the best source of my sense of purpose. I express my special thanks to Yumi Shirai. She has always encouraged me and walked together. I greatly appreciate Gensei Ishimura, who kindly provided me with an exciting opportunity to work at ELSI PR Section. From my bottom of my heart, I would like to thank my resourceful friends mostly at Kavli IPMU; Takeru Ominami, John Amari, Aya Tsuboi, Marina Komori, Motoko Kakubayashi, Hironobu Fukuda, and Ito Yoriko for having heart-to-heart talks on what we truly believe interesting is. The time I spent with them is awesome! I truly thank Yuki Moritani for always being an important role model throughout the time of my research. She works hard about observational astronomy, astronomical instrumentation, and musical instruments. Her enthusiasm about the Subaru Prime Focus Spectrograph (PFS) projects is really inspiring to me. I would like to express my deepest appreciation to Saeko Hayashi and Keiichi Kodaira for giving me the paths to the Maunakea Observatory since the Hibiya SSH oversea training program in Aug. 2008. My path here has been like a dream. Lastly, I express my sincerest gratitude to my family for always supporting me to study Observational Cosmology at ICRR/Kavli IPMU in Kashiwanoha and Astronomical Instrumentation at NAOJ in Mitaka during the period of my Ph.D.

We wish to recognize and acknowledge the very significant cultural role and reverence that the summit of Maunakea has always had within the indigenous Hawaiian community. We are most fortunate to have the opportunity to conduct observations from this mountain. The data presented in this thesis were obtained at the W. M. Keck Observatory, which is operated as a scientific partnership among the California Institute of Technology, the University of California and the National Aeronautics and Space Administration. The Observatory was made possible by the generous financial support of the W. M. Keck Foundation. This thesis has made use of the Keck Observatory Archive (KOA), which is operated by the W. M. Keck Observatory and

the NASA Exoplanet Science Institute (NExScI), under contract with the National Aeronautics and Space Administration.

Funding for the Sloan Digital Sky Survey IV has been provided by the Alfred P. Sloan Foundation, the U.S. Department of Energy Office of Science, and the Participating Institutions. SDSS-IV acknowledges support and resources from the Center for High-Performance Computing at the University of Utah. The SDSS web site is www.sdss.org. SDSS-IV is managed by the Astrophysical Research Consortium for the Participating Institutions of the SDSS Collaboration including the Brazilian Participation Group, the Carnegie Institution for Science, Carnegie Mellon University, the Chilean Participation Group, the French Participation Group, Harvard-Smithsonian Center for Astrophysics, Instituto de Astrofísica de Canarias, The Johns Hopkins University, Kavli Institute for the Physics and Mathematics of the Universe (IPMU) / University of Tokyo, the Korean Participation Group, Lawrence Berkeley National Laboratory, Leibniz Institut für Astrophysik Potsdam (AIP), Max-Planck-Institut für Astronomie (MPIA Heidelberg), Max-Planck-Institut für Astrophysik (MPA Garching), Max-Planck-Institut für Extraterrestrische Physik (MPE), National Astronomical Observatories of China, New Mexico State University, New York University, University of Notre Dame, Observatário Nacional / MCTI, The Ohio State University, Pennsylvania State University, Shanghai Astronomical Observatory, United Kingdom Participation Group, Universidad Nacional Autónoma de México, University of Arizona, University of Colorado Boulder, University of Oxford, University of Portsmouth, University of Utah, University of Virginia, University of Washington, University of Wisconsin, Vanderbilt University, and Yale University.

HETDEX is led by the University of Texas at Austin McDonald Observatory and Department of Astronomy with participation from the Ludwig-Maximilians- Universität München, Max-Planck-Institut für Extraterrestriche-Physik (MPE), Leibniz-Institut für Astrophysik Potsdam (AIP), Texas A&M University, Pennsylvania State University, Institut für Astrophysik Göttingen, The University of Oxford, Max-Planck-Institut für Astrophysik (MPA), The University of Tokyo and Missouri University of Science and Technology. In addition to Institutional support, HETDEX is funded by the National Science Foundation (grant AST-0926815), the State of Texas, the US

Air Force (AFRL FA9451-04-2- 0355), and generous support from private individuals and foundations. The observations were obtained with the Hobby-Eberly Telescope (HET), which is a joint project of the University of Texas at Austin, the Pennsylvania State University, Ludwig-Maximilians-Universität München, and Georg- August- Universität G0ttingen. The HET is named in honor of its principal benefactors, William P. Hobby and Robert E. Eberly. VIRUS is a joint project of the University of Texas at Austin, Leibniz-Institut für Astrophysik Potsdam (AIP), Texas A&M University, Max-Planck-Institut für Extraterrestriche-Physik (MPE), Ludwig-Maximilians- Universität München, The University of Oxford, Pennsylvania State University, Institut für Astrophysik Göttingen,, Max-Planck-Institut für Astrophysik (MPA) We acknowledge the Texas Advanced Computing Center (TACC) at The University of Texas at Austin for providing high performance computing, visualization, and storage resources that have contributed to the research results reported within this thesis.

Based in part on data collected at Subaru Telescope, which is operated by the National Astronomical Observatory of Japan. The TMT Project gratefully acknowledges the support of the TMT collaborating institutions. They are the California Institute of Technology, the University of California, the National Astronomical Observatory of Japan, the National Astronomical Observatories of China and their consortium partners, the Department of Science and Technology of India and their supported institutes, and the National Research Council of Canada. This work was supported as well by the Gordon and Betty Moore Foundation, the Canada Foundation for Innovation, the Ontario Ministry of Research and Innovation, the Natural Sciences and Engineering Research Council of Canada, the British Columbia Knowledge Development Fund, the Association of Canadian Universities for Research in Astronomy (ACURA) , the Association of Universities for Research in Astronomy (AURA), the U.S. National Science Foundation, the National Institutes of Natural Sciences of Japan, and the Department of Atomic Energy of India.

Finally, I acknowledge support from the JSPS through the JSPS Research Fellowship for Young Scientists and the NAOJ through the Special Inter-institutional Research Fellows.

ABSTRACT

We aim to address galaxy formation in gaseous large-scale structures (LSSs) by a spectroscopic study and TMT/IRIS instrumentation.

In the spectroscopic study, we investigate distributions of intergalactic medium (IGM) neutral hydrogen (HI) gas around $z \sim 2$ galaxies in the following three galaxy environments: a blank region (COSMOS), an extreme galaxy overdensity region (BOSS1441), and an extreme quasar overdensity region (EGS). We use large datasets of galaxies and quasars at $z \sim 2$ that are mainly constructed based on the Hobby-Eberly Telescope Dark Energy Experiment (HETDEX) and the extended Baryon Oscillation Spectroscopic Survey of the Sloan Digital Sky Survey IV (SDSS-IV/eBOSS), respectively. We probe IGM HI gas distributions at $z \sim 2$ with HI Lyα forest absorptions (HI absorptions) found in spectra of background quasars and galaxies at $z > 2$. These background quasar and galaxy spectra are taken from archival data and our Keck/LRIS spectroscopy. We perform HI tomography that is a powerful technique to reconstruct three-dimensional (3D) HI LSSs based on HI absorptions, and reveal the IGM HI gas distributions at $z \sim 2$ in the (BOSS1441, EGS) with the spectra of background (1 quasar+ 16 galaxies, 43 quasars). In the COSMOS region, we use the HI tomography map of Lee et al. (2018). These (COSMOS, BOSS1441, EGS) HI tomography maps have cosmic volumes of ($30 \times 24 \times 444$, $16 \times 19 \times 131$, $124 \times 136 \times 444$) h^{-3}comoving Mpc^3 (cMpc^3) with spatial resolutions of (2.5, 2.6, 20.0) h^{-1} cMpc at $z = 2.3$.

To study IGM HI-gas distributions around $z \sim 2$ galaxies, we carry out the following two measurements with the three HI tomography maps: spherically averaged HI radial profiles of the galaxies and spatial correlations between the galaxy overdensity and HI absorption excess (HI overdensity). In the COSMOS region, we find that galaxies (galaxy overdensities) reside in volumes with enhanced HI absorptions where none of the eBOSS quasars are found in the cosmic volume of the HI tomography map. This suggests the spatial correlations between HI gas and galaxies. In the BOSS1441 region, contrary to the results in the COSMOS region, we find that galaxies (galaxy overdensities) are in volumes with HI absorptions reduced to the cos-

mic mean level. On the other hand, we find possible suppression of HI absorptions around three eBOSS quasars found in the HI tomography map. This suggests that these quasars might have proximity zones where quasar illuminates and photo-ionizes the surrounding HI gas. A similar HI radial profile is obtained for an enormous Lyα nebula (ELAN), MAMMOTH-1 nebula, hosted by an obscured quasar, which implies that the MAMMOTH-1 nebula is probably a photo-ionized hydrogen gas cloud embedded in the cosmic web. In the EGS region, we discover an extreme quasar overdensity, dubbed EGS-QO1. Our HI tomography map reveals that EGS-QO1 is surrounded by an HI underdensity region with weak HI absorptions, and that EGS-QO1 would reside in the part of the HI underdensity. The possible correspondence between EGS-QO1 and the HI underdensity may imply that group of quasars would form a large ionizing bubble and widely photo-ionize the surrounding HI gas. The results of the COSMOS, BOSS1441, and EGS regions might suggest an evolutionary picture that HI gaseous LSSs around galaxies could be photo-ionized by quasars as overdensities of galaxies and quasars evolve and quasars photo-ionize most of the surrounding hydrogen gas.

To verify the IGM ionized hydrogen gas around $z \sim 2$ quasars, we plan near-infrared (NIR) observations of Hα emission from an ELAN at $z \sim 2$, the Slug nebula. We perform pilot observations with Subaru/MOIRCS, and present infeasibility of detecting and resolving the Hα emission from the Slug nebula with 8m-class telescopes. We then estimate the observing plans with NIR instruments for 30m-class telescopes such as InfraRed Imaging Spectrograph (IRIS) on Thirty Meter Telescope (TMT), and find feasibility to study the Hα emission from the intergalactic hydrogen gas clouds of the Slug nebula. We thus prepare the TMT/IRIS observations by contributing to the successive TMT/IRIS instrumentation.

In the TMT/IRIS instrumentation, we present results of our simulations to correct optical distortion of TMT/IRIS. We implement a self-calibration method which extracts the optical distortion by measuring the difference of pinhole positions between dithered images. We investigate the calibration performance with various parameters of pinhole mask, i.e., number of pinholes, dither length, and dither pattern, to characterize our implementation of the self-calibration algorithm. We demonstrate that

the algorithm achieves an unprecedented distortion correction accuracy of as low as 3 μarcsec when the dither length is longer than the smallest distortion scale of interest and the pinhole distribution is uniform after dithering is applied. The suggested set of parameters is consistent with the current IRIS design. Our calibration contributes to realizing scientific performance for planned instrument suites on 30m-class telescopes, which will provide a signpost toward our planned TMT/IRIS observations for testing photoionization of HI gaseous LSS.

TABLE OF CONTENTS

CHAPTER 1
INTRODUCTION

1.1 Galaxy Formation in Gaseous Large-Scale Structures

Galaxy formation in the Universe is closely linked to intergalactic medium (IGM) [1] over the cosmic time. As the Universe was born with the Big Bang, the primordial hydrogen was produced in the form of the dense and hot ionized gas. By the time the Universe was 380,000 years old, the cosmic expansion decreased the temperature of the primordial ionized gas through adiabatic expansion cooling. The recombination of hydrogen proceeded until neutral hydrogen (HI) atoms dominate the Universe. After the recombination, early galaxies emerged at $z \sim 10 - 30$, forming from the HI gas. The early galaxies ionized a large fraction of the HI gas in the IGM, forming ionized bubbles. The HI gas in the Universe is almost fully ionized in the redshift range of $z = 6 - 12$, called the Epoch of Reionization.

In the post-reionized universe at $z = 2 - 5$, the physical state of IGM HI is expected to be fully ionized. However, about half a century ago, Gunn & Peterson (1965) found remaining HI gas in intergalactic space by the HI Lyα absorption features in the spectrum of a background light such as a distant quasar. The line of sight to the background quasar was expected to pass through intervening intergalactic gas and intercept HI gas clouds, making the hundreds of distinct Lyα absorption lines (Lyα forest, e.g., Young et al., 1982). This implies that there remains numerous IGM HI gas clouds even in the post-reionized universe (Figure 1.1).

What are the IGM HI gas clouds? The cosmological hydrodynamics simulations demonstrated that the Lyα forest absorption features arise naturally within the framework of structure formation based on the cold dark matter (CDM) cosmology (e.g., Cen et al., 1994; Miralda-Escudé et al., 1996; Hernquist et al., 1996; Zhang et al., 1995). This suggests that the IGM HI gas clouds gravitationally form a network of filamentary large-scale structures (LSSs) in the Universe along the dark matter distributions (e.g., Rauch, 1998). The gaseous filamentary network of structures extends

[1] The IGM is defined as the baryonic material lying space between galaxies.

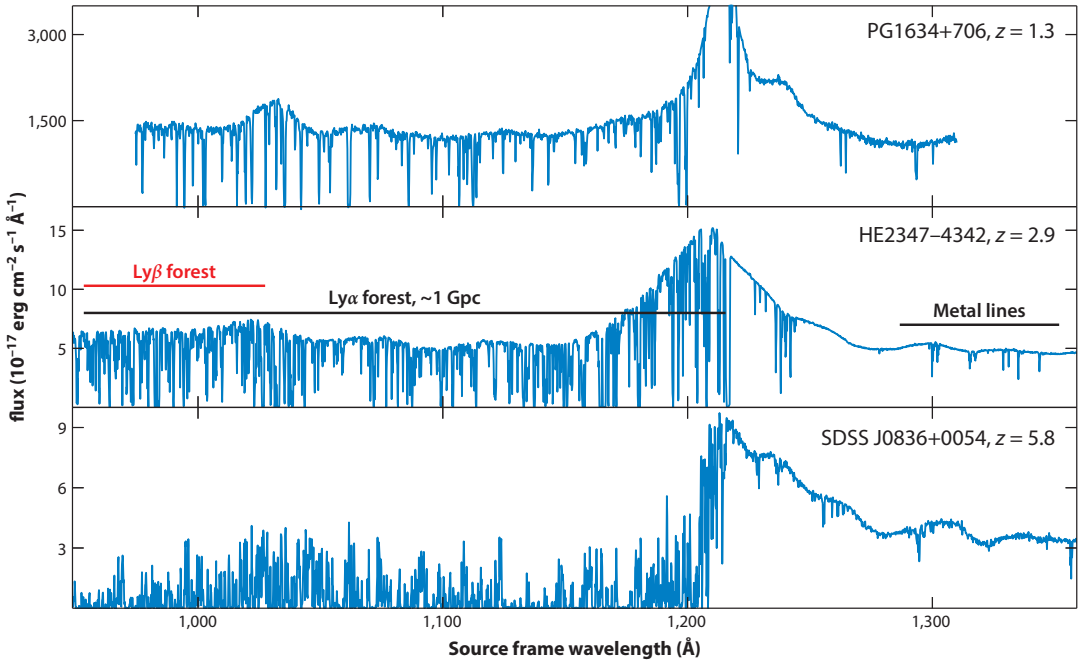

Figure 1.1: Spectra of quasars at three different redshifts from McQuinn (2016). The Lyα forest appears the blueward of the Lyα emission in the quasar rest frames. HI gas clouds intersected along the quasars sightlines cause Lyα absorption in the quasar continua by the redshifted Lyα lines at $1216 \times (1 + z_{\rm abs})$ Å in the observed frames, where $z_{\rm abs}$ is a redshift of an HI gas cloud.

over tens comoving Mpc (cMpc), and are called "cosmic web."

In the modern paradigm of the galaxy formation, galaxies form and evolve in the cosmic web (e.g., Meiksin, 2009; Mo et al., 2010). In almost a decade ago, studies of cosmological hydrodynamics simulations have suggested a picture that galaxies and the cosmic web exchange baryonic gas by gas flows (e.g., Fox & Davè, 2017; van de Voort, 2017, Figure 1.2). Cols gas ($\sim 10^4$ K) in the cosmic web accretes on to galaxies through the filamentary structures, and triggers star formation of the galaxies (e.g., Dekel et al., 2009; Kereš et al., 2005). The star formation heats up the gas, and the gas is carried out from the galaxies by feedback processes such as galactic outflow (e.g., Somerville & Davé, 2015; Viel et al., 2013). Observing the site of the gas exchange is key for understanding galaxy formation in gaseous LSSs, especially at $z \sim 2-3$ when the gas exchange peaks in the cosmic star formation peak. The connection between galaxies that form from IGM and gaseous the LSSs is poorly probed in observations (Section 1.2). How galaxies form in gaseous LSSs is one of the major questions in modern astronomy.

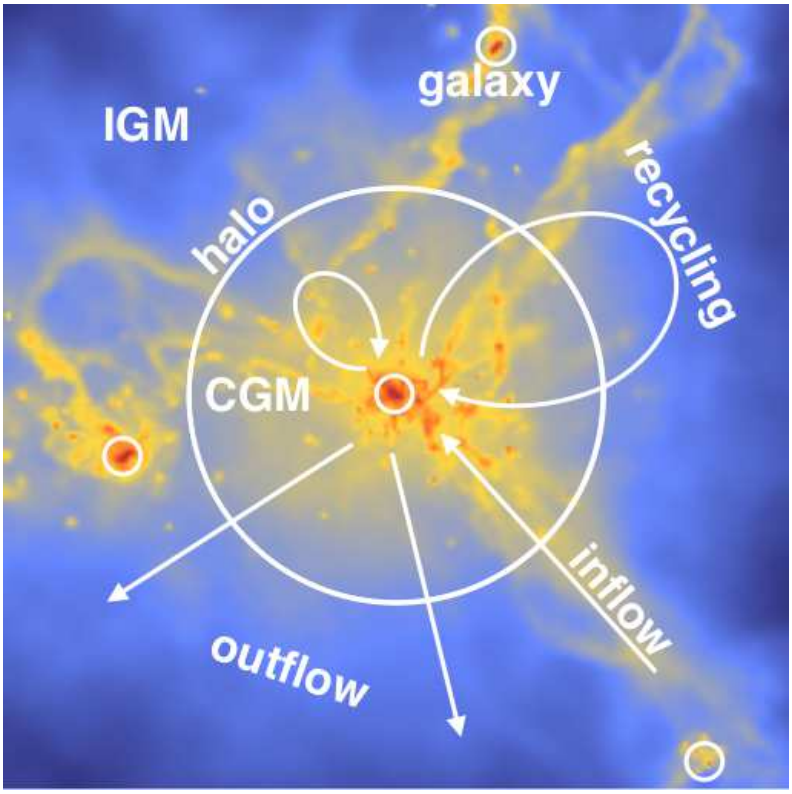

Figure 1.2: Gas density map in a box of side length 450 pkpc from van de Voort (2017). The map is centered at a 10^{12} $M_{\odot}$ halo at $z = 2$. The outer white circle marks the halo virial radius. The small white circles represent the locations of galaxies. This map shows gas exchange between LSSs and galaxies, by describing inflow through the filamentary structures, and outflow (recycling) whose gas can escape (re-accrete in) the halo. The gas in the virial halo is specifically called as Circum-galactic Medium (CGM), while intergalactic medium (IGM) is described as all the gas in the intergalactic space. In this thesis, we include CGM in IGM.

1.2 Observational Studies for Gaseous Large-Scale Structures

To study galaxy formation in gaseous LSSs, it is essential to observationally characterizing gaseous LSSs by IGM HI gas. Recent observational studies have probed the IGM HI-gas LSSs (HI LSSs) at $z \sim 2-3$, by mapping Lyα emission, or by revealing the spatial distributions of Lyα forest absorption.

In the past few years, HI LSSs have been detected in Lyα emission by deep observations of narrowband imaging and integral-field spectroscopy (IFS). Narrowband observations have discovered enormous Lyα Nebula (ELAN), extremely extended Lyα nebula whose Lyα emission extends over 400 physical kpc (pkpc) (Cantalupo et al., 2014; Hennawi et al., 2015; Cai et al., 2017a; Kikuta et al., 2019, for example, MAMMOTH1 nebula in Figure 1.3). These ELANe are found around the radio-quiet quasars in galaxy overdensities at $z \sim 2$. Since the Lyα emission spatially extends beyond virial diameter of the host quasars (~ 280 pkpc), the ELANe are thought to be photo-ionized hydrogen gas cloud embedded in the cosmic web (e.g., Cantalupo et al., 2012). On the other hand, IFS observations have revealed filamentary structures of Lyα emission across ~ 1 physical Mpc (pMpc) probably photo-ionized by star formation or quasar activity in an extreme galaxy overdensity at $z \sim 3$ (Umehata et al., 2019). However, the detections of these HI LSSs in Lyα emission are biased in specific environments such as quasar proximity or extreme galaxy overdensities.

In contrast, revealing the spatial distributions of the HI Lyα forest absorption (HI absorption) is a promising way for probing HI LSSs. Until a decade ago, HI-gas distributions around galaxies are studied by stacking analysis with pairs of foreground galaxies and background sources (e.g., Adelberger et al., 2003, 2005; Steidel et al., 2010; Bielby et al., 2017). These staking measurements have shown HI-gas absorption as a function of transverse distances to the quasar sightlines, and revealed HI-gas absorption excess around massive star-forming galaxies over $\sim 1-5\,h^{-1}$ cMpc. However, the stacked HI-gas distributions are based on the measurements in various fields, and represent the cosmic averaged distribution, losing the information of each of galaxy environments such as overdensity of galaxies and quasars. In the past few years, two

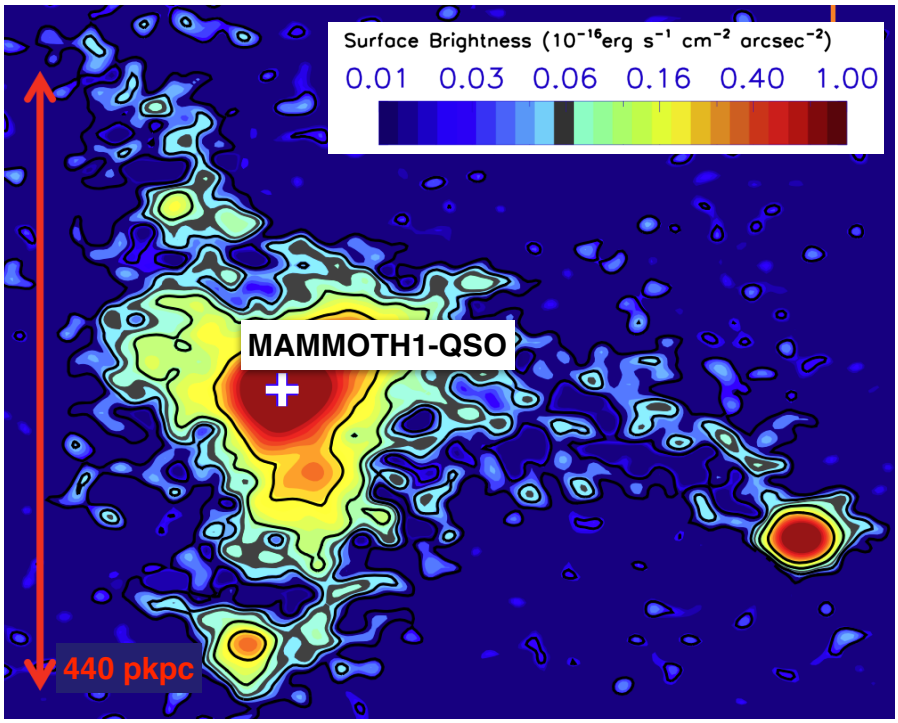

Figure 1.3: Lyα narrowband image of an ELAN, MAMMOTH-1 nebula at $z = 2.32$ from Cai et al. (2017a). The color scale shows the Lyα emission surface brightness. The white cross is the position of the host quasar, dubbed MAMMOTH1-QSO in this thesis (Section 5.4).

techniques for characterizing HI LSSs in a region of interest are developed. Lee et al. (2014a,b) have established a powerful technique, called HI tomography, to reconstruct three dimensional (3D) HI LSSs at $z \sim 2$ from HI absorptions found in multiple background galaxy spectra (Figure 1.4). Their subsequent studies (Lee et al., 2016, 2018) have successfully revealed HI LSSs with spatial resolutions of 2.5 h^{-1} cMpc in the COSMOS Lyα Mapping And Tomography Observations (CLAMATO) survey. On the other hand, Cai et al. (2016) has established a remarkable technique to identify both HI LSSs and galaxy overdensities at $z \sim 2$ from the strong IGM HI absorption group found in multiple background quasar spectra. Cai et al. (2017b) has successfully revealed a galaxy overdensity, dubbed BOSS1441 region, in the Mapping the Most Massive Overdensities through Hydrogen (MAMMOTH) survey. The background quasars in the MAMMOTH survey probe HI LSSs and galaxy overdensities with spatial resolutions of 15 h^{-1} cMpc.

The techniques of the CLAMATO and MAMMOTH surveys have enabled us to spatially characterize HI LSSs in a region of interest. However, few studies systematically investigate connections between HI LSSs and galaxies from blank regions [2] to specific regions such as galaxy overdensities. Although, the CLAMATO (MAMMOTH) survey studies HI LSS with small (large) spatial resolutions in blank (specific) regions, no studies combine the CLAMATO and MAMMOTH surveys and apply the HI tomography technique to the fields found in the MAMMOTH surveys. As a wide-field and statistical study complementary to the CLAMATO and MAMMOTH surveys, Mukae et al. (2017) have investigated spatial correlations of HI-gas overdensities and galaxy overdensities at $z \sim 2-3$, using photometric galaxies and multiple spectra of background quasars in a large 1.62 deg^2 area of the COSMOS/UltraVISTA field. The spatial correlation results suggest that a large amount of HI-gas is associated with the galaxy overdensities (APPENDIX A).

However, it is still unknown how the nature of the HI LSSs are affected by overdensities of galaxies and quasars in specific regions. As quasars emerge from galaxy overdensities, the quasars' radiation can enhance the ultraviolet background (UVB)

[2] In this thesis, we refer to a blank region as a region where any extreme galaxy overdensities are not contained.

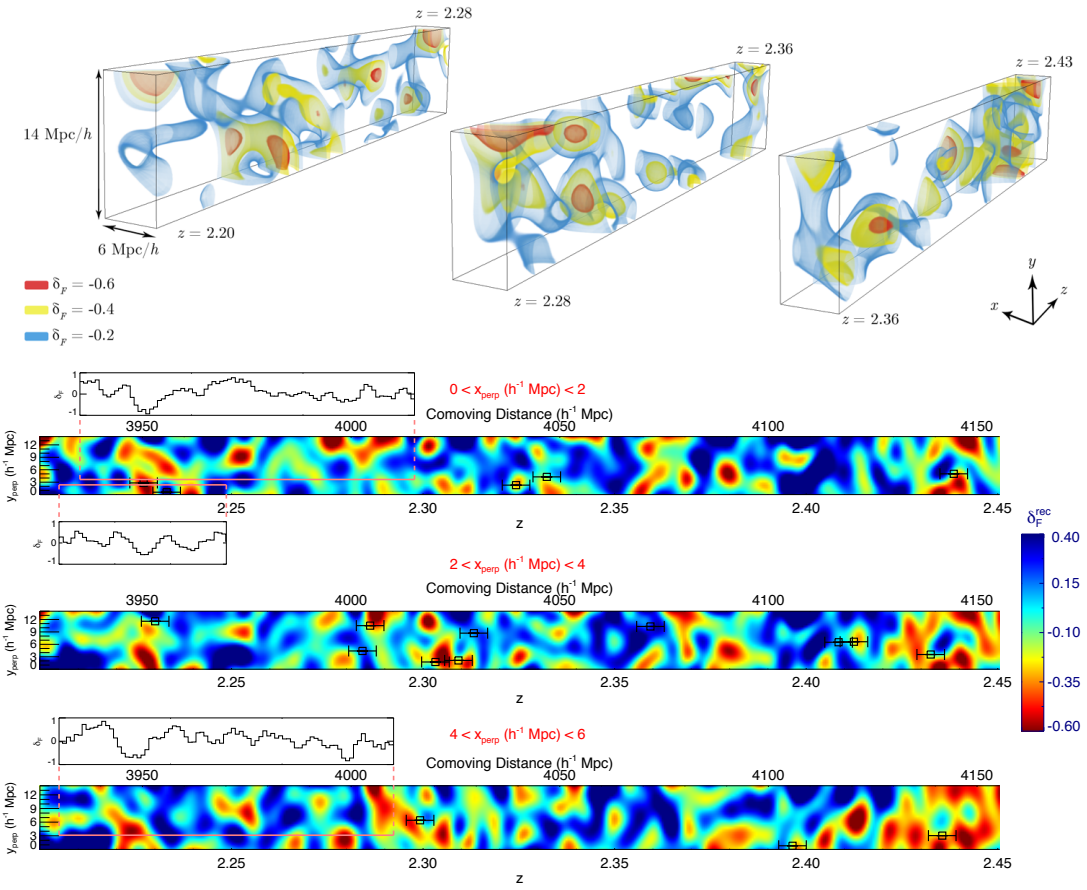

Figure 1.4: HI tomography maps reconstructed from Lyα forest absorptions found in background galaxy spectra by a pilot survey of Lee et al. (2014b). The top panel shows the HI LSS 3D maps. The bottom panel presents three slices of the 3D maps projected along the R.A. direction. The color scale shows the HI absorption strength. The red (blue) color presents the absorption strength above (below) the cosmic average that correspond to strong (week) HI absorption. The magenta lines present the positions background galaxy and redshift range of their spectra. The inset panels indicate the background galaxy spectra that are smoothed in the process of the tomographic reconstruction. The square data points denote the galaxies in the cosmic volumes of the HI tomography maps.

radiation in the overdensities, photo-ionizing the surrounding HI-gas. Moreover, the enhanced UVB radiation can suppress the formation of galaxies with low halo mass by photo-evaporation of their gas (e.g., Susa & Umemura, 2004, 2000), as implied by observational studies of galaxy number counts around quasars (e.g., Kashikawa et al., 2007; Kikuta et al., 2017). In this sense, three major elements for the galaxy formation are dark matter, HI gas, and ionization.

To understand the impact of overdensities of galaxies and quasars on the surrounding HI gas, it is important to systematically study HI-gas distributions around galaxies in various galaxy environments; from blank regions to overdensities of galaxies and quasars. On the other hand, to verify the ionized hydrogen gas around the overdensities of galaxies and quasars, it is also important to map hydrogen recombination lines such as Hα emission from intergalactic hydrogen gas. However, Hα emission from $z \sim 2$ hydrogen gas is redshifted into near-infrared (NIR) wavelength range and too faint to robustly identify with 8m-class telescopes (e.g., Leibler et al., 2018). In this context, instrumentation for the upcoming 30m-class telescopes is indispensable to high-sensitive NIR observations for understanding galaxy formation in gaseous LSSs.

1.3 Plan of This Thesis

In this thesis, we aim to address galaxy formation in gaseous LSSs by spectroscopic study and instrumentation. In the spectroscopic study, we investigate IGM HI-gas distributions around galaxies at $z \sim 2$ in the following three galaxy environments: a blank region, an extreme galaxy overdensity region, and an extreme quasar overdensity region. We use the large datasets of galaxies and quasars constructed based on the Hobby-Eberly Telescope Dark Energy Experiment (HETDEX; Hill et al., 2008), the MAMMOTH (Cai et al., 2017b), and the extended Baryon Oscillation Spectroscopic Survey of the Sloan Digital Sky Survey IV (SDSS-IV/eBOSS; Myers et al., 2015). To probe IGM HI-gas distributions at $z \sim 2$, we use HI absorptions found in spectra of background quasars and galaxies at $z > 2$. These background quasar and galaxy spectra are taken from archival data and our spectroscopy. We perform HI tomography based on the HI absorptions, and reveal 3D HI LSSs. To probe IGM ionized hydrogen gas distributions at $z \sim 2$, we aim to identify Hα emission from hydrogen gas clouds around quasars. We carry out pilot observations with Multi-Object InfraRed Camera and Spectrograph (MOIRCS; Ichikawa et al., 2006), which provides a good stepping stone toward high-sensitive observations with the planned NIR instruments on the 30m-class telescopes. We prepare the high-sensitive NIR observations by contributing to the instrumentation of InfraRed Imaging Spectrograph (IRIS; Larkin et al., 2016) on Thirty Meter Telescope (TMT; Sanders, 2013). In the TMT/IRIS instrumentation, we investigate optical distortion calibration of TMT/IRIS. We inspect a self-calibration technique that extracts the optical distortion by measuring the difference of pinhole positions between dithered images. We aim to characterize the self-calibration algorithm which we implement to calibrate high spatial frequency distortion and derives the pinhole mask parameters which satisfy the distortion correction requirement. We use optical design software ZEMAX to simulate IRIS observations, and examine the calibration performance with various parameters of pinhole mask, i.e., number of pinholes, dither length, and dither pattern.

The structure of this thesis is composed of two main parts; Spectroscopic Studies

and TMT/IRIS Instrumentation. The outline of this thesis is as follows. We begin with Spectroscopic Studies, constructing our samples of foreground/background galaxies and quasars in Chapter 2. We detail our spectroscopy and background source spectra in Chapter 3. In Chapter 4, we describe our HI tomography techniques and our HI tomography maps. We present results and discussions in Chapters 5 and 6, respectively. We move to our TMT/IRIS Instrumentation from our Spectroscopic Studies by introducing our future prospects for TMT/IRIS observations in Chapter 7. Our TMT/IRIS Instrumentation begins with the overview and our motivation in Chapter 8. We present our algorithm of the self-calibration method and our simulations in Chapter 9. Chapters 10 and Chapter 11 present results and discussions for our optical distortion correction. Finally, we summarize our major findings in this thesis in Chapter 12. Throughout this thesis, we use a cosmological parameter set: $(\Omega_m, \Omega_\Lambda, \Omega_b, h)= (0.26, 0.74, 0.045, 0.70)$ consistent with the nine-year $WMAP$ result (Hinshaw et al., 2013). We refer to kpc and Mpc in comoving (physical) units as ckpc and cMpc (pkpc and pMpc), respectively. All magnitudes are in AB magnitudes (Oke & Gunn, 1983).

CHAPTER 2
SPECTROSCOPIC STUDY:
CATALOGS AND SAMPLES

We investigate IGM HI-gas distributions around $z \sim 2$ galaxies in the three galaxy environments: a blank region, an extreme galaxy overdensity region, and an extreme quasar overdensity region. Our survey regions are the following three regions.

- COSMOS: a blank region of 0.157 deg^2 (Lee et al., 2018)
- BOSS1441: an extreme galaxy overdensity region of 0.04 deg^2 (Cai et al., 2017b)
- EGS: a blank region of 6.0 deg^2
  including an extreme quasar overdensity (Section 5.3)

In this Chapter, we describe our catalogs and samples of the following two sources of (I) and (II). (I) foreground ($z \sim 2$) sources that are star-forming galaxies (foreground galaxies; Section 2.1) and quasars (foreground quasars; Section 2.2). (II) background ($z > 2$) sources that are used for probing HI absorptions at $z \sim 2$, and are quasars (background quasars; Section 2.3) and galaxies (background galaxies; Section 2.4).

2.1 Foreground Galaxies

Our samples of foreground galaxies consist of three catalogs; the COSMOS, EGS, and BOSS1441 catalogs, below.

2.1.1 COSMOS and EGS Catalogs

The COSMOS and EGS catalogs are the Lyα emitter (LAE) catalogs that are constructed as part of HETDEX (Hill et al. 2008, Gebhardt et al. 2020, in prep.)[1]. These LAEs are observed with the Visible Integral-field Replicable Unit Spectrograph (VIRUS) on the 11 m Hobby-Eberly Telescope (HET; Figure 2.1). The HET (Ramsey et al., 1994) is an innovative telescope with 11 meter segmented primary mirror, located in West Texas at the McDonald Observatory. VIRUS (Hill et al., 2018) is a massively replicated integral field spectrograph (IFS: Hill, 2014), designed for blind spectroscopic surveys. It consists of 78 integral field units (IFUs; Kelz et al. 2014) distributed over the 22 arcmin diameter field of view of the telescope.[2] Each IFU feeds 448 1".5 diameter fibers to spectrographs (Figure 2.2). The spectrographs have a fixed spectral bandpass of $z = 3500$–5500 Å and a spectral resolution of $R \approx 800$. The HETDEX survey performs a blind emission line survey over the 450 deg^2 (Figure 2.3) with the standard dither set of 6 min $\times$ 3 dithers, and aims to identify 10^6 LAEs at $z = 1.9$–3.5 in a 9 Gpc^3 volume. The HETDEX survey constructs the emission-line database (HETDEX Data Release 1; Gebhardt et al. 2020, in prep.) where emission-

[1]HETDEX is led by the University of Texas at Austin McDonald Observatory and Department of Astronomy with participation from the Ludwig-Maximilians- Universität München, Max-Planck-Institut für Extraterrestriche-Physik (MPE), Leibniz-Institut für Astrophysik Potsdam (AIP), Texas A&M University, Pennsylvania State University, Institut für Astrophysik Göttingen, The University of Oxford, Max-Planck-Institut für Astrophysik (MPA), The University of Tokyo and Missouri University of Science and Technology. `http://www.hetdex.org/`

[2]The VIRUS array has been undergoing the deployment of IFUs and spectrograph units starting in late 2015. The data presented in this thesis were obtained with between 16 and 47 active IFUs, with up to 21,056 fibers. HETDEX Data Release 1 covers all observations from January 3, 2017 to February 09, 2019. A detailed technical description of the HET IFU and VIRUS is presented in Hill et al. (2020), in prep..

line detections are processed with the combination of broadband data such as our Subaru/HSC data (APPENDIX B).

From the COSMOS (EGS) catalog, we take 47 (27) spectroscopically identified LAEs in the COSMOS (EGS) region by the following three criterion: (i) emission-line redshifts are in the ranges of $z = 2.05$–2.55, (ii) emission-line detections are more than 6.5 σ levels, and (iii) Lyα luminosities are above $L^*_{\mathrm{Ly}\alpha} = 2.9L^*_{\mathrm{Ly}\alpha}$, where $L^*_{\mathrm{Ly}\alpha} = 2.14 \times 10^{42}$ erg s^{-1} is the characteristic Lyα luminosity at $z = 2.1 - 3.1$ (Ciardullo et al., 2012). The redshift range is chosen to match with that of the COSMOS HI tomography map (Lee et al., 2018, Section 4.2.1). The emission-line detection limit corresponds to the completeness limit for the LAEs above the Lyα luminosity threshold. The completeness limit is estimated by Zhang et al. (2020) in prep. who calculate Lyα luminosity functions (LFs) of HETDEX LAEs and confirm that the Lyα LFs are consistent with the previous narrowband studies (e.g., Konno et al., 2016; Sobral et al., 2017) above the Lyα luminosity threshold. Figures 2.4 and 2.5 present the distribution of the HETDEX LAEs in the COSMOS and EGS regions, respectively. The basic properties of the HETDEX LAEs in the COSMOS and EGS regions are summarized in Tables 2.1 and 2.2, respectively.

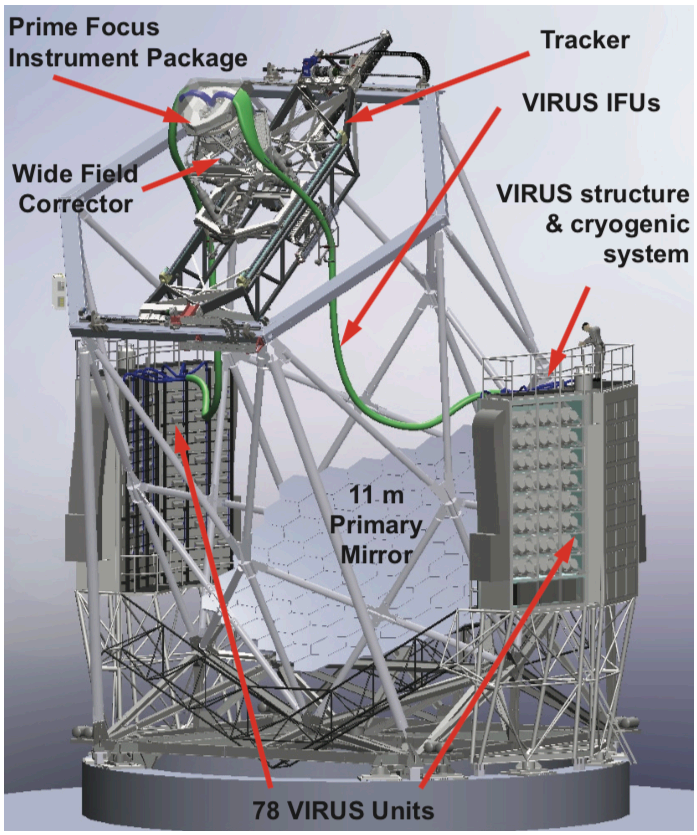

Figure 2.1: Structures of HET and VIRUS. This figure is taken from Hill & HETDEX Consortium (2016).

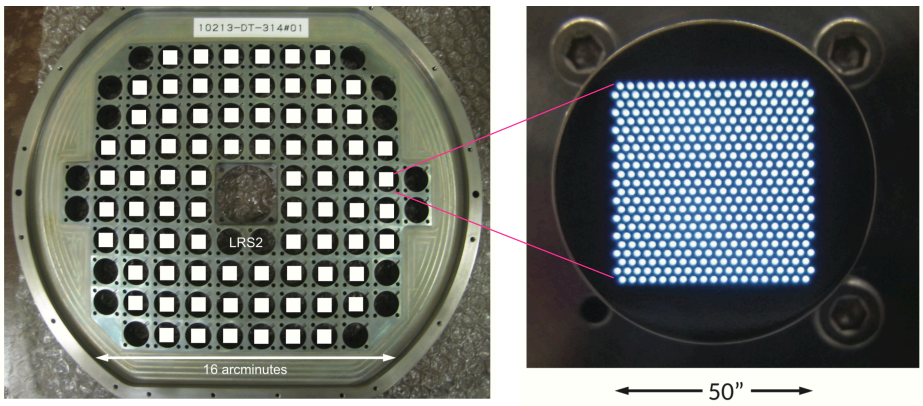

Figure 2.2: Layout of 78 VIRUS IFUs. Each IFU is composed of 448 1”.5 diameter fibers. This figure is taken from Hill & HETDEX Consortium (2016).

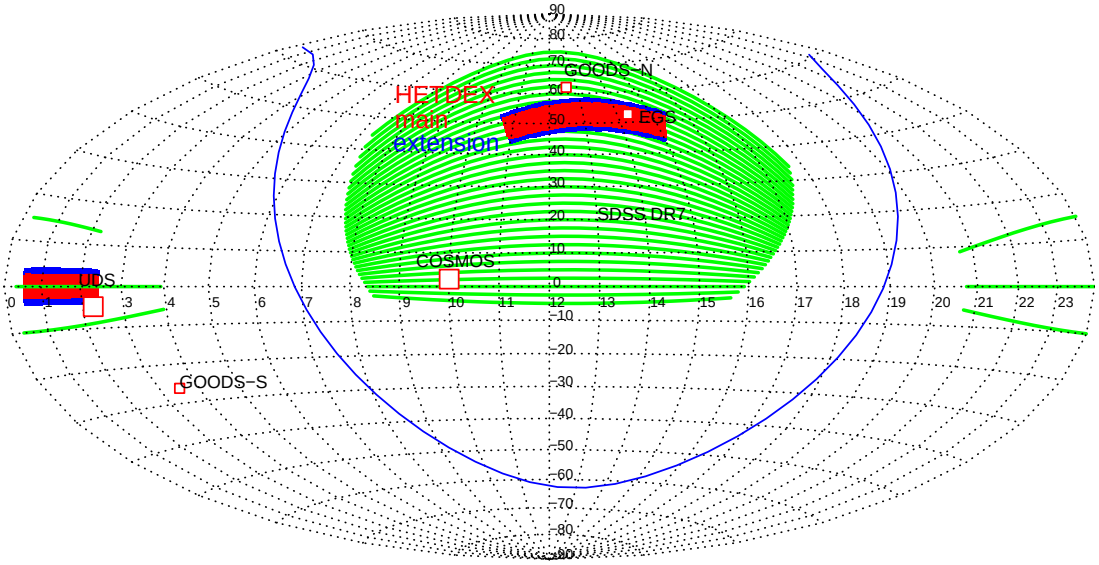

Figure 2.3: HETDEX survey fields. The red filled regions represent primary 440 deg^2 survey fields that are composed of Spring 300 deg^2 field (top center) and Fall 150 deg^2 field (left center). The red open regions indicate the calibration fields such as COSMOS and EGS. The Green regions show the SDSS DR7 footprints on the sky. We carry out Subaru/Hyper Suprime-Cam (HSC) observations over the HETDEX Spring 300 deg^2 field (APPENDIX B).

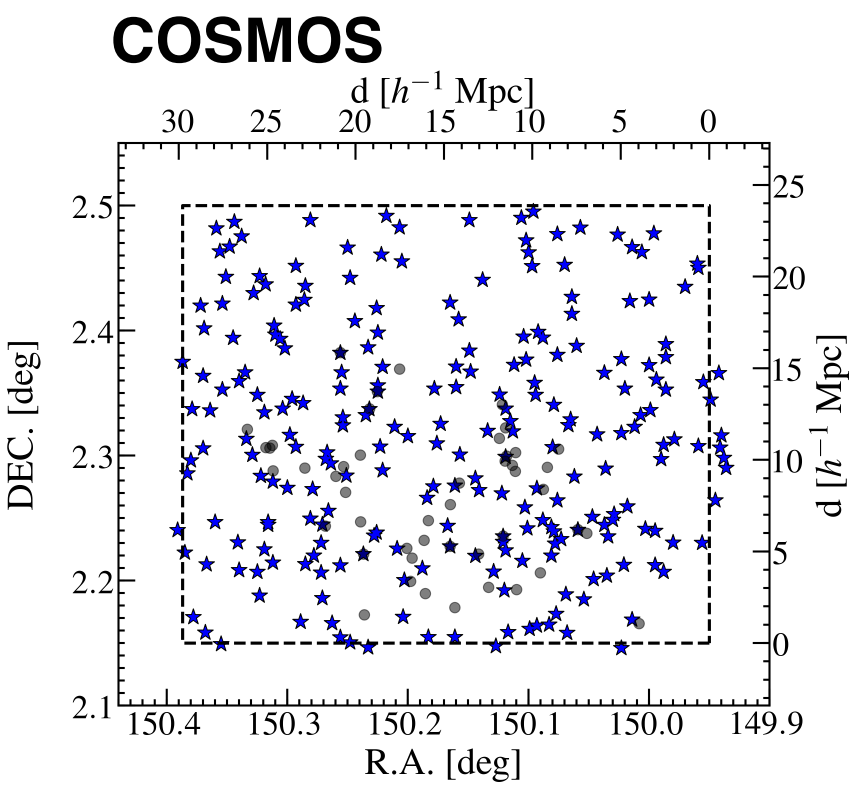

Figure 2.4: Sky distribution of background sources in the 0.157 deg^2 area of the COSMOS region. The blue stars represent the positions of background galaxies and quasars $z = 2.1$–3.1 taken from Lee et al. (2018). The dark-gray dots are our HETDEX LAEs at $z = 2.05$–2.55 (Section 2.1.1). The dashed lines are the sky area defined by the HI tomography map (Section 4.2.1).

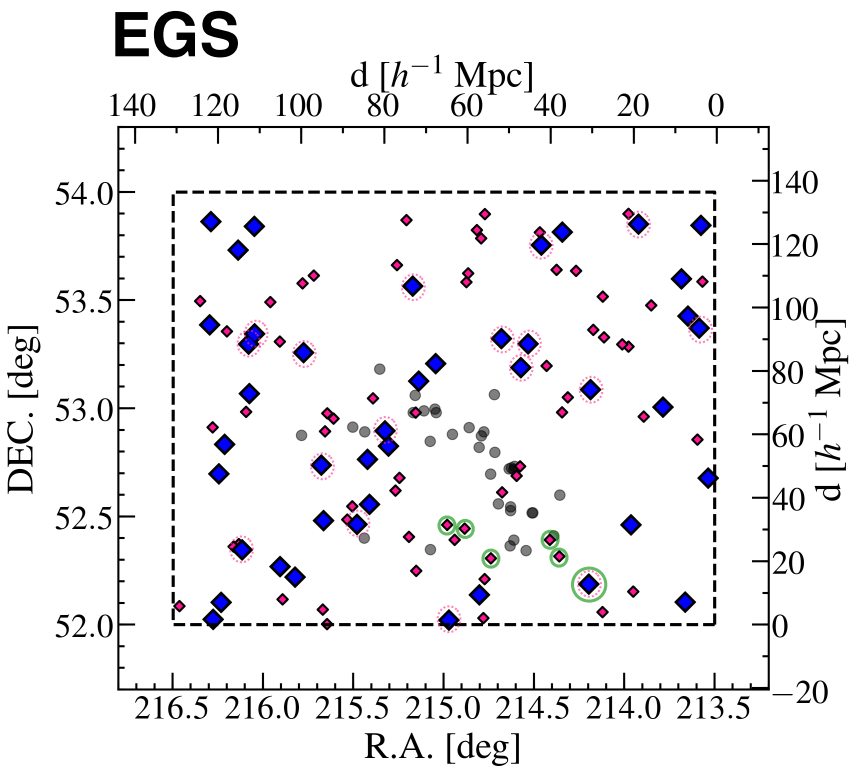

Figure 2.5: Sky distribution of our background quasars in the 6.0 deg^2 area of the EGS region. The blue diamonds are the positions of our background quasars at $z = 2.1$–3.1 (Sections 2.3 and 3.1). The magenta diamonds are the positions of our foreground quasars at $z = 2.05$–2.55 (Section 2.2). The magenta dotted circles indicate the background quasars that are also used as foreground quasars for calculating quasar overdensity (Section 5.3). The green circles represent six quasars associated with an extreme quasar overdensity, EGS-QO1 (Section 5.3). The dashed lines are the sky area defined by the HI tomography map (Section 4.2.3).

2.1.2 BOSS1441 Catalog

For the BOSS1441 region, we use the BOSS1441 catalog that is the photometric LAE catalog of Cai et al. (2017b) who found 149 LAEs at $z = 2.32$ in an extreme LAE overdensity dubbed BOSS 1441 region. The BOSS1441 catalog is constructed as part of the MAMMOTH survey (e.g., Cai et al., 2017a) and these LAEs are taken with the KPNO-4 m/MOSAIC imaging of narrowband filter NB403. The NB403 filter has the central wavelength of 4030 Å and the bandwidth of the 45 Å, which identifies LAE at the redshift range of $z = 2.30 - 2.33$. The detection limit of these LAEs is Lyα luminosity of $\sim 0.73 L^*_{\mathrm{Ly}\alpha}$ where $L^*_{\mathrm{Ly}\alpha} = 2.14 \times 10^{42}$ erg s^{-1} is the characteristic Lyα luminosity at $z = 2.1 - 3.1$ (Ciardullo et al., 2012), and corresponds to the selection completeness of $\simeq 90\%$ for the Lyα rest-frame equivalent width cut of $\mathrm{EW}_{\mathrm{Ly}\alpha} > 20$ Å (Cai et al., 2017b). The sky distribution of the LAEs in the BOSS1441 region is presented in Figure 2.6. The coordinates of the LAEs in the BOSS1441region are summarized in Tables 2.3–2.5 . Note that the HETDEX observations (Section 2.1.1) are not conducted in the BOSS1441 region.

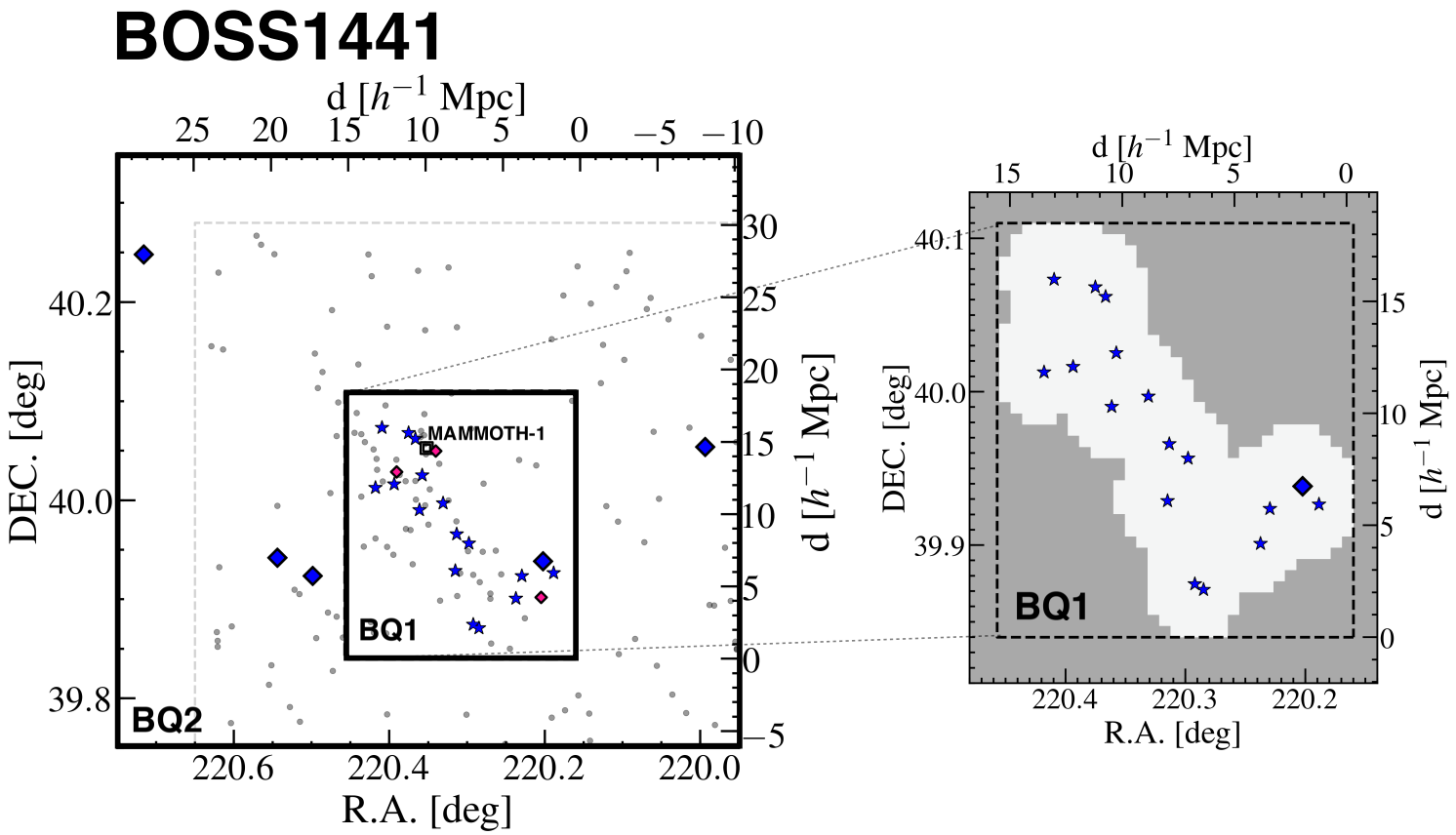

Figure 2.6: Left: Sky distribution of our background quasars and galaxies in the BQ1 and BQ2 regions of the BOSS1441 region . The blue diamonds and stars represent the positions of our background quasars and galaxies at $z = 2.4 - 2.9$, respectively (Sections 3.1 and 3.2). The dark-gray dots are the LAEs found by Cai et al. (2017b) (Section 2.1.2) whose survey boundaries are shown with light-gray dashed lines. In the BQ1 region, three are four foreground quasars at $z \sim 2.32$ that are three eBOSS quasars (the magenta diamonds; Section 2.2) and one obscure quasar that has an ELAN, MAMMOTH-1 nebula (the double square; Section 5.4) observed by Cai et al. (2017a). The top and right axes are co-moving separations relative to the bottom right corner coordinate of the BQ1 region, (R.A., Decl.) = (220.°16, 39.°84). Right: Same as left panel, but for our background quasars and galaxies in the BQ1 region of the BOSS1441 region. The dashed lines are the sky area defined by our HI tomography map (Section 4.2.2). The white area highlights regions around the sightlines around the background sources within the mean transverse sightline separation $\langle d_\perp \rangle = 2.6h^{-1}$ cMpc (Section 4.2.2).

2.2 Foreground Quasars

Our foreground quasars in our samples are taken from the SDSS DR14 Quasar catalog (hereafter DR14Q: Pâris et al., 2018). The DR14Q catalog includes all quasars identified by the SDSS-IV/eBOSS survey (eBOSS; Myers et al., 2015).

In this study, we use foreground eBOSS quasars in the cosmic volumes that are defined by our HI tomography maps (Section 4.2). We thus select our foreground eBOSS quasars by the two criterion of redshift ranges and sky areas. We search for eBOSS quasars at the redshift range $z = (2.05 - 2.55,\ 2.25 - 2.40,\ 2.05 - 2.55)$ in the (0.157, 0.04, 6.0) sky area of the (COSMOS, BOSS1441, EGS) region, and find a total of (0, 3, 78) eBOSS quasars in each of the cosmic volume. Figure 2.6 (2.5) shows the sky distribution of foreground eBOSS quasars in the (BOSS1441, EGS) region. The basic properties of the foreground eBOSS quasars in the BOSS1441 and EGS regions are summarized in Tables 2.6 and 2.7–2.8, respectively.

2.3 Background Quasars

Our background quasars in our samples are also taken from the DR14 catalog (Pâris et al., 2018). We make samples of our background quasars in the BOSS1441 and EGS regions, and do not make a sample of background quasars in the COSMOS region. This is because we use the public data of the COSMOS HI tomography map, which is sufficient for our analyses (Section 4.2.1). We thus select eBOSS quasars in the BOSS1441 and EGS regions by the two criterion of redshift ranges and sky areas.

Firstly, we construct a sample of background quasars in and around the BOSS1441 region. We search for eBOSS quasars at the redshift range $z = 2.4$–2.9 in a $6.^{\circ}0 \times 6.^{\circ}0$ sky area of the BOSS1441 region. The $6.^{\circ}0 \times 6.^{\circ}0$ area is chosen to investigate HI absorption on large scales in transverse directions. The redshift range of $z = 2.4$–2.9 is selected so that we can probe the HI Lyα absorptions at $z = 2.32$ in the background quasars' rest-frame 1041–1185Å spectral region. This spectral region is chosen to avoid contamination of HI Lyβ absorptions and stellar/interstellar absorptions associated with the quasar host galaxies (e.g., Rakic et al., 2012; Mukae et al., 2017). These two criteria yield 240 eBOSS quasars. For convenience, we divide the $6.^{\circ}0 \times 6.^{\circ}0$ region around into three regions as illustrated in Figure 2.6:

- BQ1: the inner region of BOSS1441,
- BQ2: the outer region of BOSS1441,
- BQ3: the region outside of BQ2.

The boundary between BQ1 and BQ2 is defined with a rectangle whose corners are (ΔR.A., ΔDecl.) $= (-0.^{\circ}2, -0.^{\circ}2)$, $(-0.^{\circ}2, +0.^{\circ}1)$, $(+0.^{\circ}1, +0.^{\circ}1)$, and $(+0.^{\circ}1, -0.^{\circ}2)$ relative to the coordinate of an ELAN's host quasar found in the vicinity of the LAE overdensity peak (Cai et al. 2017a; Section 5.4). Similarly, the boundary between BQ2 and BQ3 is defined with a rectangle whose corners are ΔR.A. $= \pm 0.^{\circ}4$ and ΔDecl. $= \pm 0.^{\circ}3$. In the BQ1, BQ2, and BQ3 regions, the numbers of our background quasars are 1, 4, and 235, respectively.

Secondly, we make a sample of background quasars in the EGS region. We search for eBOSS quasars at the redshift range $z = 2.1$–3.1 in the 6.0 deg^2 sky area of the

EGS region. The 6.0 deg^2 sky area of the EGS region is defined to find an extreme quasar overdensity in our large-scale HI tomography map (Section 4.2.3). The redshift range of $z = 2.1$–3.1 is selected so that we can investigate HI Lyα forest absorptions at the same redshift range as the COSMOS HI tomography map ($z = 2.05$–2.55; Section 4.2.1). These two criteria yield a total of 128 eBOSS quasars.

In our subsequent spectral analysis (Section 3.1), we narrow down the number of these eBOSS quasars to secure robust measurements of HI Lyα forest absorptions.

2.4 Background Galaxies

As shown in Figure 2.6 the number of our background quasars in the BOSS1441 BQ1 region is only 1. To increase background sightline densities for investigating the HI-gas distribution around the LAE overdensity down to a smaller scale, we need a sample of background galaxies at $z = 2.4$–2.9 in the BQ1 region.

For this purpose, we produce a multiwavelength catalog across the BQ1 region based on optical (U, V, and i) and NIR (J and H) imaging data obtained by Cai et al. (2017b) and Z. Cai et al. (in prep.) with the Large Binocular Camera (LBC; Pedichini et al., 2003) on the Large Binocular Telescope (LBT) and the Wide Field Camera (WFCAM; Casali et al., 2007) on the United Kingdom Infrared Telescope (UKIRT), respectively. We match the point spread functions (PSFs) of these images to that of the H-band image whose FWHM is the largest among them ($0\farcs9$). The 5σ limiting magnitudes in the U, V, i, J, and H bands measured with $2\farcs0$ diameter apertures are 26.6, 26.2, 26.1, 23.7, and 23.1 mag, respectively. We then create a multiwavelength source catalog by running SExtractor (Bertin & Arnouts, 1996) in dual image mode, and measure source colors with $2\farcs0$ diameter apertures.

We then select background galaxy candidates at $z = 2.4$–2.9 based on photometric redshift measurements. First of all, we apply a magnitude cut of $V < 24.85$ mag so that we can select background galaxy candidates whose continuum emission can be detected with sufficiently high S/Ns in subsequent spectroscopic observations. For the sources with $V < 24.85$ mag, we estimate their photometric redshifts with the EAZY software (Brammer et al., 2008) by fitting spectral energy distribution (SED)

templates to the observed photometric data points. The SED templates are produced with the stellar population synthesis model of Bruzual & Charlot (2003). We adopt the Chabrier initial mass function (Chabrier, 2003), a constant star formation for 0.1 Gyr, and a fixed metallicity of $Z = 0.2Z_{\odot}$. We apply the Calzetti dust attenuation (Calzetti et al., 2000) with $E(B-V) = 0.0$, 0.15, 0.30, and 0.45. We also apply attenuation by IGM absorption with a model of Inoue et al. (2014). We require selected sources to have a photometric redshift whose 1σ confidence interval is within the redshift range of $z = 2.4$–2.9. This selection yields a sample of 131 background galaxy candidates in the BQ1 region. In the subsequent Section 3.2.1, we perform follow-up spectroscopy for the background galaxy candidates.

Table 2.1: HETDEX LAEs in the COSMOS region

ID	R.A. (J2000)	Decl. (J2000)	$z_{\rm spec}$	$L_{{\rm Ly}\alpha}$ (10^{42} erg s^{-1})
1000015561	10:00:56.70	+02:10:21.69	2.298	14.12
1000017717	10:00:26.54	+02:18:08.618	2.179	7.94
1000017757	10:00:28.34	+02:17:58.49	2.492	8.37
1000018085	10:00:12.38	+02:14:16.40	2.434	9.06
1000021675	10:00:20.24	+02:17:26.17	2.102	14.41
1000021815	10:00:14.16	+02:14:27.04	2.289	19.87
1000022847	10:00:43.94	+02:14:52.75	2.486	24.07
1000030184	10:00:29.81	+02:18:49.58	2.198	8.64
1000104275	10:00:01.98	+02:09:56.07	2.256	11.97
1000468821	10:01:14.98	+02:18:29.65	2.155	15.10
1000471063	10:01:16.28	+02:18:23.24	2.322	7.95
1000471115	10:00:31.96	+02:11:40.80	2.198	10.45
1000471122	10:00:38.66	+02:10:41.90	2.445	7.35
1000471154	10:00:28.54	+02:19:19.85	2.329	7.02
1000471342	10:00:49.68	+02:22:08.99	2.391	7.77
1000471357	10:01:15.48	+02:18:21.95	2.155	9.43
1000471531	10:00:56.82	+02:13:16.52	2.433	9.96
1000471604	10:01:02.33	+02:17:00.09	2.508	16.78
1000471667	10:00:54.06	+02:21:04.39	2.473	9.53
1000471917	10:00:21.64	+02:12:22.07	2.470	13.05
1000472305	10:00:44.53	+02:11:22.63	2.533	6.93
1000472510	10:01:04.45	+02:14:36.69	2.139	9.28
1000472623	10:01:08.51	+02:17:23.78	2.403	7.66
1000472642	10:00:44.77	+02:13:55.79	2.178	8.15
1000472715	10:00:57.45	+02:18:01.47	2.163	12.34
1000472789	10:00:26.61	+02:17:14.95	2.230	8.53
1000473227	10:00:21.03	+02:16:23.11	2.441	12.46
1000473718	10:01:19.94	+02:19:15.42	2.323	9.01
1000473763	10:00:37.75	+02:16:41.09	2.385	7.75
1000473894	10:01:00.42	+02:16:13.85	2.099	7.91
1000473913	10:00:47.46	+02:11:57.85	2.282	7.59
1000523622	10:00:39.53	+02:15:38.95	2.454	9.44
1000523666	10:00:28.65	+02:17:44.24	2.099	7.39
1000523713	10:01:01.45	+02:22:56.51	2.320	6.93
1000523793	10:00:47.17	+02:13:05.05	2.340	9.62
1000523806	10:00:27.23	+02:17:31.67	2.287	11.22
1000551687	10:00:17.98	+02:18:18.43	2.444	11.20
1000567946	10:00:29.03	+02:14:07.90	2.434	6.75
1000568005	10:01:00.83	+02:17:28.66	2.470	7.19
1000568092	10:00:26.35	+02:11:34.22	2.377	12.22
1000597757	10:01:14.85	+02:17:16.14	2.175	10.77
1000597779	10:00:29.22	+02:20:27.07	2.467	17.29
1000602192	10:00:57.43	+02:14:49.48	2.499	6.33
1000658344	10:00:33.95	+02:13:16.35	2.230	10.67
1000658385	10:00:55.60	+02:20:14.40	2.465	13.99
1000658409	10:00:48.21	+02:13:33.13	2.481	8.32
1000689101	10:00:39.61	+02:13:38.54	2.441	12.73

Table 2.2: HETDEX LAEs in the EGS region

ID	R.A. (J2000)	Decl. (J2000)	$z_{\rm spec}$	$L_{{\rm Ly}\alpha}$ (10^{42} erg s^{-1})	Label[a]
1000026414	14:18:51.85	+52:47:45.85	2.451	6.35	-
1000026494	14:19:13.03	+52:49:11.22	2.156	7.26	LAE4
1000030024	14:19:06.49	+52:53:27.58	2.531	14.43	-
1000030587	14:19:26.29	+52:54:41.73	2.286	22.00	-
1000031502	14:20:17.52	+52:20:50.94	2.298	7.44	-
1000035948	14:17:25.65	+52:35:57.50	2.298	13.24	-
1000036627	14:18:10.53	+52:20:31.36	2.103	27.02	-
1000036629	14:18:26.71	+52:23:29.71	2.309	9.40	-
1000038816	14:17:33.70	+52:24:37.78	2.147	11.08	LAE3
1000039062	14:18:31.11	+52:32:39.48	2.143	11.74	LAE2
1000039126	14:18:47.25	+52:33:29.09	2.303	9.60	-
1000040154	14:21:45.40	+52:24:01.35	2.174	10.28	-
1000040791	14:23:08.85	+52:52:32.75	2.247	8.94	-
1000041960	14:18:25.87	+52:43:55.60	2.297	23.49	-
1000042184	14:21:44.87	+52:53:29.80	2.341	7.87	-
1000042206	14:22:00.68	+52:54:48.33	2.355	19.07	-
1000042449	14:18:33.14	+52:43:13.63	2.139	10.99	LAE1
1000042819	14:18:30.21	+52:43:29.81	2.299	49.07	-
1000043035	14:18:57.70	+52:41:45.47	2.185	10.39	LAE6
1000043346	14:18:26.67	+52:42:59.49	2.168	17.57	LAE5
1000043697	14:20:26.24	+52:59:19.15	2.290	8.45	-
1000043762	14:20:40.50	+52:58:50.41	2.289	13.12	-
1000044251	14:20:37.67	+53:03:35.62	2.055	9.54	-
1000044290	14:20:11.56	+52:59:48.49	2.297	11.61	-
1000044478	14:20:09.79	+52:58:49.89	2.297	11.82	-
1000044727	14:20:17.87	+52:50:52.88	2.299	11.70	-
1000044749	14:21:25.05	+53:10:52.87	2.298	7.65	-

[a] LAEs 1–6 are distributed around the extreme quasar overdensity EGS-QO1 (Section 5.3).

Table 2.3: NB403 LAEs in the BOSS1441 region

ID	R.A. (J2000)	Decl. (J2000)
BOSS1441-LAE001	14:39:34.08	+40:04:06.24
BOSS1441-LAE002	14:39:36.24	+40:09:04.32
BOSS1441-LAE003	14:39:37.20	+40:05:56.04
BOSS1441-LAE004	14:39:43.68	+40:05:04.20
BOSS1441-LAE005	14:39:45.12	+39:57:58.68
BOSS1441-LAE006	14:39:45.84	+40:02:31.56
BOSS1441-LAE007	14:39:45.84	+39:52:27.48
BOSS1441-LAE008	14:39:46.08	+40:09:47.88
BOSS1441-LAE009	14:39:47.04	+39:50:08.52
BOSS1441-LAE010	14:39:48.72	+39:50:58.20
BOSS1441-LAE011	14:39:48.72	+39:51:01.44
BOSS1441-LAE012	14:39:48.96	+40:03:31.32
BOSS1441-LAE013	14:39:49.20	+39:51:26.28
BOSS1441-LAE014	14:39:50.64	+39:53:54.60
BOSS1441-LAE015	14:39:50.64	+40:08:30.12
BOSS1441-LAE016	14:39:52.32	+39:57:08.28
BOSS1441-LAE017	14:39:55.44	+39:46:23.52
BOSS1441-LAE018	14:39:55.68	+39:53:37.32
BOSS1441-LAE019	14:39:57.12	+39:53:39.48
BOSS1441-LAE020	14:39:59.76	+40:09:57.24
BOSS1441-LAE021	14:40:03.36	+40:04:23.52
BOSS1441-LAE022	14:40:04.32	+39:47:07.44
BOSS1441-LAE023	14:40:08.64	+39:48:14.76
BOSS1441-LAE024	14:40:09.84	+40:10:57.00
BOSS1441-LAE025	14:40:12.72	+40:00:05.40
BOSS1441-LAE026	14:40:13.44	+39:49:59.16
BOSS1441-LAE027	14:40:14.40	+40:04:09.12
BOSS1441-LAE028	14:40:15.36	+40:12:15.48
BOSS1441-LAE029	14:40:16.56	+40:11:34.44
BOSS1441-LAE030	14:40:17.28	+39:57:28.08
BOSS1441-LAE031	14:40:20.16	+39:51:36.36
BOSS1441-LAE032	14:40:21.84	+40:14:58.56
BOSS1441-LAE033	14:40:22.80	+40:13:52.32
BOSS1441-LAE034	14:40:23.52	+40:08:30.84
BOSS1441-LAE035	14:40:25.20	+39:50:41.64
BOSS1441-LAE036	14:40:25.44	+39:58:42.96
BOSS1441-LAE037	14:40:25.92	+40:12:55.80
BOSS1441-LAE038	14:40:29.04	+39:59:38.76
BOSS1441-LAE039	14:40:30.00	+39:24.84.00
BOSS1441-LAE040	14:40:30.72	+40:07:05.88
BOSS1441-LAE041	14:40:33.84	+40:11:54.24
BOSS1441-LAE042	14:40:34.08	+39:45:27.00
BOSS1441-LAE043	14:40:34.32	+39:47:04.92
BOSS1441-LAE044	14:40:37.68	+39:48:11.16
BOSS1441-LAE045	14:40:37.92	+40:14:09.60
BOSS1441-LAE046	14:40:39.60	+40:06:01.44
BOSS1441-LAE047	14:40:41.76	+39:47:16.80
BOSS1441-LAE048	14:40:42.24	+40:12:24.12
BOSS1441-LAE049	14:40:45.84	+39:46:50.52
BOSS1441-LAE050	14:40:45.84	+40:09:45.72

Table 2.4: NB403 LAEs in the BOSS1441 region (continued)

ID	R.A. (J2000)	Decl. (J2000)
BOSS1441-LAE051	14:40:50.64	+40:02:06.72
BOSS1441-LAE052	14:40:55.92	+40:02:26.88
BOSS1441-LAE053	14:40:58.80	+39:51:01.44
BOSS1441-LAE054	14:41:00.24	+39:45:14.76
BOSS1441-LAE055	14:41:03.12	+39:56:56.76
BOSS1441-LAE056	14:41:04.56	+39:51:19.80
BOSS1441-LAE057	14:41:04.80	+39:54:21.60
BOSS1441-LAE058	14:41:06.96	+40:01:00.48
BOSS1441-LAE059	14:41:10.08	+39:55:28.92
BOSS1441-LAE060	14:41:10.80	+40:04:20.28
BOSS1441-LAE061	14:41:12.24	+39:47:01.68
BOSS1441-LAE062	14:41:15.12	+40:10:28.56
BOSS1441-LAE063	14:41:15.36	+39:58:43.32
BOSS1441-LAE064	14:41:16.80	+40:06:28.08
BOSS1441-LAE065	14:41:17.76	+40:14:05.28
BOSS1441-LAE066	14:41:17.76	+40:00:00.00
BOSS1441-LAE067	14:41:20.64	+40:02:12.48
BOSS1441-LAE068	14:41:23.52	+40:00:39.96
BOSS1441-LAE069	14:41:24.00	+39.58:31.44
BOSS1441-LAE070	14:41:24.72	+40:02:47.40
BOSS1441-LAE071	14:41:24.96	+39:59:42.00
BOSS1441-LAE072	14:41:24.96	+40:10:17.76
BOSS1441-LAE073	14:41:24.96	+40:03:24.84
BOSS1441-LAE074	14:41:25.20	+40:05:13.56
BOSS1441-LAE075	14:41:26.40	+40:03:49.68
BOSS1441-LAE076	14:41:27.12	+40:13:54.12
BOSS1441-LAE077	14:41:27.84	+40:00:02.52
BOSS1441-LAE078	14:41:28.80	+39:56:07.44
BOSS1441-LAE079	14:41:29.52	+39:58:12.36
BOSS1441-LAE080	14:41:30.96	+39:58:15.96
BOSS1441-LAE081	14:41:32.88	+40:01:32.52
BOSS1441-LAE082	14:41:33.84	+40:02:27.24
BOSS1441-LAE083	14:41:34.80	+39:56:42.36
BOSS1441-LAE084	14:41:36.72	+40:10:30.72
BOSS1441-LAE085	14:41:36.72	+39:57:11.16
BOSS1441-LAE086	14:41:36.72	+39:47:02.04
BOSS1441-LAE087	14:41:36.96	+39:51:56.16
BOSS1441-LAE088	14:41:37.20	+40:05:44.52
BOSS1441-LAE089	14:41:39.84	+40:01:51.24
BOSS1441-LAE090	14:41:40.32	+39:57:41.04
BOSS1441-LAE091	14:41:40.80	+39:51:59.04
BOSS1441-LAE092	14:41:41.52	+40:13:34.32
BOSS1441-LAE093	14:41:41.76	+39:52:37.2
BOSS1441-LAE094	14:41:42.48	+40:14:53.16
BOSS1441-LAE095	14:41:43.92	+39:57:12.24
BOSS1441-LAE096	14:41:44.64	+40:04:00.48
BOSS1441-LAE097	14:41:45.60	+40:08:13.56
BOSS1441-LAE098	14:41:46.08	+40:05:16.80
BOSS1441-LAE099	14:41:46.80	+40:04:04.80
BOSS1441-LAE100	14:41:50.40	+39:51:41.76

Table 2.5: NB403 LAEs in the BOSS1441 region (continued)

ID	R.A. (J2000)	Decl. (J2000)
BOSS1441-LAE101	14:41:51.84	+40:05:56.04
BOSS1441-LAE102	14:41:52.32	+39:52:57.36
BOSS1441-LAE103	14:41:52.32	+40:03:53.64
BOSS1441-LAE104	14:41:53.52	+39:49:40.44
BOSS1441-LAE105	14:41:53.76	+40:11:30.48
BOSS1441-LAE106	14:41:54.24	+40:00:25.92
BOSS1441-LAE107	14:41:54.96	+39:53:12.12
BOSS1441-LAE108	14:41:56.64	+40:07:45.84
BOSS1441-LAE109	14:41:58.08	+40:06:48.24
BOSS1441-LAE110	14:41:58.56	+39:51:39.60
BOSS1441-LAE111	14:41:59.04	+40:08:53.52
BOSS1441-LAE112	14:42:03.60	+39:46:36.12
BOSS1441-LAE113	14:42:03.84	+39:54:19.44
BOSS1441-LAE114	14:42:05.28	+39:54:34.92
BOSS1441-LAE115	14:42:06.72	+39:47:28.68
BOSS1441-LAE116	14:42:10.56	+39:59:39.84
BOSS1441-LAE117	14:42:11.52	+40:14:53.88
BOSS1441-LAE118	14:42:12.48	+39:50:00.96
BOSS1441-LAE119	14:42:13.20	+39:48:50.04
BOSS1441-LAE120	14:42:15.60	+40:15:28.44
BOSS1441-LAE121	14:42:17.04	+40:16:00.84
BOSS1441-LAE122	14:42:24.72	+39:52:22.08
BOSS1441-LAE123	14:42:24.96	+39:46:31.08
BOSS1441-LAE124	14:42:27.36	+40:09:08.28
BOSS1441-LAE125	14:42:28.56	+39:55:56.64
BOSS1441-LAE126	14:42:28.80	+40:13:47.28
BOSS1441-LAE127	14:42:29.04	+39:51:08.28
BOSS1441-LAE128	14:42:29.04	+39:51:29.16
BOSS1441-LAE129	14:42:29.28	+39:52:01.56
BOSS1441-LAE130	14:42:30.96	+40:09:19.44
BOSS1441-LAE131	14:41:07.20	+39:56:53.16
BOSS1441-LAE132	14:40:54.24	+39:52:51.24
BOSS1441-LAE133	14:41:01.44	+39:55:30.72
BOSS1441-LAE134	14:41:04.80	+39:54:00.72
BOSS1441-LAE135	14:41:07.92	+39:55:02.28
BOSS1441-LAE136	14:41:11.52	+39:56:52.44
BOSS1441-LAE137	14:41:14.16	+39:55:33.96
BOSS1441-LAE138	14:41:15.12	+39:54:13.32
BOSS1441-LAE139	14:41:20.40	+39:53:54.24
BOSS1441-LAE140	14:41:25.20	+40:03:52.92
BOSS1441-LAE141	14:41:26.16	+40:04:17.40
BOSS1441-LAE142	14:41:28.08	+40:01:11.28
BOSS1441-LAE143	14:41:30.96	+40:01:07.68
BOSS1441-LAE144	14:41:33.84	+40:01:44.40
BOSS1441-LAE145	14:41:38.16	+40:01:03.72
BOSS1441-LAE146	14:41:39.84	+40:02:29.76
BOSS1441-LAE147	14:41:40.80	+40:03:03.96
BOSS1441-LAE148	14:41:43.44	+40:03:32.76
BOSS1441-LAE149	14:41:44.64	+40:00:12.60

Table 2.6: Foreground eBOSS quasars in the BOSS1441 BQ1 region

ID	R.A. (J2000)	Decl. (J2000)	$z_{\rm spec}$	Label[a]
5172-56071-0572	14:41:33.75	+40:01:42.78	2.306	QSO1
5172-56071-0535	14:40:49.14	+39:54:07.51	2.306	QSO2
5172-56071-0568	14:41:21.66	+40:02:58.82	2.305	QSO3

[a] The three eBOSS quasars are labeled as QSOs 1–3 in Figure 4.2 and Section 5.2.

Table 2.7: Foreground eBOSS quasars in the EGS region

ID	R.A. (J2000)	Decl. (J2000)	$z_{\rm spec}$
7339-56722-0728	14:14:16.34	+53:35:08.39	2.453
7339-56799-0734	14:14:20.55	+53:22:16.67	2.217
7030-56448-0602	14:14:22.82	+52:51:20.63	2.149
7339-56722-0787	14:15:24.43	+53:28:32.77	2.153
7339-56799-0238	14:15:34.20	+52:57:43.22	2.061
7340-56837-0794	14:15:41.15	+53:51:04.20	2.420
7339-56768-0256	14:15:48.07	+52:09:09.94	2.469
7339-56799-0787	14:15:54.32	+53:53:57.02	2.191
7339-56722-0788	14:15:54.46	+53:17:06.92	2.138
7339-56799-0770	14:16:02.71	+53:17:45.03	2.207
6717-56397-0604	14:16:27.00	+53:19:40.10	2.428
7339-56799-0809	14:16:28.69	+53:31:00.40	2.273
7029-56455-0247	14:16:28.92	+52:03:29.00	2.134
7339-56722-0838	14:16:41.41	+53:21:47.17	2.214
7028-56449-0809	14:16:45.06	+53:05:10.15	2.529
7339-56772-0218	14:16:47.20	+52:11:15.26	2.158
7338-56745-0823	14:17:04.00	+53:38:07.47	2.501
7339-56799-0194	14:17:15.19	+53:03:03.76	2.164
7028-56449-0805	14:17:22.72	+52:58:51.62	2.405
7339-56751-0060	14:17:26.51	+52:18:56.51	2.151
7028-56449-0834	14:17:29.99	+53:38:25.69	2.119
7339-56722-0200	14:17:38.83	+52:23:33.07	2.153
7339-56722-0832	14:17:43.33	+53:11:45.67	2.059
7339-56799-0831	14:17:50.37	+53:45:17.76	2.177
7339-56772-0798	14:17:52.39	+53:48:49.43	2.093
7339-56799-0854	14:18:07.73	+53:17:54.02	2.278
7339-56722-0876	14:18:17.46	+53:11:16.82	2.232
7339-57518-0151	14:18:18.45	+52:43:56.05	2.136
7029-56455-0234	14:18:23.07	+52:41:18.81	2.050
7338-56745-0149	14:18:42.27	+52:36:43.97	2.128
7339-56772-0893	14:18:43.30	+53:19:20.83	2.301
7030-56448-0306	14:18:57.23	+52:18:23.39	2.167
7339-56772-0895	14:19:05.24	+53:53:54.17	2.427
7339-56799-0134	14:19:05.73	+52:12:38.07	2.219
7031-56449-0404	14:19:07.20	+52:01:51.74	2.172
7340-56825-0873	14:19:10.22	+53:47:07.11	2.373
7028-56449-0870	14:19:15.99	+53:49:24.13	2.209
7339-56772-0889	14:19:27.35	+53:37:27.70	2.368
7339-56772-0884	14:19:29.90	+53:35:01.41	2.390
7339-56799-0105	14:19:32.07	+52:26:39.46	2.162
7028-56449-0101	14:19:45.40	+52:23:33.57	2.378
7339-56799-0087	14:19:52.89	+52:01:16.87	2.229
7339-56799-0106	14:19:55.27	+52:27:41.19	2.141
7339-56722-0093	14:20:36.56	+52:14:55.05	2.212
7028-56449-0937	14:20:37.24	+52:58:51.00	2.274
7340-56837-0923	14:20:41.26	+53:33:55.30	2.421
7028-56449-0066	14:20:46.11	+52:24:21.61	2.256
7339-56799-0913	14:20:49.31	+53:52:11.59	2.221
7029-56455-0158	14:20:58.63	+52:40:44.43	2.489
7339-56772-0955	14:21:02.17	+53:39:44.14	2.292

Table 2.8: Foreground eBOSS quasars in the EGS region (continued)

ID	R.A. (J2000)	Decl. (J2000)	$z_{\rm spec}$
7028-56449-0067	14:21:03.96	+52:37:12.53	2.235
7339-56722-0074	14:21:17.99	+52:53:46.00	2.308
7028-56449-0933	14:21:33.92	+53:02:45.52	2.150
7339-56722-0062	14:21:55.20	+52:27:49.48	2.516
7339-56799-0038	14:22:01.46	+52:32:50.26	2.121
7339-56799-0037	14:22:08.12	+52:29:08.65	2.370
7029-56455-0898	14:22:26.24	+52:57:09.93	2.095
7340-56726-0034	14:22:34.46	+52:58:38.02	2.138
7030-56448-0218	14:22:34.99	+52:00:10.05	2.109
7339-56772-0038	14:22:37.49	+52:53:35.86	2.226
7032-56471-0332	14:22:40.47	+52:04:11.81	2.267
7339-56780-0074	14:22:42.59	+52:44:15.69	2.171
7339-56772-0868	14:22:52.42	+53:36:48.86	2.084
7340-56837-0978	14:23:06.05	+53:15:29.03	2.468
7028-56449-0945	14:23:07.38	+53:34:39.84	2.074
7029-56455-0086	14:23:33.95	+52:07:00.95	2.271
7339-57481-0991	14:23:37.51	+53:18:28.89	2.435
7339-56799-0984	14:23:50.24	+53:29:29.31	2.136
7339-56799-0992	14:24:11.08	+53:20:41.38	2.362
7339-56772-0972	14:24:19.18	+53:17:50.62	2.530
7339-56768-0016	14:24:22.50	+52:59:03.22	2.138
7032-56471-0306	14:24:27.85	+52:20:44.40	2.331
7029-56455-0032	14:24:32.08	+52:22:20.49	2.194
7031-56449-0346	14:24:38.98	+52:21:39.15	2.259
7031-56449-0655	14:24:48.10	+53:21:21.42	2.066
7030-56448-0159	14:25:06.97	+52:54:44.33	2.546
7032-56471-0723	14:25:23.43	+53:29:45.88	2.182
7032-56471-0298	14:25:51.03	+52:05:09.06	2.315

CHAPTER 3
SPECTROSCOPIC STUDY:
OBSERVATIONS AND SPECTRA

In Chapter 2, we have made samples of background sources for the BOSS1441 and EGS regions, respectively. In this Chapter, we obtain spectra of background quasars (Section 3.1) and background galaxies (Section 3.2) that are used for our subsequent HI tomography.

3.1 Spectra of Background Quasars

We obtain spectra of our background quasar samples from the eBOSS data (Myers et al., 2015) that are taken by the Sloan Foundation 2.5m telescope at Apache Point Observatory (Figure 3.1). The eBOSS spectra have a spectral resolution of $R \approx 2000$, covering a wavelength range of 3600–10400Å. An example spectrum is shown in the top panel of Figure 3.3.

To obtain robust measurements of HI Lyα forest absorptions, we check the qualities of the eBOSS spectra and remove quasars whose spectra do not meet the additional criteria described below. We require their eBOSS spectra have a median signal-to-noise ratio (S/N) ≥ 2 per 1.0 Å pixel over their Lyα forest wavelength range (i.e., 1041–1185Å in the rest-frame). In addition, we remove quasars whose spectra have broad absorption lines associated with themselves by applying BI < 200 km s^{-1} in the DR14Q catalog, where BI (BALnicity Index) is a measure of the strength of an absorption trough calculated for the blueward of CIV emission line. We also remove quasars whose spectra show damped Lyα systems (DLAs) in the Lyα forest wavelength range, based on the DLA catalog of Noterdaeme et al. (2012) and their updated one[1] for the SDSS DR12 quasars (Pâris et al., 2017). For quasars that have no SDSS DR12 counterpart, we visually inspect their eBOSS spectra and remove them if they show signatures of DLAs in their Lyα forest wavelength range.

[1] `http://www2.iap.fr/users/noterdae/DLA/DLA.html`

For the BOSS1441 region, our careful selection results in a sample of 117 background quasars. In the BQ1, BQ2, and BQ3 regions (see Section 2.3), the numbers of our background quasars are 1, 4, and 112, respectively. The distributions of the background quasars in BQ1 and BQ2 are presented in Figure 2.6. The basic properties of the (1.4,112) background quasars in the (BQ1,BQ2, BQ3) region are summarized in Tables (3.1, 3.2, 3.3 – 3.5).

In the EGS region, our careful selection gives a sample of 43 background quasars for our subsequent HI tomography. The distributions of the background quasars in the EGS region are shown in Figure 2.5. The basic properties of the 43 background quasars in the EGS region are summarized in Table 3.6.

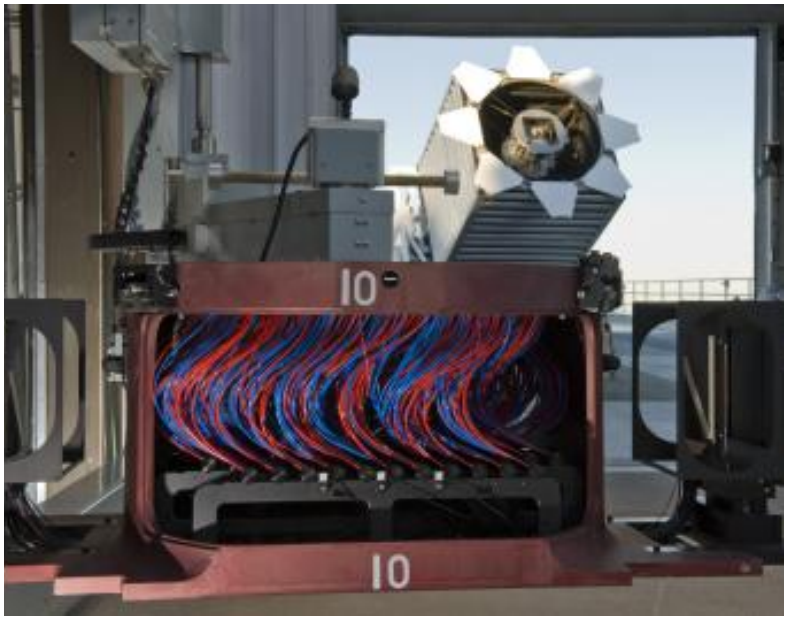

Figure 3.1: The Sloan Foundation 2.5m telescope and the BOSS fiber cartridges. One fiber cartridge contains 1000 optical fibers that guide light from an aluminum plate where 1000 holes are drilled to the BOSS spectrographs. This figure is taken from https://www.eurekalert.org/multimedia/pub/17104.php.

3.2 Spectra of Background Galaxies

In this section, we take optical spectra of our background galaxies in the BOSS1441 region, performing our spectroscopy (Section 3.2.1) and retrieving from the archival data (Section 3.2.2).

3.2.1 Follow-Up Spectroscopy

We carried out spectroscopic observations for our background galaxy candidates using the Low Resolution Imaging Spectrometer (LRIS) Double-Spectrograph (Oke et al., 1995, Figure 3.2) on the Keck I telescope on 2017 August 27 (UT) (PI: S. Mukae). We used the d560 dichroic with the B600/4000 grism on the blue arm, resulting in a wavelength coverage of 3800–5500Å. The observations were made in the multi-object slit (MOS) mode. We designed one mask for the BOSS1441 region with $1\farcs0$ slit width, yielding a spectroscopic resolution of $R \equiv \lambda/\Delta\lambda \approx 1000$. The total exposure time was 9000 s. The sky conditions were clear throughout the observing run, with an average seeing size of $0\farcs95$.

We reduce the LRIS data with the Low-Redux package[2] in the public XIDL pipeline.[3] The pipeline conducts bias subtraction, flat fielding with dome flat and twilight flat data, wavelength calibration with arc data, cosmic ray rejection, source identification, spectral trace determination, sky background subtraction, and distortion correction. We then extract one-dimensional (1D) spectra of the identified sources from the reduced two-dimensional (2D) spectra and combine them to obtain their stacked 1D spectra.

3.2.2 Archival Search

In addition to our own observations, two other LRIS programs were conducted for the BOSS1441 region in the MOS mode on 2016 April 5 (UT) (PI: X. Fan) and 2016 May 9–10 (UT) (PI: X. Prochaska) by using the same dichroic and grism as ours.

[2] `http://www.ucolick.org/~xavier/LowRedux/`

[3] `http://www.ucolick.org/~xavier/IDL/`

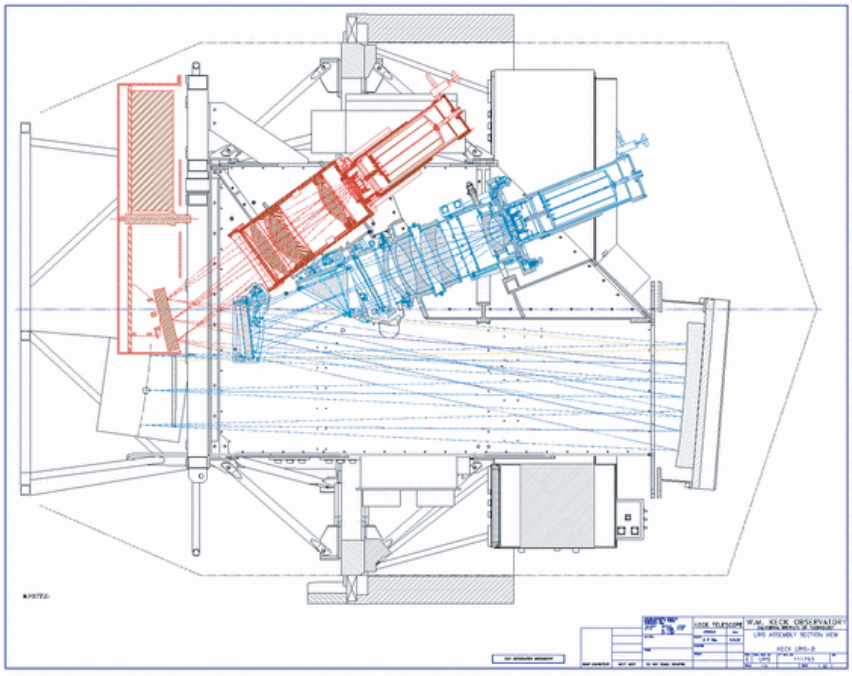

Figure 3.2: Layout of LRIS instrument and its light path. The blue (red) channel of the LRIS spectrograph is shaded in blue (red). This figure is taken from Steidel et al. (2004).

Although the original aim of their LRIS programs is to identify associated galaxies in the BOSS1441 overdense region at $z = 2.3$ (Z. Cai et al., private communication), there is a possibility that some background galaxies at $z = 2.4 - 2.9$ are included as targets in the MOS masks and identified by chance. Thus, we download the raw LRIS data from the Keck Observatory Archive (KOA)[4] and reduce them in the same way as our LRIS data.

3.2.3 Background Galaxy Identification

We determine spectroscopic redshifts, $z_{\rm spec}$ of background galaxies in the BOSS1441 region, based on the LRIS spectra obtained in Sections 3.2.1 and 3.2.2. We fit the galaxy spectrum template of Shapley et al. (2003) to the LRIS spectra and determine the best-fit $z_{\rm spec}$ by the minimum value of χ^2. We find that 20 galaxies have $z_{\rm spec}$ values in the range of 2.4–2.9.

To obtain robust measurements of HI absorptions, we require that the spectra of background galaxies have a median S/N $\geq$ 2 per 1.2 Å pixel in the Lyα forest wavelength range of 1041–1185Å in the rest-frame, in the same way as we require for the background quasars. In addition, based on our visual inspection, we remove a galaxy whose spectrum shows a possible feature of a DLA in the Lyα forest wavelength range. These selections result in a sample of 16 background galaxies for investigating HI-gas distribution around the LAE overdensity peak. Figure 2.6 shows the positions of the background quasar and galaxies in the BQ1 region. The example spectra are shown in the middle and bottom panels of Figure 3.3. The basic properties of the 16 background galaxies as well as the background quasar are summarized in Table 3.1.

[4] `https://www2.keck.hawaii.edu/koa/public/koa.php`

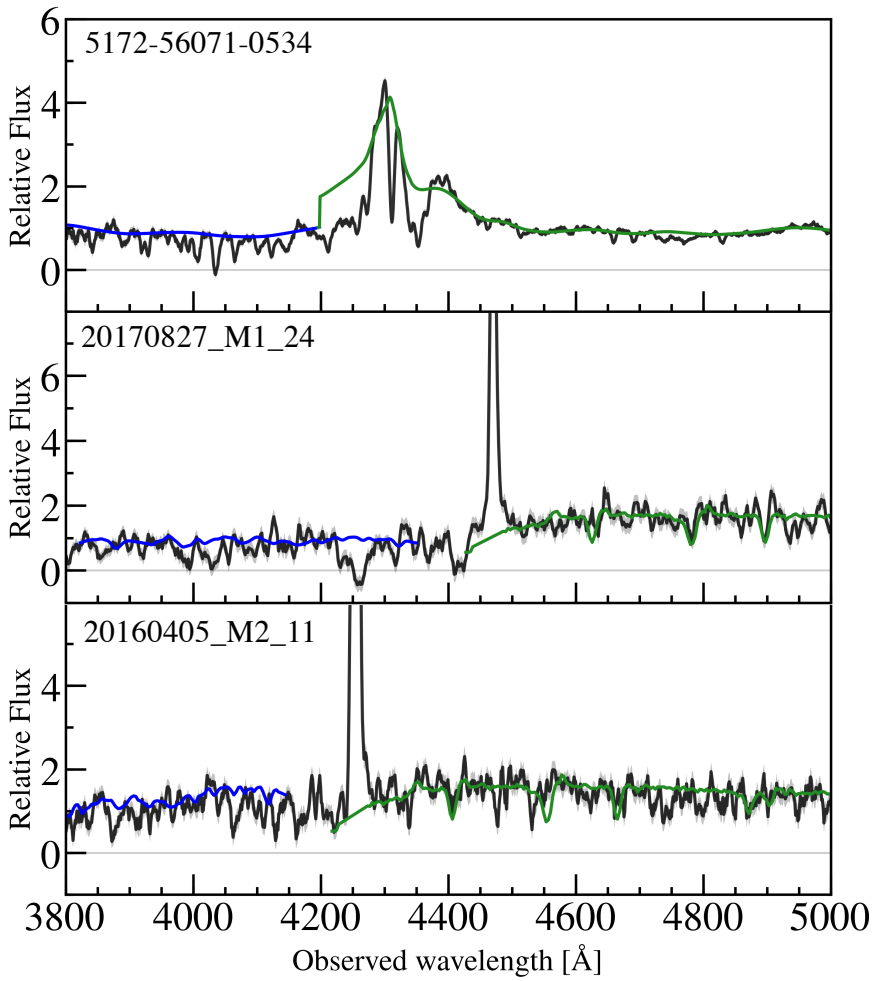

Figure 3.3: Example spectra of our background sources. Top panel is an eBOSS spectrum of a background quasar. Middle and bottom panels are Keck/LRIS spectra of background galaxies. The black lines depict the spectra smoothed with 1.25 h^{-1} cMpc scales along the sightlines and the grey shades represent the uncertainties. The grey lines are the flux zero level. The green curve(s) in the top (Middle and bottom) panel(s) are the Suzuki et al. (2005) (Shapley et al. 2003) template overplotted at the source redshifts. The blue curve(s) in the top (Middle and bottom) panel(s) are the Suzuki et al. (2005) (Berry et al. 2012) template representing the estimated continuum (continua).

Table 3.1: Background objects for HI tomography in the BOSS1441 BQ1 region.

Source	R.A. (J2000)	Decl. (J2000)	$z_{\rm spec}$	g (AB)	V (AB)	Exposure Time (s)	Sample[a]
5172-56071-0534	14:40:48.56	+39:56:18.39	2.543	20.04	-	-	eBOSS
20170827_M1_05	14:41:19.44	+39:59:49.52	2.509	-	24.04	7200	LRISs
20170827_M1_07	14:41:26.77	+39:59:25.01	2.816	-	23.40	7200	LRISs
20170827_M1_22	14:41:27.98	+40:03:43.31	2.510	-	24.50	7200	LRISs
20170827_M1_24	14:41:30.05	+40:04:05.59	2.671	-	23.58	7200	LRISs
20160510_M2_05	14:41:11.50	+39:57:24.08	2.546	-	24.11	5400	LRISa
20160510_M2_10	14:41:16.63	+39:58:51.56	2.598	-	23.21	5400	LRISa
20160510_M2_25	14:41:34.49	+40:00:58.68	2.795	-	23.61	5400	LRISa
20160509_M1_11	14:41:40.29	+40:00:46.08	2.557	-	23.05	4000	LRISa
20160509_M1_23	14:41:38.31	+40:04:23.49	2.786	-	22.84	4000	LRISa
20160405_M1_05	14:41:25.85	+40:01:31.40	2.795	-	22.82	6000	LRISa
20160405_M2_08	14:41:10.15	+39:52:28.88	2.791	-	24.27	6000	LRISa
20160405_M2_10	14:41:15.62	+39:55:43.97	2.512	-	24.42	6000	LRISa
20160405_M2_11	14:41:08.38	+39:52:15.59	2.497	-	23.68	6000	LRISa
20160405_M2_20	14:40:56.98	+39:54:03.24	2.703	-	24.34	6000	LRISa
20160405_M2_27	14:40:55.13	+39:55:25.70	2.840	-	24.37	6000	LRISa
20160405_M2_35	14:40:45.31	+39:55:35.76	2.598	-	23.07	6000	LRISa

[a] eBOSS: eBOSS spectroscopy data (Section 3.1), LRISs: Keck spectroscopy data (Section 3.2.1), LRISa: Keck archival data (Section 3.2.2)

Table 3.2: Background eBOSS quasars in the BOSS BQ2 region

ID	R.A. (J2000)	Decl. (J2000)	$z_{\rm spec}$	g (AB)
5171-56038-0020	14:39:58.56	+40:03:14.04	2.422	20.20
8498-57105-0478	14:41:59.76	+39:55:25.32	2.546	19.47
5172-56071-0616	14:42:10.56	+39:56:31.92	2.612	20.99
5172-56071-0608	14:42:51.84	+40:14:53.52	2.547	20.86

Table 3.3: Background eBOSS quasars in the BOSS1441 BQ3 region

ID	R.A. (J2000)	Decl. (J2000)	$z_{\rm spec}$	g (AB)
6060-56074-0753	14:29:24.72	+42:57:21.60	2.717	19.66
4713-56044-0860	14:29:28.32	+38:16:45.84	2.534	20.46
4713-56044-0150	14:29:29.52	+37:33:23.76	2.500	20.43
4713-56044-0160	14:29:36.00	+37:56:58.92	2.562	20.29
5171-56038-0432	14:29:42.24	+40:11:20.40	2.553	19.83
5171-56038-0416	14:29:45.36	+39:26:03.48	2.478	21.34
5171-56038-0630	14:30:06.48	+40:53:06.36	2.479	20.89
5171-56038-0614	14:30:07.92	+40:24:02.52	2.525	18.74
8502-57512-0758	14:30:21.84	+42:29:16.44	2.661	21.30
5171-56038-0680	14:30:29.28	+41:03:24.48	2.467	20.31
5171-56038-0350	14:31:14.40	+39:59:13.56	2.704	20.68
6060-56074-0840	14:31:19.20	+42:57:27.36	2.526	20.26
6060-56074-0850	14:31:47.76	+42:44:55.32	2.528	20.50
6060-56074-0860	14:31:51.12	+42:30:41.04	2.468	20.54
4714-56041-0654	14:31:54.00	+37:44:00.60	2.565	20.36
6060-56074-0122	14:31:58.56	+41:32:31.56	2.478	21.41
4713-56044-0950	14:32:07.44	+38:48:32.76	2.578	19.87
4713-56044-0072	14:32:22.56	+37:48:18.72	2.674	19.47
6060-56074-0892	14:32:22.80	+42:33:50.04	2.823	19.54
5171-56038-0322	14:32:28.56	+39:08:36.24	2.714	18.57
5171-56038-0734	14:32:38.88	+40:20:40.20	2.472	20.70
5171-56038-0294	14:32:52.80	+39:32:48.12	2.698	20.96
5171-56038-0760	14:33:06.72	+40:46:27.84	2.451	19.14
4713-56044-0968	14:33:12.72	+38:19:31.08	2.652	21.14
6061-56076-0534	14:33:48.00	+42:12:18.72	2.503	20.51
5171-56038-0776	14:33:54.96	+40:07:51.60	2.615	19.77
5171-56038-0788	14:34:00.24	+41:03:22.32	2.521	20.30
5173-56046-0469	14:34:07.92	+38:05:42.00	2.560	20.42
8502-57512-0081	14:34:16.08	+40:40:19.20	2.652	22.03
5173-56046-0546	14:34:25.92	+38:41:16.80	2.415	20.07
6060-56074-0960	14:34:26.40	+43:00:34.20	2.865	20.98
8502-57512-0075	14:34:30.48	+41:39:59.76	2.648	20.49
8502-57512-0969	14:34:36.96	+42:04:16.68	2.864	20.61
5171-56038-0846	14:35:21.60	+40:08:54.24	2.437	20.09
5171-56038-0856	14:35:21.84	+40:22:09.12	2.792	20.62
5171-56038-0854	14:35:49.44	+40:13:24.60	2.774	20.18
6061-56076-0566	14:35:50.40	+42:31:34.68	2.571	21.16
5171-56038-0152	14:36:08.16	+40:03:52.92	2.433	20.06
8502-57512-0960	14:36:37.44	+42:37:25.68	2.513	20.45
5171-56038-0918	14:36:56.88	+40:59:43.08	2.602	20.52
8502-57512-0020	14:37:07.68	+41:49:33.96	2.845	21.07
5173-56046-0672	14:37:10.56	+38:23:21.12	2.635	18.97
4714-56041-0891	14:37:11.52	+37:03:32.40	2.574	19.26
5171-56038-0946	14:37:24.72	+41:23:00.96	2.539	20.39
6061-56076-0660	14:37:33.12	+42:08:04.20	2.402	19.55
5171-56038-0926	14:37:33.36	+40:29:29.04	2.825	18.44
6061-56076-0644	14:37:40.56	+42:34:45.84	2.444	19.66
6061-56076-0646	14:37:43.44	+42:31:11.64	2.833	20.99
4714-56041-0946	14:38:04.32	+37:37:19.20	2.415	20.76
5173-56046-0681	14:38:06.72	+38:48:03.24	2.804	21.13

Table 3.4: Background eBOSS quasars in the BOSS1441 BQ3 region (continued)

ID	R.A. (J2000)	Decl. (J2000)	$z_{\rm spec}$	g (AB)
5171-56038-0056	14:38:53.52	+39:22:03.72	2.535	19.30
4714-56041-0930	14:38:53.52	+37:10:35.40	2.400	21.40
5173-56046-0789	14:39:07.92	+38:37:36.48	2.669	20.25
5171-56038-0020	14:39:58.56	+40:03:14.04	2.422	20.20
6061-56076-7066	14:40:24.96	+42:27:27.00	2.495	20.95
6061-56076-0258	14:40:39.36	+41:05:59.64	2.574	21.18
6061-56076-0260	14:40:42.48	+41:23:40.56	2.899	20.10
5172-56071-0534	14:40:48.48	+39:56:18.24	2.542	20.04
5172-56071-0521	14:40:53.04	+40:26:58.92	2.588	20.35
6061-56076-0254	14:40:55.44	+40:53:20.04	2.775	19.37
6061-56076-0220	14:41:05.52	+41:25:08.76	2.586	20.26
5173-56046-0810	14:41:13.20	+38:47:51.00	2.562	20.25
5173-56046-0190	14:41:35.76	+37:43:44.76	2.693	20.03
8498-57105-0163	14:49:35.76	+38:50:41.64	2.480	20.59
6061-56076-0834	14:41:38.88	+42:53:01.32	2.665	20.45
6061-56076-0808	14:41:41.76	+42:26:48.48	2.625	20.45
6061-56076-0836	14:41:45.36	+42:43:42.60	2.493	20.71
6061-56076-0202	14:41:46.80	+41:09:25.92	2.601	19.58
8498-57105-0478	14:41:59.76	+39:55:25.32	2.546	19.47
6061-56076-0180	14:42:12.24	+41:01:10.56	2.574	20.27
5172-56071-0586	14:42:22.56	+40:51:42.48	2.822	21.00
6061-56076-0182	14:42:24.48	+41:34:31.80	2.452	20.05
6061-56076-0132	14:42:54.72	+40:55:35.76	2.593	18.54
6061-56076-0878	14:42:55.20	+42:43:30.36	2.619	20.45
5172-56071-0410	14:42:55.92	+38:48:31.68	2.745	20.23
6061-56076-0142	14:43:05.52	+41:29:24.00	2.729	21.59
6061-56076-0898	14:43:21.12	+42:12:18.36	2.525	20.20
5173-56046-0926	14:43:35.52	+38:32:43.08	2.635	20.50
6061-56076-0900	14:44:02.40	+42:08:52.08	2.417	20.80
8498-57105-0424	14:44:19.20	+39:34:20.28	2.498	20.32
6061-56076-0934	14:44:37.44	+42:21:42.12	2.800	20.41
5173-56046-0964	14:44:48.48	+38:22:48.72	2.435	19.19
8498-57105-0396	14:45:16.32	+39:52:10.92	2.612	20.75
8498-57105-0362	14:45:44.88	+38:59:54.24	2.737	21.28
5172-56071-0272	14:45:53.52	+39:51:24.84	2.666	19.27
5172-56071-0266	14:46:06.96	+39:18:16.56	2.590	19.62
6061-56076-0026	14:46:13.20	+41:34:59.16	2.465	20.78
4718-56014-0782	14:46:14.16	+37:12:22.32	2.406	21.24
4718-56014-0783	14:46:18.24	+37:03:46.80	2.763	19.92
5174-56047-0554	14:46:36.72	+38:14:20.04	2.699	18.31
4718-56014-0822	14:46:38.16	+37:13:34.68	2.584	20.28
8498-57105-0314	14:46:52.56	+39:43:39.72	2.736	21.35
5174-56047-0479	14:46:54.96	+37:39:07.92	2.814	21.24
8498-57105-0247	14:48:55.68	+38:52:39.00	2.695	20.93
5174-56047-0352	14:49:39.36	+37:23:11.40	2.595	20.35
5172-56071-0882	14:49:47.52	+40:25:04.44	2.460	20.73
8498-57105-0190	14:49:57.60	+39:45:35.28	2.404	20.26
5174-56047-0311	14:50:01.92	+37:32:31.20	2.655	20.58
6053-56091-0612	14:50:12.00	+42:14:50.64	2.717	21.34
6053-56091-0418	14:50:22.08	+41:17:04.20	2.581	19.59

Table 3.5: Background eBOSS quasars in the BOSS1441 BQ3 region (continued)

ID	R.A. (J2000)	Decl. (J2000)	$z_{\rm spec}$	g (AB)
5174-56047-0664	14:50:25.20	+38:50:00.60	2.608	19.99
5174-56047-0718	14:51:09.12	+38:22:45.12	2.683	21.37
5174-56047-0710	14:51:16.56	+38:21:37.44	2.741	21.21
5174-56047-0714	14:51:20.64	+38:26:06.36	2.520	19.15
5174-56047-0740	14:51:22.32	+37:58:17.40	2.465	20.40
5174-56047-0270	14:51:25.20	+37:27:12.96	2.616	20.88
5174-56047-0769	14:52:17.52	+38:13:45.84	2.809	21.55
5174-56047-0239	14:52:18.96	+37:45:33.48	2.566	20.94
6053-56091-0278	14:52:44.40	+41:57:22.32	2.633	19.42
5172-56071-0984	14:52:49.68	+40:26:54.96	2.896	19.05
5166-56065-0560	14:53:05.76	+40:27:05.40	2.626	20.19
5174-56047-0836	14:53:17.28	+38:33:32.40	2.445	20.36

Table 3.6: Background eBOSS quasars in the EGS region

ID	R.A. (J2000)	Decl. (J2000)	$z_{\rm spec}$	g (AB)
7339-56799-0270	14:14:08.64	+52:40:38.64	2.790	20.59
7339-56722-0800	14:14:18.24	+53:50:46.68	2.729	21.43
7339-56799-0734	14:14:20.64	+53:22:16.68	2.212	19.54
7339-56799-0730	14:14:35.52	+53:25:36.84	2.861	20.72
7339-56722-0297	14:14:39.12	+52:06:16.20	2.914	20.93
7339-56799-0728	14:14:44.16	+53:35:55.68	2.734	21.55
7339-56722-0781	14:15:08.64	+53:29:16.80	3.204	22.08
7339-56799-0277	14:15:08.64	+53:00:19.80	2.765	21.36
7340-56837-0794	14:15:41.04	+53:51:04.32	2.420	20.81
7027-56448-0068	14:15:51.36	+52:27:40.68	2.583	19.86
7028-56449-0809	14:16:45.12	+53:05:10.32	2.529	21.68
7339-56772-0218	14:16:47.28	+52:11:15.36	2.153	18.70
7340-56837-0833	14:17:22.32	+53:48:52.92	2.726	20.71
7339-56799-0831	14:17:50.40	+53:45:17.64	2.190	20.30
7339-56799-0854	14:18:07.68	+53:17:53.88	2.274	20.67
7339-56799-0152	14:18:09.60	+52:43:00.12	3.192	21.88
7028-56449-0854	14:18:13.44	+52:52:40.08	3.287	21.14
7339-56722-0876	14:18:17.52	+53:11:16.80	2.238	20.50
7339-56772-0893	14:18:43.20	+53:19:21.00	2.298	20.56
7340-56837-0117	14:19:12.48	+52:08:17.88	2.563	19.78
7339-57510-0876	14:19:15.36	+53:55:22.80	3.350	21.47
7339-56722-0147	14:19:35.52	+52:57:10.80	3.217	20.45
7339-56799-0087	14:19:52.80	+52:01:17.04	2.224	19.48
7339-56772-0924	14:20:10.56	+53:12:23.76	2.597	20.09
7027-56448-0994	14:20:33.12	+53:07:35.04	2.880	21.55
7340-56837-0923	14:20:41.28	+53:33:55.44	2.421	20.87
7339-56722-0111	14:21:09.60	+52:38:00.24	3.387	20.50
7339-56799-0074	14:21:13.20	+52:49:30.00	2.644	19.36
7339-56722-0074	14:21:18.00	+52:53:45.96	2.306	19.95
7339-56799-0069	14:21:38.64	+52:33:24.48	2.606	20.30
7339-56799-0068	14:21:41.28	+52:45:51.84	2.654	21.04
7339-56722-0062	14:21:55.20	+52:27:49.32	2.516	21.10
7339-56799-0038	14:22:01.44	+52:32:50.28	2.119	19.99
7339-56722-0059	14:22:13.92	+52:25:08.04	3.220	21.43
7339-56768-0038	14:22:39.60	+52:28:52.68	2.989	21.61
7339-56780-0074	14:22:42.48	+52:44:15.72	2.175	20.03
7340-56837-0978	14:23:06.00	+53:15:29.16	2.468	18.29
7029-56455-0100	14:23:17.28	+52:13:12.72	2.671	21.54
7032-56471-0340	14:23:37.20	+52:16:07.68	2.894	19.73
7339-56799-0992	14:24:11.04	+53:20:41.28	2.366	20.31
6710-56416-0442	14:24:11.52	+53:50:26.88	2.769	20.96
7339-56799-0014	14:24:18.24	+53:04:06.60	2.859	19.56
7339-56772-0972	14:24:19.20	+53:17:50.64	2.530	20.49
7032-56471-0306	14:24:27.84	+52:20:44.52	2.324	20.03
7029-56455-0955	14:24:33.12	+53:43:52.68	2.711	20.51
7030-56448-0160	14:24:50.88	+52:50:01.68	2.728	19.71
7030-56448-0130	14:24:55.68	+52:06:09.72	2.631	21.20
7031-56449-0356	14:24:58.56	+52:41:49.92	3.015	21.27
7031-56449-0334	14:25:06.24	+52:01:28.92	2.736	21.92
6710-56416-0446	14:25:09.12	+53:51:49.32	3.102	21.37
7032-56471-0729	14:25:10.80	+53:23:09.60	2.861	20.73

CHAPTER 4
SPECTROSCOPIC STUDY:
HI TOMOGRAPHY TECHNIQUES AND MAPS

To spatially probe IGM HI gas around $z \sim 2$ galaxies, we carry out HI tomography that is a powerful technique to reconstruct 3D HI LSSs based on HI absorptions found in multiple background source spectra (e.g., Lee et al., 2018, 2014b,a; Caucci et al., 2008; Pichon et al., 2001). This Chapter describes how we make HI tomography maps from our background source spectra (Section 4.1), and presents the resulting HI tomography maps of the COSMOS, BOSS1441, EGS regions (Section 4.2).

4.1 HI Tomography Techniques

Our HI tomography consists of the following two processes: (1) normalizing the background source spectra by estimated continua to make input spectra for our HI tomography (Section 4.1.1) and (2) reconstructing HI LSSs from those normalized spectra (Section 4.1.2).

4.1.1 Intrinsic Continua

To probe HI absorptions along the lines of sight to the background quasars and galaxies, we estimate the Lyα forest transmission in their Lyα forest wavelength range (i.e., 1041–1185Å in the rest-frame),

$$F(z) = f_{\rm obs}/f_{\rm int}, \tag{4.1}$$

where $f_{\rm obs}$ is the observed continuum flux density and $f_{\rm int}$ is the intrinsic continuum flux density that is not affected by the Lyα forest absorptions due to the IGM.

We estimate intrinsic continuum flux densities $f_{\rm int}$ for our background quasars and galaxies by applying the MF-PCA continuum fitting technique (Lee et al., 2012) with the code developed by Lee et al. (2013) (see also Lee et al. 2014b). This technique is composed of two steps. The first step is to fit spectral templates of quasars and

galaxies with the observed spectra in the redward of Lyα to obtain initial guesses of their continuum spectra in the blueward of Lyα. In the same manner as Lee et al. (2014b), we use the spectral templates of quasars and galaxies constructed by Suzuki et al. (2005) and Berry et al. (2012), respectively. The second step is to constrain the amplitude and slope of their blueward spectra to be consistent with previous measurements of the cosmic mean Lyα forest transmission, $F_{\rm cos}(z)$. We adopt $F_{\rm cos}(z)$ estimated by Faucher-Giguère et al. (2008),

$$F_{\rm cos}(z) = \exp[-0.00185(1+z)^{3.92}]. \tag{4.2}$$

The examples of intrinsic continua are shown in Figure 3.3.

We then obtain $F(z)$ by using Equation (4.1). [1] Note that the strong stellar and interstellar absorptions of NII λ1084 and CIII λ1175 associated with the background quasars and galaxies in the Lyα forest wavelength range could bias the results. For conservative estimates, we do not use the spectra in the wavelength ranges of $\pm$5Å around these lines in the following analyses. The uncertainties of $F(z)$ are calculated from the uncertainties of the $f_{\rm obs}$ measurements and the $f_{\rm int}$ estimates based on the MF-PCA continuum fitting, the latter of which are evaluated by Lee et al. (2012) as a function of redshift and median S/N over the Lyα forest wavelength range (see their Figure 8). Specifically, we adopt MF-PCA continuum fitting errors of 7%, 6%, and 4% for spectra with median S/Ns over the Lyα forest wavelength range of 2–4, 4–10, and $>$ 10, respectively.

Based on the estimated $F(z)$ and the cosmic mean Lyα forest transmission $F_{\rm cos}(z)$, we calculate the HI overdensity δ_F spectra for our background quasars and galaxies,

$$\delta_F = \frac{F(z)}{F_{\rm cos}(z)} - 1, \tag{4.3}$$

where negative values correspond to strong HI absorptions. The uncertainties of δ_F

[1] For the background quasars and galaxies in the BQ1–3 regions, there is a possibility that the strong HI absorption group at $z = 2.32 \pm 0.03$ in the BOSS1441 region (Cai et al., 2017b) could bias the intrinsic continuum estimate. In the MF-PCA fitting, we mask out the wavelength range of 4036 ± 36Å to avoid possible contamination from the strong HI absorption group.

are calculated based on the uncertainties of $F(z)$. We confirm that the systematic effect of using different prescriptions of $F_{\rm cos}(z)$ obtained by Becker et al. (2013) and Inoue et al. (2014) is minor, only within 2%, which is not as large as the uncertainties of $F(z)$.

4.1.2 Reconstruction Processes

Once we obtain the δ_F spectra of our background quasars and galaxies, we carry out the HI tomographic reconstruction to reveal the 3D distribution of the HI gas (thus HI LSSs in this thesis). In the same manner as Lee et al. (2018, 2016, 2014b), we use the reconstruction code developed by Stark et al. (2015).[2] The reconstruction code performs the Wiener filtering for the estimated δ_F values along the sightlines of our background quasar and galaxies. The Wiener filtering is based on the following two calculations of (i) and (ii). One is (i) the gaussian smoothing with the scale of the mean transverse sightline separation $\langle d_\perp \rangle$, which determines the spatial resolution of our tomography map. The other is (ii) input pixel weighting by its S/N to avoid the bias from low S/N spectra.

Specifically, in the Wiener filtering, the reconstructed HI overdensity map $\delta_F^{\rm rec}$ is given by the following estimator (Lee et al., 2014a; Caucci et al., 2008; Pichon et al., 2001),

$$\delta_F^{\rm rec} = \mathbf{C}_{\rm MD} \cdot (\mathbf{C}_{\rm DD} + \mathbf{N})^{-1} \cdot \delta_F^{\rm obs}, \tag{4.4}$$

where $\delta_F^{\rm obs}$ is the input HI overdensity datacube comprised of our background source spectra and coordinates. $\mathbf{C}_{\rm MD}$, $\mathbf{C}_{\rm DD}$, and $\mathbf{N}$ are the map-datacube, datacube-datacube, and noise covariances, respectively. This estimator allows us to down-weight pixels in low S/N spectra. These covariances are assumed to be a Gaussian covariance between any two points $\mathbf{r_1}$ and $\mathbf{r_2}$.

$$\mathbf{C}_{\rm DD} = \mathbf{C}_{\rm MD} = \mathbf{C}(\mathbf{r_1}, \mathbf{r_2}) \tag{4.5}$$

[2] `https://github.com/caseywstark/dachshund`

and

$$\mathbf{C}(\mathbf{r_1}, \mathbf{r_2}) = \sigma_F^2 \exp\left[-\frac{(\Delta r_\parallel)^2}{2L_\parallel^2}\right] \exp\left[-\frac{(\Delta r_\perp)^2}{2L_\perp^2}\right], \tag{4.6}$$

where $\Delta r_\parallel$ and $\Delta r_\perp$ are the line-of-sight and transverse distances between $\mathbf{r_1}$ and $\mathbf{r_2}$, respectively. We adopt $L_\parallel = L_\perp = \langle d_\perp \rangle$ as well as a normalization of $\sigma_F^2 = 0.05$ in the same manner as Lee et al. (2018, 2014b). More details about the reconstruction process is presented in Stark et al. (2015) and Lee et al. (2018).

4.2 HI Tomography Maps

We perform HI tomography based on our δ_F spectra of our background quasars and galaxies, and obtain the HI tomography map of the BOSS1441 (Section 4.2.2) and EGS (Section 4.2.3) regions. In the COSMOS region, we use the HI tomography map of Lee et al. (2018) (Section 4.2.1).

4.2.1 COSMOS Region

For the COSMOS region, we use the public data of the COSMOS HI tomography map made by the CLAMATO survey (Lee et al., 2018). [3] The COSMOS HI tomography map is a 3D map of the IGM HI absorption at $z = 2.05$–2.55 in the 0.157 deg^2 area of the COSMOS region, having a $30 \times\ 24 \times\ 444\ h^{-3}$cMpc^3 cosmic volume with a spatial resolution of 2.5 h^{-1} cMpc and a grid size of 0.5 h^{-1} cMpc. The HI tomography map is reconstructed from the spectra of 240 background galaxies and quasars at $z = 2.2$–3.0. The sky distribution of these background sources are shown in Figure 2.4. Figure 4.1 presents the COSMOS HI tomography map.

For our subsequent analyses, we prepare 1000 mock HI tomography maps based on an error map also provided by the CLAMATO survey (Lee et al., 2018). The error map is estimated from the 1σ uncertainties of δ_F spectra of the background sources. We generate 1000 mock HI tomography maps that we give random perturbations following the Gaussian distribution whose sigma is defined by the data values of the error map.

[3] `https://clamato.lbl.gov/`

4.2.2 BOSS1441 Region

For the BOSS1441 region, we carry out our HI tomography with our background quasars and galaxies in the BQ1 region (Figure 2.6). The mean transverse sightline separation is $\langle d_\perp \rangle = 2.6\ h^{-1}$ cMpc, when we consider the filling factor of the sky coverage as about 0.45, which is defined as the fraction of the regions around the sightlines of the background sources within $\langle d_\perp \rangle$ in the BQ1 region. For our tomographic reconstruction, we choose a redshift range of $z = 2.25$–2.40 that covers a large distance of $\sim \pm 65\ h^{-1}$ cMpc from the LAE overdensity at $z = 2.32$ in the redshift direction, giving an overall cosmic volume of $16\ \times 19\ \times 131\ h^{-3}\mathrm{cMpc}^3$. We adopt a grid size of $0.5\ h^{-1}$ cMpc. The grid size and the spatial resolution are comparable to those of COSMOS HI tomography map (Section 4.2.1). Figure 4.2 shows the BOSS1441 HI tomography map.

For our subsequent analyses, we prepare 1000 mock HI tomography maps. Firstly, we create mock Lyα forest transmission data $F(z)$ for the 17 background sightlines by adding noises based on the uncertainties of $F(z)$ that are obtained in Section 4.1.1, and calculate the δ_F values along the 17 sightlines for the mock data. Then, we perform HI tomography with the mock data. We obtain the 1000 mock HI tomography maps by repeating this process 1000 times.

4.2.3 EGS Region

For the EGS region, we conduct our large-scale HI tomography with our background quasars (Figure 2.5). The mean transverse sightline separation is $\langle d_\perp \rangle = 20.0\ h^{-1}$ cMpc, which is about ten times larger than those of the HI tomography maps of the COSMOS (Section 4.2.1) and BOSS1441 (Section 4.2.2) regions. This large-scale HI tomography is intended to be complementary to these HI tomography maps, and to compare with extreme quasar overdensities found in the cosmic volume (Section 5.3). For our tomographic reconstruction, we choose a redshift range of $z = 2.05$–2.55 to have the redshift range same as the COSMOS HI tomography map (Lee et al., 2018, Section 4.2.1). The redshift range and the 6.0 deg^2 sky area of the EGS region gives an overall cosmic volume of $124\ \times 136\ \times 444\ h^{-3}\mathrm{cMpc}^3$. We adopt a grid size of

1.0 h^{-1} cMpc. Figure 4.3 presents the EGS HI tomography map.

For our subsequent analyses, we prepare 100 mock HI tomography maps in the same manner as those of the BOSS1441 region (Section 4.2.2). Note that we reduce the number of mock data to alleviate the calculation cost due to the large scale.

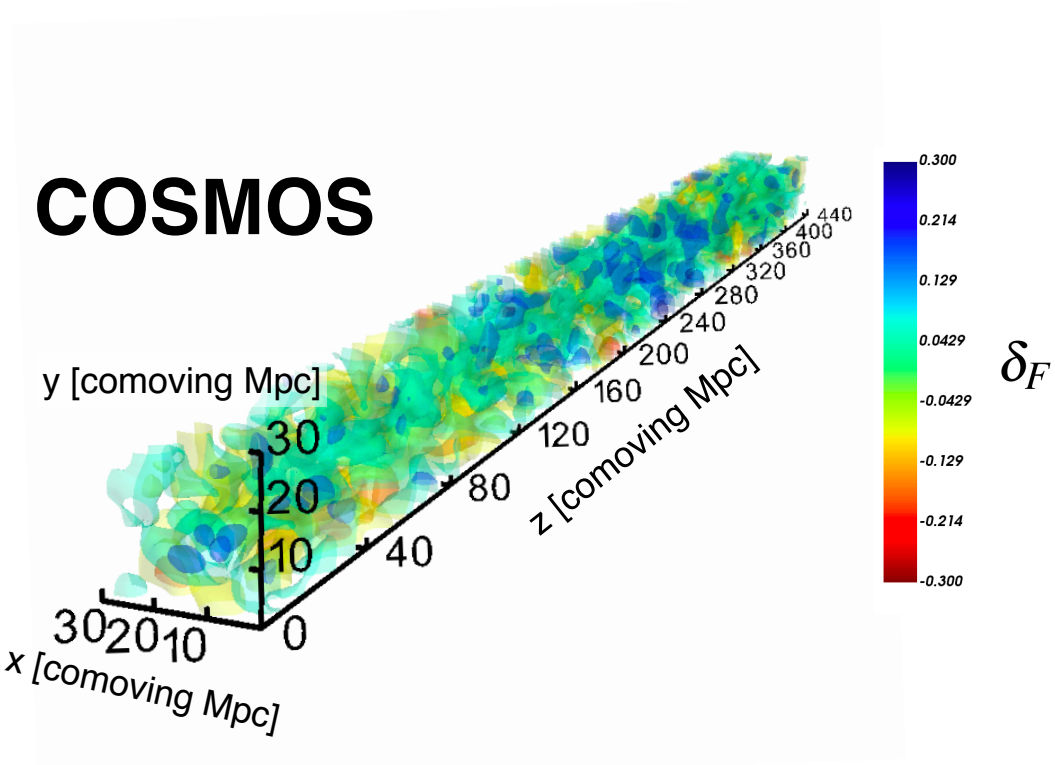

Figure 4.1: COSMOS HI tomography map reconstructed based on HI absorptions in the spectra of the background galaxies and quasars (Lee et al., 2018). The spatial axes of R.A., Decl., and z are represented as x, y, and z in co-moving scales, respectively. Here we show the HI tomography map in the redshift range of $z = 2.05$–2.55. The color contours represent the HI overdensity δ_F such that negative values (red) correspond to higher overdensities. The δ_F's maximum (minimum) scale is set to $+0.3$ (-0.3) for visualization, although some regions show higher or lower δ_F values in the range of $-0.5 < \delta_F < 0.5$.

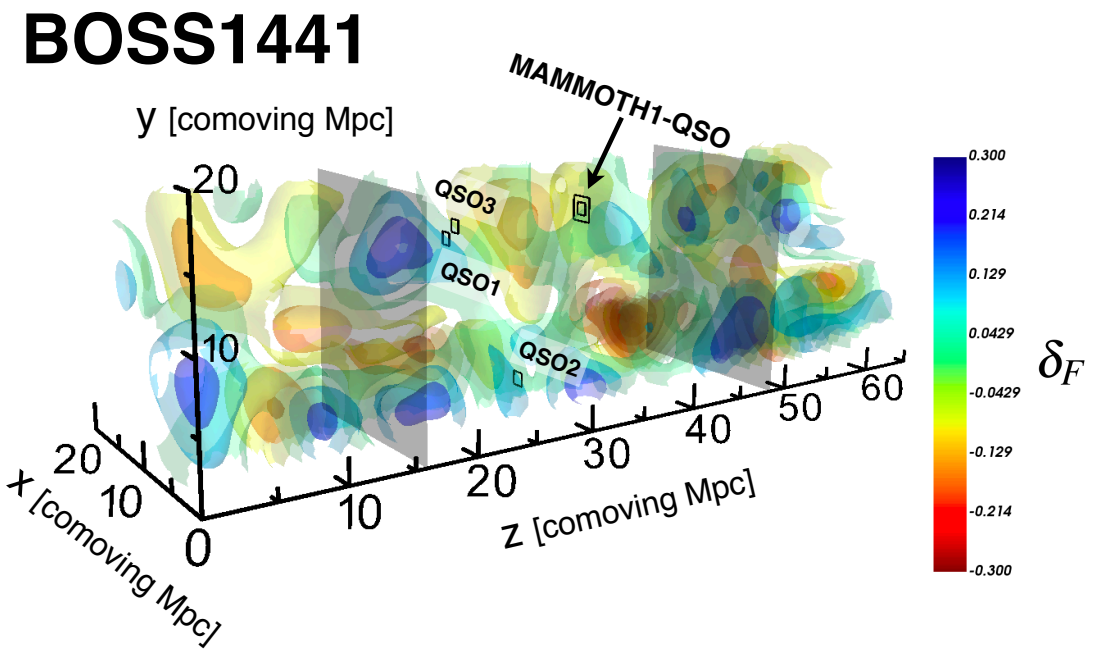

Figure 4.2: BOSS1441 HI tomography map reconstructed based on HI absorptions in the spectra of our background quasar and galaxies in the BQ1 region. The spatial axes of R.A., Decl., and z are represented as x, y, and z in co-moving scales, respectively. Here we present a zoomed map at $z = 2.28$–2.35 to clearly show the HI overdensity distribution at $z = 2.3$, although we obtain the HI tomography map in the redshift range of $z = 2.25$–2.40. The color contours represent the HI overdensity δ_F such that negative values (red) correspond to higher overdensities. The δ_F's maximum (minimum) scale is set to $+0.3$ (-0.3) for visualization, although some regions show higher or lower δ_F values in the range of $-0.6 < \delta_F < 0.4$. The single squares show the three eBOSS quasars, labeled as QSOs 1–3 (Sections 2.2 and 5.2). The double square indicates the position of an ELAN's host quasar, MAMMOTH1-QSO, found in the vicinity of the LAE density peak (Cai et al. 2017a; Section 5.4). Note that the redshift range between the two gray planes at $z = 2.30$ and $z = 2.33$ correspond to the FWHM of the narrowband filter NB403, which is used in Cai et al. (2017a,b) to detect Lyα emission at $z = 2.32$ in the BOSS1441 region (Sections 2.1.2 and 5.4).

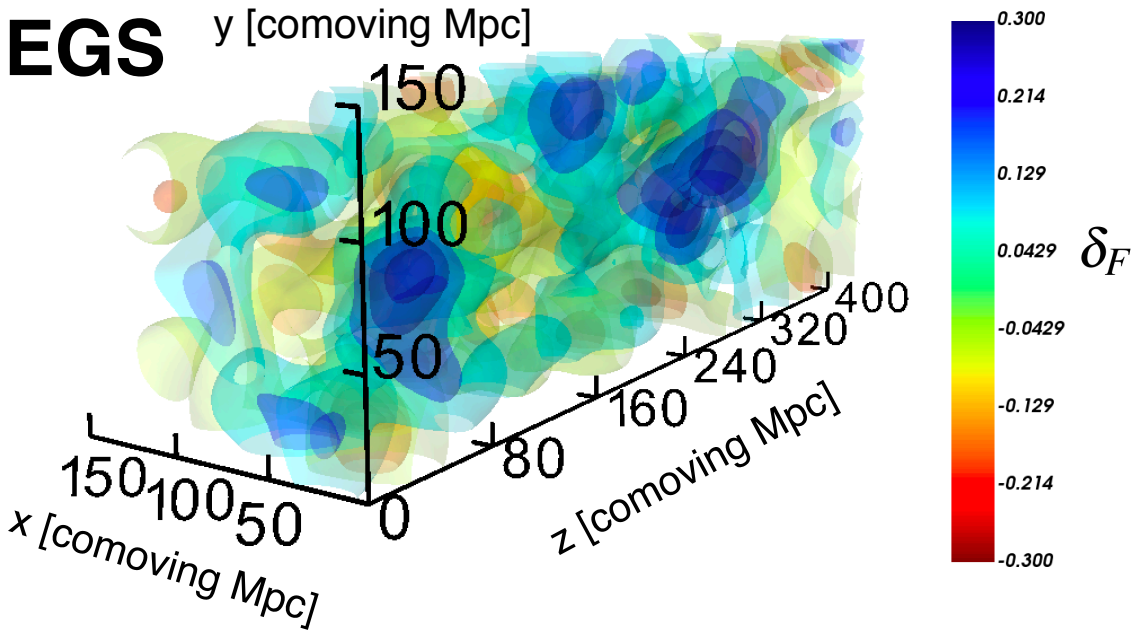

Figure 4.3: EGS HI tomography map reconstructed based on HI absorptions in the spectra of our background quasars. Note that the spatial resolution is = 20.0 h^{-1} cMpc, and is larger than those of the COSMOS (2.5 h^{-1} cMpc) and BOSS1441 (2.6 h^{-1} cMpc). The spatial axes of R.A., Decl., and z are represented as x, y, and z in comoving scales, respectively. Here we present the HI tomography map in the redshift range of z = 2.05–2.55. The color contours represent the HI overdensity $w\delta_F$ such that negative values (red) correspond to higher overdensities. The δ_F's maximum (minimum) scale is set to +0.3 (−0.3) for visualization, although some regions show higher or lower δ_F values in the range of $-0.6 < \delta_F < 0.6$.

CHAPTER 5
SPECTROSCOPIC STUDY: RESULTS

In this Chapter, we investigate IGM HI-gas distributions around $z \sim 2$ galaxies in our three HI tomography maps, and present the results of the following three regions;

- COSMOS: a blank region (Section 5.1)
- BOSS1441: an extreme galaxy overdensity region (Section 5.2)
- EGS: a blank region including an extreme quasar overdensity (Section 5.3)

We also study the IGM HI-gas distribution around an ELAN found in the BOSS1441 region, and show the result in Section 5.4.

5.1 Spatial Correlations Between HI Gas and Galaxies

In this Section, we present the results of spatial correlations between IGM HI gas and galaxies in a blank region. We use the COSMOS HI tomography map whose spatial resolution is smaller than that of the EGS HI tomography map (Section 4.2). The results are composed of two measurements: (i) HI overdensity as a function of the distances from the galaxies, and (ii) spatial correlations between the HI overdensity and the galaxy overdensity.

Firstly, we measure the spherically averaged radial profiles of HI overdensity δ_F (hereafter HI radial profiles) around our COSMOS LAEs (Section2.1.1). We obtain HI radial profile around each of our 47 LAEs, and take average of their HI radial profiles. We use the COSMOS HI tomography map (Section 4.2.1) to calculate the HI radial profile as a function of the 3D distances from the LAEs. The 3D distances from LAEs are defined as

$$R_{\rm 3D} \equiv \sqrt{d_{\rm RA}^2 + d_{\rm Dec}^2 + d_z^2}, \tag{5.1}$$

where $d_{\rm RA}$, $d_{\rm Dec}$, and d_z are the co-moving distances from the LAEs under the assumption that the HI absorbers have zero peculiar velocities relative to the LAEs. To estimate the uncertainties of the spherically averaged δ_F, we use the 1000 mock HI tomography maps (Section 4.2.1). For each mock map, we compute HI radial profiles averaged over our LAEs. We repeat this process 1000 times, and obtain 68% intervals as the 1σ confidence intervals. The black filled circles in Figure 5.1 present the HI radial profile of our COSMOS LAEs. The δ_F decreases (i.e., HI absorption strength increases) from the cosmic mean level to $\delta_F = -0.1$ with decreasing $R_{\rm 3D}$ from ~ 100 h^{-1} cMpc to ~ 1 h^{-1} cMpc around the LAEs. Note that the gray open circle represents the measurements whose spatial scales are below the spatial resolution of the HI tomography map. We do not use these measurements for our discussions. This is because the HI tomography could undersample HI absorptions such a small scales and there is a possibility that small HI gas clumps of the Lyα forest might not be considered in these small scales. The simulation studies of Lee et al. (2014a) indicate that the single HI tomography pixel could have the δ_F error of ≤ 0.05 due to the undersampling of the Lyα forest.

Secondly, we measure HI overdensity δ_F as a function of the LAE overdensity. We estimate both the HI overdensity and the LAE overdensity with a sphere whose radius is 10 h^{-1} cMpc at $z = 2.3$. The LAE overdensity $\delta_{\rm LAE}$ is defined as

$$\delta_{\rm LAE} \equiv \frac{n_{\rm LAE}}{\overline{n}_{\rm LAE}} - 1, \tag{5.2}$$

where $n_{\rm LAE}$ ($\overline{n}_{\rm LAE}$) is the (mean) number density of LAEs in a sphere. We calculate both $\delta_{\rm LAE}$ and the volume-averaged δ_F where we center our COSMOS LAEs in the spheres. The errors of $\delta_{\rm LAE}$ and δ_F are estimated with the Poisson errors and the 1σ confidence interval of the mock 1000 HI tomography maps (Section 4.2.1), respectively. Figure 5.2 shows the spatial correlation between δ_F and $\delta_{\rm LAE}$. The black and red circles represent the individual and binned measurements, respectively. The δ_F decreases (i.e., HI absorption strength increases) with increasing the $\delta_{\rm LAE}$.

These two results indicate the HI absorption excesses around the galaxies over Mpc scales, and thus the spatial correlation between HI gas and galaxies as we see in

the COSMOS HI tomography map (Figure 5.3). Note that our spatial correlations may not be affected by bright quasars, because none of eBOSS quasars at $z = 2.05$–2.55 are found in the cosmic volume of the COSMOS HI tomography map (Section 2.2).

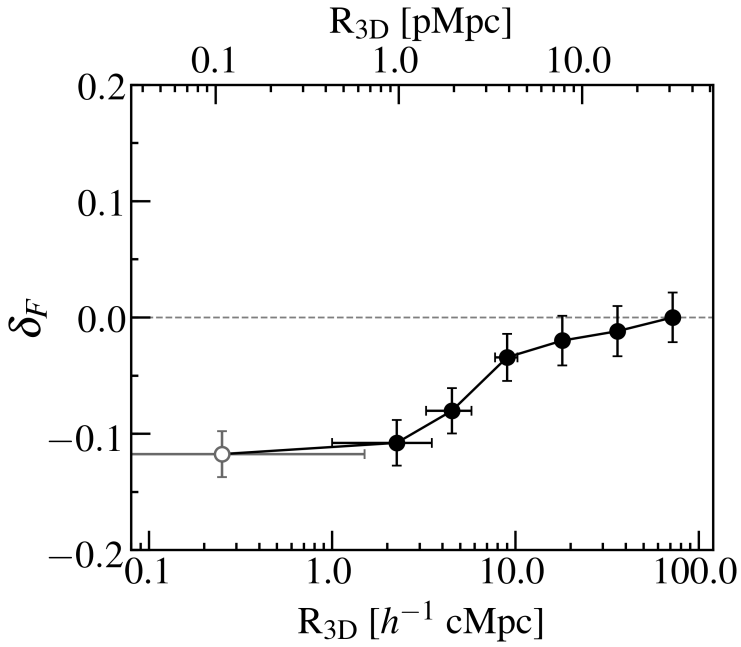

Figure 5.1: HI radial profile around galaxies. The black filled circles are the results of our COSMOS LAEs. The gray open circle presents the measurements of HI tomography map pixels where the LAEs reside and these spatial scales are below the spatial resolution of the HI tomography map which is shown as horizontal bars for reference. The gray dashed line is the cosmic mean level of the IGM HI absorption at $z = 2.3$.

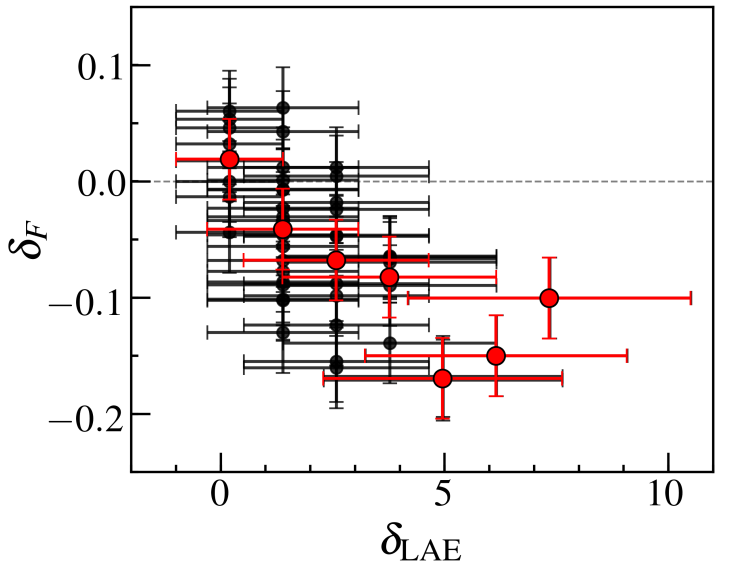

Figure 5.2: HI overdensity δ_F as a function of the galaxy overdensity. The black (red) circles represent the individual (binned) measurements of our COSMOS LAEs (Section 2.1.1). The gray dashed line is the cosmic mean level of the IGM HI absorption at $z = 2.3$.

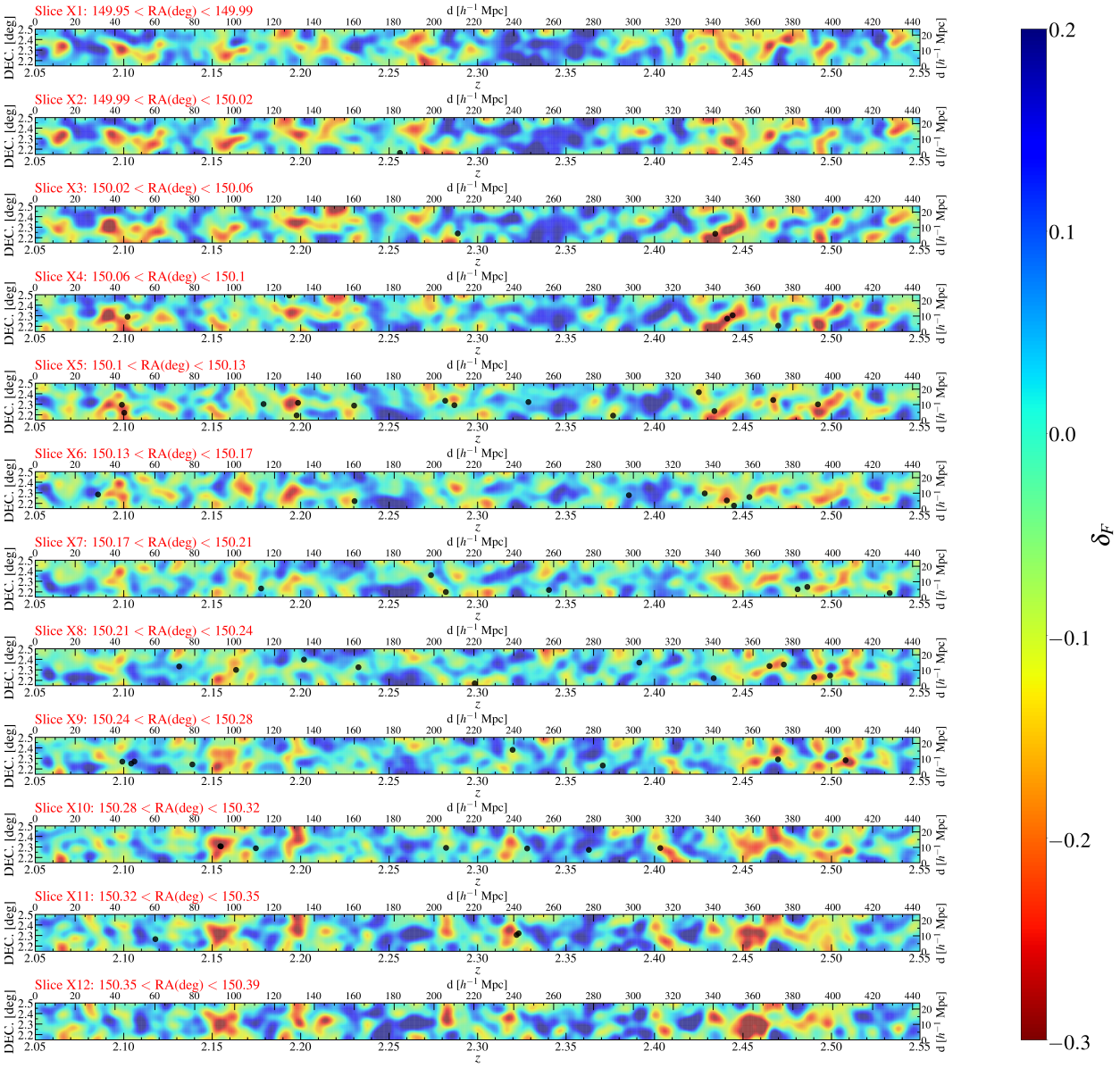

Figure 5.3: Projections of our HI tomography map across 2.5 h^{-1} cMpc (comparable to the spatial resolution; Section 4.2.1) slices in the R.A. direction. The color contours represent the HI overdensity δ_F such that negative values (red) correspond to higher overdensities. The black dots indicates the position of COSMOS LAEs.

5.2 HI-Gas Distributions Around Overdensities of Galaxies and Quasars

The results in Section 5.1 indicate the spatial correlations between HI gas and galaxies. Based on this indication, we expect the larger HI overdensities in the larger galaxy overdensities. In this Section, we investigate the IGM HI-gas distributions around galaxies in an extreme galaxy overdensity, the BOSS1441 region. We use the BOSS1441 HI tomography map whose spatial resolution is comparable to the that of the COSMOS HI tomography map (Section 4.2).

Firstly, we measure the HI radial profile around our BOSS1441 LAEs (Section 2.1.2). We obtain HI radial profile around each of our 60 LAEs inside the BOSS1441 HI tomography map (Section 4.2.2), and take average of their HI radial profiles. Since our BOSS1441 LAEs are photometrically selected LAEs at $z = 2.30$–2.33, we calculate the HI overdensity δ_F averaged over the redshift range of $z = 2.30$–2.33, and measure mean δ_F on annuluses whose radii are transverse distances $R_{\rm 2D}$ from our LAEs. The uncertainties of the averaged δ_F are estimated with the 1000 mock HI tomography maps (Section 4.2.2). in the same manner as Section 5.1. We also give measurements beyond 10 h^{-1} cMpc, by using the δ_F measurements along the sightlines of the background quasars in the BQ2–3 regions (Section 2.3). The black filled circles and black open squares in Figure 5.4 show the HI radial profile of our BOSS1441 LAEs obtained in the BQ1 region and BQ2/BQ3 regions, respectively. We find the increased δ_F (reduced HI absorptions) comparing to galaxies in the blank region and the δ_F is constant at the cosmic mean level across $\sim 1 - 100$ h^{-1} cMpc. Note that the gray open circle presents the measurements whose spatial scales are below the spatial resolution of the HI tomography map. There is a possibility that the average of δ_F along redshift direction would erase the HI absorption correlation signal around galaxies. To evaluate this possibility, we use the results in Section 5.1, and calculate the HI radial profile as a function of $R_{\rm 2D}$ from our COSMOS LAEs. The black and red circles in Figure 5.5 present the $R_{\rm 3D}$ and $R_{\rm 2D}$ measurements for our COSMOS LAEs, respectively. Note that the COSMOS HI tomography map allows us to obtain the HI radial profile up to around $R_{\rm 2D} \sim 20$ h^{-1} cMpc which is limited

due to the transverse size of the HI tomography map. We find that the absorption excess mildly remains below the cosmic mean level at 2σ levels for the $R_{\rm 2D} \sim 1 - 20$ h^{-1} cMpc measurements. This might suggest that the average of δ_F along redshift direction would not completely erase the HI absorption correlation signal around galaxies.

Next, we measure HI overdensity δ_F as a function of the LAE overdensity. Because our BOSS1441 LAEs are photometrically selected LAEs at $z = 2.30$–2.33, we estimate both the HI overdensity and the LAE overdensity with a cylinder. We define the cylinder length as the NB403 redshift range [1] of 32 h^{-1} cMpc. We choose the cylinder radius as 6 h^{-1} cMpc at $z = 2.3$ so that the cosmic volume is same as the sphere we used in the δ_F – $\delta_{\rm LAE}$ measurements in the Section 5.1. We measure both $\delta_{\rm LAE}$ and the volume-averaged where we center our BOSS1441 LAEs in the cylinder. Since the BOSS1441 LAEs are identified in the extreme galaxy overdensity, we take the mean number density from literature. Here, we follow the $\delta_{\rm LAE}$ measurements of Cai et al. (2017b), and use the mean number density of 4.0×10^{-4} h^3 cMpc^{-3}. This number density is estimated by integrating the LAE luminosity function at $z = 2.1$ (Ciardullo et al., 2012) down to $\sim 0.73 L^*_{{\rm Ly}\alpha}$ that is the detection limit of the BOSS1441 LAEs (Section 2.1.2). The errors of $\delta_{\rm LAE}$ and δ_F are estimated with the Poisson errors and the 1σ confidence interval of the mock 1000 HI tomography maps (Section 4.2.2), respectively. Figure 5.6 shows the results of δ_F – $\delta_{\rm LAE}$ measurements. The black and red circles represent the individual and binned measurements, respectively. The δ_F also keep constant at the cosmic mean level with increasing the $\delta_{\rm LAE}$.

These two results might indicate that the reduced HI absorptions around the galaxies in this extreme galaxy overdensity, contrary to the results in Section 5.1. There is a possibility that the HI-gas distributions around galaxies is photo-ionized by quasars in the BOSS1441 regions. In Section 2.2, we have found three eBOSS quasars, dubbed QSOs 1–3, in the cosmic volume of the BOSS1441 HI tomography map (Fig 4.2). To investigate the quasar photo-ionizatiion effect on the HI-gas distributions, we measure HI radial profile averaged over the three eBOSS quasars in the same manner as Section 5.1. The black filled circles and black open squares in Figure 5.7 show

[1] The exact redshift range of the NB403 is $z = 2.296$–2.333.

the HI radial profile around the three eBOSS quasars obtained in the BQ1 region and BQ2/BQ3 regions, respectively. We find that δ_F decreases (i.e., HI absorption strength increases) from the cosmic mean level to $\delta_F = -0.06 \pm 0.02$ with decreasing R_{3D} from 100 h^{-1} cMpc to $\simeq 8$ h^{-1} cMpc and δ_F then increases to $\delta_F \simeq 0.05$ with further decreasing R_{3D} from $\simeq 8$ h^{-1} cMpc to 1 h^{-1} cMpc. In other words, the HI radial profile of the three eBOSS quasars shows an interesting turnover at $R_{3D} \simeq 8$ h^{-1} cMpc. The trend of δ_F increasing (i.e., HI absorption strength decreasing) within $R_{3D} \simeq 8$ h^{-1} cMpc implies that the QSOs 1–3 are in volumes with weak HI absorption comparing to galaxies in the blank region. This result suggests that QSOs 1–3 might have proximity zones where HI gas is photo-ionized and HI absorption is suppressed due to ionizing radiation from the quasars.

We check the HI environments of QSOs 1–3 in the BOSS HI tomography map and the top three panels of Figure 5.8 present 2D slices of the BOSS HI tomography map projected across $\Delta x = 2.6h^{-1}$ cMpc along the x (R.A.) direction around QSOs 1–3. In Figure 5.8, we find that the QSOs 1–3 are associated with or surrounded by HI underdense regions with sizes of $\simeq 5 - 10$ h^{-1} cMpc at least toward observers, which might be created by strong photo-ionizing radiation from the quasars. Interestingly, these sizes are comparable to the estimated sizes of proximity zones of $z \sim 2$ quasars (D'Odorico et al., 2008).

The results of the HI-gas distributions around galaxies and quasars in Sections 5.1 and 5.2 might indicate that the large galaxy overdensities can be associated with a large amount of HI gas (Figures 5.1 and 5.2), but the quasars that emerge from the galaxy overdensities might photo-ionize the surrounding HI gas (Figures 5.7), suppressing the HI absorption around the galaxies (Figures 5.4 and 5.6). Note that statistical studies of HI gas in extreme galaxy overdensities are required to characterize the balance between HI-gas distributions and the impacts of the quasar photo-ionization.

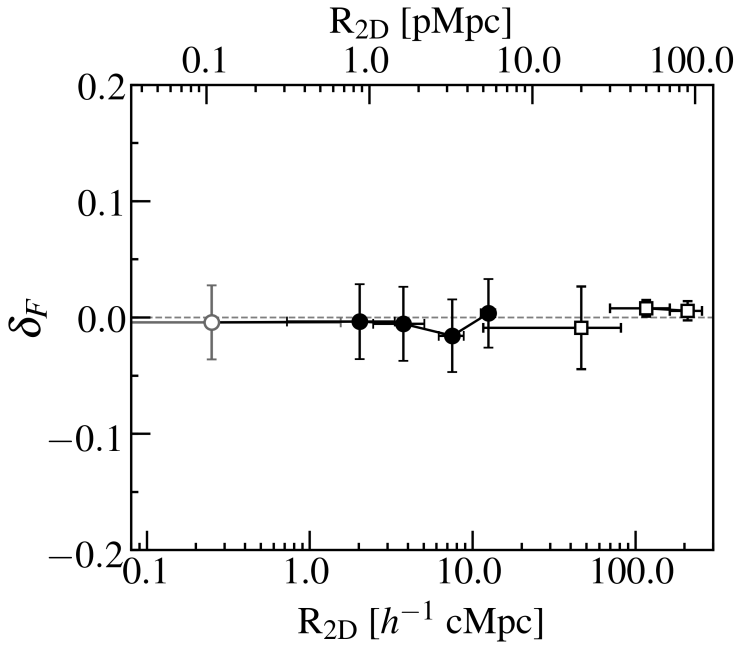

Figure 5.4: HI radial profile around galaxies. The black filled circles (open squares) are the results of our BOSS1441 LAEs obtained in the BQ1 region (BQ2 and BQ3 regions). The gray open circle presents the measurements of HI tomography map pixels whose spatial scales are below the spatial resolution of the HI tomography map which is shown as horizontal bars for reference. The gray dashed line is the cosmic mean level of the IGM HI absorption at $z = 2.3$.

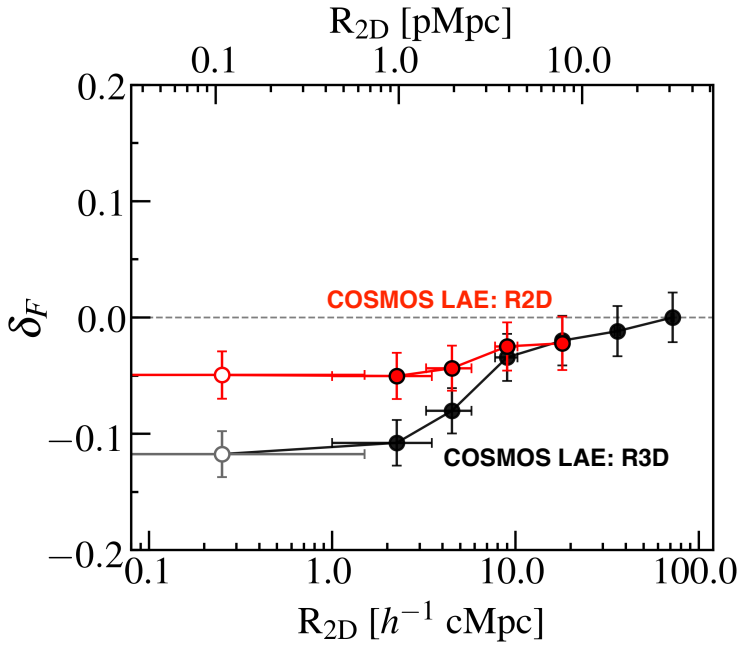

Figure 5.5: Same as Figure 5.1, but we overplot the HI radial profile as a function of R_{2D} from our COSMOS LAEs in the COSMOS HI tomography map. It is noted that the HI tomography map allows us to measure the HI radial profile up to around $R_{2D} \sim 20\ h^{-1}$ cMpc due to the limited transverse size of the HI tomography map.

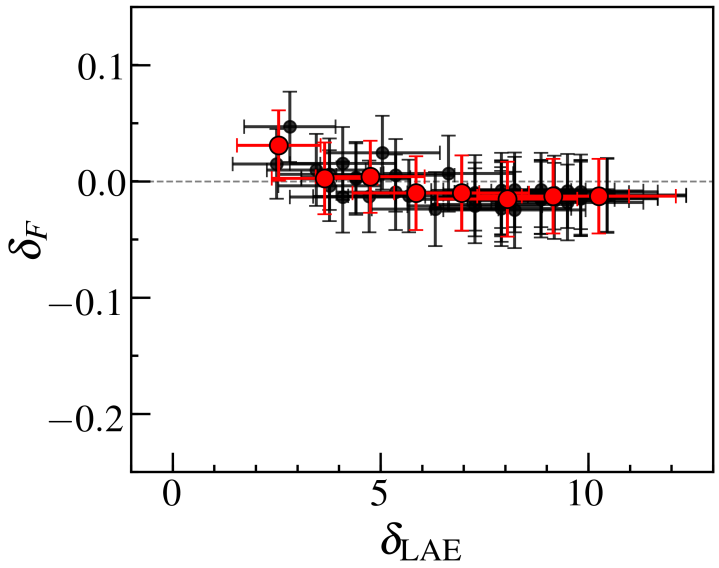

Figure 5.6: HI overdensity δ_F as a function of the galaxy overdensity. The black (red) circles represent the individual (binned) measurements of our BOSS1441 LAEs. The gray dashed line is the cosmic mean level of the IGM HI absorption at $z = 2.3$.

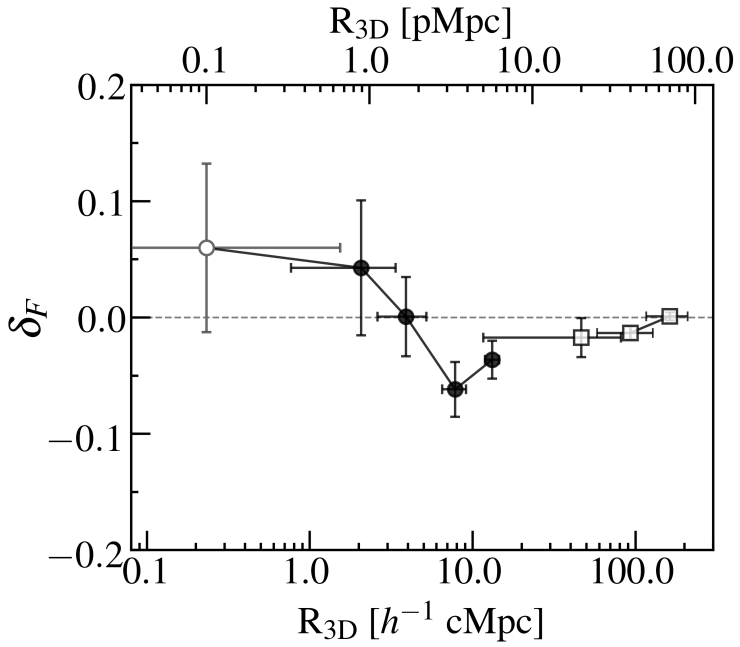

Figure 5.7: Same as Figure 5.1, but for our three eBOSS quasars in the cosmic volume of the BOSS1441 HI tomography map. The black filled circles (open squares) are the results of our three eBOSS quasars obtained in the BQ1 region (BQ2 and BQ3 regions).

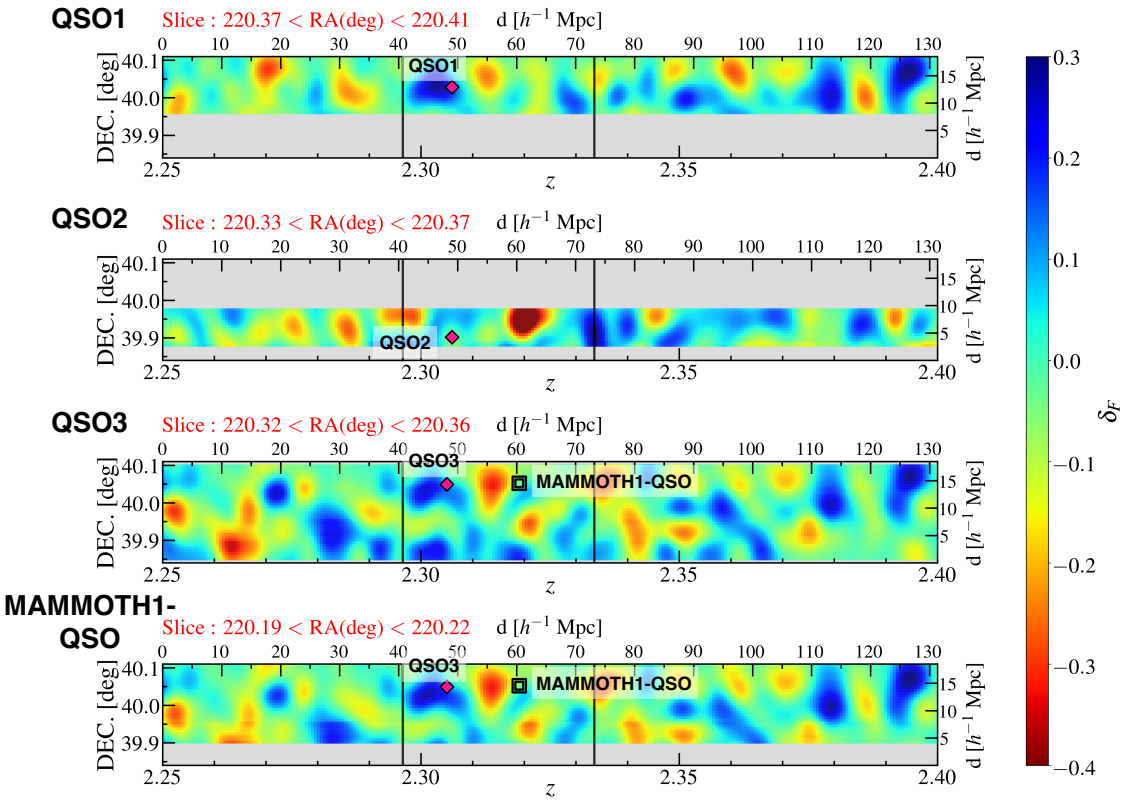

Figure 5.8: Projections of our HI tomography map across 2.6 h^{-1} cMpc (comparable to the spatial resolution; Section 4.2.2) slices in the R.A. direction around QSOs 1–3 (Fig 4.2) and an ELAN's host quasar, MAMMOTH1-QSO, (Section 5.4) from top to bottom. The color contours represent the HI overdensity δ_F such that negative values (red) correspond to higher overdensities. The single squares show QSOs 1–3, and the double square indicates the position of MAMMOTH1-QSO. The magenta diamonds are the positions of our foreground eBOSS quasars (Section 2.2). The two vertical lines at $z \simeq 2.30$ and $z \simeq 2.33$ denote the redshift range whose Lyα emission can be probed with NB403 used in Cai et al. (2017a,b) (Section 5.4).

5.3 HI–Gas Distributions Around an Extreme Quasar Overdensity

The results in Section 5.2 indicate that the quasars might photo-ionize the surrounding HI gas associated with the overdensities of galaxies and quasars, and suppress the HI absorption strength. Based on this indication, we expect the significantly weak HI absorption strength in extreme quasar overdensities. In this Section, we investigate the IGM HI-gas distributions around quasars and galaxies in extreme quasar overdensities.

Firstly, we search for extreme quasar overdensities in the 6.0 deg^2 area of the EGS region. We need a large cosmic volume to find the extreme quasar overdensities that are rare systems (e.g., Cai et al., 2017b; Hennawi et al., 2015; Arrigoni Battaia et al., 2018). We use the 78 foreground eBOSS quasars (Section 2.2), and estimate quasar overdensities with a sphere whose radius is 20 h^{-1} cMpc at $z = 2.3$.

$$\delta_{\rm QSO} \equiv \frac{n_{\rm QSO}}{\overline{n}_{\rm QSO}} - 1, \tag{5.3}$$

where $n_{\rm QSO}$ ($\overline{n}_{\rm QSO}$) is the (mean) number density of eBOSS quasars in a sphere. We calculate $\delta_{\rm QSO}$ at the EGS HI tomography map pixel positions, and make the $\delta_{\rm QSO}$ map whose cosmic volume is comparable to the HI map. We then look for the largest quasar overdensity in the $\delta_{\rm QSO}$ map, and find an extreme overdensity, dubbed EGS-QO1, whose quasar overdensity is $\delta_{\rm QSO} = 16.2\pm7.0$. The top panel of Figure 5.9 shows projections of our $\delta_{\rm QSO}$ map across 40.0 h^{-1} cMpc slices in the R.A. direction. The color contours indicate the quasar overdensity $\delta_{\rm QSO}$ whose positive values correspond to higher overdensities. The magenta diamonds represent the foreground eBOSS quasars (Section 2.2). The dashed cyan circle points EGS-QO1 where six eBOSS quasars are associated. Note that the quasar overdensity of EGS-QO1 could be comparable to the BOSS1441 region where Cai et al. (2017b) reported a total of six eBOSS quasars in a similar cosmic volume. However, if we estimate quasar overdensity with a bit large cosmic volume such as a 40.0^3 h^{-3} cMpc^3 cubic, EGS-QO1 has a bit larger quasar overdensity than that of BOSS1441. The number of EGS eBOSS quasars

is eight whereas we search BOSS1441 eBOSS quasars from the DR14Q catalog and obtain the seven eBOSS quasars in the cosmic volume.

Next, we check HI environments of EGS-QO1 with the EGS HI tomography map and the bottom panel of Figure 5.9 shows the HI environments projected in the same slice as the top panel of Figure 5.9. By comparing the two panels of Figure 5.9, we find that there might be correspondence between EGS-QO1 and an HI underdensity. This might indicate that EGS-QO1 would reside in an HI underdensity. One caveat is that the center of HI underdensity (RA $= 214.^{\circ}0 - 215.^{\circ}0$ and DEC $\sim 52.^{\circ}5 - 53.^{\circ}0$) is unfortunately penetrated by none of background quasar sightlines (see Figure 2.5). The HI underdensity around EGS-QO1 is mainly reconstructed by the background quasar sightlines in the outer region (RA $= 213.^{\circ}9 - 215.^{\circ}4$ and DEC $\sim 52.^{\circ}0 - 52.^{\circ}5$). If the correspondence between EGS-QO1 and the HI underdensity at least at DEC $< 52.^{\circ}5$ is true, the quasar overdensity and the HI underdensity suggest that the group of quasars would have a large ionizing bubble where HI gas is widely photo-ionized and HI absorption is suppressed due to the strong ionizing radiation by these quasars. To investigate HI-gas distributions in the inner region of the HI underdensity, we need to increase background sightline densities and plan to carry out LRIS spectroscopy of background galaxies in the EGS region.

We then measure HI radial profile averaged over the six eBOSS quasars associated with the extreme quasar overdensity EGS-QO1. The black filled circles in Figure 5.10 represent the HI radial profile around the six eBOSS quasars. The δ_F increases (i.e., HI absorption strength decreases) from the cosmic mean level to $\delta_F = +0.15$ with decreasing $R_{\rm 3D}$ from ~ 100 h^{-1} cMpc to ~ 10 h^{-1} cMpc around the quasars. This might indicate the strongly suppressed HI absorptions around the eBOSS quasars in the extreme quasar overdensity comparing to the results in the extreme galaxy overdensity region. Note that the gray open circle shows the measurements whose scales are below the spatial resolution of this HI tomography map.

In the cosmic volume of the EGS HI tomography map, we find six LAEs at $z =$ 2.13–2.19 distributed around the extreme quasar overdensity EGS-QO1. These six LAEs, dubbed LAE1-6, are shown with white labels in the Figure 5.9 and their spectra are shown in Figure 5.11. We then investigate the IGM HI-gas distributions around

the LAEs 1–6 in the same manner as Sections 5.1 and 5.2. Figures 5.12 and 5.13 are the results of the HI radial profile and the δ_F - $\delta_{\rm LAE}$ measurements, respectively. Note that we estimate both δ_F and $\delta_{\rm LAE}$ with a sphere whose radius is comparable to the spatial resolution of the EGS HI tomography map (20 h^{-1} cMpc at $z = 2.3$). We find that HI radial profile is similar to those of eBOSS quasars in EGS-QO1 and the δ_F slightly increases (i.e., HI absorption strength decreases) with increasing $\delta_{\rm LAE}$ increases. These two results might indicate the suppressed HI absorptions around the LAEs (LAE overdensities) in the extreme quasar overdensity comparing to the results in the extreme galaxy overdensity region. The suppressed HI absorptions might be made by the quasar photoionization in EGS-QO1.

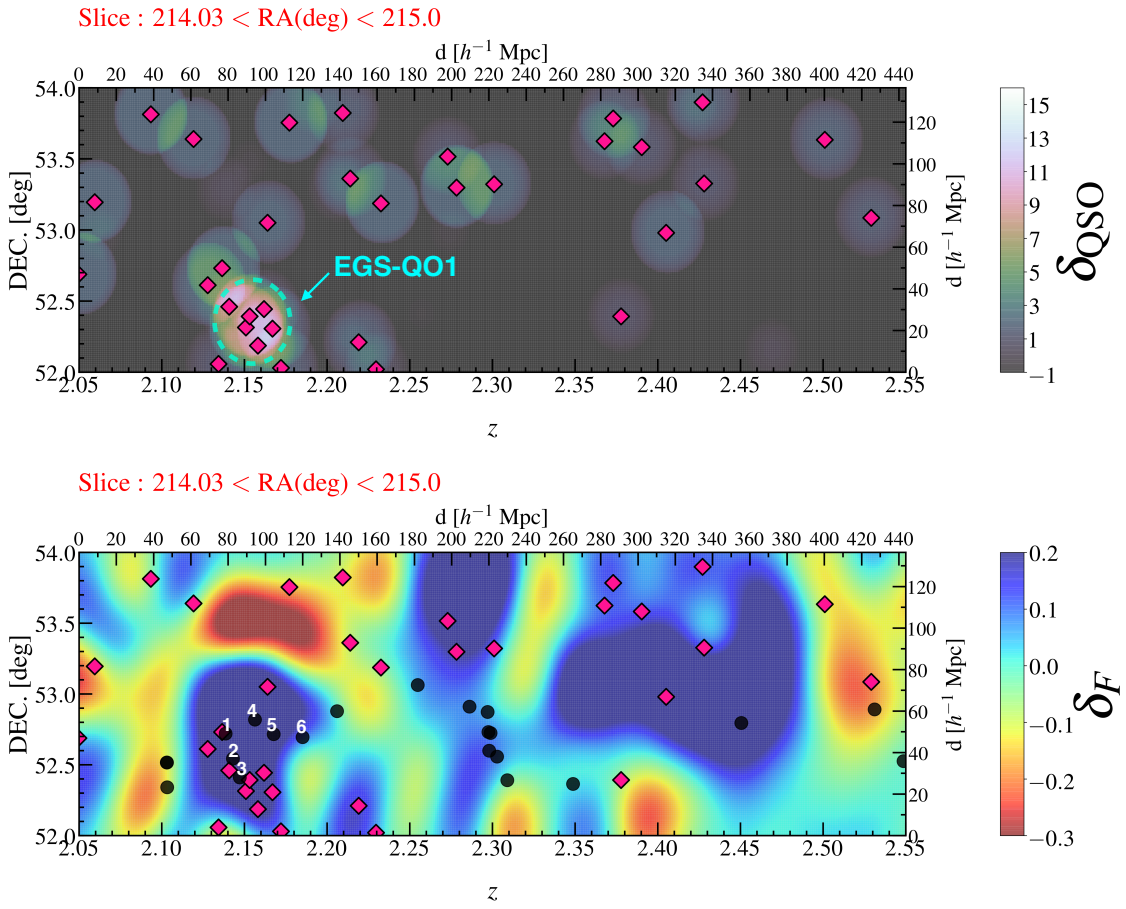

Figure 5.9: Top panel: Projections of our $\delta_{\rm QSO}$ map across 40.0 h^{-1} cMpc slices in the R.A. direction. The color contours represent the quasar overdensity $\delta_{\rm QSO}$ such that positive values correspond to high overdensities. The magenta diamonds represent the foreground eBOSS quasars (Section 2.2). The dashed cyan circle indicates an extreme quasar overdensity EGS-QO1. Bottom panel: Projections of our HI tomography map across 40.0 h^{-1} cMpc (comparable to twice the spatial resolution; Section 4.2.3) slices in the R.A. direction. The color contours represent the HI overdensity δ_F such that negative values (red) correspond to higher overdensities. The magenta diamonds represent the foreground eBOSS quasars (Section 2.2). The black dots indicates the position of EGS LAEs (Section 2.1.1).

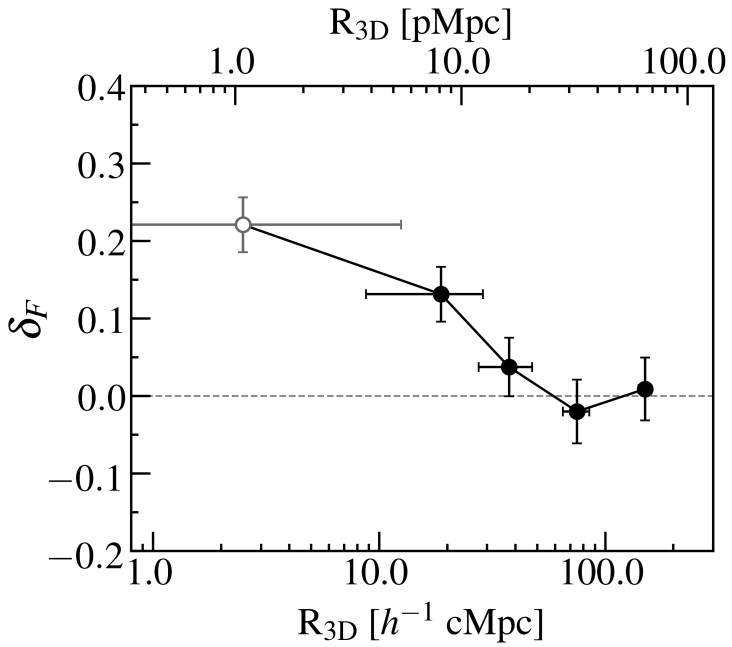

Figure 5.10: Same as Figure 5.7, but for the six eBOSS quasars associated with the extreme quasar overdensity EGS-QO1 found in the EGS HI tomography map.

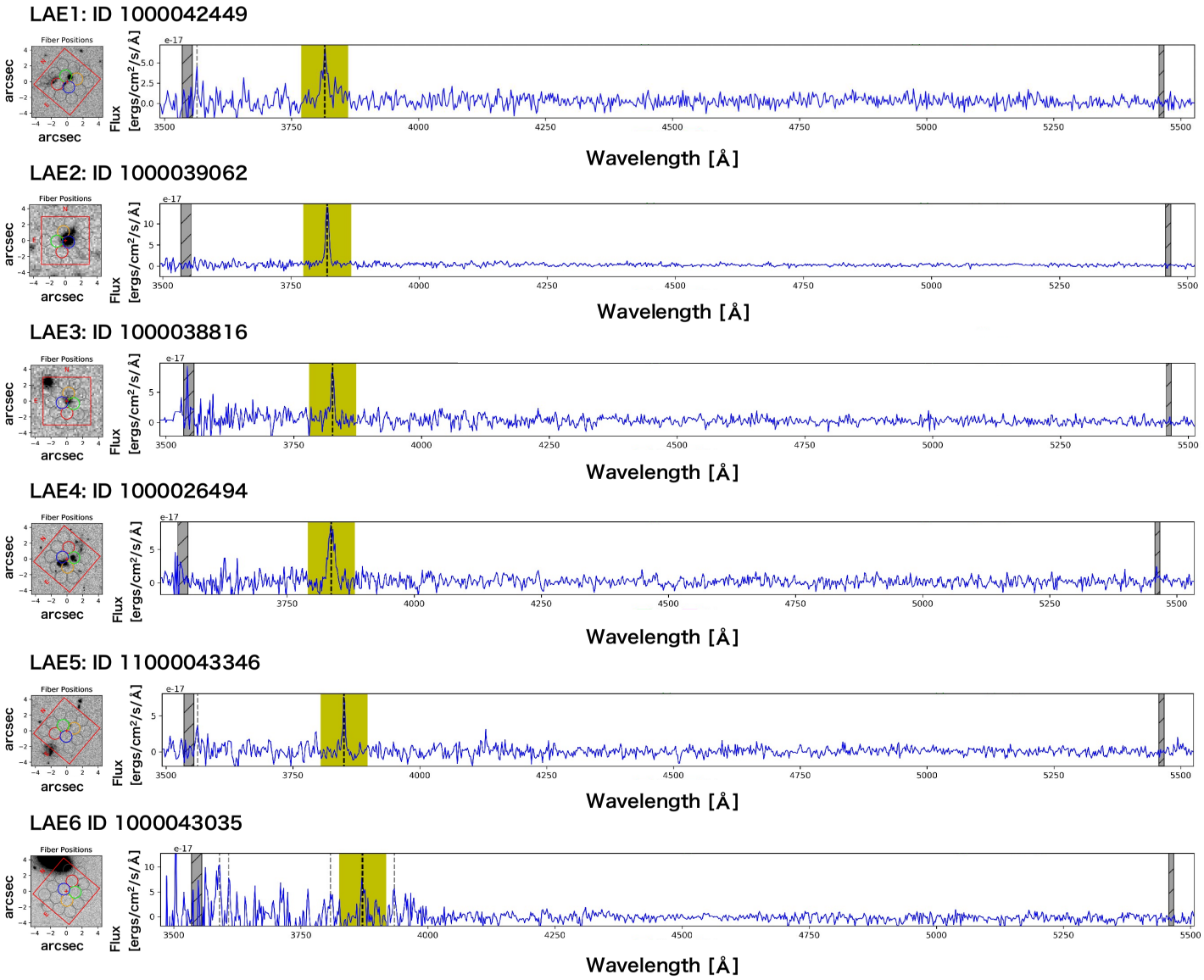

Figure 5.11: HETDEX spectra of the LAEs 1–6 distributed around the extreme quasar overdensity EGS-QO1. Left: Fiber positions atop the ancillary broadband images such as CFHT/MegaCam and HST/WFC3. Right: the weighted and summed spectra. Detected emission lines (centers) are highlighted with the yellow shades (the black dashed lines).

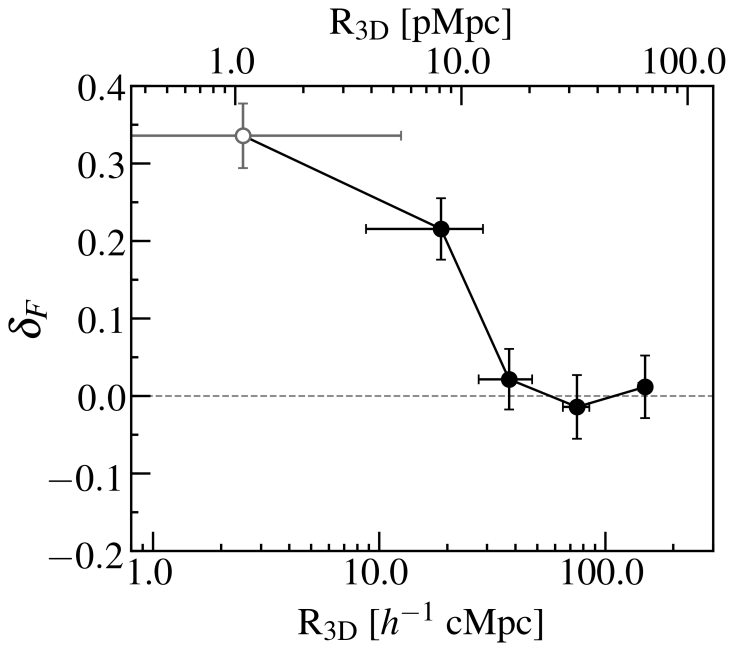

Figure 5.12: Same as Figure 5.1, but for our EGS LAEs distributed around the extreme quasar overdensity EGS-QO1.

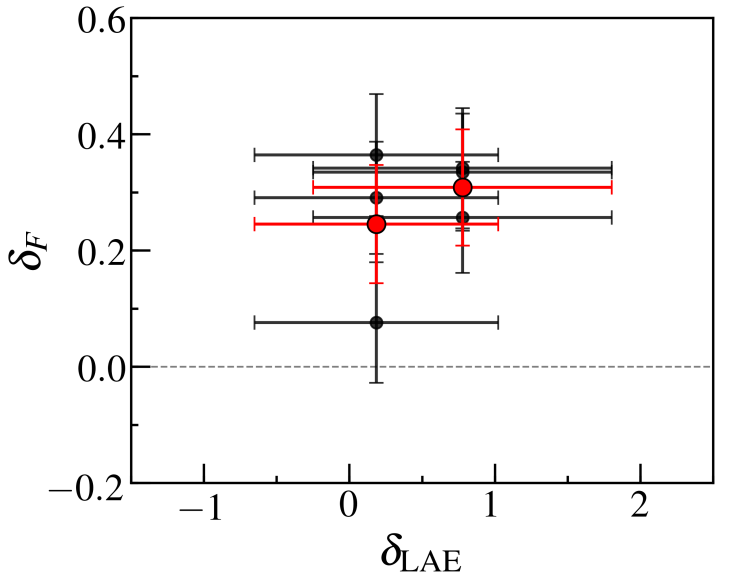

Figure 5.13: Same as Figure 5.2, but for our six EGS LAEs at $z = 2.13$–2.19 distributed in the extreme quasar overdensity EGS-QO1. Note that we estimate both δ_F and $\delta_{\rm LAE}$ with a sphere whose radius is 20 h^{-1} cMpc at $z = 2.3$.

5.4 HI–Gas Distributions Around an ELAN

The BOSS1441 region has the overdensities of galaxies and quasars (Section 5.2). In the overdensities, there is an obscured quasar [2] that has an ELAN at $z = 2.32$, dubbed MAMMOTH-1 nebula (Cai et al., 2017a). Since the origin of ELAN is thought to be quasar photo-ionization of HI LSSs (Section 1.2), the HI absorption around the MAMMOTH-1 nebula is expected to be suppressed. However, it has not been observationally explored IGM HI distribution around ELANe's host quasars.

Here, we investigate the HI-gas distributions around the MAMMOTH-1 host quasar (hereafter MAMMOTH1-QSO; Table 5.1) in the same manner as our three eBOSS quasars in the BOSS1441 region (Section 5.2). The red circles in Figure 5.14 represent the results of our HI radial profile measurements. We find that the HI radial profile of MAMMOTH1-QSO is comparable to (a bit weaker than[3])those of the three eBOSS quasars across 100 h^{-1} cMpc, showing a common turnover at $R_{\rm 3D} \simeq 8\ h^{-1}$ cMpc. The bottom panel of Figure 5.8 shows the 2D slice of the BOSS HI tomography map projected across $\Delta x = 2.6h^{-1}$ cMpc along the x (R.A.) direction around MAMMOTH1-QSO. In Figure 5.8, we find that MAMMOTH1-QSO is also associated with HI underdense region with sizes of $\simeq 5 - 10\ h^{-1}$ cMpc. These results suggest that MAMMOTH1-QSO has a proximity zone where HI gas is photo-ionized and HI absorption is suppressed. In this picture, the ELAN around MAMMOTH1-QSO is probably a photo-ionized hydrogen gas cloud embedded in the cosmic web.

Table 5.1: Properties of MAMMOTH1-QSO

ID	R.A. (J2000)	Decl. (J2000)	$z_{\rm spec}$	V (AB)	Ref.[a]
MAMMOTH1-QSO	14:41:24.46[b]	+40:03:09.20[b]	2.319	24.20	C17

[a] C17: Cai et al. (2017a)
[b] Updated coordinates in Keck/KCWI observations of Z. Cai et al. (in prep.)

[2] This obscured quasar is not observed in the eBOSS survey because of its faintness (V = 24.20).

[3] On the other hand, HI radial profile of MAMMOTH1-QSO is higher (i.e., stronger HI absorptions) than those of galaxies in the BOSS1441 and COSMOS regions. This would indicate a scenario that the ELAN could be a phase between quasars and galaxies in the galaxy evolution. More statistical studies on HI-gas distributions around ELANe are required to test this scenario.

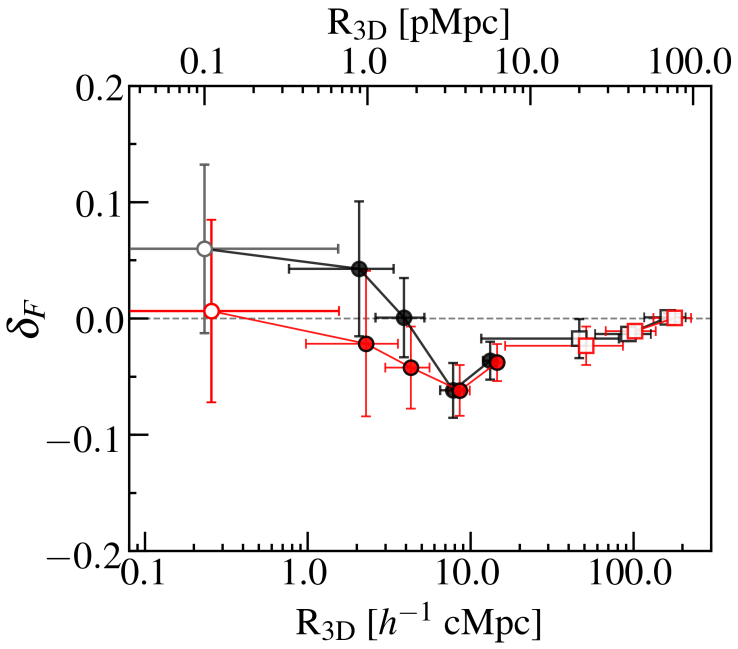

Figure 5.14: Same as Figure 5.7, but we overplot the HI radial profile around MAMMOTH1-QSO.

CHAPTER 6
SPECTROSCOPIC STUDY: DISCUSSIONS

In this Chapter, we discuss our results, using the schematic pictures of Figure 6.1. Figure 6.1 (a), (b), and (c) represent possible pictures of the hydrogen gas associated with galaxies in the three galaxy environments of (a) a blank region, (b) an overdensity of galaxies and quasars, and (c) an extreme quasar overdensity, respectively. Below, we summarize these three possible pictures based on our findings.

In Section 5.1, we have investigated spatial correlations between IGM HI-gas and galaxies in the COSMOS region where none of the eBOSS quasars are found in the cosmic volume of the HI tomography map. Our results suggest that HI-gas is distributed around galaxies across $\sim 100\ h^{-1}$ cMpc scales, and that large galaxy overdensities are associated with large HI gas overdensities, respectively. These indicate a picture shown in Figure 6.1 (a): HI gas excess around galaxies in a blank region.

In Section 5.2, we have measured the IGM HI-gas distributions around the overdensities of galaxies and quasars in the BOSS1441 region. Contrary to the results in the blank region, our results suggest that HI absorptions are reduced and almost constant at the cosmic mean level around galaxies across $\sim 100\ h^{-1}$ cMpc scales. In contrast to these galaxies, we find possible suppression of HI absorptions around the three eBOSS quasars in the cosmic volume. Our results might suggest that large galaxy overdensities can be associated with a large amount of HI gas, but quasars that emerge from the galaxy overdensities might photo-ionize the surrounding HI gas and suppress the HI absorptions around the galaxies. One might expect that the HI absorption suppression is made by the lack of hydrogen gas. However, as we see in Section 5.4, enormously extended Lyα objects such as MAMMOTH1-QSO has HI environment comparable to those of the three eBOSS quasars. This supports the photoionization of the HI gas around the quasars. These provide a possible picture shown in Figure 6.1 (b): hydrogen gas photo-ionized by quasars.

In Section 5.3, we have studied HI environments of the extreme quasar overdensity EGS-QO1 found in the EGS region. The quasar overdensity of EGS-QO1 is

comparable to or a bit larger than that of the BOSS1441 region. Our results show that EGS-QO1 is surrounded by an HI underdensity region with weak HI absorptions. The possible correspondence between EGS-QO1 and the HI underdensity indicate the group of quasars would form a large ionizing bubble where most of the surrounding HI gas is widely photo-ionized. These provide a possible picture shown in Figure 6.1 (c): hydrogen gas mostly photo-ionized by group of quasars and galaxies.

For the three survey regions, our results and Figure 6.1 might suggest an evolutionary picture of photoionization of HI gaseous LSS: HI gaseous LSSs around galaxies might be photo-ionized by quasars as the overdensities of galaxies and quasars evolve in the structure formation.

Note that the evolutionary picture is based on two interesting systems; one extreme galaxy overdensity (BOSS1441) and one quasar overdensity (EGS-QO1). It is not obvious whether other extreme galaxy/quasar overdensities have HI environments consistent with our results. The evolutionary picture can be studied with the wide-field galaxy surveys such as the ongoing HETDEX survey (Hill et al. 2008, Gebhardt et al. 2020, in prep.). The HETDEX survey will complete the blind spectroscopic observations in 2020s, and provide 10^6 galaxies at $z = 1.9$–3.5 in a 9 Gpc^3 volume. The HETDEX survey will reveal the galaxy - IGM HI relation as a function of eBOSS quasar overdensities in one continuous field such as the HETDEX Spring field (300 deg^2; APPENDIX B). The galaxy - IGM HI relation with HETDEX will enable us to conduct statistical studies for probing photoionization of HI gaseous LSS. The statistical studies of LSS photoionization could shed light on not only the suppression of the formation of low-mass galaxies in the enhanced UVB radiation, but also the ionization mechanism of galaxy clusters' intra-cluster medium.

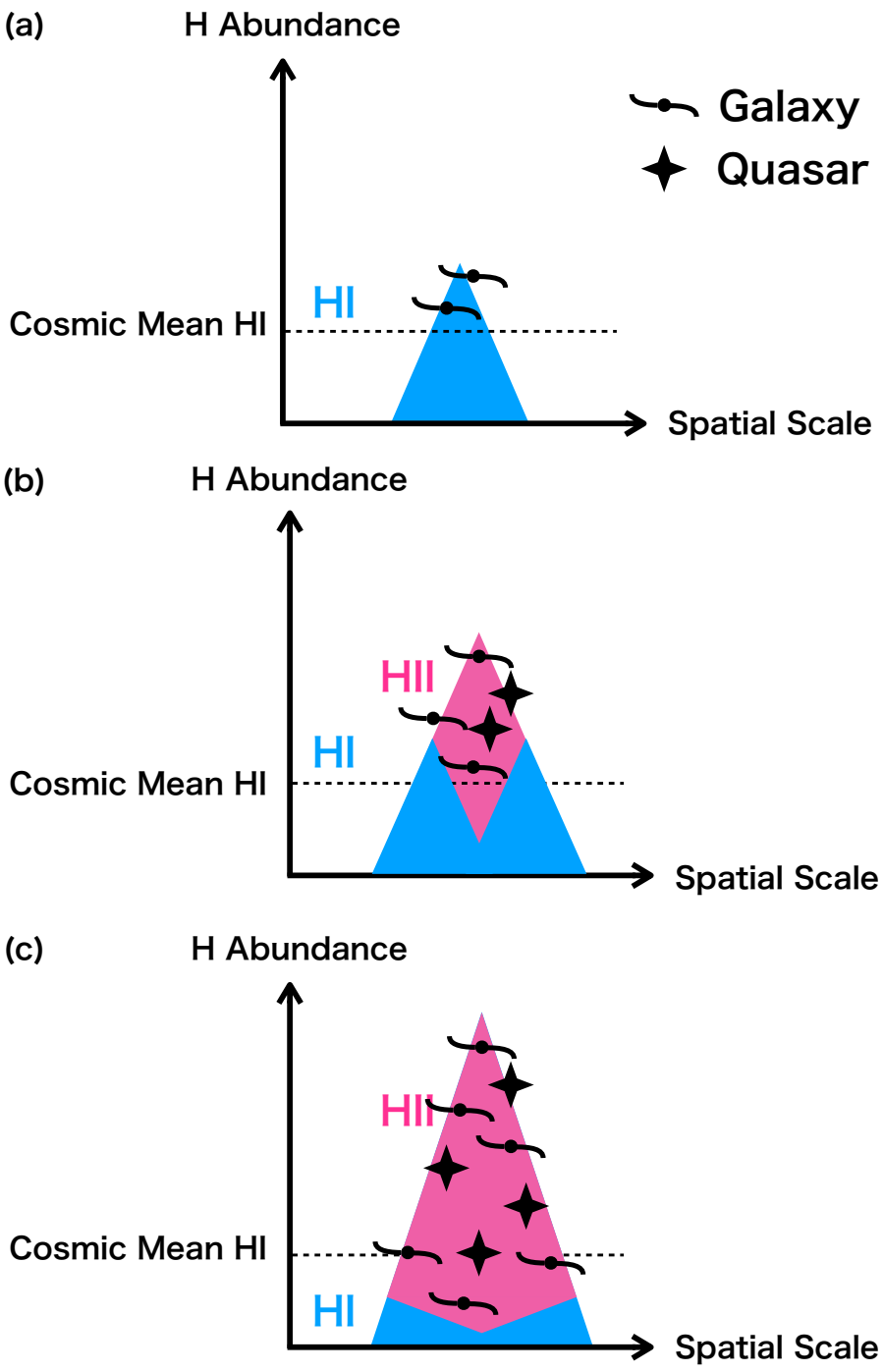

Figure 6.1: Schematic pictures that summarize our findings. The pictures (a), (b), and (c) show the hydrogen gas associated with galaxy environments of (a) a blank region, (b) an overdensity of galaxies and quasars, and (c) an extreme quasar overdensity, respectively.

CHAPTER 7
SPECTROSCOPIC STUDY: FUTURE PROSPECTS

The results and discussions in the previous Chapters suggest that quasars may photo-ionize the surrounding HI gas and weaken the HI-gas absorption strength. To directly test the quasar photoionization of HI gas, one can investigate the existence of ionized hydrogen gas with hydrogen recombination lines such as Hα emission line. Note that the Hα emission from intergalactic hydrogen gas clouds (hereafter intergalactic Hα emission) at $z = 2$ is redshifted into NIR wavelength range (e.g., Leibler et al., 2018; Yang et al., 2014), which requires NIR observations. In this Chapter, we describe future prospects of NIR observations toward directly testing the quasar photoionization of HI gaseous LSS.

7.1 Subaru/MOIRCS Observations

To identify the intergalactic Hα emission around quasars, we have carried out pilot observations with MOIRCS (Ichikawa et al., 2006) on the 8m Subaru telescope. Our target is Slug nebula that is the largest ($\sim$ 460 pkpc) and the brightest ($L_{\mathrm{Ly}\alpha} \sim 1.4 \times 10^{45}$ erg s^{-1}) ELAN around two quasars at $z = 2.28$ (Cantalupo et al., 2014, the left panel in Figure 7.1). Cantalupo et al. (2014) investigate the origin of the extended Lyα emission with radiative transfer simulations, and suggest a scenario that the Slug nebula can be explained by a photo-ionized hydrogen gas cloud embedded in the cosmic web (see also Sections 1.2 and 5.4). In the photo-ionization scenario, the hydrogen gas clouds are predicted to have clumpy structures on scales of $\simeq$ 100 pc to reproduce the Lyα surface brightness. Specifically, the ionized hydrogen gas is predicted to have high clumping factor C ($=< n_e^2 > / < n_e >^2$, where n_e is electron density) of $C \simeq 1000$ to increase the density of individual gas clump $n \sim 1 - 10$ cm^{-3} in a total gas mass ($M_{\mathrm{gas}} \sim 10^{10.5-11.5} M_{\odot}$) of the simulated quasar dark matter haloes. However, both the photo-ionization and the clumpy structures can not be distinguished with the Lyα emission due to its resonant nature.

Here, one can spatially test the photo-ionization scenario with intergalactic Hα emission and a criteria of the emission line ratio of Lyα/Hα = 8.7, assuming the case-B recombination (Osterbrock, 1989). We thus have performed NIR imaging of the Slug nebula with MOIRCS in half a night on 2019 September 9 (UT) (PI: Shiro Mukae). To identify the Hα emission line at $z = 2.28$, we use the BrG narrowband filter whose central wavelength is 2.165 μm and bandwidth is 0.025 μm. The sky conditions were clear with an average seeing size of 0".4. The total exposure time was $\sim$ 8000 sec, resulting the 5σ limiting magnitude of 22.9 mag per arcsec^2. The right panel in Figure 7.1 shows our MOIRCS BrG narrowband image. The black contour shows flux-excess regions of 2σ, 3σ, 5σ, and 10σ levels, giving the magnitude levels 23.9, 23.5, 22.9, and 22.2 mag per arcsec^2, respectively. From the figure, Hα excesses are found only in the position of quasars ('a' and 'b' in the left panel of Figure 7.1) and galaxies (e.g., 'c' in the left panel of Figure 7.1). We did not see significant intergalactic Hα emission and its clumpy structures around the quasars.

Our pilot survey suggests that it is challenging to detect the intergalactic Hα emission and to resolve the clumpy structures with the 8m-class telescopes. Firstly, we focus on the detection of intergalactic Hα emission, and estimate a requisite observation. We aim at detecting the intergalactic Hα emission in bright Lyα regions of the Slug nebula where surface brightness is $SB_{\mathrm{Ly}\alpha} \geq 3.0 \times 10^{-18}$ erg s^{-1} cm^{-2} arcsec^{-2} (the left panel in Figure 7.1). To estimate the surface brightness of the intergalactic Hα emission, we adopt the case-B recombination line ratio of Lyα/Hα = 8.7. We then expect the surface brightness of the Hα emission will be $SB_{\mathrm{H}\alpha} \geq 3.4 \times 10^{-19}$ erg s^{-1} cm^{-2} arcsec^{-2} that corresponds to 26.5 mag per arcsec^2. If we detect such intergalactic Hα emission with 3σ levels per arcsec^{-2}, it is required to carry out observations with $\sim$ 3 mag deeper (i.e., S/N levels 10 times higher) than our pilot observations. For simplicity, we expect to take long exposure time for increasing the S/N levels under the fixed telescope aperture because the S/N levels can be increased by the square root of the exposure time. Thus, if we will detect the intergalactic Hα emission with MOIRCS, we need to perform deep observations whose exposure time will be 100 times longer than our 0.5 night observations. This ends up the observations with 50 nights, expensive for the single target. Secondly, we examine the requisite resolving

scale, and find it very difficult. The 100 pc gas clumps corresponds to 10 milli-arcsec scale that is an order of smaller than the MOIRCS pixel scale (116 milli-arcsec/pixel). Thus, it is challenging to identify and resolve the intergalactic Hα emission with the 8m-class telescopes even for the largest and the brightest ELAN.

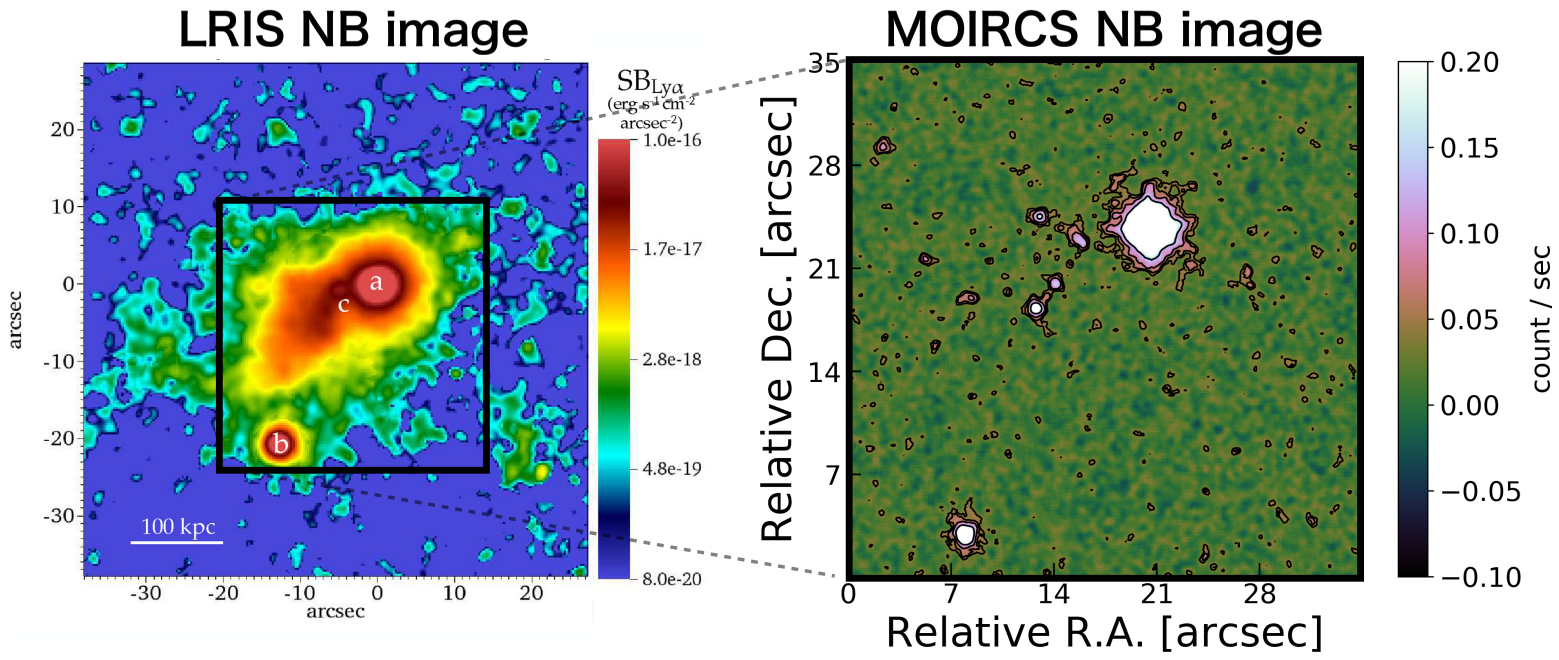

Figure 7.1: Left: Lyα narrowband image of an ELAN, Slug nebula at $z = 2.28$ taken by Keck/LRIS from Cantalupo et al. (2019). The white characters represent position of sources embedded in the Slug nebula. The 'a' and 'b' present the two host quasars at $z = 2.28$. The 'c' is a galaxy at $z = 2.28$. The color scale shows the Lyα emission surface brightness. The black square indicates the zoom-in regions that are shown in left panel. Right: our MOIRCS BrG image taken by our pilot observations. The color scales represent flux levels. The black contour shows flux-excess regions of 2σ, 3σ, 5σ, and 10σ levels the corresponds to the magnitude levels of 23.9, 23.5, 22.9, and 22.2 mag per arcsec^2, respectively.

7.2 TMT/IRIS Observing Plans

In the previous Section, we have shown the difficulty in detecting the intergalactic Hα emission with the 8m-class telescopes. Here, instruments for 30m-class telescopes may resolve this difficulty. We then estimate a requisite exposure time for observations with the 30m-class telescopes such as IRIS (Larkin et al., 2016) on TMT Sanders (2013). In Section 7.1, the requisite observations need S/N levels 10 times higher than our pilot observations (see Section 7.1). Observations with the 30m-class telescopes improve the S/N levels by the aperture ratios (e.g., $\sqrt{30^2/8^2} \sim \sqrt{10}$) assuming the same exposure time. To achieve the requisite S/N levels (10 times higher than the current value with the 8m-class telescope), we then need exposure time 10 times longer than our 0.5-nights observation. This results in observations with 5 nights, which can be feasible comparing to the observations with the 8m-class telescopes. Moreover, the diffraction limit imaging of IRIS reaches the 10 milli-arcsec comparable to the requisite gas clump scale, which enables us in principle to investigate the clumpy structures.

Our estimations motivate the observations of the intergalactic Hα emission with the planned NIR instruments on the 30m-class telescopes such as TMT/IRIS. Here, we contribute to the TMT/IRIS instrumentation, and prepare the TMT/IRIS observations for testing photoionization of HI gaseous LSS. From the next chapters, our TMT/IRIS instrumentation is presented.

CHAPTER 8
TMT/IRIS INSTRUMENTATION: OVERVIEW AND MOTIVATION

8.1 Overview

TMT (Sanders, 2013) is a large optical infrared telescope with a 30 meter aperture. Construction of TMT is underway at the summit of Mauna Kea on the island of Hawaii, and to be completed in the early 2030s. TMT is an international project organized by Japan, United States, Canada, China, and India. IRIS (Larkin et al., 2016) is one of the first light science instruments for TMT. IRIS has an imaging mode and an IFS mode with two types of spectrographs; image slicer and lenslet array. IRIS enables high spatial resolution and high sensitivity observations in the wavelength range of 0.84-2.4 μm, using diffraction limit performance (reaching 10 milli-arcsec) assisted by an adaptive optics (AO) system of Narrow Field InfraRed Adaptive Optics (NFIRAOS; Herriot et al., 2014) on the Nasmyth platform. The imaging mode covers $34'' \times 34''$ field of view (FoV) with 4 milli-arcsec/pix sampling. The IFS mode provides a spatial sampling of 4, 9, 25, and 50 milli-arcsec/spaxel and a spectral resolution of 4,000, 8,000, and 10,000. Figure 8.1 presents 3D model images of TMT and IRIS, and shows the imager and IFS systems inside the vacuum cryostat.

The instrumentation of IRIS is in the final design phase (timeline: 2017-2021), and is currently conducted by the international collaborations among Japan, United States, Canada, and China. Design and development of the IRIS imager is led by Advanced Technology Center (ATC) of National Astronomical Observatory of Japan (NAOJ). Optical, mechanical, and software designs of the IRIS imager are developed in ATC (Figure 8.2). Here, I am preparing the TMT/IRIS observations of intergalactic Hα emission around $z \sim 2$ quasars, by making the following two contributions toward the TMT/IRIS operations; (I) calibrating optical distortion of the IRIS optics and (II) prototyping mirror coatings for the IRIS optics. From next sections, we present the study of (I) optical distortion calibration. The study of (II) mirror coating prototypes is presented in APPENDIX C.

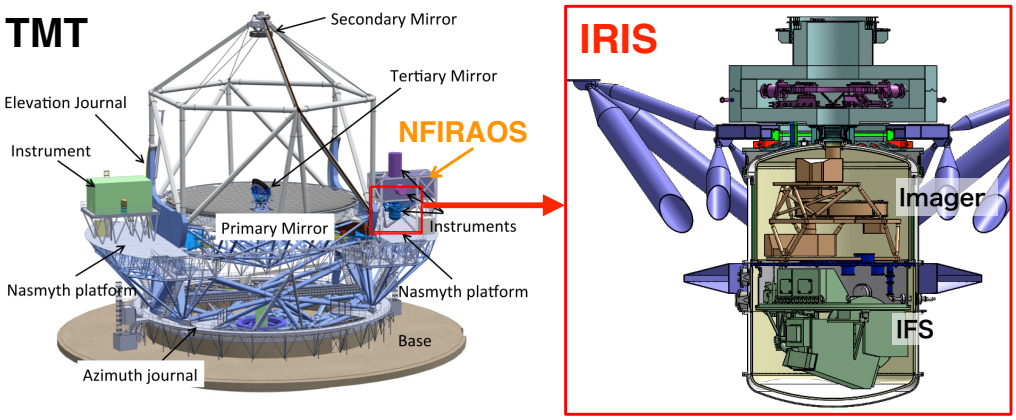

Figure 8.1: 3D model images of TMT and IRIS. IRIS has the imaging and IFS systems inside the vacuum cryostat. This figure is taken from IRIS Design Description Document (TMT.INS.TEC.16.051.REL01).

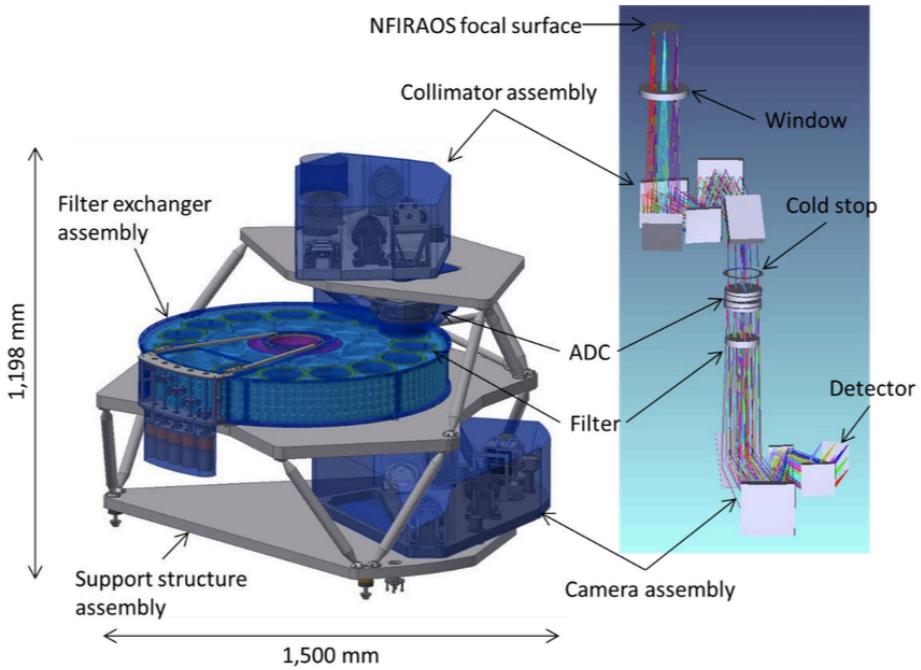

Figure 8.2: Mechanical and optical designs of the IRIS imager. This figure is taken from IRIS Design Description Document (TMT.INS.TEC.16.051.REL01).

8.2 Motivation

The observation of IRIS is performed in conjunction with the adaptive optics system NFIRAOS (Herriot et al., 2014) on the Nasmyth platform. A diffraction-limited observing capability that IRIS and NFIRAOS provide enables high-precision relative astrometry in the near-infrared wavelength range at an unprecedented level (Wright et al., 2016). TMT specifies that IRIS and NFIRAOS achieve relative astrometric errors of 50 μ arcsec [1] for one of the most important key science cases: fundamental tests of General Relativity through high-precision mapping of stellar orbits around the central black hole in the Galactic Center (Skidmore et al., 2015).

The relative astrometric errors of 50 μ arcsec are divided into five error terms (Schöck et al., 2014): reference source catalog errors, atmospheric refraction errors, AO correction errors, opto-mechanical errors, and measurement errors. Among these error terms, opto-mechanical errors are one of the major error terms: the requirement for calibrating the optical distortion in the NFIRAOS and IRIS optics is specified to be 10 μarcsec over 34×34 arcsec^2 FoV (Schöck et al., 2016). This requirement corresponds to 20 nm accuracy over 70×70 mm^2 at the telescope focal plane.

The optical distortion of most near-infrared instruments has been routinely calibrated by a reference method where a-priori knowledge of pinhole positions serves as references to calibrate the optical distortion[2] . However, the reference method does not work in our case since the pinhole positions cannot be known to better than 20 nm over 70×70 mm^2 even with the highest accuracy 3D measuring tools.

The IRIS development team thus decided to adopt a self-calibration technique where the optical distortion is extracted by comparing pinhole positions as a pinhole mask is dithered multiple places on the telescope focal plane. The self-calibration technique is firstly developed by Anderson & King (2004) who study the distortion correction on HST/ACS and achieve a correction accuracy of 200 μ arcsec. Our

[1]Note that our planned TMT/IRIS observations of the intergalactic Hα emission around $z \sim 2$ quasars (Section 7.2) does not require such a high-precision measurements. Here, achieving the specification is indispensable to manufacturing the IRIS instrument, installing on the TMT, and finally carrying out our planned observations.

[2]For reference, the optical distortion of the telescope optics is calibrated with field stars on sky.

distortion correction strategy follows the one in Anderson & King (2004) which has the following three steps corresponding to the spatial frequency of the distortion:

1. linear transformation correction
2. low order distortion correction by a polynomial solution
3. high order distortion correction by a look-up-table solution

However, it is not obvious whether the self-calibration algorithm works for the NFIRAOS and IRIS optics and achieves the requisite accuracy of 10 μarcsec that is an order of magnitude smaller than the correction accuracy of HST/ACS (Anderson & King, 2004). If it turns out that the distortion correction with the self-calibration algorithm could not satisfy the requisite accuracy, the current optical design (or the latest science case) should be revised, which have huge impacts on the schedule of the NFIRAOS and IRIS development. Thus, it is important to characterize the performance of the method to avoid the possible impacts as much as possible.

In this thesis, we focus on the look-up-table based self-calibration algorithm adopted in NFIRAOS and IRIS. We characterize the performance of the algorithm by the distortion correction accuracy with various parameters. We then suggest a set of parameters for NFIRAOS and IRIS to achieve the distortion correction accuracy of 10 μarcsec, in consideration of design, operation, and performance aspects. The TMT/IRIS instrumentation part in this thesis is organized as follows. Our self-calibration algorithm and simulation flow is outlined in Chapter 9. Chapter 10 presents the main results of the analysis and our findings. Chapter 11 begins with the suggested parameters for NFIRAOS and IRIS followed by some future plans to improve the analysis.

CHAPTER 9
TMT/IRIS INSTRUMENTATION: ALGORITHM AND DATA

9.1 Algorithm

The self-calibration algorithm used in this work is based on Anderson & King (2004). Each process is laid out as follows and schematically shown in Fig. 9.1. The basic idea is that we correct the optical distortion by using the differential position between multiple dithered positions.

1. measuring pinhole image coordinates at different dithered positions
2. making pairs of any two pinhole images
3. applying linear transformation to all the pairs
4. measuring coordinate differences for all the pairs
5. defining a coarse lookup table with uniform grid cells
6. taking average of these coordinate differences over each grid cell in the coarse lookup table
7. defining a fine lookup table with uniform grid cells
8. making the fine lookup table by interpolating the coarse lookup table
9. applying table correction to all of the pinhole images with the fine lookup table
10. iterating step 3 – 9 until the coordinate differences become small enough

In this work, we use the 32×32 (128×128) grid cells for a coarse (fine) lookup table. We limit the maximum number of the iterations to 100. The final calibrated pinhole image is obtained by the final lookup table correction.

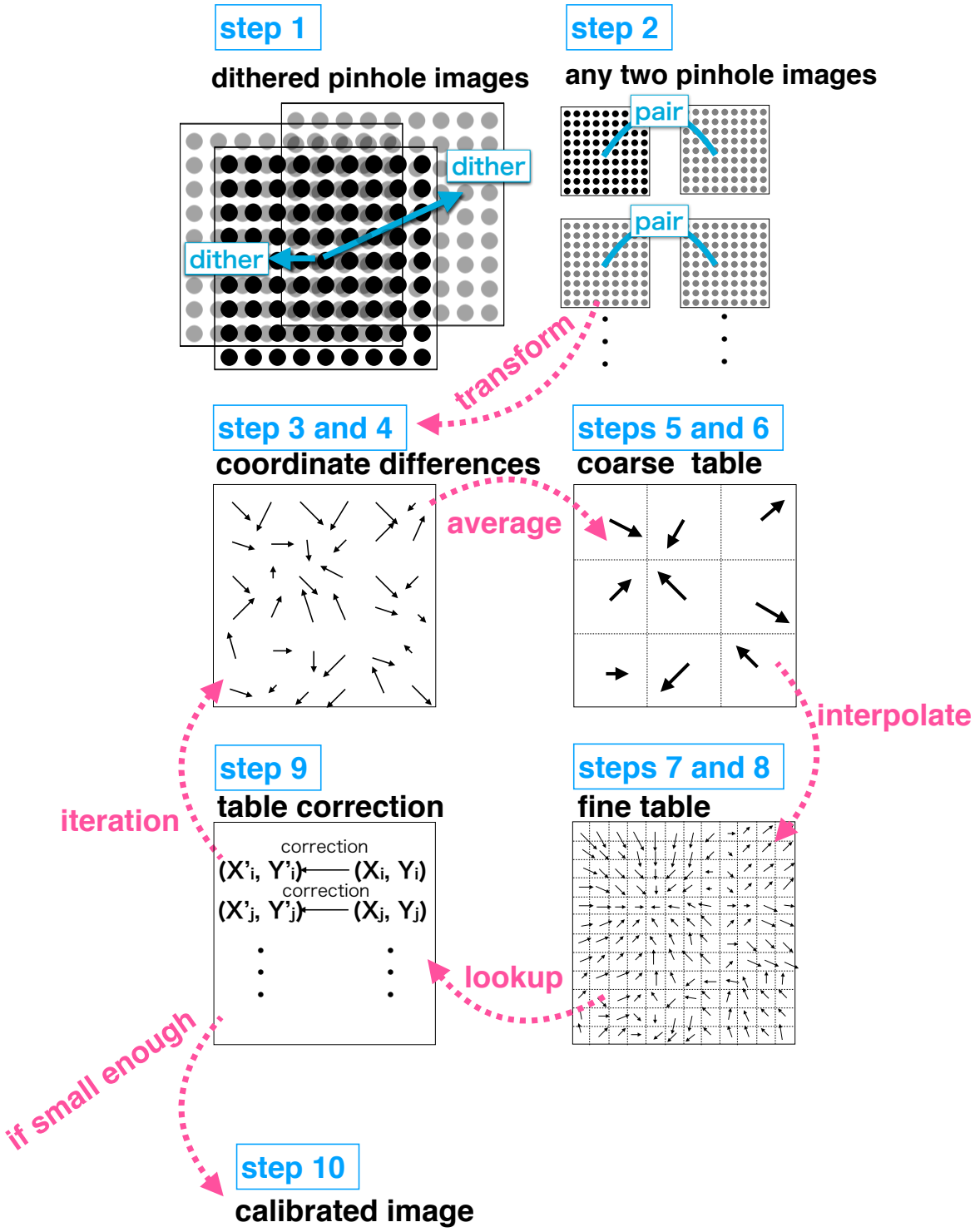

Figure 9.1: Schematic picture of the self-calibration method.

9.2 Data

This section describes how we generate observed pinhole coordinates that are expected through NFIRAOS and IRIS optics, and are input catalogs to the distortion correction process using the self-calibration. We model NFIRAOS and IRIS optical systems using an optical design software ZEMAX to generate observed pinhole positions in the detector coordinate. We use the latest optical prescription of NFIRAOS with four off-axis parabolas (Herriot et al., 2010) and IRIS with six mirrors design (Tsuzuki et al., 2016) that are summarized in Figure 9.2.

We add the polishing errors on selected optical surfaces to take into account high spatial frequency distortion. The polishing error is assumed to follow a power spectrum density (PSD) in the form of 1D power law with a slope of 2.5. The PSD is normalized such that the total polishing error is 6 nm rms on optical surfaces. The polishing error is added on the last two camera mirrors (Camera 2nd and 3rd) and the two surfaces of the entrance window (Window Front and Back) in IRIS optics. These surfaces are identified by the analytical studies as major contributors to the astrometry errors due to polishing errors (see APPENDIX D).

The observed pinhole position in the detector coordinate (X) is calculated as $X = (X_c + L \times T_c)$ where, X_c is a detector coordinate that a chief ray intercepts the detector surface, L is a distance between the exit pupil and the detector, and T_c is a wavefront tilt in radian on the exit pupil plane against the chief ray. The true pinhole coordinates are also generated assuming a paraxial magnification between the telescope focal plane and the detector plane for a purpose of evaluating distortion correction accuracy. The detector coordinates are converted to the sky coordinates in unit of arcsec with a paraxial plate scale on the detector plane.

There are three parameters that characterize the pinhole mask on the telescope focal plane: the number of pinholes N_{pinhole}, the dither pattern N_{dither}, and the dither length $\pm d_{\mathrm{dither}}$. For simplicity, the pinholes and the dithers are configured on a uniform grid. Note that the number of pinholes fills one of four IRIS detectors which covers 17×17 arcsec^2. Tab. 9.1 summarizes the pinhole mask parameters used in this work.

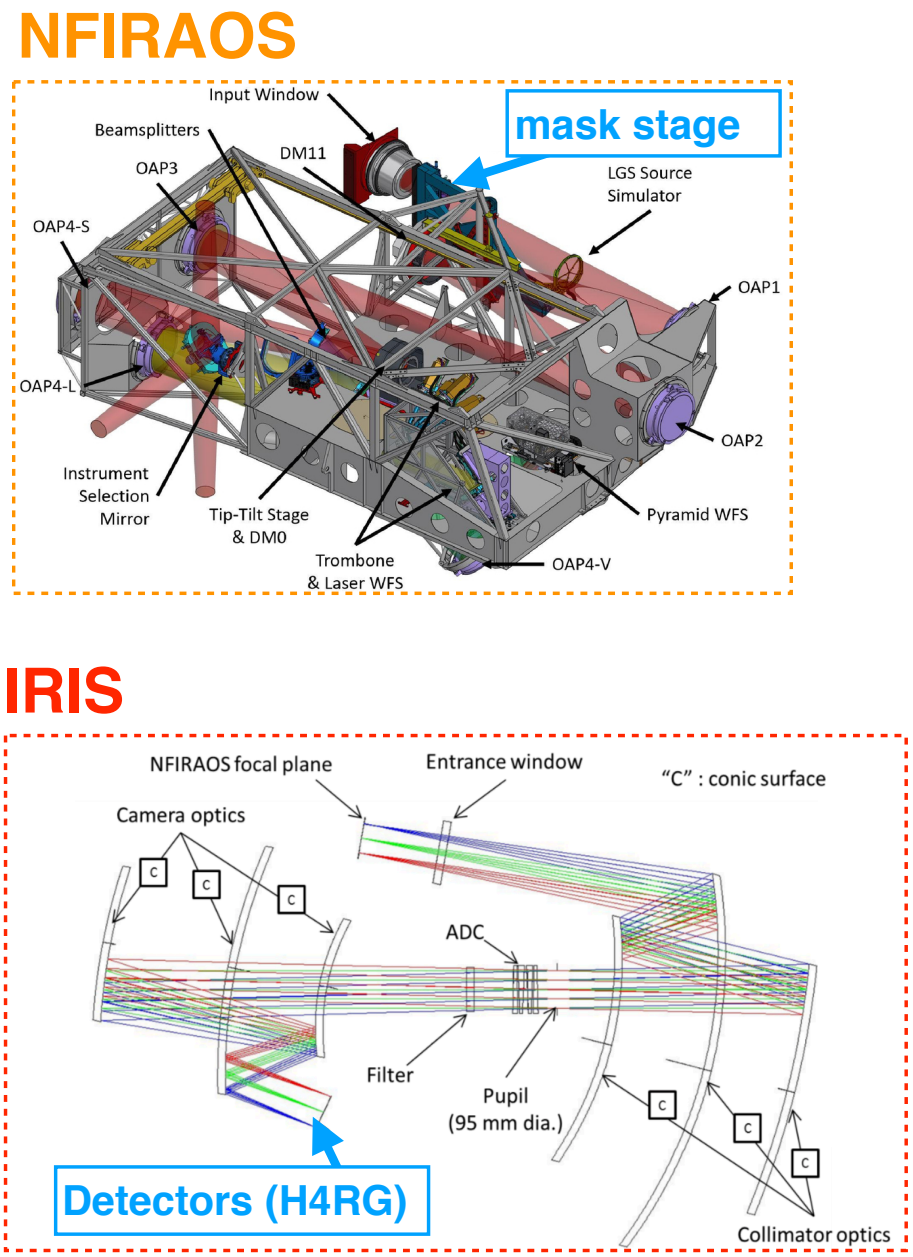

Figure 9.2: Top panel: the optical model and the optical path of NFIRAOS (Herriot et al., 2010). 7 mirrors are used in the optics. This figure is taken from NFIRAOS Design Description Document (TMT.AOS.TEC.18.086.REL01). Bottom panel: the optical model and the optical path of the IRIS imager (Tsuzuki et al., 2016). 9 mirrors are used in the optics. This figure is taken from IRIS Design Description Document (TMT.INS.TEC.16.051.REL01).

Table 9.1: Pinhole mask parameters used in this work.

Parameter	Range
d_{dither}	from 0.2 to 2.2 arcsec, in 0.2 arcsec increments
N_{pinhole} (pinhole interval)	9×9 (2".12), 17×17 (1".06), and 33×33 (0".53)
N_{dither}	3×3, and 5×5

CHAPTER 10
TMT/IRIS INSTRUMENTATION: ANALYSIS AND RESULTS

10.1 Data Analysis

Once we take the look-up-table solution and distortion-corrected pinhole position catalogs, we remove low spatial frequency distortion from the pinhole positions with 5th order polynomial to represent the polynomial-based distortion correction mentioned in Chapter 8.2. The distortion correction accuracy σ_{DC} is finally calculated as an rms of differences between calibrated pinhole coordinates and true pinhole coordinates.

10.2 Correction-Table Resolution

It is worth mentioning here the R_{table} parameter, hereafter table resolution, which is a resolution of the coarse table introduced in step 5 of the algorithm in Section 9.1. The table resolution is important because any distortion with higher frequency than the table resolution is not sensed by our algorithm, due to an averaging operation within the table resolution in step 6 of the algorithm in Section 9.1.

We calculate the unsensed high-frequency distortion as a function of R_{table} by integrating the PSD of the distortion over the frequency higher than R_{table} scale. Fig. 10.1 shows PSD of the distortion over the 17×17 arcsec^2 field. The table resolution of 0.53 arcsec (corresponding to 128 pixels) makes the unsensed high spatial frequency distortion smaller than 1μ arcsec. This table resolution gives the number of elements of the coarse table $N_{\mathrm{table}} = 32 \times 32$.

10.3 Parameter Analysis

We examine the correction performance of our self-calibration method by changing the pinhole mask parameters d_{dither}, N_{pinhole}, and N_{dither}. Fig. 10.2 compares the distortion correction accuracy σ_{DC} as a function of dither length for different number

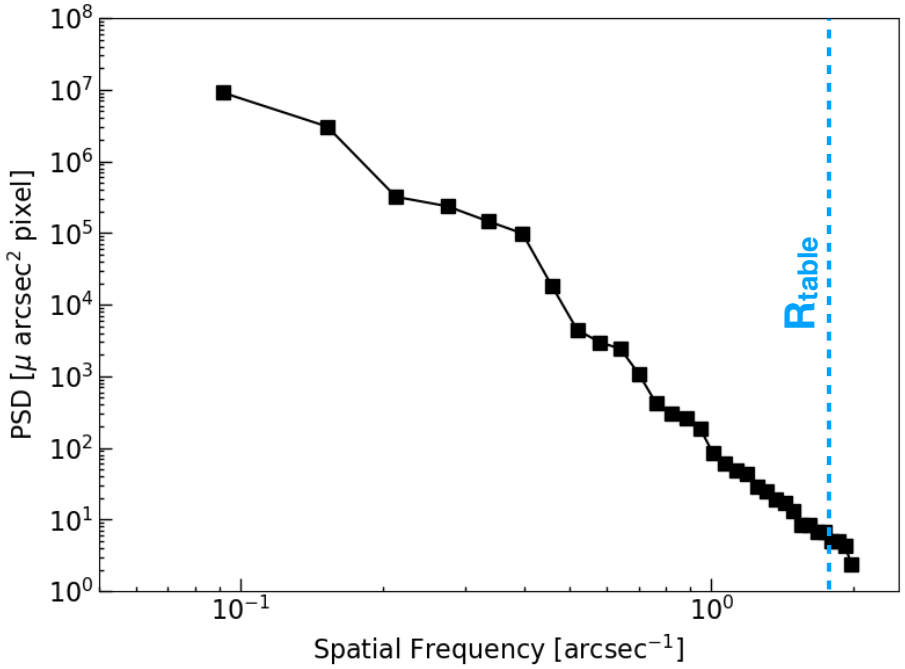

Figure 10.1: PSD of optical distortion across the IRIS field of view. Black squares represent measurements in our optical model. Blue dashed line presents R_{table} of 0.53 arcsec (corresponding to 128 pixels) chosen in this work.

of pinholes N_{pinhole} with the dither pattern fixed at $N_{\text{dither}} = 3 \times 3$. All three plots show that the larger dither length and larger number of pinholes generally results in better distortion correction accuracy. There seems a floor of the distortion correction accuracy at ~ 3 μarcsec.

The plot for $N_{\text{pinhole}} = 9 \times 9$ indicates that the distortion correction accuracy is improved when the dither length is a multiple of half the pinhole interval. This is reasonable because the condition assures that there are multiple pinholes within a single table resolution. The multiple pinholes within a table resolution increase the number of data to be averaged as well as increase spatial scale which the table resolution covers (Fig. 10.3). The distortion correction accuracy peak at $d_{\text{dither}} = 1.4$ arcsec may be a result of having only one pinhole in a table resolution.

Better correction accuracy in the case of $N_{\text{pinhole}} = 33 \times 33$ may be understood that multiple pinholes are always within a table resolution when the dither length becomes longer than the table resolution. We see, in the plot for $N_{\text{pinhole}} = 33$, that the distortion correction accuracy improves with increasing dither length until it hits a floor when the dither length becomes equal to the table resolution. The decreasing trend is reasonable because the more pinhole coordinate differences in step 4 of the algorithm in Section 9.1 are canceled out in step 6 when the dither length is smaller than the table resolution. Fig. 10.4 shows the same plots with a different number of dithers. Increasing the number of dithers is another effective way to improve the correction accuracy σ_{DC} even when the dither stroke is limited.

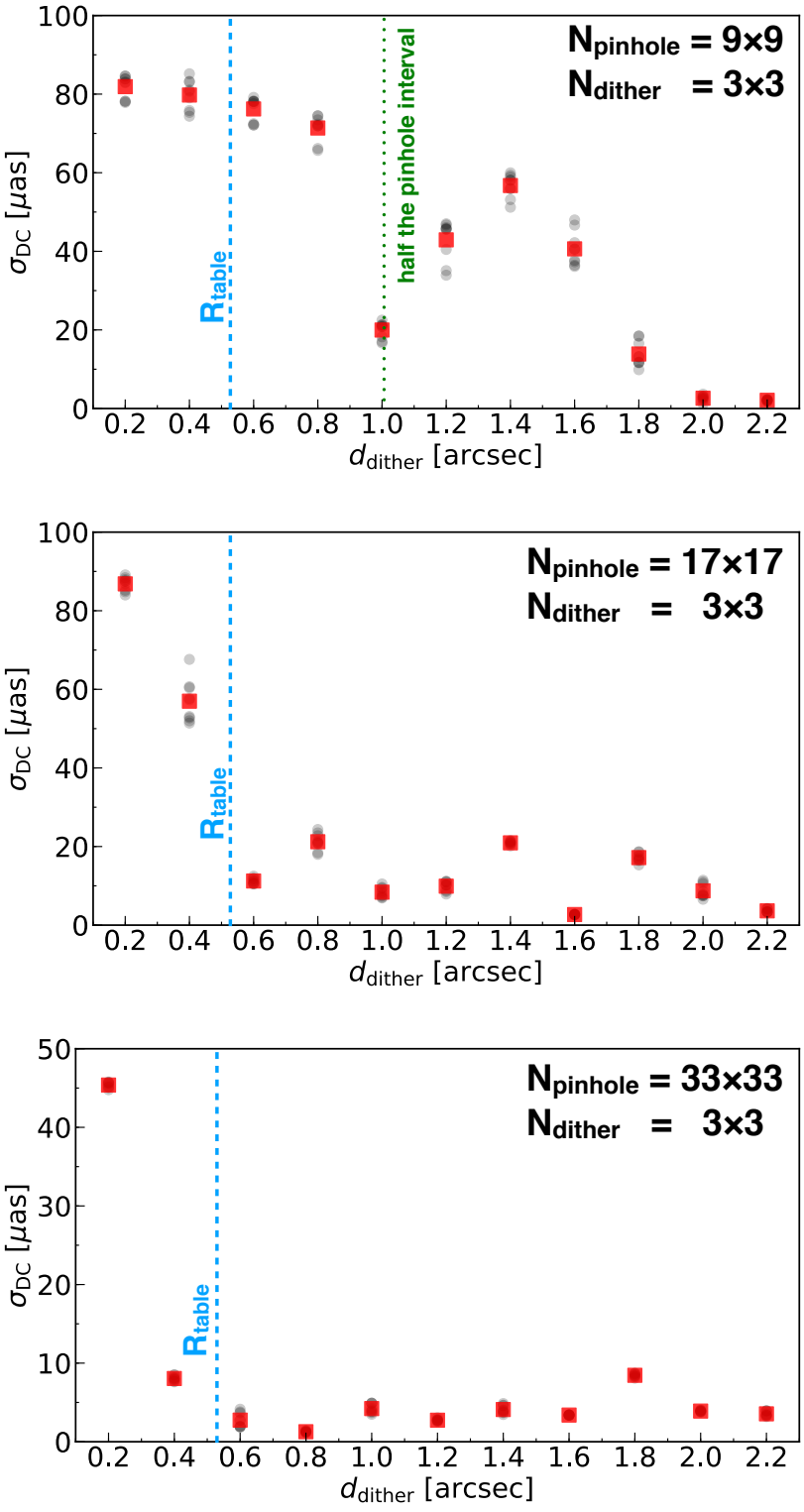

Figure 10.2: Distortion correction error $\sigma_{\rm DC}$ as a function of dither length $d_{\rm dither}$ for different number of pinholes $N_{\rm pinhole}$ with the dither pattern fixed at $N_{\rm dither} = 3 \times 3$ Black circles present $\sigma_{\rm DC}$ at each of dithered positions. Red squares represent $\sigma_{\rm DC}$ averaged over the all dithered positions.

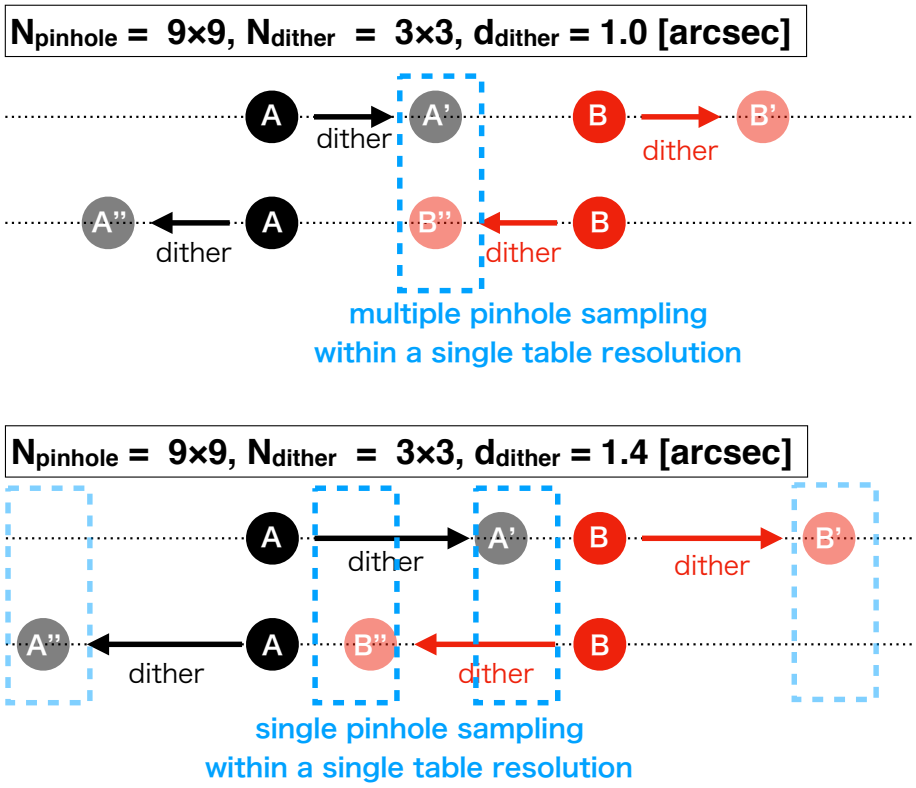

Figure 10.3: Schematic pictures of pinhole configurations for two cases: different dither lengths of $d_{\rm dither} = 1.0$ (top) and 1.4 (bottom) arcsec with the number of pinholes fixed at $N_{\rm pinhole} = 17 \times 17$ and the dither pattern fixed at $N_{\rm dither} = 3 \times 3$. For simplicity, we consider 1D coordinates of a pinhole A and a pinhole B next to each other on the x axis. These pinhole A and B are dithered by $\pm d_{\rm dither}$ along the x direction. Blue rectangles represent single table resolutions.

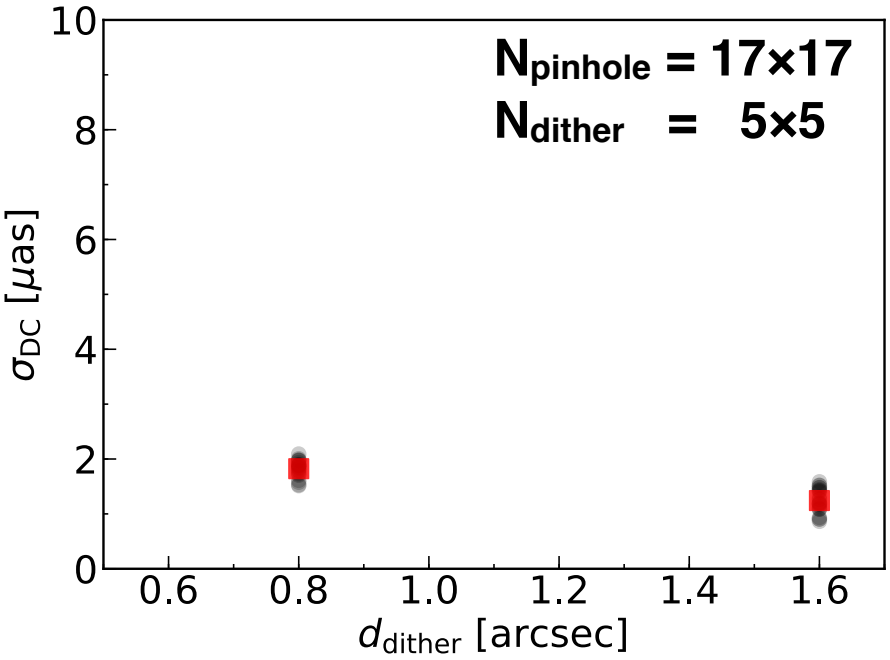

Figure 10.4: Same as Fig. 10.2, but for different dither patterns with the number of pinholes fixed at $N_{\mathrm{pinhole}} = 17 \times 17$.

CHAPTER 11
TMT/IRIS INSTRUMENTATION: DISCUSSIONS AND FUTURE PROSPECTS

11.1 Suggested Pinhole Mask Parameters for NFIRAOS and IRIS

In the previous chapter, we study parameter setting procedures that are generally helpful to reduce the distortion correction errors. There are, however, constraints coming from other aspects of performance and design which limit the parameters. For example, too many pinholes, hence a small pinhole interval, could cause adjacent pinholes to blend together. Too many dithers leads to longer calibration time which could be an issue in terms of stability. The dither length is limited to 0.69 arcsec (corresponding to 1.5 mm) due to space limitation for the X translation stage used to dither the pinholes which is deployed on the telescope focal plane in NFIRAOS. The pinhole interval is fixed at 1 mm (corresponding to $N_{\rm dither} = 38 \times 38$) for fabrication.

With these constraints in mind, we choose ($R_{\rm table}$, $d_{\rm dither}$, $N_{\rm pinhole}$, $N_{\rm dither}$) = (0.53 arcsec, 0.69 arcsec, 38×38, 3×3) which are consistent with the current IRIS design, and result in the best distortion correction error of 2.6 ± 0.5 μarcsec (Figure 11.1). This correction accuracy corresponds to an unprecedented level of 1/1600 pixels. The dither length is equal to the maximum stroke of the X stage in NFIRAOS. A combination of $R_{\rm table}$ and $N_{\rm table}$ provides multiple pinholes in all table resolutions while keeping the condition that dither length exceeds the table resolution. The number of pinhole corresponds to 1 mm pinhole pitch on the telescope focal plane or 0.458 arcsec on the sky. The pinhole interval is fine enough that it can be used as a reference once the pinhole mask is calibrated. It provides enough number of pinholes while still avoiding crosstalk between adjacent pinholes. The number of dithers is kept minimum to save the calibration time. Once the distortion is calibrated in a single configuration (i.e., a combination of filter, rotator angle, ADC angle), subsequent distortion calibration in many other configurations can be simplified by using the reference method with the calibrated pinhole mask as a reference.

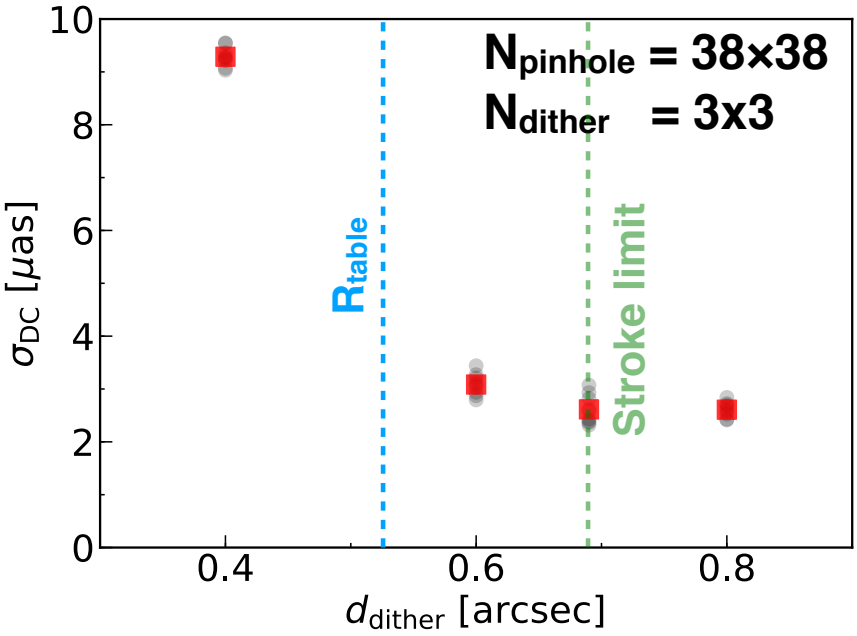

Figure 11.1: Same as Fig. 10.2, but for the best pinhole mask parameters ($d_{\rm dither}$, $N_{\rm pinhole}$, $N_{\rm dither}$) = (0.69 arcsec, 38×38, 3×3). For reference, we plot measurements of $d_{\rm dither} = 0.4, 0.6$, and 0.8.

11.2 Future Prospects

In this section, we describe future prospects of this work toward finalizing the pinhole mask parameters and estimating distortion correction accuracy.

11.2.1 Measurement Errors

We do not apply measurement errors in the simulated pinhole coordinates as this study specifically focuses on distortion correction accuracy which is inherent to the algorithm that we adopted. We will certainly run another set of simulations with the measurement errors added to the pinhole coordinates in the future. However, we do not expect that the measurement error will change the results significantly because the measurement error of less than 5 μarcsec is achievable with S/N $\sim$ 1000 (Lindegren, 1978) by taking exposure time long enough to make high intensity of the pinhole images, and an averaging process within a table resolution helps to further reduce the effect of measurement errors.

11.2.2 Vibration Effects

We have assumed that pinhole image is stable during the dithering for the sake of simplicity. In the real world, however, a vibration of optical elements causes the pinhole images to move around and impacts the position accuracy/precision especially at the level of several 10 nm. There is another effect of vibration which is related to a detector readout scheme. It takes 1.3 sec for HAWAII-4RG detector arrays to read out or scan whole detector pixels. This rolling shutter effect coupled with the vibration causes an apparent distortion. The NFIRAOS and IRIS development teams have been investigating the effects of vibration on the image quality given the input vibration by the observatory environment. While we will incorporate the results into our distortion correction simulation, possible mitigation includes (1) making exposure time long enough to average out the vibration and (2) making exposure time short enough to freeze the vibration.

11.2.3 Platescale Distortions

We also assume that a plate scale is stable during the calibration. The plate scale, in reality, can be changed by the variable temperature inside/outside the instrument enclosure and by real-time feedback from on-instrument wavefront sensors which pick up the different distortion at each dither position. The first order analysis indicates that the plate scale variation due to the temperature drift expected during the calibration is small enough as NFIRAOS and IRIS optics are well temperature-controlled and an entrance pupil to IRIS is far away enough from the input focal plane to IRIS. We turn off the on-instrument wavefront sensors during the calibration not to disturb the plate scale stability. This operation leaves the stability of the deformable mirrors a source of plate scale variation which is expected quite stable. Another possible mitigation when unexpected happens is to rotate the pinhole mask, as Service et al. (2019) recently found that the plate scale variation during the distortion calibration can be compensated by rotating the pinhole masks.

CHAPTER 12
SUMMARY

We aim to address galaxy formation in gaseous LSSs, and conduct the following two studies: Spectroscopic Study and TMT/IRIS Instrumentation. This Chapter summarize our major results in the two studies.

Spectroscopic Study

We have investigated IGM HI gas distributions around $z \sim 2$ galaxies in the three galaxy environments: a blank region (COSMOS), an extreme galaxy overdensity region (BOSS1441), and an extreme quasar overdensity region (EGS). By mainly combining the large survey datasets of HETDEX, MAMMOTH, and SDSS-IV/eBOSS, we make samples of foreground galaxies and quasars at $z \sim 2$. We also make samples of background quasars and galaxies at $z > 2$, and obtain spectra from the eBOSS database and our Keck/LRIS spectroscopy. We reconstruct 3D HI LSSs by performing HI tomography based on HI absorptions found in the spectra of the background galaxies and quasars in the BOSS1441 and EGS regions. For the COSMOS region, we utilize the HI tomography map of Lee et al. (2018). These (COSMOS, BOSS1441, EGS) HI tomography maps have the cosmic volumes of ($30 \times 24 \times 444$, $16 \times 19 \times 131$, $124 \times 136 \times 444$) h^{-3} cMpc^3 with the spatial resolutions of (2.5, 2.6, 20.0) h^{-1} cMpc at $z = 2.3$. We have investigated spherically averaged HI radial profiles of the foreground galaxies in the three HI tomography maps and spatial correlations between the galaxy overdensity and HI overdensity. Our findings are listed below.

1. In the COSMOS region, the spherically averaged HI radial profiles of galaxies decrease (i.e. HI absorption strength increases) with decreasing R_{3D} and the HI overdensity enhances (i.e. HI absorption strength increases) with increasing the galaxy overdensity. These results suggest the spatial correlations between HI gas and galaxies. Note that none of eBOSS quasars are found in the cosmic volume of the COSMOS HI tomography map.

2. In the BOSS1441 region, both the HI radial profiles of galaxies and HI overden-

sity could be reduced to the cosmic mean level in the extreme galaxy overdensity, contrary to the results in the blank region. In the cosmic volume of BOSS1441 HI tomography map, we find three eBOSS quasars whose HI radial profile has a turnover at $R_{3D} \simeq 8\ h^{-1}$ cMpc, and increases (i.e. HI absorption strength decreases) with decreasing R_{3D} within the turnover distance. This suggests that these quasars might have proximity zones where HI gas is photo-ionized and HI absorption is suppressed due to ionizing radiation from the quasars.

3. In the EGS region, the HI radial profiles of quasars and galaxies associated with the extreme quasar overdensity EGS-QO1 significantly increase (i.e. HI absorption strength decreases) with decreasing R_{3D} and the HI overdensity is suppressed (i.e. HI absorption strength decreases) with increasing galaxy overdensity. Our HI tomography map reveals that EGS-QO1 is surrounded by an HI underdensity region, and that EGS-QO1 would reside in the part of the HI underdensity. The possible correspondence between EGS-QO1 and the HI underdensity may imply that group of quasars would form a large ionizing bubble and widely photo-ionize the surrounding HI gas.

4. The HI radial profile of MAMMOTH1-QSO, hosting an ELAN in the BOSS1441 region, has a turnover at $R_{3D} \simeq 8\ h^{-1}$ cMpc and increases (i.e. HI absorption strength decreases) with decreasing R_{3D}, which is comparable to those of the eBOSS quasars in the BOSS1441 region. This indicates that MAMMOTH1-QSO might also have a proximity zone and the ELAN is probably originated from a photo-ionized hydrogen gas cloud embedded in the cosmic web.

Our findings of the COSMOS, BOSS1441, EGS regions might suggest a possible evolutionary picture of photoionization of HI gaseous LSS: HI gaseous LSSs around galaxies $z \sim 2$ could be photo-ionized by quasars as overdensities of galaxies and quasars evolve in the structure formation. To directly test the quasar photoionization of HI gas, we plan TMT/IRIS observations of intergalactic Hα emission around $z \sim 2$ quasars. We thus prepare the TMT/IRIS observations by contributing to the subsequent TMT/IRIS instrumentation.

TMT/IRIS Instrumentation

We plan to calibrate the optical distortion of TMT/IRIS by using a self-calibration technique. We aim to characterize the self-calibration algorithm which we implement to calibrate high spatial frequency distortion and derives the pinhole mask parameters which satisfy the distortion correction requirement. The pinhole coordinate catalogs are generated using the latest NFIRAOS and IRIS optics prescriptions with polishing errors added to the selected mirror surfaces to take into account the high spatial frequency distortion. The catalogs then become an input to the look-up-table based self-calibration algorithm outlined in Chapter 10. The distortion correction accuracy is calculated as a deviation of the output distortion solution from the true distortion solution. The process is repeated with various pinhole mask parameters and the distortion correction accuracy is compared to characterize our self-calibration algorithm. Our findings in characterizing our self-calibration algorithm are listed as follows.

1. The table resolution should to be smaller than the smallest spatial scale of the distortion that you want to calibrate. The smallest distortion scale can be calculated by the analytical model or by raytracing if the polishing error maps are available.

2. The dither length should be longer than the table resolution.

3. The number of pinholes, the number of dithers, and the dither length should be chosen to make sure that there are a sufficient number of data points in all table resolutions. Multiple pinholes in a single table resolution further improve the distortion correction accuracy.

4. A larger number of pinholes, larger number of dithers, and larger dither length generally results in better distortion correction accuracy.

With our findings of parameter setting procedures and some design and performance constraints, including the limited stroke of the XY translation for the pinhole mask, we choose d_{dither}=0.69 arcsec, N_{pinhole}=38 $\times$ 38, N_{dither}=3 $\times$ 3, and R_{table}=0.53 arcsec as suggested parameters for the pinhole mask, its XY stage, and the self-calibration algorithm. The parameter set is consistent with the current IRIS design,

and results in the unprecedented calibration accuracy of ~ 3 μ arcsec which is well below the requirement, Finally, future prospects are given on the measurement errors, vibration, and plate scale stability, toward our goal to complete distortion calibration analysis and to perform our TMT/IRIS observations for testing photoionization of HI gaseous LSS.

APPENDIX A
COSMIC GALAXY-IGM HI RELATION AT $Z \sim 2-3$ PROBED IN THE COSMOS/ULTRAVISTA 1.6 DEG^2 FIELD

A.1 Overview

This appendix is based on Mukae et al. (2017), where we present spatial correlations of galaxies and IGM HI in the COSMOS/UltraVISTA 1.62 deg^2 field. Our data consist of 13,415 photo-z galaxies at $z \sim 2-3$ with $K_s < 23.4$ and the Lyα forest absorption lines in the background quasar spectra selected from SDSS data with no signature of damped Lyα system contamination. We estimate a galaxy overdensity $\delta_{\rm gal}$ in an impact parameter of 2.5 pMpc, and calculate the HI overdensity $\delta_{\langle F \rangle}$ whose negative values correspond to the strong Lyα forest absorption lines. We identify weak evidence of an anti-correlation between $\delta_{\rm gal}$ and $\delta_{\langle F \rangle}$ with a Spearman's rank correlation coefficient of -0.39 suggesting that the galaxy overdensities and the Lyα forest absorption lines positively correlate in space at the $\sim 90\%$ confidence level. This positive correlation indicates that high-z galaxies exist around an excess of HI gas in the Lyα forest. We find four cosmic volumes, dubbed $\rm A_{obs}$, $\rm B_{obs}$, $\rm C_{obs}$, and $\rm D_{obs}$, that have extremely large (small) values of $\delta_{\rm gal} \simeq 0.8$ (-1) and $\delta_{\langle F \rangle} \simeq 0.1$ (-0.4), three out of which, $\rm B_{obs}$–$\rm D_{obs}$, significantly depart from the $\delta_{\rm gal}$-$\delta_{\langle F \rangle}$ correlation, and weaken the correlation signal. We perform cosmological hydrodynamical simulations, and compare with our observational results. Our simulations reproduce the $\delta_{\rm gal}$-$\delta_{\langle F \rangle}$ correlation, agreeing with the observational results. Moreover, our simulations have model counterparts of $\rm A_{obs}$–$\rm D_{obs}$, and suggest that the observations pinpoint, by chance, a galaxy overdensity like a proto-cluster, gas filaments lying on the quasar sightline, a large void, and orthogonal low-density filaments. Our simulations indicate that the significant departures of $\rm B_{obs}$–$\rm D_{obs}$ are produced by the filamentary large-scale structures and the observation sightline effects. We study $\rm A_{obs}$ for more details with the medium high spectral resolution VLT/X-shooter spectrum, and find three absorbers, dubbed Systems 1,2 and 3, with CII, SiIV, CIV and MgII. This is the first

time to identify multiple metal absorbers in a proto-cluster candidate. Our results of photoionization modeling and Lyα + Lyβ fitting suggest that System 2 is a typical Lyman Limit System, and that Systems 1 and 3 have moderately low HI column densities of $\log N_{\rm H_I}$ (cm^{-2}) $\sim 16.0 - 16.5$ with a high metallicity of $Z/Z_\odot \simeq 0.3 - 1.0$ indicative of gas clumps in the CGM and/or the intra-cluster medium of the proto-cluster candidate.

A.2 Motivation

The link between baryons and the cosmic web is a clue to understand both the galaxy formation and the baryonic processes in the large-scale structures (LSSs). The processes between galaxies and the intergalactic medium (IGM) are the inflow which represents gas accretion on to galaxies and the outflow driven by supernovae and active galactic nuclei. Neutral hydrogen HI in the IGM is probed with the Lyα forest absorption lines in spectra of background quasars (e.g., Faucher-Giguère et al., 2008; Becker et al., 2013; Prochaska et al., 2013) and bright star-forming galaxies (e.g., Steidel et al., 2010; Thomas et al., 2014; Mawatari et al., 2016).

The detailed properties of galaxy-IGM HI relations (hereafter galaxy-HI relation) have been studied by spectroscopic observations of the Keck Baryonic Structure Survey (KBSS: Rudie et al., 2012; Rakic et al., 2012; Turner et al., 2014), Very Large Telescope LBG Redshift Survey (VLRS: Crighton et al., 2011; Tummuangpak et al., 2014), and other programs (e.g., Adelberger et al., 2003, 2005). These spectroscopic observations target HI gas of the circumgalactic medium (CGM) around Lyman break galaxies (LBGs) that are high-z star-forming galaxies identified with a bright UV and blue continuum.

These LBG spectroscopy for the galaxy-HI studies alone do not answer to the following two questions. One is the relation between IGM HI and galaxies that are not selected as LBGs. Because LBGs are identified in their dust-poor star-forming phase, dust-rich and old-stellar population galaxies are missing in the past studies. In fact, the average star-formation duty cycle (DC) of LBGs is estimated to be $\sim 30 - 60\%$ (Lee et al., 2009; Harikane et al., 2016). A large fraction of galaxies is not investigated

in the studies of the galaxy-HI relation. The other question is what the galaxy-HI relation in a large-scale is. To date, the previous studies have investigated LBG-HI relations around sightlines of background quasars within ~ 1 deg^2 corresponding to $\sim 70 \times 70$ cMpc^2 at $z \sim 2-3$ (Adelberger et al., 2003; Rudie et al., 2012; Tummuangpak et al., 2014). There has been no study on the galaxy-HI relation in a large-scale (> 1 deg^2) at $z \sim 2-3$. Only at $z \leq 1$, Tejos et al. (2014) conduct spectroscopic surveys to investigate galaxy-HI relations in a large-scale (> 1 deg^2). Tejos et al. (2014) present the clustering analysis of spectroscopic galaxies and HI absorption line systems. At $z \sim 2-3$, Cai et al. (2016) have studied the galaxy-HI relation focusing on extremely massive overdensities with $\sim 6,000$ SDSS quasar spectra by the MAMMOTH survey, but the galaxy-HI relations have not been systematically explored.

We investigate spatial correlations of K_s-band selected galaxies with no DC dependence and IGM HI at $z \sim 2-3$ in a large 1.62 deg^2 area of COSMOS/UltraVISTA field, in conjunction with the comparisons with our models of the cosmological hydrodynamical simulations. We probe one large field contiguously covering LSSs. Our study of the galaxy-HI spatial correlation is complementary to the on-going programs of the MAMMOTH and the Lyα forest tomography survey of the CLAMATO survey (Lee et al., 2014b, 2016) which aims at illustrating the distribution of IGM HI gas in LSSs. In contrast, our study focuses on a spatial relation between galaxies and IGM HI gas.

This appendix is organized as follows. We describe the details of our sample galaxies and background quasars in Section A.3. In Section A.4, our data analysis is presented. We investigate the galaxy-HI relation based on the observational data in Section A.5. We introduce our simulations to examine the galaxy-HI relation of our observational results in Section A.6. In Section A.7, we compare observation and simulation results, and interpret our observational findings. Throughout this appendix, we adopt AB magnitudes (Oke & Gunn, 1983). We use a cosmological parameter set of $(\Omega_m, \Omega_\Lambda, \Omega_b, \sigma_8, n_s, h) = (0.26, 0.74, 0.045, 0.85, 0.95, 0.72)$ consistent with the nine-year $WMAP$ result (Hinshaw et al., 2013).

A.3 Data

A.3.1 Photometric Galaxy Samples

We investigate galaxy overdensities in the COSMOS/UltraVISTA field. Our photometric galaxy sample is taken from the COSMOS/UltraVISTA catalog that is a K_s-band selected galaxy catalog (Muzzin et al., 2013a) made in the 1.62 deg^2 area of UltaVISTA DR1 imaging region (McCracken et al., 2012) in the COSMOS field (Scoville et al., 2007).

The COSMOS/UltraVISTA catalog consists of point-spread function matched photometry of 30 photometric bands. These photometric bands cover the wavelength range of 0.15-24 μm that includes the *GALEX* FUV and NUV (Martin et al., 2005), Subaru/SurimeCam (Taniguchi et al., 2007), CFHT/MegaCam (Capak et al., 2007), UltraVISTA (McCracken et al., 2012), and *Spitzer* IRAC+MIPS data (Sanders et al., 2007). Photometric redshifts for all galaxies are computed with the EAZY code (Brammer et al., 2008). The catalog contains $\sim 150,000$ galaxies at $z \sim 0-5$. Stellar masses are determined by SED fitting by the FAST code (Kriek et al., 2009) with stellar population synthesis models.

We use the criteria of Chiang et al. (2014) to select $z \sim 2-3$ photo-z galaxies from the catalog. We apply a 90% completeness limit of $K_s < 23.4$ mag that corresponds to a stellar mass limit of $\log_{10}(M_*/M_\odot) > 9.7$ at $z \sim 2.5$. Note that this stellar mass limit of $z = 2.5$ differs only by 3% at the edges of our redshift window, $z = 2$ and 3. This stellar mass limit is as large as $\sim 0.1M^*$ at $z \sim 2.5$ where M^* is the characteristic stellar mass of a Schechter function parameter (Schechter, 1976) for the stellar mass functions (SMFs) taken from Muzzin et al. (2013b). We remove objects ($\sim 4\%$) whose photometric redshifts show broad and/or multi-modal redshift probability distributions indicating poorly determined redshifts. Here, the photo-z galaxies that we use have the redshift distribution function whose 80-percentile probability distribution extend no larger than $\Delta z = 0.2$ from the best estimate redshift. Finally, our photometric samples consist of 13,415 photo-z galaxies at $z \sim 2-3$ with $K_s < 23.4$.

A.3.2 Background Quasar Samples

We search for the Lyα forest absorption lines found in background quasar spectra in the COSMOS/UltraVISTA field. Our background quasar spectra are primarily taken from the BOSS Data Release 9 (DR9) Lyman-alpha Forest Catalog (Lee et al., 2013, hereafter L13). L13 has reproduced quasar continua by the technique of mean-flux regulated principal component analysis (MF-PCA) continuum fitting (Lee et al., 2012). Because L13 does not include all quasars identified by the SDSS-III surveys (Eisenstein et al., 2011), our background quasar spectra are also taken from the BOSS Data Release 12 (BOSS DR12) and the SDSS-III Data Release 12 (SDSS DR12) (Alam et al., 2015). The BOSS DR9 and DR12 spectra are covered in the wavelength range of 3600-10400Å. The SDSS DR12 spectra are obtained in the wavelength range of 3800-9200Å that is slightly narrower than the BOSS wavelength range. Both the BOSS and the SDSS spectra have the spectral resolution of $R \equiv \lambda/\Delta\lambda \approx 2000$.

Because L13 compile spectra of quasars with a redshift range of $z_{\rm qso} > 2.15$, we search for background quasars at $z_{\rm qso} > 2.15$ from the BOSS and the SDSS data. We find a total of 26 background quasars in the COSMOS/UltraVISTA field. We remove 4 background quasars that are located at the edge of the COSMOS/UltraVISTA field, because the cylinder volumes of these background quasars are cut by the COSMOS/UltraVISTA-field border by $> 50\%$.

To identify the Lyα forest absorption lines, we adopt the Lyα forest wavelength range of $1041 - 1185$Å in the quasar rest frame. With the speed of light c, this wavelength range is defined as

$$\lambda_{{\rm Ly}\beta}\left(1 + \frac{5000\ {\rm km\,s^{-1}}}{c}\right) < \lambda < \lambda_{{\rm Ly}\alpha}\left(1 - \frac{8000\ {\rm km\,s^{-1}}}{c}\right), \tag{A.1}$$

where $\lambda_{{\rm Ly}\beta}$ and $\lambda_{{\rm Ly}\alpha}$ are the rest-frame wavelengths of the hydrogen Lyβ (1025.72Å) and Lyα (1215.67Å) lines, respectively. Here, we include the velocity offsets of 5000 and 8000 km s^{-1}, avoiding the Lyβ forest contamination and the quasar proximity effect, respectively.

In the observed spectra, the Lyα forest wavelength range shifts by a factor of

$(1+z_{\rm qso})$. We search for background quasars whose Lyα forest wavelength ranges cover Lyα absorption lines. Because we investigate Lyα absorption lines at $2 \leq z_{\rm Ly\alpha} \leq 3$ of the COSMOS/UltraVISTA field, Lyα absorption wavelength range is $3647\text{Å} \leq \lambda_{\rm Ly\alpha}(1 + z_{\rm Ly\alpha}) \leq 4862\text{Å}$ in the observed frame that requires $2.08 \leq z_{\rm qso} \leq 3.67$. Limiting $z_{\rm qso} > 2.15$ given by the L13 spectra, we select 21 background quasars at $2.15 < z_{\rm qso} \leq 3.67$ further removing 1 spectrum at $z_{\rm qso} > 3.67$.

Then, we investigate qualities of background quasar spectra. We define $\rm S/N_{Ly\alpha}$ as the median signal-to-noise ratio (S/N) per pixel over the Lyα forest wavelength range $(1041 - 1185\text{Å})$. Because we find that the absorption signals are not reasonably obtained in 7 background quasar spectra with $\rm S/N_{Ly\alpha} < 2$ by visual inspection, we remove these 7 quasar spectra in our analysis.

We discard 4 broad absorption line (BAL) quasar spectra referring to the SDSS database. In addition, we check background quasar spectra by visual inspection, and remove 1 spectra with large flux fluctuations originated from unknown systematics.

Finally, we use 9 background quasar spectra in the COSMOS/UltraVISTA field. Figure A.1 shows the distribution of the background quasars in the COSMOS/UltraVISTA field. The mean $\rm S/N_{Ly\alpha}$ in our quasar samples is $\rm S/N_{Ly\alpha} \sim 5$.

A.4 Galaxy Overdensity and HI Absorption

A.4.1 Galaxy Overdensity

We estimate galaxy overdensities around the quasar sightlines where the Lyα forest absorption lines are observed. The galaxy overdensities are calculated with the COSMOS/UltraVISTA catalog (§ A.3.1). The galaxy overdensity $\delta_{\rm gal}$ is defined as

$$\delta_{\rm gal} \equiv \frac{n_{\rm gal}(z)}{\overline{n}_{\rm gal}(z)} - 1, \tag{A.2}$$

where $n_{\rm gal}$ ($\overline{n}_{\rm gal}$) is the galaxy (average) number density in a cylinder at the redshift z of the cylinder center. The redshift range of $n_{\rm gal}$ and $\overline{n}_{\rm gal}$ are defined by the redshift range of the cylinder length. The base area of the cylinder is defined by a radius

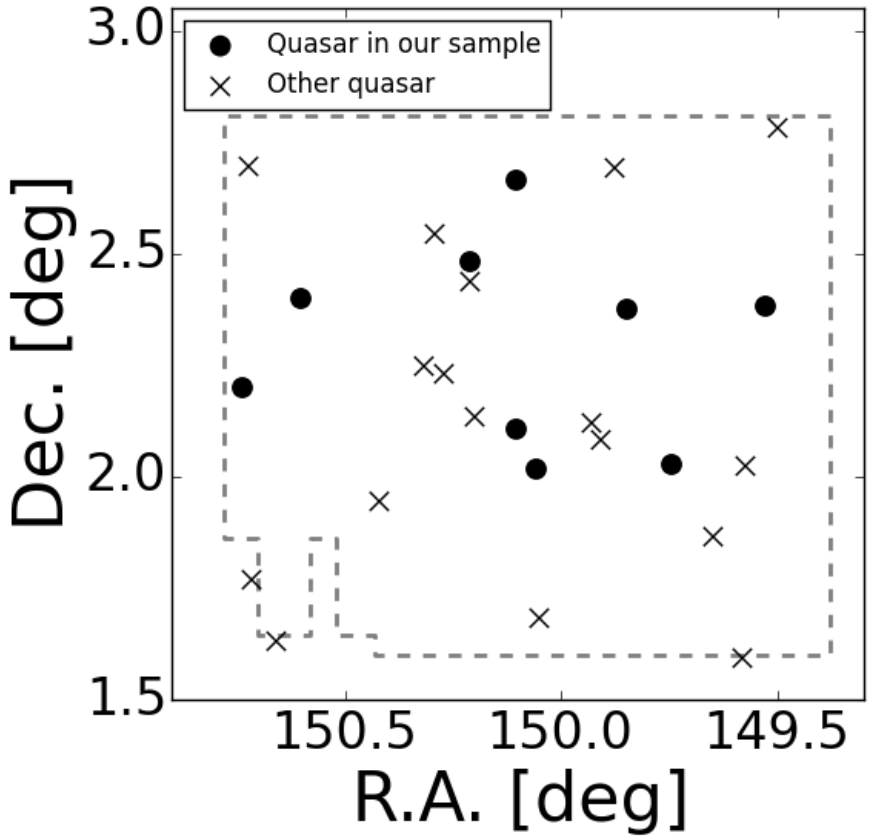

Figure A.1: Sky distribution of the 26 background quasars found in the COSMOS/UltraVISTA field. The circles indicate background quasars at $z_{\rm qso} > 2.15$ analyzed in our study, while the crosses are those removed from our analysis. The gray dashed lines show the coverage of the COSMOS/UltraVISTA.

of $r = 5'$ corresponding to an impact parameter of ~ 2.5 pMpc at $z \sim 2.5$. The length of the cylinder along a line of sight is given by an average photometric redshift uncertainty that corresponds to 25 pMpc. The estimated average photometric redshift uncertainty is $\sigma_z = 0.025(1 + z)$ for galaxies with $K_s < 23.4$ mag at $2 \leq z \leq 3$ (Scoville et al., 2013). The error of $\delta_{\rm gal}$ is estimated with the combination of the photo-z uncertainties and the Poisson errors.

A.4.2 Lyα Forest Absorption Lines

To investigate the Lyα forest absorption lines, we do not use spectra in the wavelength range where damped Lyα systems (DLAs) contaminate the spectra. Here, we search for DLAs in our spectra, performing DLA catalog matching and visual inspection. As explained in § A.3.2, our spectra are taken from the three data sets of L13, BOSS DR12, and SDSS DR12. For the data set of L13, DLAs are already removed based on the DLA catalog of Noterdaeme et al. (2012) who identify DLAs in the BOSS spectra by Voigt profile fitting. For the data set of BOSS DR12, we find no DLAs in the Lyα forest wavelength range in the Noterdaeme et al.'s DLA catalog. For the data set of SDSS DR12, we perform visual inspection, and identify no DLAs.

Quasar host galaxies cause intrinsic strong metal absorption lines of SIV λ1062.7, CIII λ1175.7, NII λ1084.0, and NI λ1134.4 in the Lyα forest wavelength range. We mask out the sufficient wavelength width $\pm$ 5Å around these metal absorption lines.

The study of L13 has reproduced quasar continua by the MF-PCA continuum fitting technique (Lee et al., 2012). The MF-PCA continuum fitting technique is essentially composed of two steps: (i) an initial PCA fit to the redward of the Lyα emission line to reproduce the Lyα forest continuum, and (ii) tuning the Lyα forest continuum amplitude extrapolated to the blueward of the Lyα emission line with the cosmic Lyα forest mean transmission of Faucher-Giguère et al. (2008). We obtain quasar continua of the BOSS DR12 and the SDSS DR12 spectra by the MF-PCA technique with the code used in L13. We include estimated median r.m.s, continuum fitting errors that are (7, 5.5, 4.5, 4%) for spectra with $\mathrm{S/N_{Ly\alpha}} = (2-4,\ 4-6,\ 6-10,\ 10-15)$ at $z \sim\ 2.5-3$ (Lee et al., 2012). We calculate the Lyα forest transmission

$F(z)$ at each pixel:

$$F(z) = f(z)/C(z), \tag{A.3}$$

where $f(z)$ and $C(z)$ are the observed flux and the quasar continuum in the Lyα forest wavelength range, respectively.

We investigate the Lyα forest absorption lines in the cylinders used by the galaxy overdensity calculation (§ A.4.1). We carry out binning for our spectra with the redshift range of $dz = 0.025(1+z)$ that corresponds to the length of the cylinder, and obtain an average Lyα forest transmission $\langle F \rangle_{dz}$ and its error $\langle \sigma_F \rangle_{dz}$. Here, $\langle \sigma_F \rangle_{dz}$ is estimated with pixel noises in the spectra and continuum fitting errors. The absorption of the Lyα forest is defined as $DA \equiv 1 - \langle F \rangle_{dz}$. We refer to the signal-to-noise ratio of the DA detection $\mathrm{S/N}_{\langle F \rangle}$ as $DA/\langle \sigma_F \rangle_{dz}$. We calculate the $\mathrm{S/N}_{\langle F \rangle}$ in the Lyα forest wavelength range, and determine z_h where z_h is the redshift of the highest $\mathrm{S/N}_{\langle F \rangle}$. We put the first cylinder centered at z_h in each spectrum. We place additional cylinders that lie next to each other around the first cylinder.

To obtain statistically reliable results, we make use of the cylinders whose $\mathrm{S/N}_{\langle F \rangle}$ is the highest in each sightline. However, there is a possibility that this procedure for the cylinder placement would bias the results. Here, we change the central redshift of the first cylinder from z_h to the following two redshifts, I) and II). The two redshifts provide cylinders that cover I) the lowest and II) the highest wavelength ranges of the Lyα forest. Taking these different central redshifts of the cylinders, we find that our statistical results of Section A.5 change only by 4-5%.

Each quasar sightline has 2-4 cylinders usable for our analysis. In total, there are 26 cylinders. The number of cylinders is determined by the wavelength range where the following 2 ranges of i) and ii) overlap. The two ranges are i) the Lyα forest wavelength range, $1041(1+z_{\rm q})\text{Å} \leq \lambda \leq 1185(1+z_{\rm q})\text{Å}$ and ii) the $z_{\rm Ly\alpha} = 2-3$ Lyα forest absorption line range, $3647\text{Å} \leq \lambda \leq 4862\text{Å}$, in the observed frame (§ A.3.2). For example, a quasar at $z_{\rm q} = 3.36$ has $4539\text{Å} \leq \lambda \leq 5166\text{Å}$ for i). The wavelength range of the i) and ii) overlap is $4539\text{Å} \leq \lambda \leq 4862\text{Å}$. This wavelength range corresponds to $2.73 \leq z_{\rm Ly\alpha} \leq 3.0$. Because the length of a cylinder is $0.025(1+z) \sim 0.1$ at this

redshift range, we obtain 2 cylinders from this sightline of the $z_{\rm q} = 3.36$ quasar.

We use the data of the cylinders with $\mathrm{S/N}_{\langle F\rangle} \geq 4$, and estimate both $\delta_{\rm gal}$ and $\langle F\rangle_{dz}$ in the cylinders. Here we test whether this cut of $\mathrm{S/N}_{\langle F\rangle} \geq 4$ gives impacts on our results. We change the $\mathrm{S/N}_{\langle F\rangle}$ cut from 4 to 3 and 5, and carry out the same analysis to evaluate how much different results can be obtained by the different S/N cuts. We find that results of $\mathrm{S/N}_{\langle F\rangle} \geq 3$ and ≥ 5 cuts are very similar to those of $\mathrm{S/N}_{\langle F\rangle} \geq 4$. Thus, the different S/N cut within this range has a minimal impact on our results. Note that the $\mathrm{S/N}_{\langle F\rangle}$ cut below 3 raises the noise level and that the correlation signals are diminished. Moreover, the $\mathrm{S/N}_{\langle F\rangle}$ cut beyond 5 gives number of spectra too small to investigate the correlations.

By these definitions and selections of the cylinders, we have a total of 16 cylinders for the $\delta_{\rm gal}$ - $\langle F\rangle_{dz}$ measurements. In each cylinder, we calculate the HI overdensity whose negative values correspond to a strong Lyα absorption:

$$\delta_{\langle F\rangle} \equiv \frac{\langle F\rangle_{dz}}{F_{\rm cos}(z)} - 1, \tag{A.4}$$

where $F_{\rm cos}(z)$ is the cosmic Lyα forest mean transmission. We adopt $F_{\rm cos}(z)$ estimated by Faucher-Giguère et al. (2008),

$$F_{\rm cos}(z) = \exp[-0.001845(1+z)^{3.924}]. \tag{A.5}$$

The error of $\delta_{\langle F\rangle}$ is estimated with the Lyα forest transmission errors $\langle\sigma_F\rangle_{dz}$.

A.5 Galaxy-IGM HI Correlation

Figure *A*.2 presents $\delta_{\rm gal}$ and $\delta_{\langle F\rangle}$ values in the cylinders. We calculate a Spearman's rank correlation coefficient $\rho_{\rm obs}$ of a nonparametric measure to investigate the existence of a correlation between $\delta_{\rm gal}$ and $\delta_{\langle F\rangle}$. We obtain $\rho_{\rm obs} = -0.39$ that corresponds to the $\sim$ 90% confidence level [1] (Wall & Jenkins, 2012). We estimate the errors of $\rho_{\rm obs}$ by the perturbation method (Curran, 2015). We generate 1000 data sets of

[1] We find $\rho_{\rm obs} = -0.57$ that corresponds to the $\sim$ 96% confidence level, if we remove outliers (§ A.7.2).

16 cylinders whose data values include random perturbations following the gaussian distribution whose sigma is defined by the observational errors of the 16 cylinders. We obtain 1000 Spearman's ρ values for the 1000 data sets. We define the error of $\rho_{\rm obs}$ as the range of 68 percentile distribution for the 1000 Spearman's ρ values. The estimated error of $\rho_{\rm obs}$ is 0.2 at the 1σ level. The 1σ-error range of $\rho_{\rm obs}$ is thus $\rho_{\rm obs} = -0.6 - (-0.2)$. This range of $\rho_{\rm obs}$ corresponds to the confidence level range of $\sim 80 - 100\%$. In other words, the $\rho_{\rm obs}$ error changes the results of the $\sim 90\%$ confidence level only by $\pm \sim 10\%$.

We then apply chi-square fitting to the relation of $\delta_{\rm gal}$-$\delta_{\langle F\rangle}$, and obtain the best-fit linear model,

$$\delta_{\langle F\rangle} = -0.17^{+0.06}_{-0.06} - 0.14^{+0.06}_{-0.16} \times \delta_{\rm gal} \tag{A.6}$$

that is shown with the solid line in Figure $A.2$. Figure $A.2$ and Equation $(A.6)$ suggest weak evidence of an anti-correlation between $\delta_{\rm gal}$ and $\delta_{\langle F\rangle}$. The suggestive anti-correlation between $\delta_{\rm gal}$ and $\delta_{\langle F\rangle}$ indicates that high-z galaxies exist around an excess of HI gas in the Lyα forest.

There is a possibility that the spatial correlation in the same sightlines would bias the results. To evaluate this possible bias, we choose one cylinder for each sightline that does not have any spatial correlations with the other cylinders, and conduct the same analysis. We find an anti-correlation at the $\sim 80\%$ confidence level that falls in the 1σ error range of the results with all of the cylinders. We thus conclude that the results do not change by the bias of the correlation that is not as large as the one of statistical uncertainties.

Strong Lyα absorption lines can be made by the CGM of galaxies that lie near the quasar sightlines. Rudie et al. (2012) have studied velocities and spatial locations of HI gas surrounding star-forming galaxies at $z \sim 2-3$, and found that the HI column density rapidly increases with decreasing an impact parameter within 200 pkpc. We investigate the Lyα absorption lines associated with the CGM. In each cylinder used in § A.4.2, we calculate revised $\delta_{\rm gal}$ values whose galaxy numbers are estimated in hollow cylinders whose inner radius is $0.'4$ corresponding to an impact parameter of

200 pkpc. We find that there are only $0-1$ galaxies in a $0.'4$ radius cylinder. The white circles in Figure $A.3$ represent the hollow cylinder results that are very similar to the black circles in Figure $A.2$. Figure $A.3$ indicates no significant differences in the $\delta_{\rm gal}$-$\delta_{\langle F\rangle}$ distributions and the $\rho_{\rm obs}$ value, and suggests that the CGM of galaxies is not the major source of the small $\delta_{\langle F\rangle}$ values.

A.6 Simulations

We perform cosmological hydrodynamical simulations with the RAMSES code (Teyssier, 2002) to investigate the spatial correlations of galaxies and IGM HI of our observational results (Section A.5). The initial conditions are generated with the COSMIC package (Bertschinger, 1995), and are evolved using Zel'dovich approximation. We include both dark matter and baryon using N-body plus Eulerian hydrodynamics on a uniform grid. The simulations are performed in a box size of $80h^{-1}$ cMpc length with 512^3 cells and a spatial resolution of $156h^{-1}$ ckpc. We use 512^3 dark matter particles with a mass resolution of $3.16\times10^8 M_\odot$. The mean gas mass per cell is $5.4\times10^7 M_\odot$.

We include the ultraviolet background model of Haardt & Madau (1996) at the reionization redshift $z_{\rm reion}=8.5$. We investigate the gas temperature value at the mean gas density in the simulations, and find $T=1.4\times10^4$K that is consistent with observational measurements at $z\sim2-3$ (Becker et al., 2011). We assume the photoionization equilibrium. We apply the optically thin limit, and do not produce any DLAs. Note that our simulations do not include feedback effects on the Lyα forest. Because the feedback mostly affects high-density absorbers with $N_{\rm HI}>10^{16}$ cm^{-2} (Theuns et al., 2001), the lack of the feedback effects does not significantly change the large-scale correlation of galaxy overdensities and Lyα forest absorption lines.

Dark matter haloes in the simulations are identified by the HOP algorithm (Eisenstein & Hut, 1998). We use dark matter haloes containing more than 1000 dark matter particles. We have compared the halo mass functions at $z\sim2.5$ in our simulations with the halo mass function of the high-resolution N-body simulations (Reed et al.,

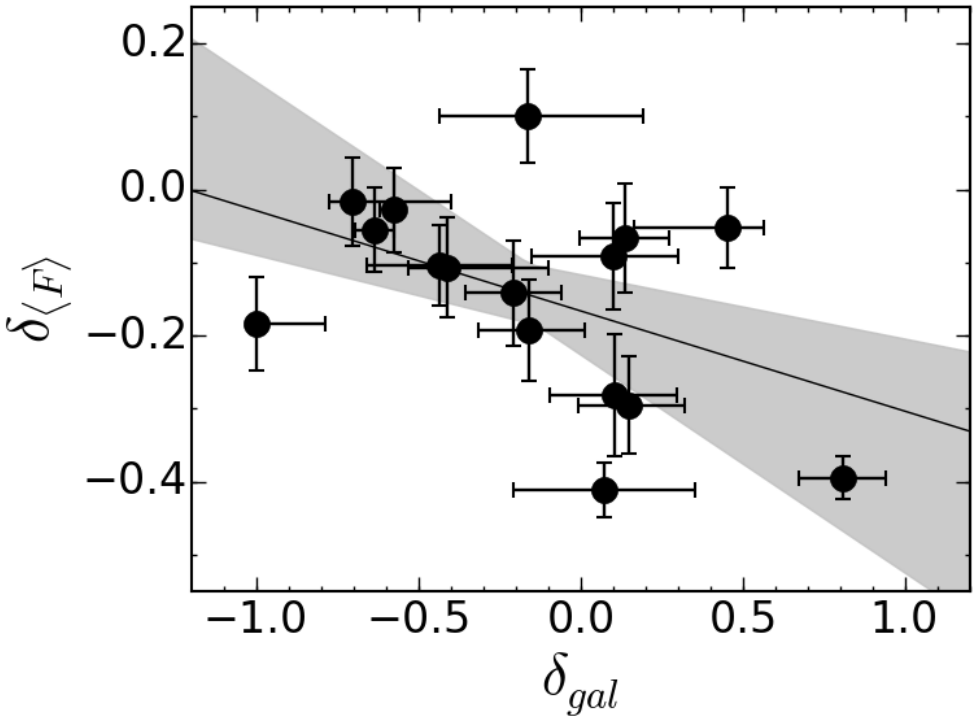

Figure A.2: HI overdensity $\delta_{\langle F \rangle}$ as a function of the galaxy overdensity $\delta_{\rm gal}$. The circles with the error bars represent the galaxy-HI properties of the cylinders. The best-fit linear model of Equation $A.6$ is represented by a solid line, with the shaded region indicating the 1σ uncertainty range that is calculated by the perturbation method.

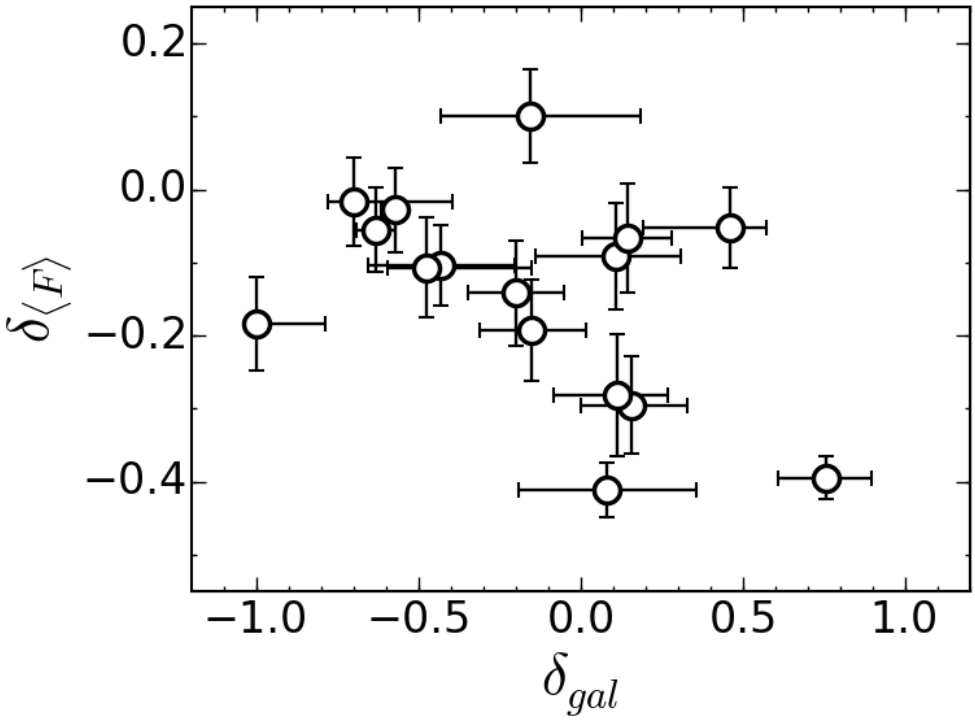

Figure A.3: Same as Figure A.2, but for revised $\delta_{\rm gal}$ values with hollow cylinders. The galaxy numbers of the revised $\delta_{\rm gal}$ are estimated in hollow cylinders whose inner and outer radii are $0.'4$ and $5'$, which corresponds to 200 pkpc and 2.5 pMpc at $z \sim 2.5$, respectively.

2007), and found a good agreement within $\sim 30\%$ in abundance. Our simulations resolve dark matter haloes with a mass of $\log_{10} M_h/M_\odot > 11$.

A.6.1 Mock Galaxy Catalog

We create mock galaxy catalogs from the simulations using the abundance matching technique (e.g., Peacock & Smith, 2000; Vale & Ostriker, 2004; Moster et al., 2010; Behroozi et al., 2013) that explains observational results of stellar mass functions. We make simulated galaxies, populating each halo with one galaxy. We assume the stellar-to-halo mass ratio (SHMR) with a functional form

$$M_*/M_h = f_0 \frac{(M_h/M_1)^\alpha}{1 + (M_h/M_1)^{\alpha-\beta}}, \tag{A.7}$$

where f_0, M_1, α, and β are free parameters. We produce SMFs at $z \sim 2.5$ with many sets of these parameters. We compare these SMFs with observed SMFs (Muzzin et al., 2013b; Tomczak et al., 2014), and find the best-fit parameter set reproducing the observed SMFs. The best-fit parameter set is $(M_1, \alpha, \beta, f_0) = (1.2{\times}10^{12} M_\odot, 1.0, -0.3, 0.04)$. The SHMR with these best-fit parameters is consistent with the one estimated by Behroozi et al. (2013) within the 1σ error levels. We use the simulated galaxies whose stellar mass is $\log_{10}(M_*/M_\odot) > 9.7$ that is the same stellar mass limit in the COSMOS/UltraVISTA catalog (§A.3.1). The stellar mass limit corresponds to the minimum halo mass of $M_h > 4.4 \times 10^{11} M_\odot$. The simulated galaxies consist of 2221 galaxies at $z = 2.4 - 2.5$ that agree with the number of galaxies at $z = 2.4 - 2.5$ in our COSMOS/UltraVISTA photometric samples.

A.6.2 Lyα Forest Catalog

In the simulation boxes, we make mock spectra along the random sightlines parallel to a principal axis defined as the redshift direction. The Lyα transmitted flux is computed with the fluctuating Gunn-Peterson approximation (FGPA; e.g., Weinberg et al., 1998, 2003; Meiksin, 2009; Becker et al., 2015), because the FGPA method is simple and fast in computing. We ignore the gas velocities and the effect of redshift-

space distortion on the Lyα forest, testing whether this method gives reliable results. The FGPA is a good approximation for absorbers with densities around and below the cosmic mean (Rakic et al., 2012).

We choose two typical sightlines, and conduct full optical depth calculations with gas velocities and redshift-space distortions (e.g., Meiksin et al., 2015; Lukić et al., 2015). We then compare the results of these two sightlines with those given by our original method. We find that the difference is only $< 6\%$ that is not as large as the one of statistical uncertainties.

The FGPA gives the Lyα optical depth as

$$\tau = \frac{c\sigma_\alpha \bar{n}_{\rm H}(z)}{\nu_\alpha H(z)} x_{\rm HI} \Delta_b \propto \Delta_b^{2-0.72(\gamma-1)}, \tag{A.8}$$

where σ_α is the Lyα cross section, $\bar{n}_{\rm H}(z)$ is the cosmic mean density of hydrogen atoms at redshift z, ν_α is the Lyα resonance frequency, $H(z)$ denotes the Hubble constant at redshift z, $x_{\rm HI}$ is the fraction of neutral hydrogen, Δ_b is the baryonic density in units of the mean density, and γ is the power-law slope of the temperature-density relation in the IGM (Hui & Gnedin, 1997). The γ value is set as $\gamma = 1.5$ that is consistent with observations of the Lyα forest transmissions (Becker et al., 2011; Boera et al., 2014). We investigate the fidelity of our simulated Lyα forest model. We compare the 1D power spectrum of the transmitted flux in our simulations with the SDSS and the BOSS measurements (McDonald et al., 2006; Palanque-Delabrouille et al., 2013), and we find a good agreement. We scale the mean Lyα transmitted flux to the cosmic Lyα forest mean transmission of Faucher-Giguère et al. (2008) (Equation (A.5)). This scaling method is widely used in the literature (e.g., White et al., 2010; Lukić et al., 2015). We rebin the simulated spectra, and produce the SDSS and the BOSS pixel width of 69km s^{-1}. We add Gaussian noises to the simulated spectra, accomplishing the S/N$_{\rm Ly\alpha} \sim 5$ that corresponds to the typical S/N$_{\rm Ly\alpha}$ in our quasar samples (§A.3.2).

A.6.3 Simulated Galaxy-IGM HI Correlation

In Figure *A*.4, the red dots represent a cylinder of $\delta_{\rm gal}$ and $\delta_{\langle F\rangle}$ in our simulations. We make 1000 sets of the 16 cylinders selected from the simulations, mocking our observed 16 cylinders. The red circles in Figure A.4 denote one example set of the 16 mock cylinders. We fit a linear model to each of these 1000 sets of the 16 mock cylinders, and obtain Spearman's rank correlation coefficient $\rho_{\rm sim}$ values for the 1000 sets. We find that a 1 σ distribution of $\rho_{\rm sim}$ corresponds to the range of $-0.35-(-0.60)$ that indicates the existence of the anti-correlation between $\delta_{\rm gal}$ and $\delta_{\langle F\rangle}$in the simulations. This $\rho_{\rm sim}$ distribution corresponds to the $\sim 90\% \pm 10\%$ confidence level that is the same as our conclusions for the observational data (Section A.5).

We perform simulations that have a box size of 80 h^{-1} cMpc length with 256^3 cells. In the same manner as our simulations with 512^3 cells (§ A.6.3), we calculate a Spearman's rank correlation coefficient of the 256^3-cell simulations ρ_{256}, using 16 cylinders that are randomly chosen from the 256^3-cell simulation results. We obtain $\rho_{256} \sim -0.4$ that corresponds to the $\sim 90\%$ confidence level. We find that results are very similar to those of our simulations with 512^3 cells.

We test whether the noise distribution makes significant changes from our conclusions. We use the $\rm S/N_{Ly\alpha}$ probability distribution same as the one of our observational spectra of the 16 cylinders. We add noise to our 16 simulation spectra, following the $\rm S/N_{Ly\alpha}$ probability distribution. We calculate Spearman's rank correlation coefficient $\rho_{\rm sim}$ values for 16 simulation spectra with the noise. Conducting this test for ~ 10 times, we find that the $\rho_{\rm sim}$ values are not different from our original result beyond the statistical errors.

We estimate how the correlation changes when the full redshift range of the observations is considered. From $z = 2.5$ (3) to $z = 2$ (2.5), the structure growth increases only by $\sim 14\%$. The galaxy clustering and Lyα forest clustering are expected to grow accordingly by $\sim 10\%$. In Figure *A*.4, this redshift evolution shifts $\delta_{\rm gal}$ ($\delta_{\langle F\rangle}$) values of the simulation data points rightward (downward) only by $\sim 10\%$ that is not as large as the one of the statistical uncertainties.

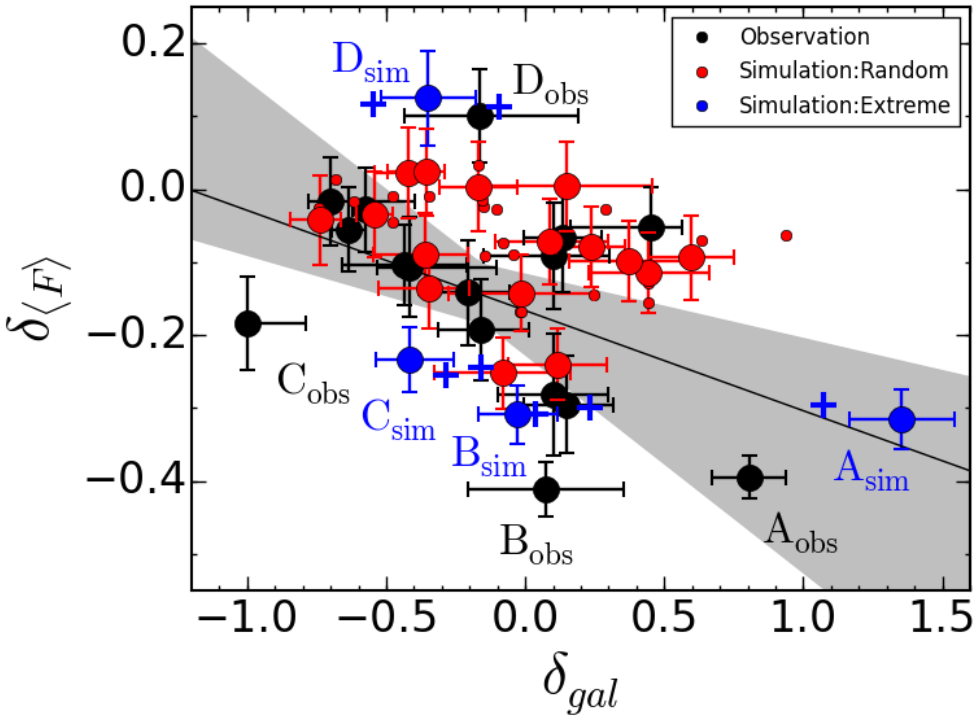

Figure A.4: Same as Figure A.2, but we overplot our simulation results. The black circles represent the observation data. The red dots are the simulation results. The red circles show an example of 16 cylinders that are randomly chosen from our simulation results (red dots). The blue circles present the simulated results for the four cylinders that have extreme values of $\delta_{\rm gal}$ and/or $\delta_{\langle F \rangle}$ similar to $\rm A_{obs}$-$\rm D_{obs}$ (§ A.7.2). The blue crosses are other counterparts found in our simulations.

A.7 Discussions

A.7.1 Comparison between the Observation and the Simulation Results

Sections A.5 and A.6.3 present the observation and the simulation results. Both observation and simulation results indicate weak evidence of the anti-correlation between $\delta_{\rm gal}$ and $\delta_{\langle F\rangle}$ (Figure A.4). Moreover, the Spearman's rank correlation coefficient $\rho_{\rm obs} = -0.39$ from the observations (Section A.5) falls in the $\rho_{\rm sim}$ range of $-0.35 - (-0.60)$, indicating that simulations well reproduce observational results.

A.7.2 Four Cylinders with an Extreme Value

In Figure *A*.4, we find four cylinders with the labels of $\rm A_{obs}$, $\rm B_{obs}$, $\rm C_{obs}$, and $\rm D_{obs}$ that have the largest (smallest) values of $\delta_{\rm gal}$ or $\delta_{\langle F\rangle}$ among the observational data points. Note that, in Figure *A*.4, $\rm A_{obs}$ falls on the best-fit linear model within the errors, and that the other three cylinders, $\rm B_{obs}$, $\rm C_{obs}$, and $\rm D_{obs}$, show significant departures from the best-fit linear model by $0.1 - 0.2$ in $\delta_{\langle F\rangle}$ at the $2 - 3\sigma$ significance levels. These three cylinders weaken the anti-correlation signal found in Section A.5. If we exclude these three cylinders, we obtain $\rho_{\rm obs} = -0.57$ that corresponds to the $\sim 96\%$ confidence level. [2]

We present background quasar spectra of the four cylinders in Figure *A*.5. The full width of the abscissa axis in the four panels of Figure *A*.5 corresponds to the full redshift range of the cylinder. The black points in Figure *A*.5 present the positions of galaxies with the best estimate of photometric redshifts and the impact parameter b in reference to quasar sightlines. We note that the photometric redshift uncertainty is comparable to the full redshift range of the cylinder.

We investigate the physical origin of the extreme $\delta_{\rm gal}$ and/or $\delta_{\langle F\rangle}$ values in the four cylinders from our observations. We use the simulations performed in Section 5, and search for cylinders in the simulations whose $\delta_{\rm gal}$-$\delta_{\langle F\rangle}$ values are similar to the

[2] In our simulations, there exist sets of cylinders that show significant ($> 95\%$) confidence levels after we remove extreme cylinders, which agrees with our observational results.

four cylinders from our observations. With the simulation data, we create the sky map (Figure *A*.6), and identify four mock cylinders that show $\delta_{\rm gal}$-$\delta_{\langle F\rangle}$ values most similar to $\rm A_{obs}$-$\rm D_{obs}$. We refer to these mock cylinders as the $\rm A_{sim}$, $\rm B_{sim}$, $\rm C_{sim}$, and $\rm D_{sim}$. The Maps of $\delta_{\langle F\rangle}$ around the sightlines of $\rm A_{sim}$-$\rm D_{sim}$ are shown in Figures *A*.7 and *A*.8, respectively. In Figure *A*.4, we overplot the $\delta_{\rm gal}$-$\delta_{\langle F\rangle}$ values of $\rm A_{sim}$-$\rm D_{sim}$. Below, we describe properties and comparisons of $\rm A_{obs}$-$\rm D_{obs}$ and $\rm A_{sim}$-$\rm D_{sim}$.

Cylinder A: $\rm A_{obs}$ has the largest $\delta_{\rm gal}$ and one of the smallest $\delta_{\langle F\rangle}$ values. The top panel of Figure *A*.5 indicates that $\rm A_{obs}$ has the largest number of galaxies and one of the strongest Lyα forest absorption lines among the four cylinders of $\rm A_{obs}$-$\rm D_{obs}$. The large $\delta_{\rm gal}$ and the small $\delta_{\langle F\rangle}$ values of $\rm A_{obs}$ suggest that a large galaxy overdensity is associated with the large amount of HI gas (Cucciati et al., 2014; Chiang et al., 2015; Cai et al., 2016; Lee et al., 2016). Our simulation results in Figure *A*.7 present that the sightline of $\rm A_{sim}$ penetrates gas filaments of LSSs and a galaxy overdensity like a proto-cluster at $z \sim 2.46$ (label 'a'). Moreover, the top panel of Figure *A*.8 indicates that $\rm A_{sim}$ would include a Coherently Strong Lyα Absorption system (CoSLA) that traces massive overdensities on the scale of $\sim 15h^{-1}$cMpc (Cai et al., 2016).

Because there exists the high-quality spectra of $\rm A_{obs}$ taken with VLT/X-shooter (Vernet et al., 2011). we show the characteristic of the $\rm A_{obs}$ sightline based on the X-shooter spectrum in Appendix A.7.4.

Cylinder B: $\rm B_{obs}$ has the moderate $\delta_{\rm gal}$ and the smallest $\delta_{\langle F\rangle}$ values. The second top panel of Figure *A*.5 shows that $\rm B_{obs}$ has the strong Lyα forest absorption lines over the entire redshift range of the cylinder. In our simulations, Figure *A*.7 presents that the sightline of $\rm B_{sim}$ goes through gas filaments at $z \sim 2.43$ (label 'b'). Our simulations indicate that the sightline of $\rm B_{obs}$ would penetrate gas filaments with the moderate number of galaxies.

Cylinder C: $\rm C_{obs}$ has the smallest $\delta_{\rm gal}$. Note that $\rm C_{obs}$ has $\delta_{\rm gal} = -1$ corresponding to no galaxy in the cylinder. The second bottom panel of Figure *A*.5 indicates that $\rm C_{obs}$ does not have galaxies but the moderately strong Lyα forest absorption lines. In our simulations, we identify $\rm C_{sim}$ that has $\delta_{\rm gal}$-$\delta_{\langle F\rangle}$ values most similar to those of $\rm C_{obs}$. Our simulation results in Figure *A*.7 show that the sightline of $\rm C_{sim}$ penetrates a large void of LSSs at $z \sim 2.43$ (label 'c1') and goes across gas filaments at $z \sim 2.45$

(label 'c2'). Our simulations suggest that C_{obs} would penetrate a large void, and go across gas filaments. Note that C_{sim} has $\delta_{gal} \sim -0.5$ that is larger than the δ_{gal} value of C_{obs}. Our simulations find no cylinders with $\delta_{gal} = -1$ and $\delta_{\langle F \rangle} \sim -0.2$ that C_{obs} has. This is the difference between C_{obs} and C_{sim}. This difference is probably made, because (1) photometric redshifts of galaxies in C_{obs} have catastrophically large errors, (2) there exist faint galaxies whose luminosities are just below the observational limit of $K_s = 23.4$ mag, or (3) a void of galaxies similar to C_{obs} is missing in the limited box size of the simulations.

Cylinder D: The cylinder with the largest $\delta_{\langle F \rangle}$ is D_{obs}. The bottom panel of Figure *A*.5 presents that D_{obs} has the moderately weak Lyα forest absorption lines. In our simulations, Figure *A*.7 shows that the sightline of D_{sim} crosses the low-density filaments. Our simulation results suggest that D_{obs} would go through the orthogonal low-density filaments.

With the results of Figures A.5 and A.8, we count the numbers of galaxies with photo-z errors in each cylinder. We find (29, 6, 7) galaxies in (A_{obs}, B_{obs}, D_{obs}), while there are (32, 15, 10) galaxies in (A_{sim}, B_{sim}, D_{sim}). These numbers agree within the $\sim 1 - 2\sigma$ levels. However, the number of galaxies in C_{obs} is 0 that is significantly smaller than the one of C_{sim} (see above for the difference of C_{obs} and C_{sim}).

In addition to A_{sim}- D_{sim}, there exist counterparts of A_{obs}-D_{obs} in our simulations. We find additional two counterparts for each extreme cylinder, B_{obs}, C_{obs}, or D_{obs}, in different volumes of the simulations, which are referred to as ($B1_{sim}$, $B2_{sim}$), ($C1_{sim}$, $C2_{sim}$), or ($D1_{sim}$, $D2_{sim}$). Moreover, we identify one additional counterpart of A_{obs}, $A1_{sim}$. We cannot find another counterpart of A_{obs}, because the large δ_{gal} and $\delta_{\langle F \rangle}$ values of A_{obs} are very rare in the simulation box. Figure *A*.4 presents the δ_{gal} and $\delta_{\langle F \rangle}$ values of these additional counterparts with the blue crosses. These δ_{gal}-$\delta_{\langle F \rangle}$ values are comparable with those of A_{sim}- D_{sim} at the $\sim 1\sigma$ error levels. Figure A.9 shows that these sightlines penetrate large overdensities, gas filaments parallel with (orthogonal to) the sightline, or large voids.

We investigate properties of other sightlines that do not have extreme values of δ_{gal} and $\delta_{\langle F \rangle}$. We find that these sightlines penetrate neither dense structures, filaments in parallel, nor large voids.

A.7.3 Summary of the Simulation Comparisons

In § A.7.2, we discuss the physical origins of four cylinders (A_{obs}, B_{obs}, C_{obs}, D_{obs}) that have extremely large (small) values of δ_{gal} and $\delta_{\langle F\rangle}$. We use the simulations performed in Section A.6, and identify four cylinders (A_{sim}, B_{sim}, C_{sim}, D_{sim}) whose δ_{gal}-$\delta_{\langle F\rangle}$ values are close to (A_{obs}, B_{obs}, C_{obs}, D_{obs}). The comparisons between A_{obs}-D_{obs} and A_{sim}-D_{sim} suggest that sightlines in the observation would penetrate (1) a galaxy overdensity like a proto-cluster in A_{obs}, (2) gas filaments in B_{obs}, (3) a large void in C_{obs}, and (4) orthogonal low-density filaments in D_{obs}. In this way, our simulations provide the possible physical pictures of these four cylinders based on the structure formation models.

The similarity between our observation and simulation results (Figure A.4) supports the standard picture of galaxy formation scenario in the filamentary LSSs (Mo et al., 2010) on which our simulations are based.

As noted in Section A.7.2, the three cylinders, B_{obs}, C_{obs}, and D_{obs} depart from the anti-correlation of δ_{gal} and $\delta_{\langle F\rangle}$ in Figure *A*.4. Because the simulation counterparts of these three cylinders penetrate gas filaments, a large void, and orthogonal low-density filaments by chance, the comparisons with our simulations suggest that the significant departures from the anti-correlation are produced by the filamentary LSSs and the observation sightlines. These chance alignment effects reduce the anti-correlation signal.

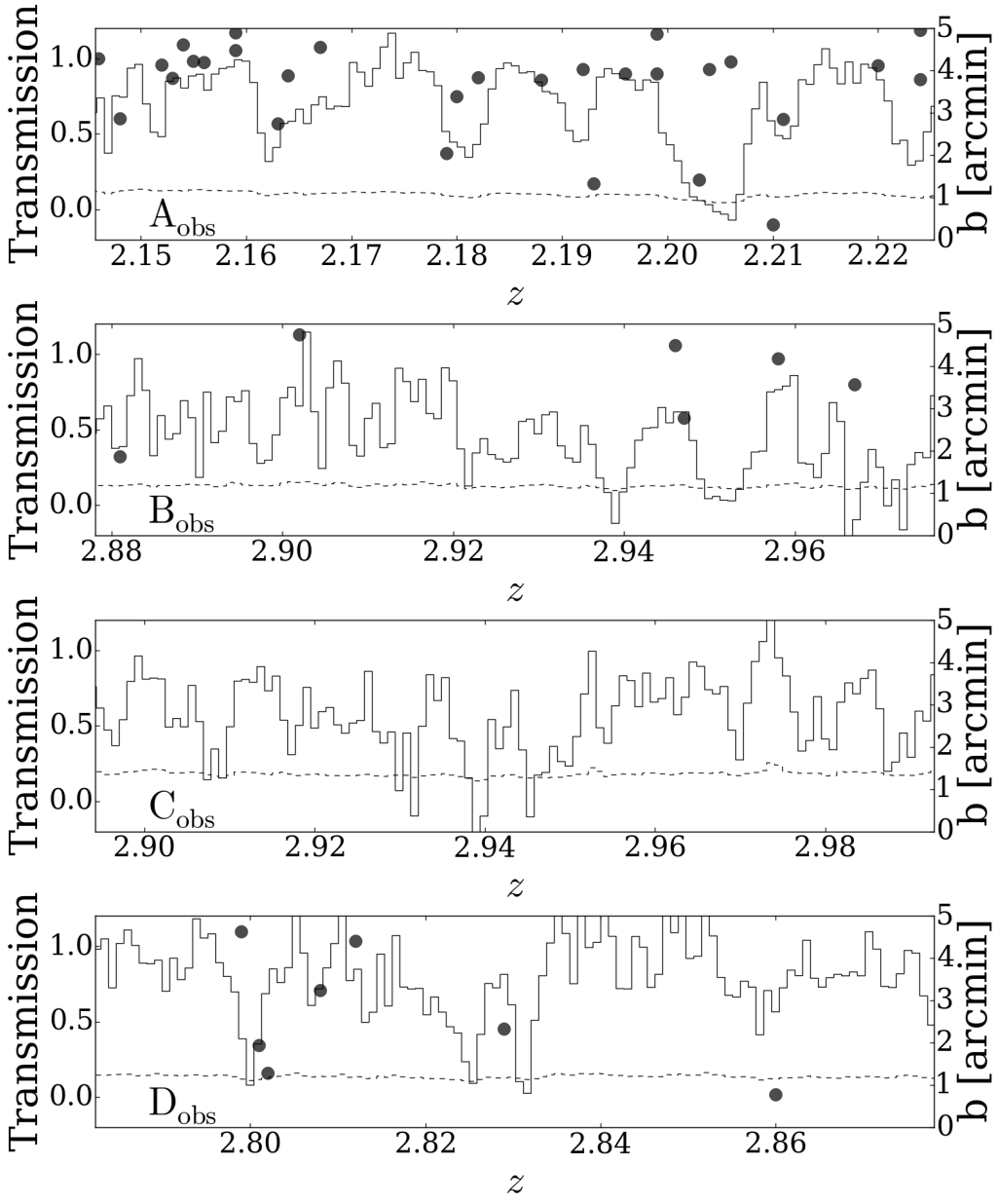

Figure A.5: Observed background quasar spectra of the four cylinders that have extreme values of $\delta_{\rm gal}$ and/or $\delta_{\langle F \rangle}$ (§ A.7.2). The solid lines depict transmission per pixel as a function of redshift for the Lyα forest absorption lines (left-hand axis). The dashed lines represent the noise per pixel. The black points denote redshifts and impact parameters (right-hand axis) of our photo-z galaxies in the cylinders. Note that the photometric redshift uncertainty is comparable to the full redshift range of the cylinder.

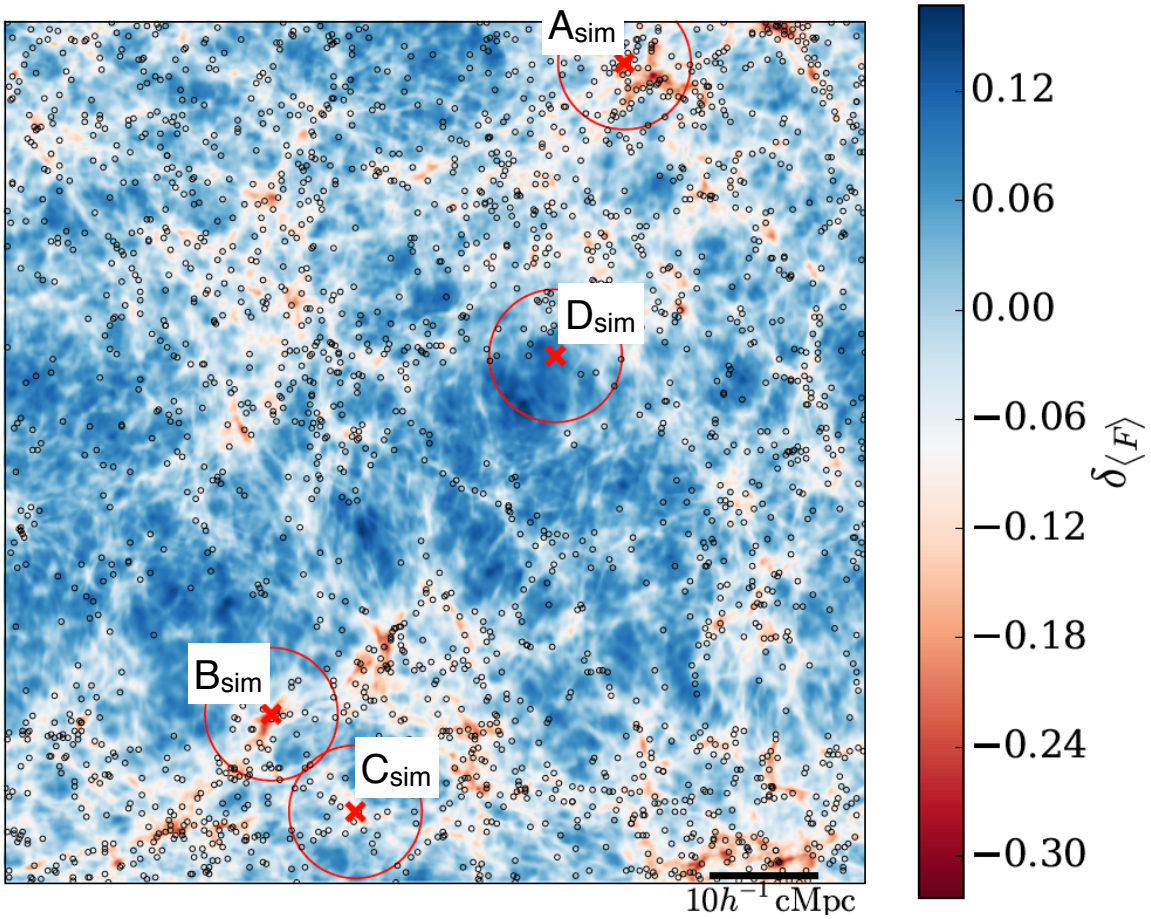

Figure A.6: Projected sky map of the distribution of the mock galaxies and the Lyα forest absorption lines. The black circles represent mock galaxies whose stellar masses fall in $\log_{10} M_*/M_\odot > 9.7$. Note that the background color scale represents $\delta_{\langle F\rangle}$ defined in the full redshift range. The positions of sightlines are indicated by the red crosses enclosed by the red circles corresponding to the circumference of cylinders. In the simulations, $10h^{-1}$cMpc corresponds to $8.'5$ at $z \sim 2.5$.

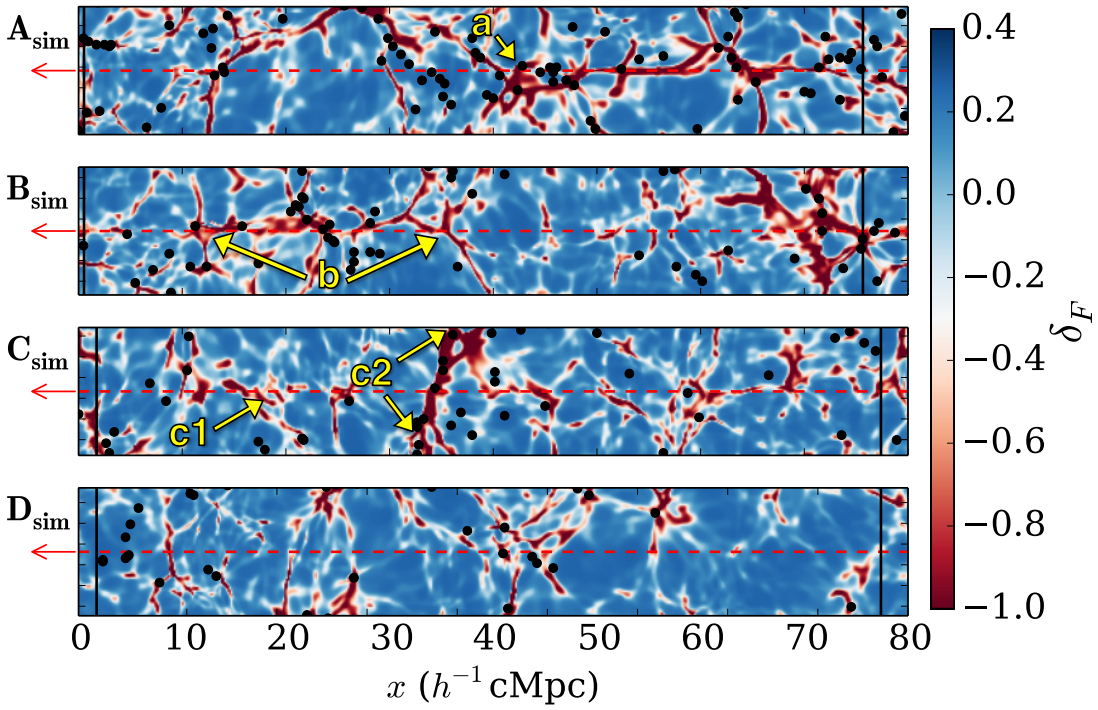

Figure A.7: Maps of $\delta_{\langle F \rangle}$ around the sightlines of A_{sim}, B_{sim}, C_{sim}, and D_{sim} (§ A.7.2). The black points are projected positions of the mock galaxies in the cylinders. The background color scale represents a $\delta_{\langle F \rangle}$ value per pixel. The black vertical lines represent the lower and upper edges of each cylinder. The red dashed lines represent the sightlines of A_{sim}, B_{sim}, C_{sim}, and D_{sim}. The arrows indicate a galaxy overdensity in A_{sim}(label 'a'), two edges of gas filaments in B_{sim} and C_{sim} (labels 'b' and 'c2'), and a galaxy void with gas filaments in C_{sim}(label 'c1').

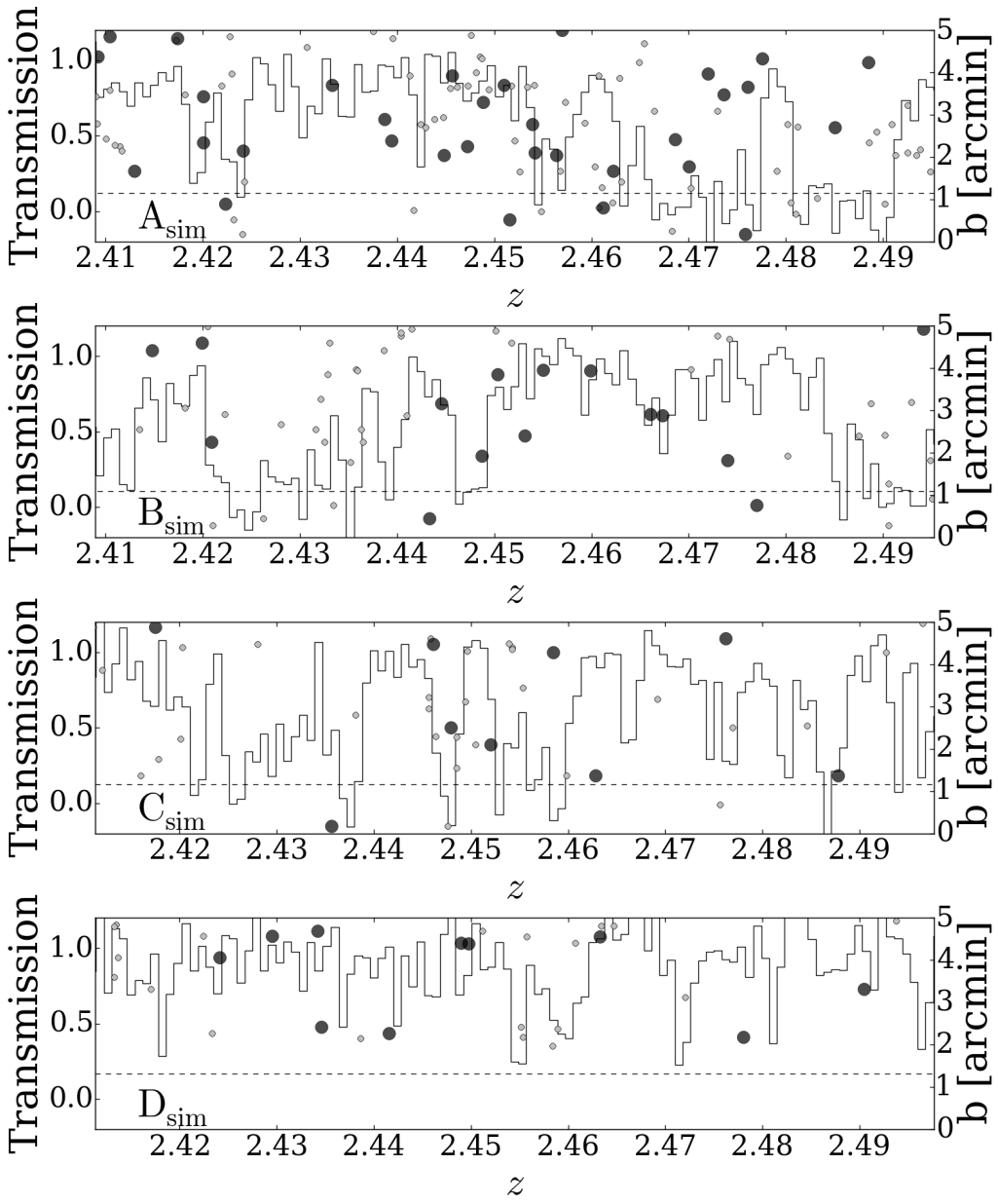

Figure A.8: Same as Figure A.5, but for the background quasar spectra in the simulations. Each panel corresponds to a cylinder that has extreme values of $\delta_{\rm gal}$ and/or $\delta_{\langle F \rangle}$ in the simulations (§ A.7.2). The black points denote redshifts and impact parameters (right-hand axis) of our photo-z galaxies in the cylinders. The gray points present photo-z galaxies without photometric redshift uncertainties.

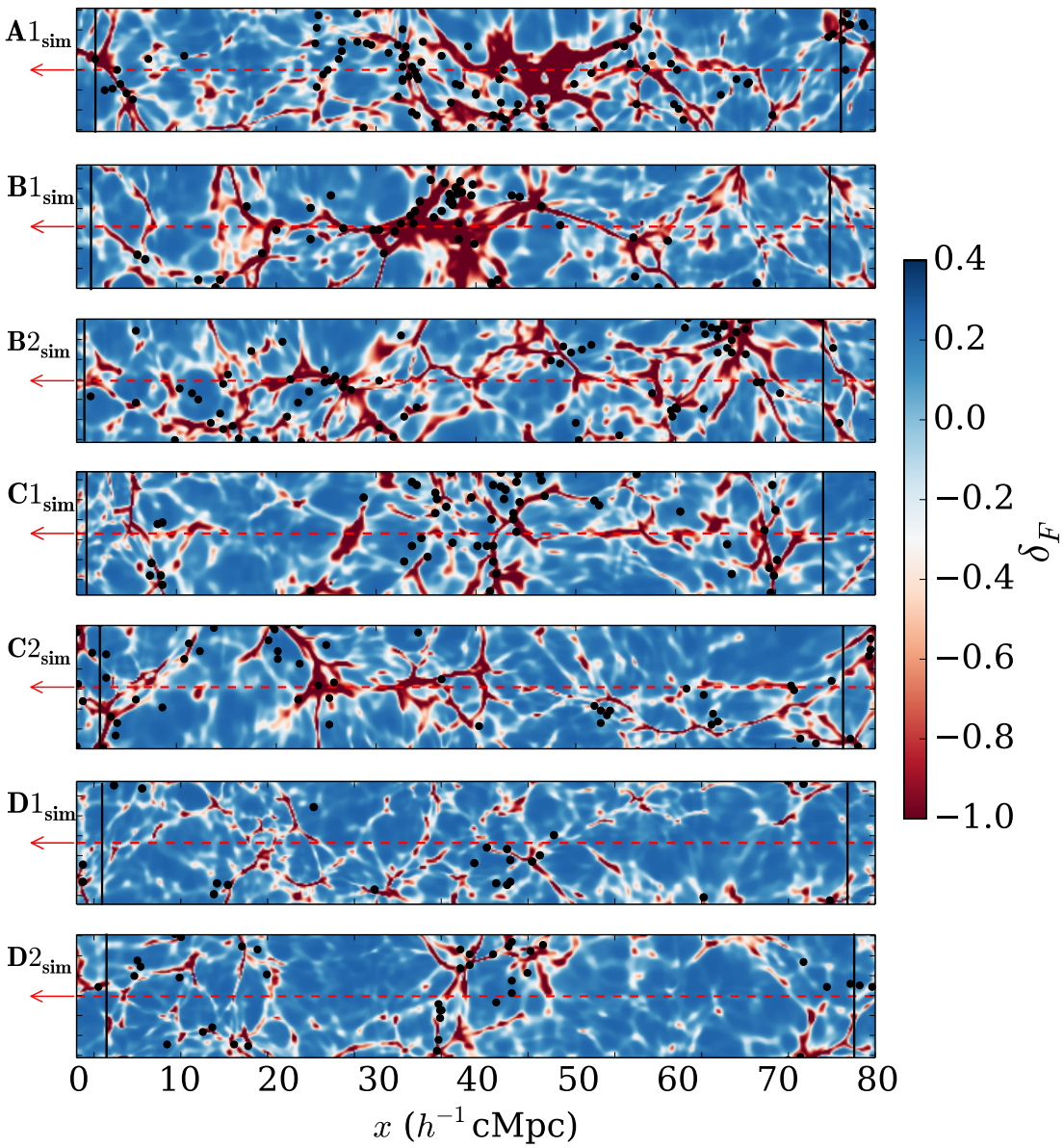

Figure A.9: Same as Figure A.7, but for $\mathrm{A1_{sim}}$, $\mathrm{B1_{sim}}$, $\mathrm{B2_{sim}}$, $\mathrm{C1_{sim}}$, $\mathrm{C2_{sim}}$, $\mathrm{D1_{sim}}$, and $\mathrm{D2_{sim}}$.

A.7.4 Detail Properties of the $A_{\rm obs}$ Sightline

In this subsection, we show the supplementary VLT/X-shooter observations for the background quasar of $A_{\rm obs}$. The X-shooter observations were carried out in the service mode on 2010 December 31 (Program ID: 086.A-0974, PI: S. Lilly). We use the reduced X-shooter spectra that are publicly available on the European Southern Observatory (ESO) Science Archive Facility.[3] We select the spectra of the UVB and VIS arms, which cover the wavelength ranges of 3000–5595Å and 5595–10240Å, respectively. The spectral resolutions of the UVB and VIS arms are medium high, $R \sim 4000$ and $R \sim 7400$, respectively. The observational details are summarized in Table A.1.

Figure A.10 shows the X-shooter spectrum of the background quasar of $A_{\rm obs}$ in the same wavelength range as Figure A.5. Although the spectral resolution of the X-shooter spectrum is significantly higher than that of the BOSS spectrum (Figure A.5), we confirm that the sightline of $A_{\rm obs}$ has Lyα forest absorption lines with no signature of DLAs. The only exception is the absorbers at $z \sim 2.203$, where saturated Lyα absorption lines are detected. The top left panel of Figure A.11 presents a zoom-in X-shooter spectrum around the saturated Lyα absorption lines. Note that their Lyβ absorption lines are also covered by the X-shooter spectrum. However, as shown in the bottom left panel of Figure A.11, the Lyβ absorption lines are also saturated. Moreover, the Lyβ absorption lines are contaminated by foreground Lyα absorbers at $z \sim 1.70$, which makes it difficult to precisely measure HI column densities of the HI absorption lines.

As shown in the right panel of Figure A.11, we identify metal absorption lines of CII, SiIV, CIV and MgII at $z \sim 2.203$ in the X-shooter spectrum. There are three metal absorptions dubbed Systems 1, 2 and 3 that are labeled in Figure A.11. We fit Voigt profiles to these metal lines with VPFIT[4] to measure column densities. The best-fit profiles for the metal lines are presented in the right panel of Figure A.11. Table A.2 summarizes the measured column densities.

[3] http://archive.eso.org

[4] http://www.ast.cam.ac.uk/~rfc/vpfit.html

To estimate HI column densities of Systems 1-3, we first make photoionization models with the input observational measurements of CII, SiIV, CIV, and MgII with those predicted from photoionization models. We perform multi-phase photoionization calculations with version 13.04 of the CLOUDY software (Ferland et al., 2013). We conduct the CLOUDY modeling for high-ionization phase clouds (CIV, SiIV) and low-ionization phase clouds (MgII, CII) (e.g. Misawa et al., 2008). We model these clouds in each phase, assuming a gas slab exposed by a uniform ultraviolet background (Haardt & Madau, 2012) with a range of ionization parameters $U \equiv \Phi/cn_{\rm H}$ ($-4.2 < \log U < -0.6$), where $n_{\rm H}$ and Φ are the hydrogen volume density and the ionizing photon flux incident on the gas cloud, respectively. The solar relative abundances of Asplund et al. (2009) are assumed. We then search for the best-fit model that minimizes χ^2 between the measured metal column densities and the photoionization model predictions. We find that the best-fit models for Systems 1, 2, and 3 have HI column densities of $\log N_{\rm H_I}$ (cm^{-2}) $\sim$ 16.0, 19.0, and 16.5, respectively. We then fit Voigt profiles to the spectrum in the wavelength ranges of the Lyα absorption lines (top left panel of Figure A.11) and Lyβ absorption lines (bottom left panel of Figure A.11) by using the column densities of the CLOUDY model results. Because the spectrum in the Lyβ wavelength range is contaminated by the foreground Lyα absorbers at $z \sim 1.70$, we conduct simultaneous fitting to the spectrum in these two wavelength ranges with the $z \sim 2.203$ Lyα and Lyβ absorbers, and $z \sim 1.70$ contaminations, together with the other Lyα absorbers. We obtain a self-consistent model that is shown with the red and blue curves in the left panels of Figure A.11.

Based on the CLOUDY model results, we find that System 2 is classified as a Lyman limit system (LLS), which is an optically thick clouds with an HI column density of $17.2 \leq \log N_{\rm H_I}$ (cm^{-2}) ≤ 20.3. Note that the presence of this LLS does not change our conclusions. We confirm that the weak anti-correlation between $\delta_{\rm gal}$ and $\delta_{\langle F \rangle}$ is found at the $\sim$ 80 % confidence level, even if the LLS is masked out in the BOSS spectrum. Our CLOUDY model indicates that System 2 has a metallicity $Z/Z_{\odot} \simeq 0.02$ and an ionization parameter $\log U \simeq -3.0$ that are comparable with those of typical LLSs at $z \sim 2$ (Fumagalli et al., 2016, 2013).

Because Systems 1 and 3 have HI column densities of $\log N_{\rm H_I}$ (cm^{-2}) $\sim$ 16.0 and

16.5, Systems 1 and 3 are classified as Lyα forest absorbers based on the moderately low column densities. However, the CLOUDY models imply that their metallicities are $Z/Z_{\odot} \simeq 0.3$ (System 1) and 1.0 (System 3), which are two orders of magnitude higher than the median IGM metallicity (Simcoe, 2011). These results would suggest that Systems 1 and 3 are gas clumps in the CGM and/or the intra-cluster medium of the proto-cluster candidate discussed in Section A.7.2.

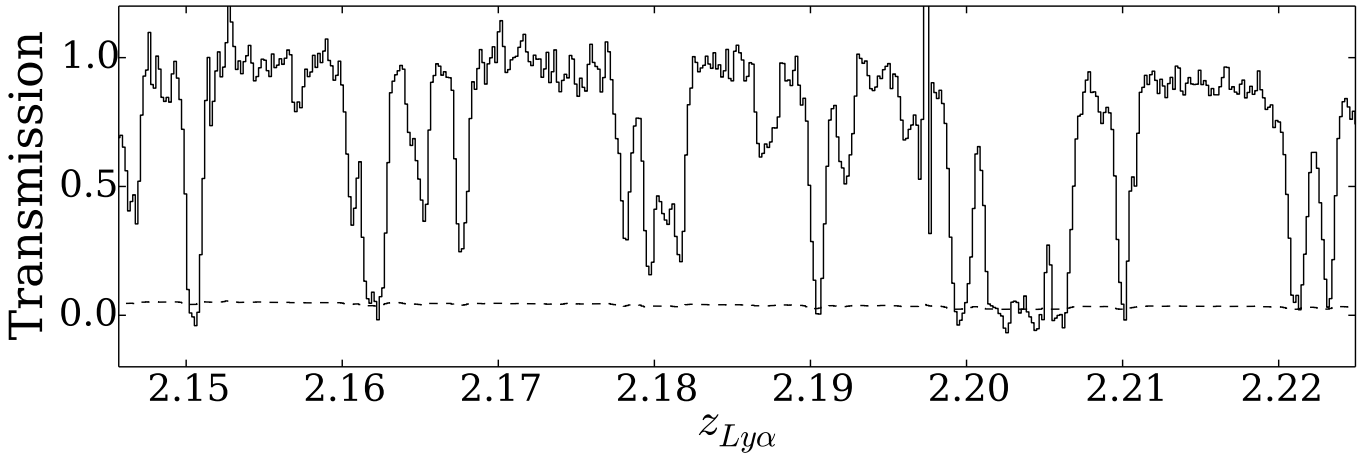

Figure A.10: VLT/X-shooter spectrum of the background quasar of A_{obs}. The solid lines represent transmission per pixel as a function of redshift for the Lyα forest absorption lines. The dashed curve denotes the noise per pixel.

Table A.1: X-shooter Observations

Source	R.A. (J2000)	Decl. (J2000)	Integration Time (s)	Dates of Observations x	S/N[c] [pix^{-1}]
COSMOS-QSO-199[a]	09 58 58.72	+02 01 38.6	UVB: 2700[b]	31 Dec 2010	27
COSMOS-QSO-199[a]	09 58 58.72	+02 01 38.6	VIS: 2700[b]	31 Dec 2010	20

[a] The background quasar of A_{obs}, [VV2006] J095858.7+020138 at $z = 2.448$.
[b] Three individual exposures of 900 sec.
[c] Median S/N per pixel for the combined spectra.

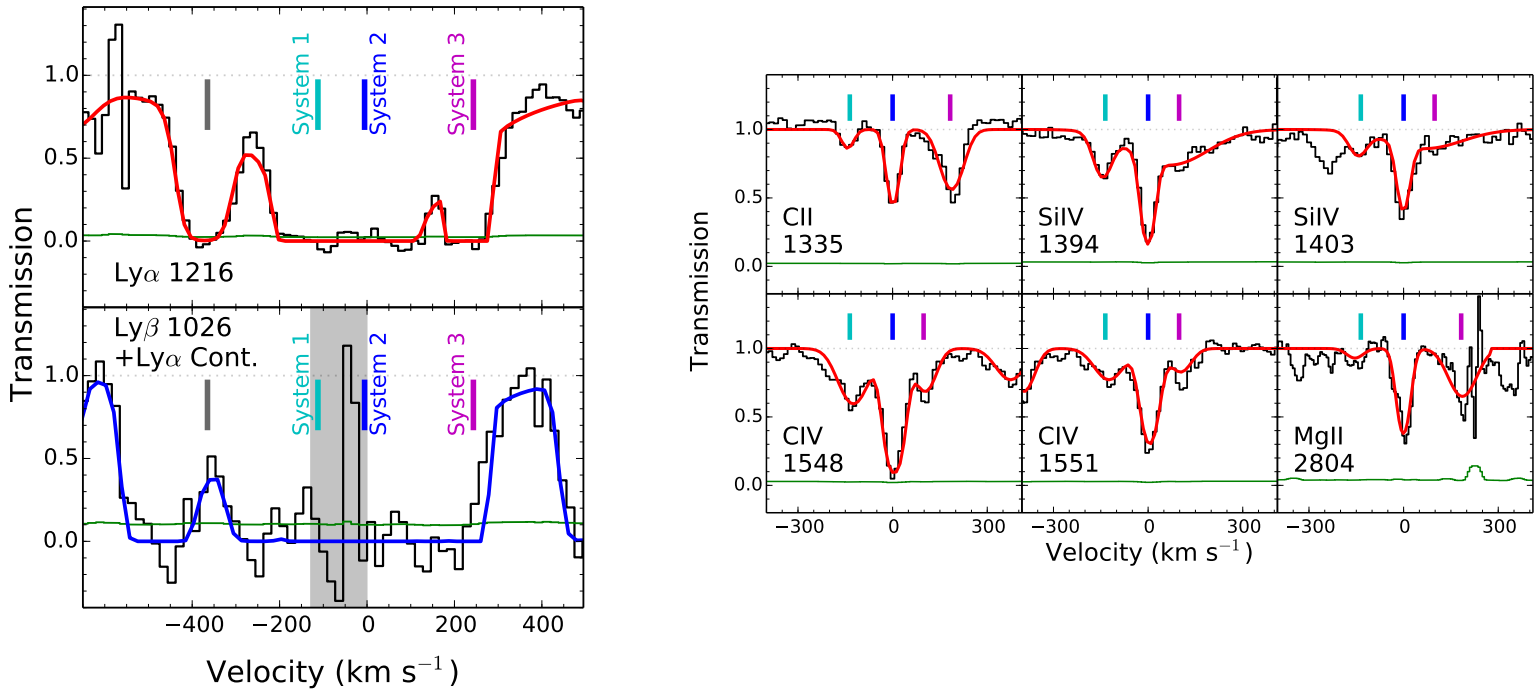

Figure A.11: Left panel: Zoom-in X-shooter spectrum around the $z \sim 2.203$ HI Lyα absorption systems (top) and Lyβ absorption systems with $z \sim 1.70$ Lyα absorption contaminations (bottom). The black (green) histogram presents the transmission (1σ noise) per pixel. The Voigt-profile decompositions (red curve) are made of the three Lyα absorption systems, System 1 (cyan ticks), System2 (blue ticks), System 3 (magenta ticks), and a Lyα absorption system that has no metal lines (gray ticks). The blue curve shows the fitting results for the Lyβ absorption systems and $z \sim 1.70$ Lyα absorption contaminations. Note that we simultaneously fit $z \sim 2.203$ Lyα and Lyβ absorbers and $z \sim 1.70$ Lyα absorption contaminations. The decompositions indicate that System 2 is the LLS at $z = 2.203$. The gray shaded region in the bottom panels presents the wavelength range where we find a large sky subtraction systematic errors. Right panel: Same as the left panel, but for metal absorption lines associated with the Lyα absorption systems at $z \sim 2.203$.

Table A.2: Column Densities of the Ions in the $z \sim 2.203$ Absorption Systems

Ion	CII	SiIV	CIV	MgII
System 1				
$\log N$ (cm^{-2})	13.19 ± 0.70	13.14 ± 0.57	13.86 ± 0.19	12.31 ± 0.68
System 2				
$\log N$ (cm^{-2})	13.92 ± 0.17	13.58 ± 0.24	14.29 ± 0.12	13.31 ± 0.21
System 3				
$\log N$ (cm^{-2})	14.03 ± 0.16	13.54 ± 0.35	13.59 ± 0.35	13.29 ± 0.13

A.8 Future Prospects

In Section *A*.7.2, we identify the remarkable cosmic volume, dubbed A_{obs}, which has the largest δ_{gal} and the smallest $\delta_{\langle F \rangle}$ values (Figure *A*.4). A_{obs} resides in PC1 reported by Chiang et al. (2014). However, Chiang et al. (2014) use photo-z galaxies, and the distribution of member galaxies in the PC1 is still unknown. Recently, Chiang et al. have conducted the Gemini/GMOS observations for PC1, but, so far, only a few galaxies are identified due to the shallow spectroscopy of the GMOS program mainly targeting Lyα emitters (LAEs). In Section A.7.4, we investigate the background quasar spectrum of A_{obs} taken with VLT/Xshooter. We identify multiple HIImetal absorption lines at $z \sim 2.2$ (Figure A.11). However, the large photo-z uncertainty does not allow us to identify galaxies responsible for these multiple HIImetal absorption lines. We plan to conduct deep spectroscopy for galaxies in the remarkable field of A_{obs}. We detail two spectroscopic observation studies below.

i) We aim at understanding correlations between galaxies and HIImetal absorbers. We target the continuum-magnitude limited ($i_{AB} < 25$) sample of galaxy candidates in A_{obs} at $z \sim 2.2$. We select the target galaxies based on photometric redshifts from Ilbert et al. (2009). We will observe 20 galaxies with $i_{AB} < 25$, complementing the Chiang et al.'s shallow GMOS spectroscopy LAEs. We will examine which galaxies around the background quasar sightline are associated with the multiple metal absorption lines and HI Lyα absorption lines at $z \sim 2.2$. We will constrain on the maximum impact parameter for the metal-galaxy connection for the metal enrichment in the large scale. Moreover, the galaxy-HI correlation will allow us to investigate the distribution of galaxies and the multiple HI clouds probably in filamentary LSSs. We study these associations with the accuracy of $\sim$200 km s^{-1} that is comparable to "finger of god" (Rakic et al., 2012) and blueshifted metal absorption lines in the continuum of the galaxy candidates.

ii) We aim at mapping out IGM HI distribution by the Lyα forest tomography. We target 30 background galaxies with $g_{AB} < 24.85$ at $z \simeq 2.2 - 2.7$ to carry out Lyα

forest tomographic reconstruction. Performing the Lyα forest tomography in the same manner as Lee et al. (2016), we will map out IGM HI in A_{obs} with the average sightline separation of $\langle d_\perp \rangle \sim 2.4h^{-1}$Mpc. Note that $z \sim 2.2$ is an efficient redshift for the Lyα forest tomography (Lee et al., 2016). With the 3D tomography map of HI distribution in the remarkable A_{obs} system, we will investigate the mass/ionization distribution and the metal absorber positions in the system. We will also study a connection between this A_{obs} (+PC1) system and HI LSSs beyond the size of this system. It should be noted that there is an on-going program of the CLAMATO (Lee et al.) that is mapping out $z \sim 2-3$ IGM across a ~ 1 deg^2 area of the COSMOS field. However, our A_{obs} field is not included in the CLAMATO survey field (Figure A.12). No existing observation programs will take deep spectra of the background galaxies useful for tomography in A_{obs}.

A_{obs} is a great laboratory for understanding correlations between three components, metal absorbers, IGM HI, and galaxy overdensity. This A_{obs} is distinguished from the galaxy-HI overdensity systems previously reported by Lee et al. (2016) and Chiang et al. (2015) that do not have multiple metal absorber detections. This is the first time to report the gas clumps in a proto-cluster candidate (cf. Steidel et al., 1998; Adelberger et al., 2003). Moreover, A_{obs} has the highest galaxy overdensity among them. The remarkable system of A_{obs} will give us the correlations of the three important components directly in one system. We plan to carry out Keck/LRIS observations.

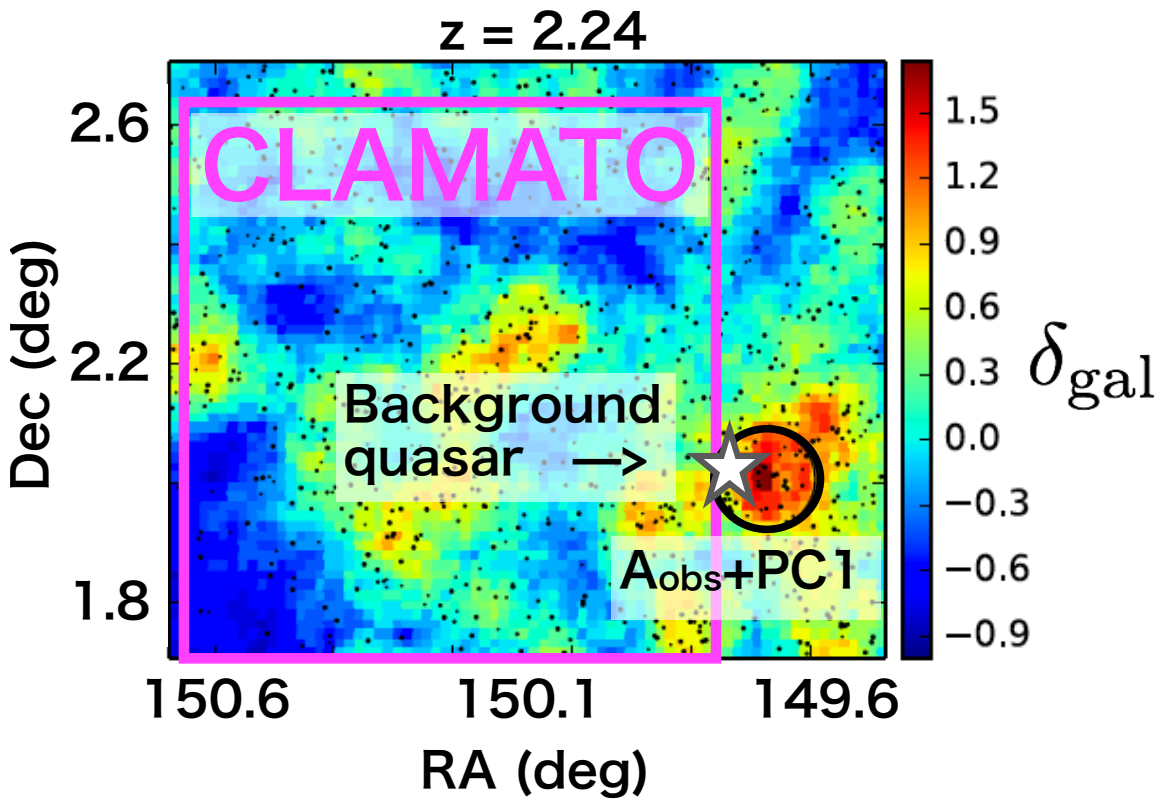

Figure A.12: The $\delta_{\rm gal}$ maps in the COSMOS/UltraVISTA field (Chiang et al., 2014). The circle indicates $A_{\rm obs}$ and PC1. The star represents the position of background quasar sightline. The magenta box shows the CLAMATO survey field.

APPENDIX B
SUBARU/HSC SURVEY FOR HOBBY-EBERLY TELESCOPE DARK ENERGY EXPERIMENT

We conduct Subaru/Hyper Suprime-Cam (HSC) observations over the HETDEX Spring 300 deg^2 field, and provide imaging data essential for removing contaminants of [OII] λ 3727 doublet emitters ([OII] emitters). It is a challenge for VIRUS to distinguish high-redshift LAEs and low-redshift [OII] emitters. Because VIRUS has a narrow spectral range of 3500-5500 Å and a poor sensitivity. Thus, LAEs at $1.9 < z < 3.5$ and [OII] emitters at $z < 0.5$ will be identified as a single-line emitters. Because the spectral resolution of VIRUS ($R \sim 800$) can not resolve the asymmetry of the Lyα emission line profiles and the [OII] λ3727 doublet, LAEs and [OII] emitters are not classified (Figure B.1).

The selection criterion based on the equivalent width (EW) measurements is a reliable method to separate high-redshift LAEs and low-redshift [OII] emitters, and has been demonstrated in the HETDEX Pilot Survey (HPS: Adams et al., 2011). LAEs at $2 < z < 3$ have observed EW ($\sim 200 - 300$ Å: Gronwall et al., 2007) larger than those of [O II] emitters at $0 < z < 0.5$ ($\sim 20 - 30$ Å: Ciardullo et al., 2013). Exploiting this clear range differences of LAEs and [OII] emitters, one can isolate LAEs from the single emitter catalog using the EW measurements with the combination of the broadband imaging data.

In these efforts, we've conducted the HSC r-band imaging survey whose data are complementary to the existing r-band imaging data of the Kitt Peak 4-m Mosaic camera and the CFHT Wide-Field Legacy survey. We have so far carried out a total of 3-night HSC observations in 2015-2018 (PI: Andreas Schulze) and in 2019-2020 (PI: Shiro Mukae), and collected the HSC imaging data over ~ 250 deg^2 of the HETDEX Spring field (Figure B.2) with a 10σ depth of $r = 25.1$ mag. For these data, we have completed data reduction and source detections, and shared the survey data with the HETDEX Collaboration that are important to the success of HETDEX.

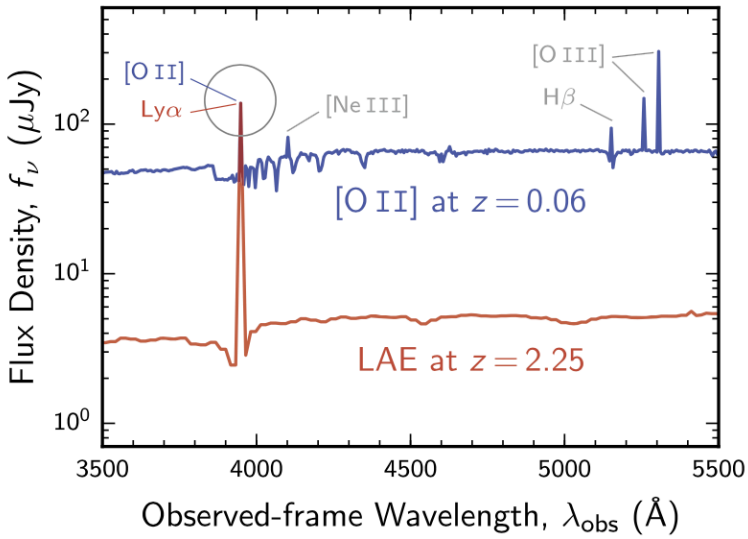

Figure B.1: Model spectra of high-redshift LAEs and low-redshift [OII] emitters over the spectral range of HETDEX. This figure is taken from (Leung et al., 2017).

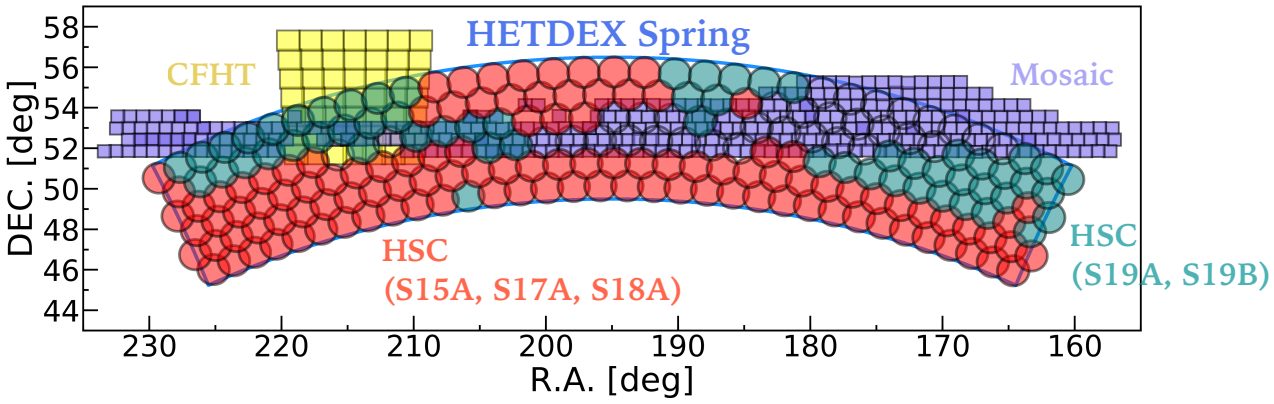

Figure B.2: Outline of the HETDEX Spring field ($\sim$ 300 deg^2; blue lines), along with the footprints from our HSC runs in 2015 – 2018 (red circles) and 2019 – 2020 (teal circles), the Kitt Peak 4-m Mosaic (purple), and the CFHT Wide-Field Legacy survey (yellow). Our HSC survey has finally obtained all of the HSC imaging data ($\sim$ 250 deg^2) for the fields outside of the CFHT+Mosaic imaging data, taking five years.

APPENDIX C
TMT/IRIS INSTRUMENTATION: PERFORMANCE EVALUATION OF PROTOTYPED MIRROR COATINGS FOR IRIS IMAGER

C.1 Overview

This appendix is a contribution of TMT/IRIS instrumentation, where we have prototyped two types of mirror coatings, which are the multi-layer dielectric coating and the enhanced silver coating, to decide which mirror coating is suitable for the TMT/IRIS imager optics. We measure reflectance and thermal deformation, and estimate wavefront error contribution at 77 K when the coatings are applied to the IRIS imager. Our results suggests that the multi-layer dielectric coating has the high reflectance and the small mirror surface deformation, and is suitable for the IRIS imager.

C.2 Motivation

Throughput and wavefront error (WFE) are two important parameters for instruments with diffraction limit capabilities which are directly related to observing sensitivity and scientific outputs. Since the IRIS imager employs an all-reflective optics, reflectance of mirror coating is directly connected to the imager throughput.

One of the challenging requirements for the IRIS imager is to achieve WFE of less than 40 nm rms. WFE is largely attributable to aberrations of the optical design, and errors associated to fabrication, assembly, temperature environment, and measurements. There is two error terms which are associated to the mirror coatings.

1. Generally, different materials are used for the mirror substrate and the mirror coating. When the mirror is cooled from the room temperature to the operating temperature, thermal deformation occurs due to differential thermal contraction between the mirror substrate and the mirror coating, which degrades WFE.

2. A silver coating with some dielectric coating layers for protective purposes (enhanced silver) is routinely used as a mirror coating for the near-infrared instruments. While its reflectance is medium low ($98\% - 99\%$), the thermal deformation is expected to be small because of thin coating layers. In contrast to it, multi-layer dielectric (MLD) coatings with hundreds of layers will reproduce higher reflectance of nearly 100% at the expense of larger thermal deformation.

If it turns out that reducing WFE due to the thermal deformation involves technical challenges which require new development components, they have a huge impact on the cost and schedule of the project. It is therefore important to estimate coating effects on WFE at an early stage of development.

We then have prototyped two types of mirror coatings mentioned above to investigate reflectance, WFE due to thermal deformation, and the possible technical challenges associated to reducing WFE. In this APPENDIX, we describe our efforts to measure reflectance and thermal deformation of the prototyped mirrors, and estimate WFE when the coatings are applied to the IRIS imager optics. We aim to obtain reflectance and WFE of the prototyped mirrors, which are essential to the observing sensitivity and science outputs, to decide which mirror coating is suitable in this regard.

C.3 Prototyped Mirror Coatings

Table C.1 summarizes mirror coatings prototyped for the IRIS imager. The samples consist of (1) MLD coating (Sample A), and (2) enhanced silver (hereafter eAg) coating (Sample B and C). Both coatings are applied on ϕ25mm x t3mm substrates made of a synthetic silica which is the same material as the IRIS imager optics. FigureC.1 shows pictures of the three samples investigated in this study.

Table C.1: Mirror Coating Samples

Coating Sample	Substrate	Layer	Reflectance [a,b]	Vendor
Sample A	Synthetic Silica	MLD	99.7%	SOC
Sample B	Synthetic Silica	eAg	98-99%	SOC
Sample C	Synthetic Silica	eAg	98-99%	OCJ

[a] Wavelength range in 0.84 - 2.4 μm
[b] Data provided by the vendors.

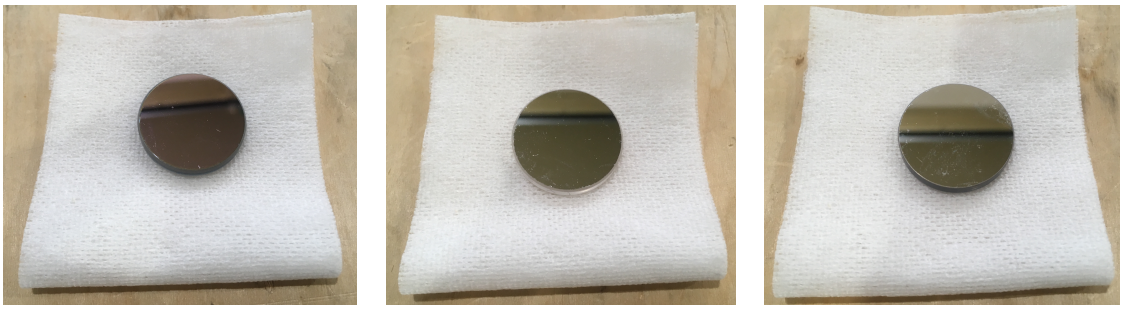

Figure C.1: Mirror coatings prototyped for the IRIS imager. Left: MLD coating (SOC). Center: eAg coating (SOC). Right: eAg coating (OCJ).

C.4 Reflectance Measurements

While the mirror coating reflectances have been provided by the vendors, we nevertheless measure the reflectances of our samples, since they are important performance that affects the instrument sensitivity. This is a part of an acceptance test when a product is delivered from the vendor, and it is good to double-check the vendor deliverable to make sure if there is any systematic errors. We measured spectra in the wavelength range of 0.8 - 2.4 μm, using a spectrophotometer (SolidSpec-3700) that Advanced Technology Center (ATC) of National Astronomical Observatory of Japan (NAOJ) owns. However, we could not obtain spectra at longer wavelength than 1.65 μm where the detector switches from InGaAs to PbS due to unstable performance of the spectrophotometer. Here we present the measured spectra in the wavelength range of 0.8-1.65 μm in Figures C.2, C.3, and C.4. We find that the measured spectral shapes are consistent with the data provided by the vendors. Spectra at longer wavelength than 1.65 μm will be measured at external institutions.

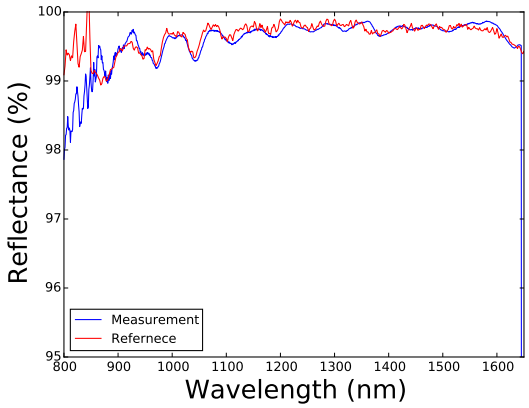

Figure C.2: Measured spectrum of Sample A. Blue: Our measurement. Red: Data provided by the vendor.

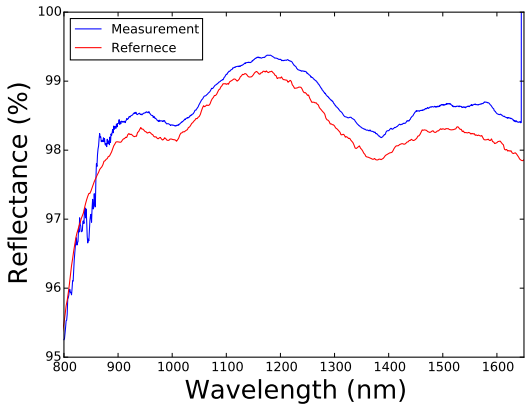

Figure C.3: Measured spectrum of Sample B. Blue: Our measurement. Red: Data provided by the vendor.

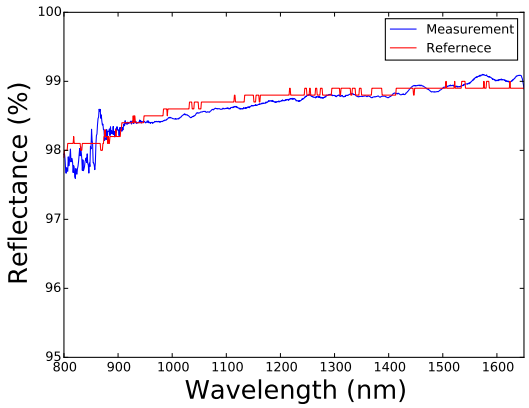

Figure C.4: Measured spectrum of Sample C. Blue: Our measurement. Red: Data provided by the vendor.

C.5 Measuring and Modeling Mirror Surface Deformation

C.5.1 Surface Shape Measurements of the Mirror Substrates

To measure a surface shape of the mirrors at cryogenic temperatures, we have first established a measurement system which consists of a mirror holder, temperature sensors, vacuum dewar, vacuum pump, liquid nitrogen (LN2), and a laser interferometer (Zygo GPI). Figure C.5 and C.6 presents our measurement setup.

When the mirror substrate is cooled in the vacuum environment, temperature of the mirror substrate is determined by thermal equilibrium between thermal radiation and thermal conductivity. We implement a radiation shield made of aluminum to substantially reduce the thermal radiation load. Thermal conductivity depends on a contact area and a contact pressure between the mirror substrate and the mirror holder.

To avoid putting strong contact pressure that may distort the mirror substrate, we hold the mirror substrate on the mirror holder (77K stage in Figure C.5), using three leaf springs made of phosphor bronze whose contact pressure strength is accurately controlled not to distort the mirror substrate (see Figure C.5).

If we glue temperature sensors to the mirror substrate to monitor the mirror substrate temperature, the differential thermal contraction between the mirror substrate and the glue, will distort the mirror substrate as well. We then obtain the temperature profile of the mirror substrate in advance such that the mirror substrate temperature during the surface shape measurement can be deduced from the pre-acquired temperature profile.

We then measure surface shape with a laser interferometer Zygo GPI at 632.8 nm (see Figure C.6). Since we use LN2 as a refrigerant, it is expected that the mirror substrate cannot reach the temperature as low as 77K which is an operating temperature of the IRIS imager. We thus carry out surface shape measurements at various temperatures during warming-up process, and deduce the surface shape at 77K by extrapolation.

Figures C.7, C.8, and C.9 show surface shape maps obtained at room temperature

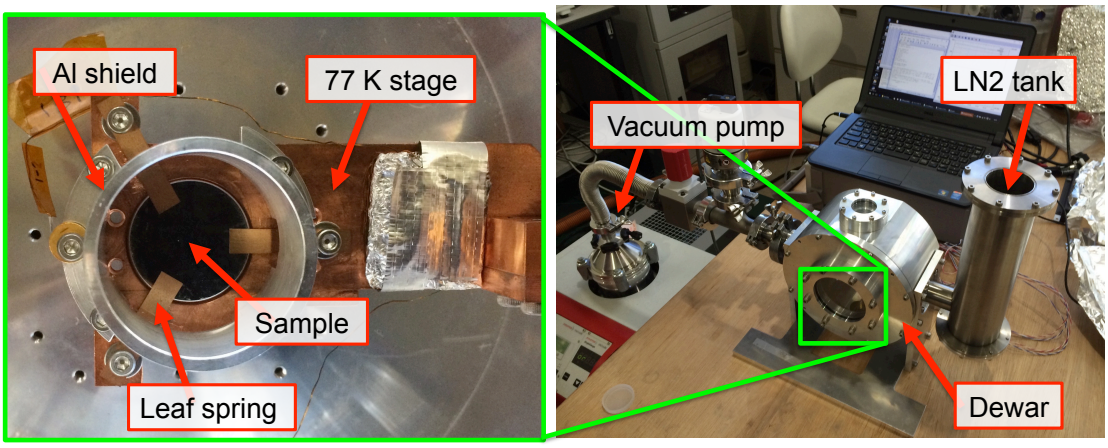

Figure C.5: Established measurement system for cooling mirror substrate with a mirror holder, vacuum dewar, vacuum pump, and LN2.

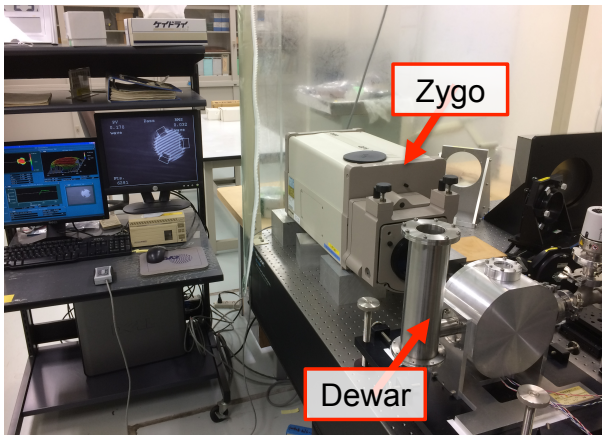

Figure C.6: Measurements of surface shape using the laser interferometer Zygo GPI.

and the coldest temperature that is finally reached for each sample. Samples A, B, and C get to170, 106, and 109 K, respectively.

Sample B and C reached lower temperature than that of Sample A because radiation load from outside the dewar for Sample B and C is expected to be reduced significantly by the high reflectance of silver at the wavelength of 5-10 μm where the blackbody radiation at room temperature has its peak. Sample A may absorb the radiation more because the reflectance of the MLD coatings may not be high in the wavelength of 5-10 μm due to broken interference conditions.

294 K

170 K

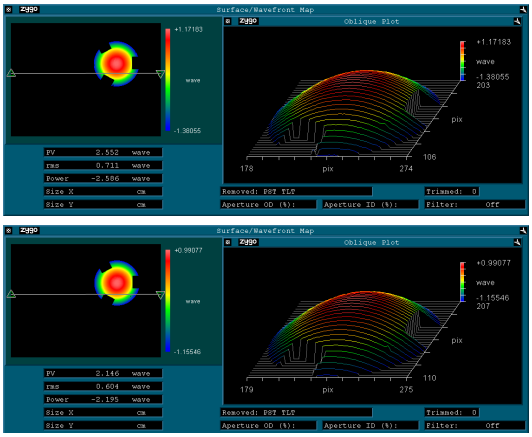

Figure C.7: Surface shape maps obtained at room temperature and the coldest temperature (Sample A).

294 K

106 K

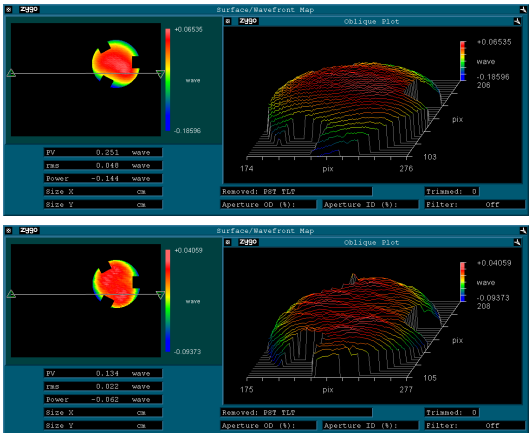

Figure C.8: Surface shape maps obtained at room temperature and the coldest temperature (Sample B).

294 K

109 K

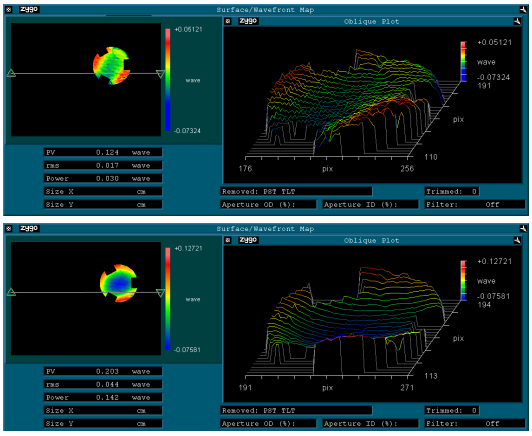

Figure C.9: Surface shape maps obtained at room temperature and the coldest temperature (Sample C).

C.5.2 Estimating Thermal Deformation

In this subsection, we describe how we derive the surface shape at 77 K, which is an operating temperature of the IRIS imager, from the data obtained at various temperatures.

First, we mention surface shape expected from a theory. For a single layer thin coating, surface shape and stress in the coating are related by the Stoney's formula (Stoney, 1909),

$$\frac{1}{R} = \frac{6(1-\nu_s)t_c}{E_s {t_s}^2}\sigma_c, \tag{C.1}$$

where R is a radius of curvature, ν_s is Poisson ratio of the substrate, E_s is Young's modulus of the substrate, t_s is a thickness of the substrate, t_c is a thickness of the coating, and σ_c is a stress in the coating. The stress σ_c in our case is induced by differential thermal contraction between the substrate and the coating.

The physics working for the multi-layer coatings is expected the same as the case of the single layer, i.e., the substrate bends until the stress induced by a bending moment of the substrate reaches equilibrium with the stress induced in the coating due to the thermal deformation. Therefore, thermal deformation during cool-down is expected to have a spherical shape with a single curvature radius, in the same manner as that of the single layer coating.

We then derive the thermal deformation of the substrate by subtracting a surface shape at room temperature from that of cooled temperature. We use data of the measured surface shape within $\sim 90\%$ of the substrate diameter which does not overlap with the three leaf springs. The thermal deformation at the coldest temperature reached for our samples are presented in Figures C.10, C.11, and C.12. We find that the thermal deformation is well represented by a biaxial surface with two different curvatures in two orthogonal directions rather than a sphere as we expected above. Especially, eAg coatings (Samples B and C) show significant departure from a sphere, having a cylindrical shape with an order of magnitude difference in the two curvatures.

We thus model the thermal deformation using the biaxial surface with a functional

form of

$$z = z_0 + \frac{c_x x^2 + c_y y^2}{1 + \sqrt{1 - {c_x}^2 y^2 - {c_y}^2 y^2 - {c_{xy}}^2 xy}}, \tag{C.2}$$

where

$$c_x = 1/R_x, \tag{C.3}$$

$$c_y = 1/R_y, \tag{C.4}$$

$$R_x < R_y \tag{C.5}$$

and derive the two curvatures (note that we hereafter use curvature instead of curvature radius) by applying Eq. C.2 to the measured thermal deformations. Figures C.13, C.14, and C.15 present the two curvatures as a function of substrate temperature.

For the MLD coating (Sample A), the two curvatures seem to follow a linear relation with the temperature between room temperature and the coldest temperature. For the eAg coatings (Sample B and C), on the other hand, the larger and smaller curvatures exhibit characteristic non-linear behaviors between temperature and the curvatures. A left panel of Figure C.15, shows that the larger curvature of Sample C becomes flat at $\sim$ 130 K and lower. This trend is consistent with a fact that the thermal expansion rate of silver is linear to the temperature above 130 K and slows down at lower temperature (see Figure C.16 from Pobell 2007). We therefore apply a linear fitting function to the measured data above 130 K and extrapolate the curvature at 77 K from the linear function, conservatively. The same method is applied to Sample B.

On the other hand, the smaller curvatures of Samples B and C show a profile which has (1) a curve with a peak at $\sim$ 220 K at temperature above 170 K, and (2) a flat below 170 K. This characteristic profile is very similar to that of a coated substrate which has undergone non-linear deformation beyond the elastic regime (Lee et al., 2001). The non-linear profiles seen in Figures C.14 and C.15 may indicate that the

silver coatings experience stress beyond the tensile strength (which is a representative of elastic limit) and the non-linear deformation occurs. As a calculation supporting this implication, Figure C.17 plots shear stress in silver as a function of temperature when silver/synthetic silica layers are cooled from room temperature. This figure indicates that the shear stress in silver exceeds the tensile strength of 200 MPa at $\sim$ 220 K which coincides with the peak temperature in Figures C.14 andC.15 . We therefore only use the data below 170 K and apply a linear fitting function when we extrapolate the 77 K curvature of Samples B and C. The extrapolated curvature at 77 K for our samples are summarized in Table C.2. The thermal deformation of the MLD coating (Sample A) is larger than the eAg coatings (Sample B and C) as we expected.

Table C.2: Extrapolated curvature at 77 K

Coating Sample	R_x [m]	R_y [m]
Sample A	126	149
Sample B	756	9772
Sample C	412	1432

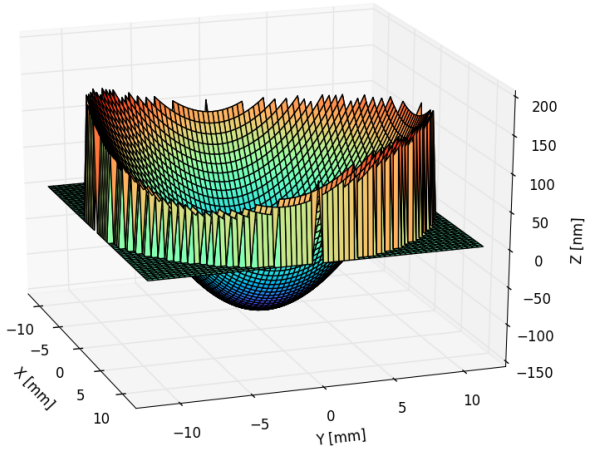

Figure C.10: Thermal deformation at the coldest temperature (Sample A).

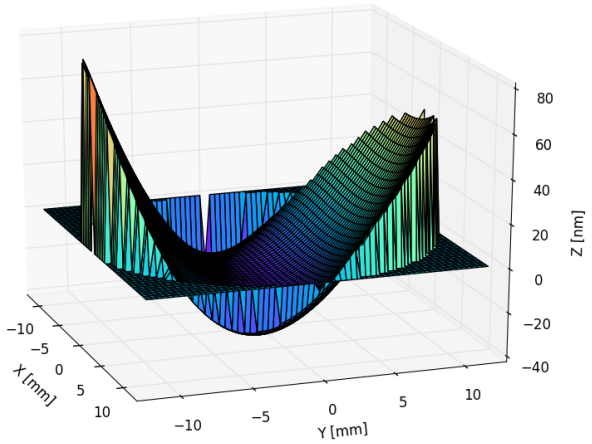

Figure C.11: Thermal deformation at the coldest temperature (Sample B).

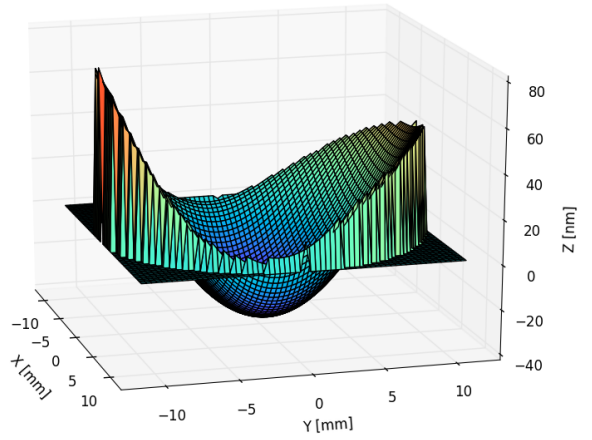

Figure C.12: Thermal deformation at the coldest temperature (Sample C).

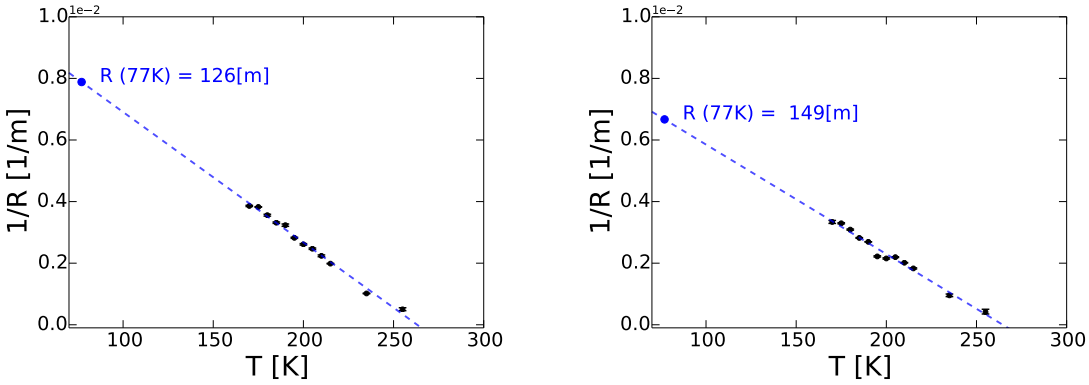

Figure C.13: Two curvatures (left:$1/R_x$, right:$1/R_y$) as a function of substrate temperature (Sample A). The dashed blue lines represent the best-fit linear functions. The blue dots are extrapolated curvatures at 77 K.

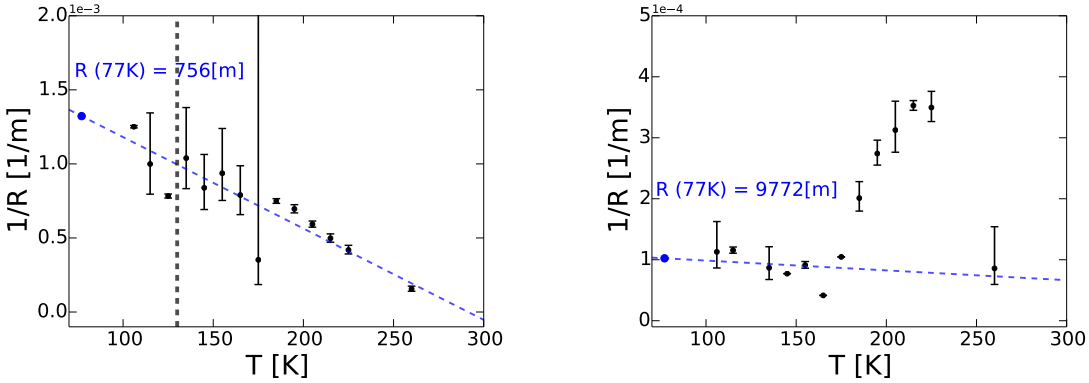

Figure C.14: Same as Figure C.13, but for Sample B.

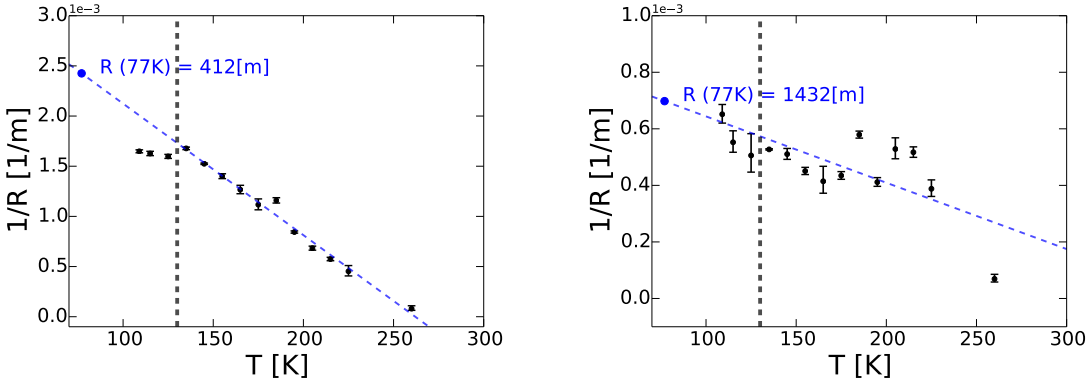

Figure C.15: Same as Figure C.13, but for Sample C.

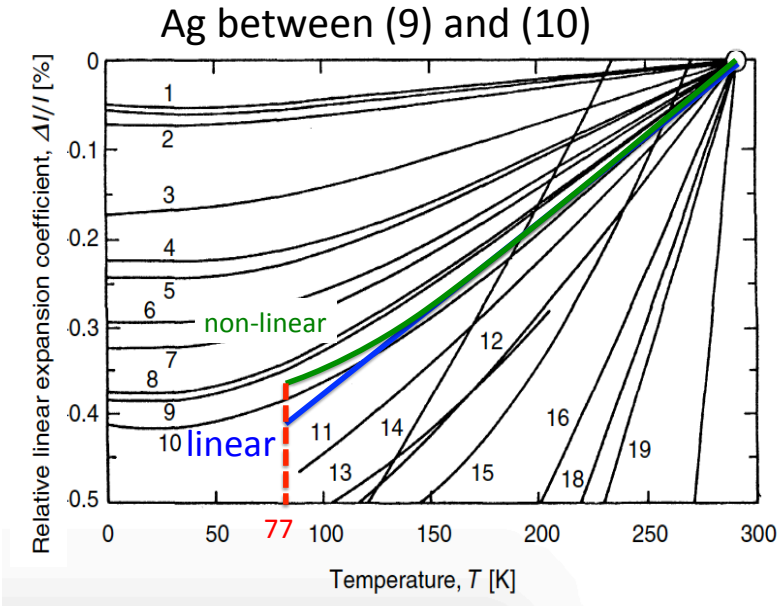

Figure C.16: Thermal expansion rate of silver as a function of temperature is represented with a linear (blue line) and a non-linear (green line) function. The red dashed lines indicate temperature at 77 K. This figure is taken from Pobell (2007).

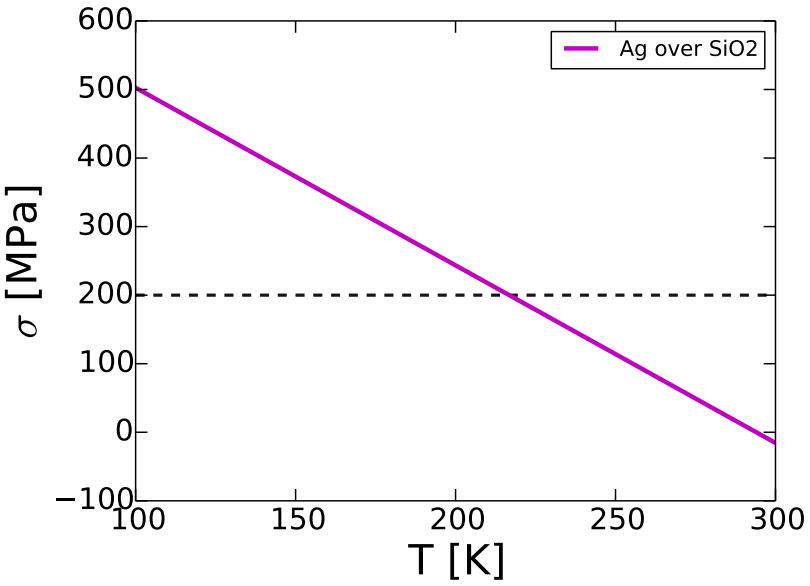

Figure C.17: Purple line represents shear stress in silver as a function of temperature when silver/synthetic silica layers are cooled from room temperature. The shear stress in silver exceeds the tensile strength of 200 MPa at $\sim$ 220 K.

C.5.3 WFE Evaluation Using the IRIS Imager Optics

Next, we translate the thermal deformations obtained from the prototyped mirrors into the thermal deformation expected when the coatings are applied to the IRIS imager mirrors. The IRIS imager has 9 rectangle mirrors with width and height varying in $80 - 200$ mm range for each mirrors. The thickness also varies in $20 - 50$ mm range. Since the same mirror coating and the mirror substrate will be used for the IRIS imager optics as the prototyped mirrors, equation C.1 indicates that the curvature scales as square of the substrate thickness (t_s^2). We apply this scaling to the curvatures summarized in Table C.2 for each of 9 mirrors.

The expected thermal deformations at 77 K, which are represented by a biaxial surface with the scaled curvatures, are applied to an IRIS imager optical models using an optical design software ZEMAX. The WFE is finally computed by raytracing at the detector location. Figures C.18, C.19, and C.20 present resulting WFE maps in the IRIS imager FoV for our samples. WFE contribution by cooling the mirror coating is estimated by subtracting WFE with coatings from WFE without them. The WFE contributions are 139.9, 21.1, and 35.9 nm for Sample A, B, and C, respectively, as summarized in Table C.3 (column: without DM). Since the WFE requirement to IRIS imager is 40 nm, we find that these WFE contributions either exceed the requirement or occupy a significant part of the WFE budget.

Table C.3: ZEMAX Results

Coating Sample	WFE contribution [nm] [a]	
	without DM	with DM
Sample A	139.9	4.5
Sample B	21.1	3.3
Sample C	35.9	3.3

[a] Maximum variations in WFE values in the IRIS FoV.

Because IRIS works together with NFIRAOS, some WFE can be corrected by using two Deformable Mirrors (DMs) in NFIRAOS. WFE maps after the DM corrections are shown in Figures C.21, C.22, and C.23, and the WFE contributions by cooling the mirror coating are summarized in Table C.3 (column: with DM). The

WFE contributions are significantly reduced to 4.5, 3.3, and 3.3 nm for Samples A, B, and C, respectively. Our results reveal, for all prototyped mirror coatings, that DM correction is necessary to reduce WFE caused by cooling the mirror coatings, and the WFE contribution is 3-5 nm after the DM corrections.

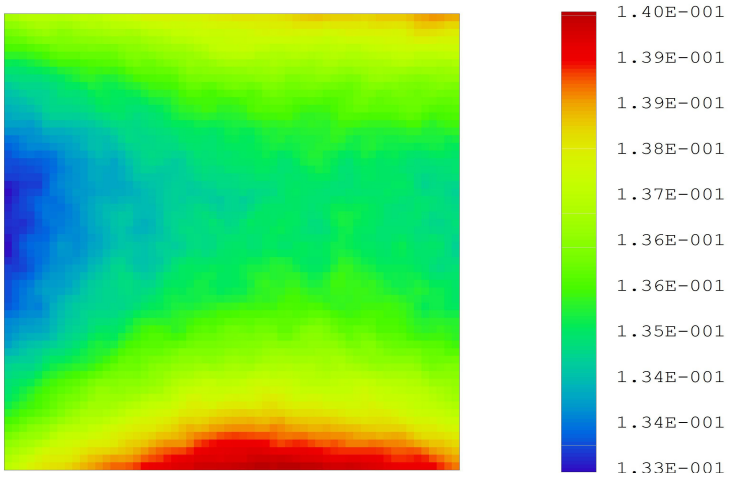

Figure C.18: WFE maps in IRIS imager FoV without DM correction (Sample A). The color scale represent the WFE which is normalized by 1 μm.

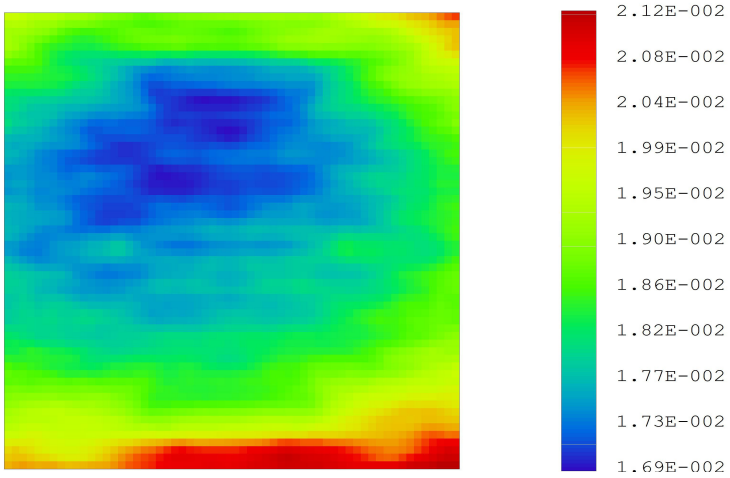

Figure C.19: Same as Figure C.18 but for Sample B.

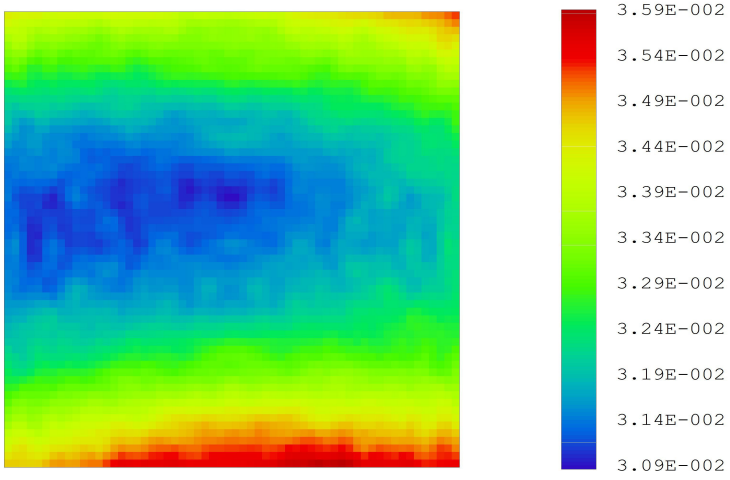

Figure C.20: Same as Figure C.18 but for Sample C.

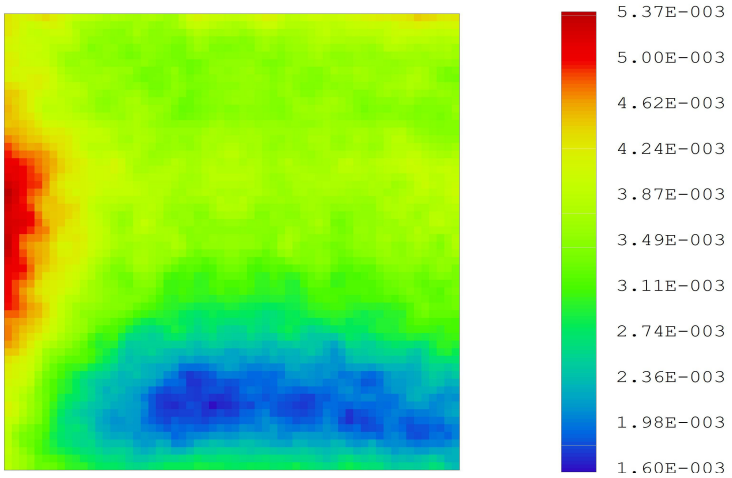

Figure C.21: WFE maps in IRIS imager FoV after DM correction (Sample A). The color scale represent the WFE which is normalized by 1 μm.

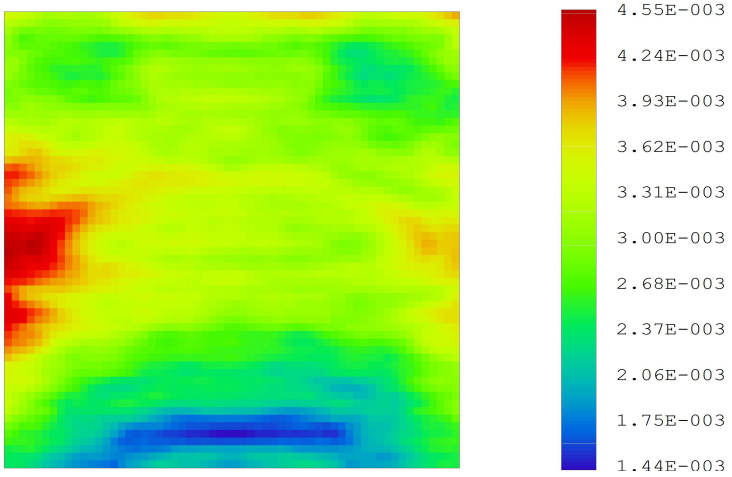

Figure C.22: Same as Figure C.21 but for Sample B.

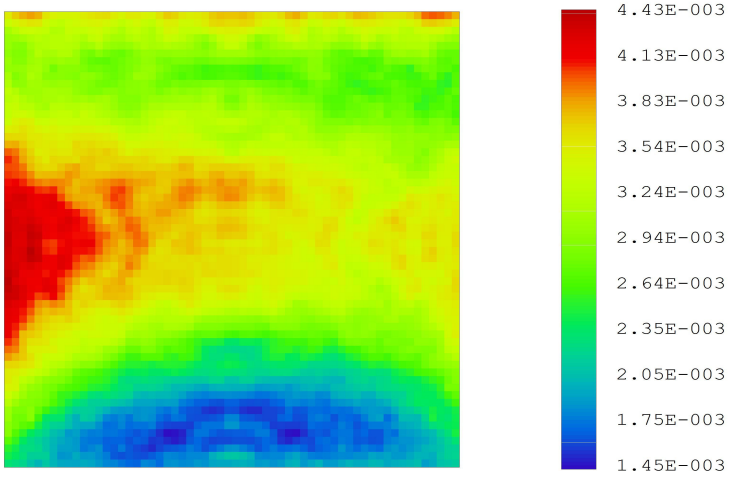

Figure C.23: Same as Figure C.21 but for Sample C.

C.6 Discussions and Future Prospects

We have measured reflectance and thermal deformation of two types of mirrors (MLD coating and eAg coating) prototyped for the IRIS imager, and estimated the WFE due to the thermal deformation when the coatings are applied to the IRIS imager. The results of our study are summarized below.

1. Measured reflectances are consistent with the data provided by the vendors in the wavelength range of 0.8 - 1.65 μm, while we could not carry out reliable measurement at wavelength longer than 1.65 μm due to unstable performance of the spectrophotometer. Reflectance at the longer wavelength will be measured in the future at an external institutions.

2. We have established a system to measure the surface shape of the mirror at cryogenic temperatures, using a mirror holder, temperature sensors, a vacuum dewar, a vacuum pump, LN2, and a laser interferometer. With thermal radiation and thermal conductivity properly considered, Sample A, B, and C are cooled to 170, 106, and 109 K, respectively.

3. We find that the thermal deformation is well described by a biaxial surface with two different curvatures in two orthogonal directions (see equation C.2) rather than a spherical surface which is expected from the Stoney's formula. The eAg coatings (Sample B and C) exhibit a cylindrical deformation with two curvatures having an order of magnitude difference. This extreme biaxial deformation indicates that the silver layer experiences stress which exceeds the tensile strength due to differential thermal contraction with the substrate, and the silver layer undergoes non-linear deformation beyond the elastic regime as discussed by Lee et al. (2001).

4. Radius of curvature of the thermal deformation at 77 K extrapolated from the measurements at various temperatures are summarized in Table C.3. The thermal deformation of the MLD coating (Sample A) is larger than the eAg coatings (Samples B and C) as expected.

5. The thermal deformation at 77 K derived from the prototyped mirrors are scaled to that of the IRIS imager mirrors, and incorporated into the IRIS imager optics model. The WFE analysis by raytracing shows that the WFE contributions by cooling the mirror coatings are 139.9, 21.1, and 35.9 nm for Samples A, B, and C, respectively. The WFE contributions are significantly reduced to 4.5, 3.3, and 3.3 for Samples A, B, and C after NFIRAOS's DM corrections are applied to the WFE. We find that the DM correction is necessary to reduce WFE contribution by cooling the mirrors well below the WFE requirement of 40 nm.

Based on our results that Sample A has the high reflectance and the small mirror surface deformation when it is cooled, we conclude that the MLD coating (Sample A) is suitable for the IRIS imager optics.

As the next step forward, we are planning to perform the same study with the MLD coating applied to a concave sphere surface using a 160 x 160 x 40 mm substrate whose sizes are comparable to one of the IRIS imager mirrors. The substrate will be cooled to 77 K using a mechanical cooler. This study will provide more realistic and accurate WFE estimates than the current study presented here by (1) minimizing errors in scaling the substrate size, (2) minimizing errors in translating substrate shape, (3) using a curved substrate, and (4) measuring thermal deformation directly at the operating temperature. The measured thermal deformation will also be used to create an accurate FE model which can be applied to all IRIS imager mirrors. Below, we discuss four assumptions made in our study and the future prospects to validate these assumptions.

Assumption 1: Thermal deformation follows the biaxial surface. To investigate residual from the biaxial surface, we decompose the thermal deformation into Zernike polynomials (Figures C.24, C.25, and C.26). We find that the thermal deformation of Samples A, B, and C are mostly composed of low-order terms such as defocus (Z3) and astigmatism (Z4 and Z5). However, it is noted that Sample B has 10 nm in trefoil terms (Z9 and Z10). We are not sure if the existence of the trefoil profiles

is real or not because it is hard to expect that the substrate deforms in this manner considering high uniformity of the substrate and coating layers. Thus, we will confirm reproducibility of the trefoil deformation, and estimate sample variance by multiple measurements of multiple samples. We will investigate how thermal deformation in higher order terms are scaled when the substrate thickness changes using a FE model. We will also investigate how DM correction improves the WFE produced by these higher order terms using the IRIS imager optics model.

Assumption 2: Circular plate substrate deforms in the same manner as rectangular plate substrate. This assumption is validated by the FE analysis which models the substrate deformation when the stress is applied to the substrate surface. It is noted that the assumption is true within 90% of the substrate aperture (i.e., 90 % of the substrate diameter or 90% of a side for the rectangular substrate).

Assumption 3: The Stoney's formula holds for the IRIS imager mirrors which are curved substrates with a non-uniform thickness . The Stoney's formula only applies to a substrate with a uniform thickness. This assumption is based on the fact that thickness variation is small compared to the substrate thickness, and will be investigated by creating a FE model which reproduces the thermal deformation of the prototyped mirrors in our study, and applying the model to the curved substrate with a non-uniform thickness. We may otherwise repeat the thermal deformation measurements for the curved substrates.

Assumption 4: The Stoney's formula holds for the biaxial surface in obtaining the thermal deformation of the substrate with different thickness. This assumption will also be investigated by a FE model or by repeating the thermal deformation measurements for the substrates with different thickness.

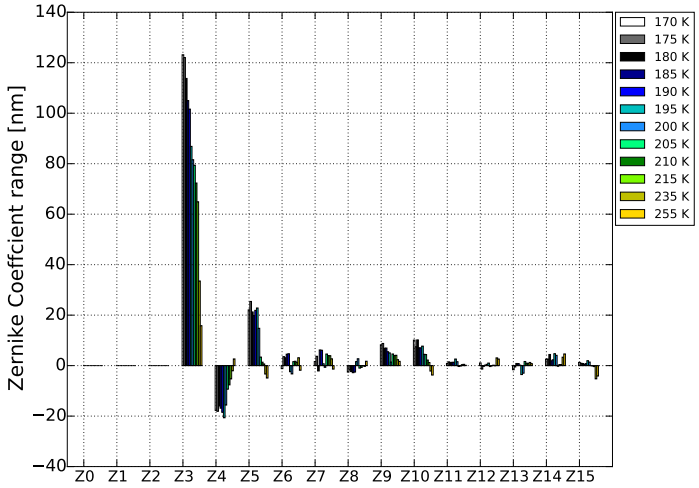

Figure C.24: Zernike polynomial decompositions of WFE (Sample A).

Figure C.25: Zernike polynomial decompositions of WFE (Sample B).

Figure C.26: Zernike polynomial decompositions of WFE (Sample C).

APPENDIX D
TMT/IRIS INSTRUMENTATION: ANALYTICAL MODEL OF UNDERSAMPLING ERRORS

In our optical model (Section 9.2), we add the polishing errors on selected optical surfaces that are major contributors to the high spatial frequency distortion. This appendix is about how we choose these optical surface based on the analytical model of Ellerbroek (2013, hereafter E13). E13 developed an engineering formula to estimate astrometry errors of calibration undersampling (hereafter undersampling error). Undersampling error is residual error due to optical distortion that is sampled by a finite number of reference sources. We thus apply the analytic model of undersampling error for IRIS and NFIRAOS optics, and examine astrometry errors contributed from each of the optical elements.

In the analytic model of E13, undersampling error due to surface errors of optical element j is given by

$$\sigma^2_{\mathrm{US},j} = \frac{64\pi (D/R_{\mathrm{C}_j})^{p-2} (\sigma_{\mathrm{opd}}/D)^2}{I'_1(p) - 16 I_2(p) - 12 I_3(p)} \int_{\frac{D}{\sqrt{\pi} h_j d_{\mathrm{sampling}}}}^{\infty} d\nu \left| \frac{4 J_2(\pi\nu)}{\pi\nu} \right|^2 \nu^{1-p}, \tag{D.1}$$

where D is the telescope aperture diameter, R_{C_j} is the surface radius in telescope object space, σ_{opd} is rms of the optical path error over the surface, p is the power law slope of the surface error PSD, h_j is the conjugate height in the telescope object space, d_{sampling} is the sampling interval, and J_2 is a Bessel function of the first kind. Here, the quantities $I'_1(p)$ and $I_n(p)$ are similar to the integrals computed by Noll (1976)Noll (1976), and defined by

$$I'_1(p) = \frac{\pi^p \Gamma(p+1)}{\{\Gamma[(p+2)/2]\}^2 \Gamma[(p+4)/2] \Gamma(p/2) \sin[\pi(p-2)/2]} \tag{D.2}$$

$$I_n(p) = \frac{\pi^{(p-1)} \Gamma(p+1) \Gamma[(2n-p)/2]}{4\{\Gamma[(p+2)/2]\}^2 \Gamma[(2n+2+p)/2]}, \tag{D.3}$$

where Γ is the Gamma function. Note that this model assumes that the optical distortion is sampled by a grid of reference sources with spacing d_{sampling}, and as-

sumes that the calibration is correct for the distortion with angular frequency less than $1/2d_{\rm sampling}$. More details about the undersampling error is presented in E13 Ellerbroek (2013).

We calculate undersampling error $\sigma_{\rm US}$ as a function of pinhole interval $d_{\rm pinhole}$ (that is $d_{\rm sampling}$ in Eq. D.1) for the optical elements of IRIS and NFIRAOS with the parameters summarized in Tab. D.1 and Tab. D.2, respectively. We use $D = 30$ m for the telescope aperture diameter and $p = 2.5$ for the power law slope of the surface error PSD. Fig.D.1 and Fig.D.2 show the undersampling errors of IRIS and NFIRAOS optical elements, respectively.

We find that optical elements with large h_j and $\sigma_{\rm opd}$, Camera 3rd, Camera 2nd, IRIS Window front, and IRIS Window back, show $\sigma_{\rm US}$ larger than 1 μ arcsec at $d_{\rm pinhole} = 1$ arcsec (and larger than other optical elements by about an order of magnitude). We regard the four optical elements as major contributors to astrometry errors.

Table D.1: Parameters for IRIS optical elements

Surface	Surface irregularity (nm rms)	h^a (km)	R_C (km)	Refractive index	σ^b_{opd} (nm rms)
IRIS Window front	6.0	1037.8	136.0	1.426	2.556
IRIS Window back	6.0	964.2	127.4	1.426	2.556
Flat mirror1	3.0	310.3	51.2	-0.414	4.243
Collimator 1st	6.0	221.6	40.8	-1.000	12.000
Collimator 2nd	6.0	151.1	32.6	-1.000	12.000
Collimator 3rd	6.0	64.2	22.5	-1.000	12.000
Flat mirror2	3.0	16.9	17.0	-0.414	4.243
Filter front	6.0	-20.0	17.3	1.442	2.652
Filter back	6.0	-21.4	17.5	1.442	2.652
F-P1A	6.0	-5.3	15.6	1.813	4.878
B-P1A	6.0	-5.9	15.7	1.813	4.878
F-P1B	6.0	-6.3	15.7	1.486	2.916
B-P1B	6.0	-7.1	15.8	1.486	2.916
F-P2B	6.0	-8.1	15.9	1.486	2.916
B-P2B	6.0	-8.9	16.0	1.486	2.916
F-P2A	6.0	-9.3	16.1	1.813	4.878
B-P2A	6.0	-9.9	16.1	1.813	4.878
Flat mirror3	3.0	-60.6	22.1	-0.414	4.243
Camera 1st	6.0	-115.4	28.5	-1.000	12.000
Camera 2nd	6.0	-328.6	53.3	-1.000	12.000
Camera 3rd	6.0	-887.8	118.5	-1.000	12.000

a: Negative value means that the conjugate surface is under the ground in telescope object space.
b: Optical path error over the surface is defined as |(Surface irregularity)*((Refractive index) - 1) |.

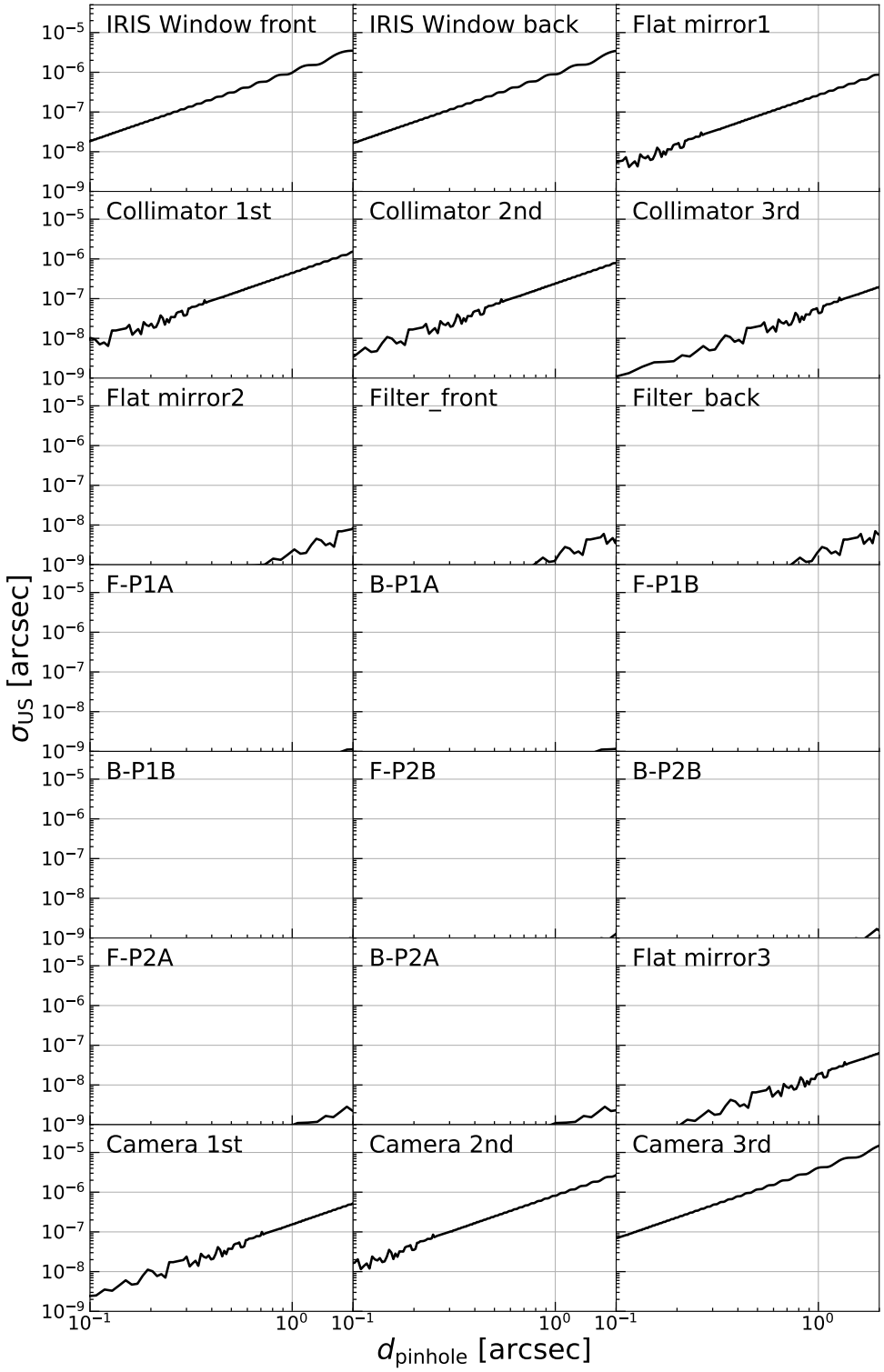

Figure D.1: Undersampling error σ_{US} as a function of pinhole interval $d_{pinhole}$ for the optical elements of IRIS. Note that F-P1A, B-P1A, F-P1B, B-P1B, F-P2B, B-P2B result in σ_{US} below 10^{-9} μ arcsec across the shown $d_{pinhole}$.

Table D.2: Parameters for NFIRAOS optical elements

Surface	Surface irregularity (nm rms)	h^a (km)	R_C (km)	Refractive index	σ^b_{opd} (nm rms)
OAP 1	6.0	49.4	20754.5	-1	12.000
DM11.8	0.0	11.8	16376.7	-1	0.000
OAP 2	6.0	-37.0	19314.6	-1	12.000
OAP 3	6.0	35.6	19145.2	-1	12.000
DM0	0.0	0.1	15011.3	-1	0.000
beamsplitter	12.5	-9.7	16125.3	1.426	5.325
rear on Sci BS	12.5	-10.1	16177.3	1.426	5.325
OAP 4	6.0	-44.1	20136.1	-1	12.000
Sci fld mirror	15.0	-85.8	24996.8	-1	30.000

a: Negative value means that the conjugate surface is under the ground in telescope object space.
b: Optical path error over the surface is defined as |(Surface irregularity)*((Refractive index) - 1) |.

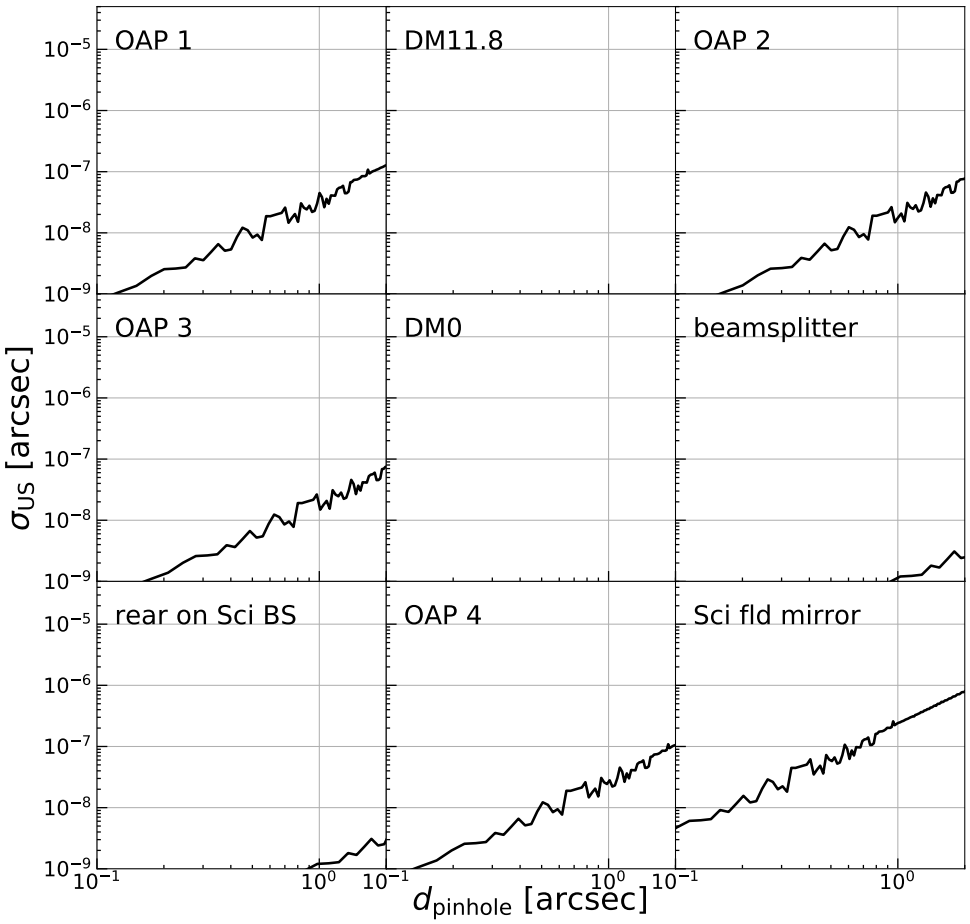

Figure D.2: Same as Fig. D.1, but for the optical elements of NFIRAOS. Note that DM11.8 and DM0 result in $\sigma_{\mathrm{US}} = 0$ since their σ_{opd} is set to 0.

REFERENCES

Adams, J. J., Blanc, G. A., Hill, G. J., et al. 2011, ApJS, 192, 5

Adelberger, K. L., Shapley, A. E., Steidel, C. C., et al. 2005, ApJ, 629, 636

Adelberger, K. L., Steidel, C. C., Shapley, A. E., & Pettini, M. 2003, ApJ, 584, 45

Alam, S., Albareti, F. D., Allende Prieto, C., et al. 2015, ApJS, 219, 12

Anderson, J., & King, I. R. 2004, Instrument Science Report ACS 2004-15, 51 pages, 3

Arrigoni Battaia, F., Prochaska, J. X., Hennawi, J. F., et al. 2018, MNRAS, 473, 3907

Asplund, M., Grevesse, N., Sauval, A. J., & Scott, P. 2009, ARA&A, 47, 481

Becker, G. D., Bolton, J. S., Haehnelt, M. G., & Sargent, W. L. W. 2011, MNRAS, 410, 1096

Becker, G. D., Bolton, J. S., & Lidz, A. 2015, PASA, 32, e045

Becker, G. D., Hewett, P. C., Worseck, G., & Prochaska, J. X. 2013, MNRAS, 430, 2067

Behroozi, P. S., Wechsler, R. H., & Conroy, C. 2013, ApJ, 770, 57

Berry, M., Gawiser, E., Guaita, L., et al. 2012, ApJ, 749, 4

Bertin, E., & Arnouts, S. 1996, A&AS, 117, 393

Bertschinger, E. 1995, ArXiv Astrophysics e-prints, astro-ph/9506070

Bielby, R. M., Shanks, T., Crighton, N. H. M., et al. 2017, MNRAS, 471, 2174

Boera, E., Murphy, M. T., Becker, G. D., & Bolton, J. S. 2014, MNRAS, 441, 1916

Brammer, G. B., van Dokkum, P. G., & Coppi, P. 2008, ApJ, 686, 1503

Bruzual, G., & Charlot, S. 2003, MNRAS, 344, 1000

Cai, Z., Fan, X., Peirani, S., et al. 2016, ApJ, 833, 135

Cai, Z., Fan, X., Yang, Y., et al. 2017a, ApJ, 837, 71

Cai, Z., Fan, X., Bian, F., et al. 2017b, ApJ, 839, 131

Calzetti, D., Armus, L., Bohlin, R. C., et al. 2000, ApJ, 533, 682

Cantalupo, S., Arrigoni-Battaia, F., Prochaska, J. X., Hennawi, J. F., & Madau, P. 2014, Nature, 506, 63

Cantalupo, S., Lilly, S. J., & Haehnelt, M. G. 2012, MNRAS, 425, 1992

Cantalupo, S., Pezzulli, G., Lilly, S. J., et al. 2019, MNRAS, 483, 5188

Capak, P., Aussel, H., Ajiki, M., et al. 2007, ApJS, 172, 99

Casali, M., Adamson, A., Alves de Oliveira, C., et al. 2007, A&A, 467, 777

Caucci, S., Colombi, S., Pichon, C., et al. 2008, MNRAS, 386, 211

Cen, R., Miralda-Escudé, J., Ostriker, J. P., & Rauch, M. 1994, ApJ, 437, L9

Chabrier, G. 2003, PASP, 115, 763

Chiang, Y.-K., Overzier, R., & Gebhardt, K. 2014, ApJ, 782, L3

Chiang, Y.-K., Overzier, R. A., Gebhardt, K., et al. 2015, ApJ, 808, 37

Ciardullo, R., Gronwall, C., Wolf, C., et al. 2012, ApJ, 744, 110

Ciardullo, R., Gronwall, C., Adams, J. J., et al. 2013, ApJ, 769, 83

Crighton, N. H. M., Bielby, R., Shanks, T., et al. 2011, MNRAS, 414, 28

Cucciati, O., Zamorani, G., Lemaux, B. C., et al. 2014, A&A, 570, A16

Curran, P. A. 2015, ArXiv e-prints, arXiv:1411.3816

Dekel, A., Birnboim, Y., Engel, G., et al. 2009, Nature, 457, 451

D'Odorico, V., Bruscoli, M., Saitta, F., et al. 2008, MNRAS, 389, 1727

Eisenstein, D. J., & Hut, P. 1998, ApJ, 498, 137

Eisenstein, D. J., Weinberg, D. H., Agol, E., et al. 2011, AJ, 142, 72

Ellerbroek, B. 2013, Journal of Astrophysics and Astronomy, 552, A41

Faucher-Giguère, C.-A., Prochaska, J. X., Lidz, A., Hernquist, L., & Zaldarriaga, M. 2008, ApJ, 681, 831

Ferland, G. J., Porter, R. L., van Hoof, P. A. M., et al. 2013, RMxAA, 49, 137

Fox, A., & Davè, R. 2017, Gas Accretion onto Galaxies, Vol. 430 (Basel: Springer International Publishing AG), doi:10.1007/978-3-319-52512-9

Fumagalli, M., O'Meara, J. M., & Prochaska, J. X. 2016, MNRAS, 455, 4100

Fumagalli, M., O'Meara, J. M., Prochaska, J. X., & Worseck, G. 2013, ApJ, 775, 78

Gronwall, C., Ciardullo, R., Hickey, T., et al. 2007, ApJ, 667, 79

Gunn, J. E., & Peterson, B. A. 1965, ApJ, 142, 1633

Haardt, F., & Madau, P. 1996, ApJ, 461, 20

—. 2012, ApJ, 746, 125

Harikane, Y., Ouchi, M., Ono, Y., et al. 2016, ApJ, 821, 123

Hennawi, J. F., Prochaska, J. X., Cantalupo, S., & Arrigoni-Battaia, F. 2015, Science, 348, 779

Hernquist, L., Katz, N., Weinberg, D. H., & Miralda-Escudé, J. 1996, ApJ, 457, L51

Herriot, G., Andersen, D., Atwood, J., et al. 2010, Society of Photo-Optical Instrumentation Engineers (SPIE) Conference Series, Vol. 7736, NFIRAOS: TMT's facility adaptive optics system, 77360B

Herriot, G., Andersen, D., Atwood, J., et al. 2014, in , 914810

Hill, G. J. 2014, Advanced Optical Technologies, 3, 265

Hill, G. J., & HETDEX Consortium. 2016, in Astronomical Society of the Pacific Conference Series, Vol. 507, Multi-Object Spectroscopy in the Next Decade: Big Questions, Large Surveys, and Wide Fields, ed. I. Skillen, M. Barcells, & S. Trager, 393

Hill, G. J., Gebhardt, K., Komatsu, E., et al. 2008, in Astronomical Society of the Pacific Conference Series, Vol. 399, Panoramic Views of Galaxy Formation and Evolution, ed. T. Kodama, T. Yamada, & K. Aoki, 115

Hill, G. J., Kelz, A., Lee, H., et al. 2018, in Society of Photo-Optical Instrumentation Engineers (SPIE) Conference Series, Vol. 10702, Proc. SPIE, 107021K

Hinshaw, G., Larson, D., Komatsu, E., et al. 2013, ApJS, 208, 19

Hui, L., & Gnedin, N. Y. 1997, MNRAS, 292, 27

Ichikawa, T., Suzuki, R., Tokoku, C., et al. 2006, Society of Photo-Optical Instrumentation Engineers (SPIE) Conference Series, Vol. 6269, MOIRCS: multi-object infrared camera and spectrograph for SUBARU, 626916

Ilbert, O., Capak, P., Salvato, M., et al. 2009, ApJ, 690, 1236

Inoue, A. K., Shimizu, I., Iwata, I., & Tanaka, M. 2014, MNRAS, 442, 1805

Kashikawa, N., Kitayama, T., Doi, M., et al. 2007, ApJ, 663, 765

Kelz, A., Jahn, T., Haynes, D., et al. 2014, Society of Photo-Optical Instrumentation Engineers (SPIE) Conference Series, Vol. 9147, VIRUS: assembly, testing and performance of 33,000 fibres for HETDEX, 914775

Kereš, D., Katz, N., Weinberg, D. H., & Davé, R. 2005, MNRAS, 363, 2

Kikuta, S., Imanishi, M., Matsuoka, Y., et al. 2017, ApJ, 841, 128

Kikuta, S., Matsuda, Y., Cen, R., et al. 2019, PASJ, 71, L2

Konno, A., Ouchi, M., Nakajima, K., et al. 2016, ApJ, 823, 20

Kriek, M., van Dokkum, P. G., Labbé, I., et al. 2009, ApJ, 700, 221

Larkin, J. E., Moore, A. M., Wright, S. A., et al. 2016, in , 99081W

Lee, H., Rosakis, A. J., & Freund, L. B. 2001, Journal of Applied Physics, 89, 6116

Lee, K.-G., Hennawi, J. F., White, M., Croft, R. A. C., & Ozbek, M. 2014a, ApJ, 788, 49

Lee, K.-G., Suzuki, N., & Spergel, D. N. 2012, AJ, 143, 51

Lee, K.-G., Bailey, S., Bartsch, L. E., et al. 2013, AJ, 145, 69

Lee, K.-G., Hennawi, J. F., Stark, C., et al. 2014b, ApJ, 795, L12

Lee, K.-G., Hennawi, J. F., White, M., et al. 2016, ApJ, 817, 160

Lee, K.-G., Krolewski, A., White, M., et al. 2018, ApJS, 237, 31

Lee, K.-S., Giavalisco, M., Conroy, C., et al. 2009, ApJ, 695, 368

Leibler, C. N., Cantalupo, S., Holden, B. P., & Madau, P. 2018, MNRAS, 480, 2094

Leung, A. S., Acquaviva, V., Gawiser, E., et al. 2017, ApJ, 843, 130

Lindegren, L. 1978, in IAU Colloq. 48: Modern Astrometry, 197

Lukić, Z., Stark, C. W., Nugent, P., et al. 2015, MNRAS, 446, 3697

Martin, D. C., Fanson, J., Schiminovich, D., et al. 2005, ApJ, 619, L1

Mawatari, K., Inoue, A. K., Kousai, K., et al. 2016, ApJ, 817, 161

McCracken, H. J., Milvang-Jensen, B., Dunlop, J., et al. 2012, A&A, 544, A156

McDonald, P., Seljak, U., Burles, S., et al. 2006, ApJS, 163, 80

McQuinn, M. 2016, ARA&A, 54, 313

Meiksin, A., Bolton, J. S., & Tittley, E. R. 2015, MNRAS, 453, 899

Meiksin, A. A. 2009, Reviews of Modern Physics, 81, 1405

Miralda-Escudé, J., Cen, R., Ostriker, J. P., & Rauch, M. 1996, ApJ, 471, 582

Misawa, T., Charlton, J. C., & Narayanan, A. 2008, ApJ, 679, 220

Mo, H., van den Bosch, F. C., & White, S. 2010, Galaxy Formation and Evolution (Cambridge: Cambridge Univ. Press)

Moster, B. P., Somerville, R. S., Maulbetsch, C., et al. 2010, ApJ, 710, 903

Mukae, S., Ouchi, M., Kakiichi, K., et al. 2017, ApJ, 835, 281

Muzzin, A., Marchesini, D., Stefanon, M., et al. 2013a, ApJS, 206, 8

—. 2013b, ApJ, 777, 18

Myers, A. D., Palanque-Delabrouille, N., Prakash, A., et al. 2015, ApJS, 221, 27

Noll, R. J. 1976, Journal of the Optical Society of America (1917-1983), 66, 207

Noterdaeme, P., Petitjean, P., Carithers, W. C., et al. 2012, A&A, 547, L1

Oke, J. B., & Gunn, J. E. 1983, ApJ, 266, 713

Oke, J. B., Cohen, J. G., Carr, M., et al. 1995, PASP, 107, 375

Osterbrock, D. E. 1989, Astrophysics of gaseous nebulae and active galactic nuclei

Palanque-Delabrouille, N., Yèche, C., Borde, A., et al. 2013, A&A, 559, A85

Pâris, I., Petitjean, P., Ross, N. P., et al. 2017, A&A, 597, A79

Pâris, I., Petitjean, P., Aubourg, É., et al. 2018, A&A, 613, A51

Peacock, J. A., & Smith, R. E. 2000, MNRAS, 318, 1144

Pedichini, F., Giallongo, E., Ragazzoni, R., et al. 2003, in Proc. SPIE, Vol. 4841, Instrument Design and Performance for Optical/Infrared Ground-based Telescopes, ed. M. Iye & A. F. M. Moorwood, 815–826

Pichon, C., Vergely, J. L., Rollinde, E., Colombi, S., & Petitjean, P. 2001, MNRAS, 326, 597

Pobell, F. 2007, Matter and Methods at Low Temperatures (Springer-Verlag Berlin Heidelberg)

Prochaska, J. X., Hennawi, J. F., Lee, K.-G., et al. 2013, ApJ, 776, 136

Rakic, O., Schaye, J., Steidel, C. C., & Rudie, G. C. 2012, ApJ, 751, 94

Ramsey, L. W., Sebring, T. A., & Sneden, C. A. 1994, Society of Photo-Optical Instrumentation Engineers (SPIE) Conference Series, Vol. 2199, Spectroscopic survey telescope project, ed. L. M. Stepp, 31–40

Rauch, M. 1998, ARA&A, 36, 267

Reed, D. S., Bower, R., Frenk, C. S., Jenkins, A., & Theuns, T. 2007, MNRAS, 374, 2

Rudie, G. C., Steidel, C. C., Trainor, R. F., et al. 2012, ApJ, 750, 67

Sanders, D. B., Salvato, M., Aussel, H., et al. 2007, ApJS, 172, 86

Sanders, G. H. 2013, Journal of Astrophysics and Astronomy, 34, 81

Schechter, P. 1976, ApJ, 203, 297

Schöck, M., Do, T., Ellerbroek, B. L., et al. 2014, in , 91482L

Schöck, M., Andersen, D., Rogers, J., et al. 2016, in , 9908AD

Scoville, N., Aussel, H., Brusa, M., et al. 2007, ApJS, 172, 1

Scoville, N., Arnouts, S., Aussel, H., et al. 2013, ApJS, 206, 3

Service, M., Lu, J. R., Chun, M., et al. 2019, Journal of Astronomical Telescopes, Instruments, and Systems, 5, 039005

Shapley, A. E., Steidel, C. C., Pettini, M., & Adelberger, K. L. 2003, ApJ, 588, 65

Simcoe, R. A. 2011, ApJ, 738, 159

Skidmore, W., TMT International Science Development Teams, & Science Advisory Committee, T. 2015, Research in Astronomy and Astrophysics, 15, 1945

Sobral, D., Matthee, J., Best, P., et al. 2017, MNRAS, 466, 1242

Somerville, R. S., & Davé, R. 2015, ARA&A, 53, 51

Stark, C. W., White, M., Lee, K.-G., & Hennawi, J. F. 2015, MNRAS, 453, 311

Steidel, C. C., Adelberger, K. L., Dickinson, M., et al. 1998, ApJ, 492, 428

Steidel, C. C., Erb, D. K., Shapley, A. E., et al. 2010, ApJ, 717, 289

Steidel, C. C., Shapley, A. E., Pettini, M., et al. 2004, ApJ, 604, 534

Stoney, G. G. 1909, Proceedings of the Royal Society of London A: Mathematical, Physical and Engineering Sciences, 82, 172

Susa, H., & Umemura, M. 2000, ApJ, 537, 578

—. 2004, ApJ, 600, 1

Suzuki, N., Tytler, D., Kirkman, D., O'Meara, J. M., & Lubin, D. 2005, ApJ, 618, 592

Taniguchi, Y., Scoville, N., Murayama, T., et al. 2007, ApJS, 172, 9

Tejos, N., Morris, S. L., Finn, C. W., et al. 2014, MNRAS, 437, 2017

Teyssier, R. 2002, A&A, 385, 337

Theuns, T., Mo, H. J., & Schaye, J. 2001, MNRAS, 321, 450

Thomas, R., Le Fèvre, O., Cassata, V. L. B. P., et al. 2014, ArXiv e-prints, arXiv:1411.5692

Tomczak, A. R., Quadri, R. F., Tran, K.-V. H., et al. 2014, ApJ, 783, 85

Tsuzuki, T., Suzuki, R., Harakawa, H., et al. 2016, Society of Photo-Optical Instrumentation Engineers (SPIE) Conference Series, Vol. 9908, The Infrared Imaging Spectrograph (IRIS) for TMT: optical design of IRIS imager with "co-axis double TMA", 9908AE

Tummuangpak, P., Bielby, R. M., Shanks, T., et al. 2014, MNRAS, 442, 2094

Turner, M. L., Schaye, J., Steidel, C. C., Rudie, G. C., & Strom, A. L. 2014, MNRAS, 445, 794

Umehata, H., Fumagalli, M., Smail, I., et al. 2019, arXiv e-prints, arXiv:1910.01324

Vale, A., & Ostriker, J. P. 2004, MNRAS, 353, 189

van de Voort, F. 2017, Astrophysics and Space Science Library, Vol. 430, The Effect of Galactic Feedback on Gas Accretion and Wind Recycling, ed. A. Fox & R. Davé, 301

Vernet, J., Dekker, H., D'Odorico, S., et al. 2011, A&A, 536, A105

Viel, M., Schaye, J., & Booth, C. M. 2013, MNRAS, 429, 1734

Wall, J. V., & Jenkins, C. R. 2012, Practical Statistics for Astronomers (Cambridge: Cambridge Univ. Press)

Weinberg, D. H., Davé, R., Katz, N., & Kollmeier, J. A. 2003, in American Institute of Physics Conference Series, Vol. 666, The Emergence of Cosmic Structure, ed. S. H. Holt & C. S. Reynolds, 157–169

Weinberg, D. H., Burles, S., Croft, R. A. C., et al. 1998, ArXiv Astrophysics e-prints, astro-ph/9810142

White, M., Pope, A., Carlson, J., et al. 2010, ApJ, 713, 383

Wright, S. A., Walth, G., Do, T., et al. 2016, in , 990905

Yang, Y., Zabludoff, A., Jahnke, K., & Davé, R. 2014, ApJ, 793, 114

Young, P., Sargent, W. L. W., & Boksenberg, A. 1982, ApJ, 252, 10

Zhang, Y., Anninos, P., & Norman, M. L. 1995, ApJ, 453, L57